UNIVERSITY OF CALIFORNIA, SAN DIEGO

Investigating and Optimizing Interfacial Properties of Electrode Materials for Lithium-ion and Sodium-ion Batteries

A dissertation submitted in partial satisfaction of the
requirements for the degree Doctor of Philosophy

in

Materials Science and Engineering

by

Judith E. Alvarado

Committee in charge:

Professor Ying Shirley Meng, Chair
Professor Renkun Chen
Professor Darren J. Lipomi
Professor Ping Liu
Professor Yu Qiao

2017

The Dissertation of Judith E. Alvarado is approved, and it is acceptable in quality and form for publication on microfilm and electronically:

Chair

University of California, San Diego

2017

DEDICATION

To my parents: Irma and Ricardo Alvarado, Monique and Walter Kim

To my loving and supportive husband, Emil Kim

TABLE OF CONTENTS

LIST OF FIGURES

LIST OF TABLES

LIST OF SCHEMES

ACKNOWLEDGEMENTS

I would like to acknowledge that it takes a village to obtain a PhD and any success that I have had as a researcher has been due to the infinite support of many. First, I would like to thank my PhD advisor Dr. Ying Shirley Meng for her generous guidance, mentorship, and financial support. It has been an honor working alongside her. Because of Dr. Meng, I have accomplished things I had never thought possible. Thank you for believing in me from the beginning. I would also like to express my deepest gratitude to my committee members: Professor Ping Liu, Professor Darren J. Lipomi, Professor Yu Qiao, and Professor Renkun Chen for their time and guidance.

I am especially grateful for my loving family. I would like to thank my parents, Ricardo and Irma Alvarado and Walter and Monique Kim, who came to this country with nothing and gave their children everything. They have influenced, inspired, and shown me the true meaning of hard work and dedication! I am the person I am today because of my parents. I would like to thank my loving husband, Emil Kim, for taking this journey with me. His endless support, love, encouragement, and understanding I could not do without. When things got difficult he was always there to reassure me that everything works out in the end. Thank you for empowering me to be the strong and confident person that I am today. To my siblings Jessica Alvarado, Ricardo Alvarado Jr, Stelet Kim and Parag Ladhawala, thank you for all your support, love, and advice throughout my PhD. They are some of the reasons why I am standing in the position I am in today. I would like to thank my extended family; in particular, Mary and Martin Alvarado, for their encouragement and love throughout my academic career. I would also like to thank my science sisters Brenda Andrade, Eaindar Soe, and Heidi Redden for encouraging me and

inspiring me in all aspects of life. I am honored to have such intelligent, strong, and inspiring women in my life.

My research could not have been completed without the help of many brilliant minds. I would like to acknowledge my collaborators and co-authors at UC San Diego: Dr. Chuze Ma, Dr. Jing Xu, Dr. Mahsa Sina, Dr. Minghao Zhang, Dr. Xuefeng Wang, Mr. Shen Wang, Mrs. Jungwoo Lee, Mr. Thomas Wynn, Ms. Kimberly Nguyen, and Mr. Moses Kodur with whom I have had thoughtful discussions and long but fulfilling research nights. The Laboratory for Energy Storage and Conversion group (past and present) have helped, encouraged, and motivated me to become a better researcher. I would also like to express my deepest gratitude to Dr. Kang Xu from the US Army Research Laboratory for allowing me to intern and work alongside his talented group. I learned so much from Dr. Xu and his group in such a short period of time. Additionally, I would like to thank my external collaborators and co-authors: Dr. Thomas Yersak at General Motors, Dr. Marshall Schroeder, Dr. Oleg Borodin, Dr. Eric Gobrogge, Dr. Marco Olguin, and Dr. Michael Ding at the US Army Research Laboratory, Dr. Kjell Schroder and Dr. Keith J. Stevenson at University of Texas at Austin, Dr. Nancy Dudney and Juchuan Li at Oak Ridge National Laboratory, and Mr. Hitoshi Shobukawa at Asahi–Kasei Corporation of Japan for their help in advancing my research projects. I would like to acknowledge that some of the figures in this dissertation were designed and created by Emil Kim. Every single person played a vital role in completing each research project, and I truly appreciate all of their hard work and dedication.

Finally, I would like to thank my funding sources: Energy Efficiency and Renewable Energy, Office of Vehicle Technologies, U.S. Department of Energy under Contract No. DEAC02-05CH11231, Subcontract No. 7073923 under the Advanced Battery Materials

Research (BMR) Program and the USA National Science Foundation under award number 1057170, 1608968, the AGEP GSR fellowship—a supplement fund to the DMR1057170, and the Oakridge Associate Universities Journeymen fellowship with the US Army Research Laboratory.

Chapter 4, in full, is a reprint of the material "The Effect of Fluoroethylene Carbonate as an Additive on the Solid Electrolyte Interphase on Silicon Lithium-ion Electrodes" as it appears in the Chemistry of Materials, Schroder, K; Alvarado, J; Yersak, T.A; Li, J; Dudney, N; Webb, L; Meng, Y.S; Stevenson, K.J, 2015, 27, 5531. The dissertation author was the co-primary investigator and author of this paper. All of the electrochemical tests were performed by the author except for the TOF-SIMS data analysis and interpretation. Both Schroder and the author designed and analyzed, and wrote the results.

Chapter 5, in full, is a reprint of the material "Direct Visualization of the Solid Electrolyte Interphase and Its Effects on Silicon Electrochemical Performance" as it appears in Advanced Materials Interfaces, Sina, M; Alvarado, J; Shobukawa, H; Alexander, C; Manichev, V; Feldman, L; Gustafsson, T; Stevenson, K; Meng, Y.S, 2016, 1600438. The dissertation author was the co-primary investigator and author of this paper. All of the experiment parts were performed by the author except for the HIM and STEM EELS analysis.

Chapter 6, in full, is currently being prepared for submission for publication "Bridging the Gap: Electrolytes for Efficient Coupling of Lithium Metal Anodes with Next Generation Cathodes" Alvarado, J; Schroeder, M; Borodin, O; Lee, J-W; Wang, X; Wynn, T; Zhang, M; Xu, K; Meng, Y.S. The dissertation author was the co-primary investigator and author of this paper. All of the experiment parts were performed by the author except for the Cryo-FIB.

Chapter 7, in full, is currently being prepared for submission for publication “Solvent-Salt Synergy Offers Fresh Pathway to Unlock Next Generation Li-ion Chemistries” Alvarado, J; Schroder, M; Borodin, O; Gobrogge, E; Olguin, M; Ding, M; Meng, Y.S.; Xu, K. The dissertation author was the co-primary investigator and author of this paper. All of the experiment parts were performed by the author except for the full cell electrochemistry data, FTIR analysis, conductivity measurements, and computational analysis.

Chapter 8, in full, is a reprint of the material “Improvement of the Cathode Electrolyte Interphase on P2-$Na_{2/3}Ni_{1/3}Mn_{2/3}O_2$ by Atomic Layer Deposition” as it appears in ACS Applied Materials and Interfaces, Alvarado, J; Ma, C; Wang, S; Nguyen, K; Kodur, M; Meng, Y.S, 2017, 9 (31), 26518. The dissertation author was the co-primary investigator and author of this paper. The author conducted all of the experimental test and data analysis.

VITA

2009 Bachelor of Science in Chemistry

California State University, San Bernardino

2012 Master of Science in Inorganic Chemistry

California State University, Los Angeles

2017 Doctor of Philosophy in Materials Science and Engineering

University of California, San Diego

PUBLICATIONS

1. **Alvarado, J**; Hanrahan, G; Nguyen, H.T.H; Gomez, F.A "Implementation of a Genetically Tuned Neural Platform in Optimizing Fluorescence from Receptor–Ligand Binding Interactions on Microchips" Electrophoresis, 2012, 33, 2711

2. Lu, Y.C; Ma, C; **Alvarado, J**; Kidera, T; Dimov, N; Meng, Y.S; Okada, S "Electrochemical Properties of Tin Oxide Anodes for Sodium-Ion Batteries" Journal of Power Sources, 2015, 284, 287

3. Schroder, K***; Alvarado, J***; Yersak, T.A; Li, J; Dudney, N; Webb, L; Meng, Y.S; Stevenson, K.J "The Effect of Fluoroethylene Carbonate as an Additive on the Solid Electrolyte Interphase on Silicon Lithium-ion Electrodes" Chemistry of Materials, 2015, 27 (16), 5531

4. Lu, Y.C; Ma, C; **Alvarado, J**; Kidera, T; Dimov, N; Meng, Y.S; Okada, S "Improved Electrochemical Performance of Tin-sulfide Anodes for Na-ion Battery" Journal of Materials Chemistry A, 2015,3, 16971

5. Ma, C; Xu, J; **Alvarado, J**; Qu, B; Somnerville, J; Lee, J.Y; Meng, Y.S "Investigating the Energy Storage Mechanism of SnS_2-rGO Composite Anode for Advanced Na-ion Batteries" Chemistry of Materials, 2015, 27 (16), 5633

6. Sina, M*; **Alvarado, J***; Shobukawa, H; Alexander, C; Manichev, V; Feldman, L; Gustafsson, T; Stevenson, K; Meng, Y.S "Direct Visualization of the Solid Electrolyte Interphase and Its Effects on Silicon Electrochemical Performance" Advanced Materials Interfaces, 2016, 1600438

7. Shobukawa, H; Shin, J-W; **Alvarado, J**; Rustomji, C.J; Meng, Y.S "Electrochemical reaction and surface chemistry for performance enhancement of a Si composite anode using a bis(fluorosulfonyl)imide-based ionic liquid", Journal of Materials Chemistry A, 2016, 4, 15117

8. Clément, R.J; Xu, J; Middlemiss, D; **Alvarado, J**; Ma, C; Meng, Y.S; Grey, C.P. "Direct evidence for high Na^+ mobility and high voltage structural processes in P2-$Na_x[Li_yNi_zMn_{1-y-z}]O_2$ (x, y, z≤ 1) cathodes from solid-state NMR and DFT calculations" Journal of Materials Chemistry A, 2017, 5, 41

9. Shobukawa, H; **Alvarado, J**; Yang, Y; Meng, Y.S "Electrochemical Performance and Interfacial Investigation on Si Composite Anode for Lithium Ion Batteries in Full Cell" Journal of Power Sources, 2017, 359, 173

10. **Alvarado, J***; Ma, C*; Wang, S; Nguyen, K; Kodur, M; Meng, Y.S "Improvement of the Cathode Electrolyte Interphase of P2-$Na_{2/3}Ni_{1/3}Mn_{2/3}O_2$ by Atomic Layer Deposition" ACS Applied Materials & Interfaces, 2017, 9(31), 26518

11. **Alvarado, J***; Schroeder, M*; Borodin, O; Gobrogge, E; Olguin, M; Ding, M; Meng, Y.S; Xu, K "Solvent-Salt Synergy Offers Fresh Pathway to Unlock Next Generation Li-Ion Chemistries" (in preparation)

12. **Alvarado, J***; Schroeder, M*; Lee, J-W .Z; Wang, X; Borodin, O; Wynn, T; Zhang, M; Xu, K; Meng, Y.S "Bridging the Gap: Electrolytes for Efficient Coupling of Lithium Metal Anodes with Next Generation Cathodes" (in preparation)

13. Wang, X; Zhang, M; **Alvarado, J**; Wang, S; Sina, M; Lu, Bingyu; Bouer, J; Xu, Wu; Xiao, J; Meng, Y.S "New Insights on the Structure of Electrochemically Deposited Lithium Metal and Its Solid Electrolyte Interphase via Cryogenic TEM" ACS Nano Letters, 2017, DOI: 10.1021/acs.nanolett.7b03606

14. Radin, M.D; **Alvarado, J**; Meng, Y.S; Van der Ven, A "Role of Crystal Symmetry in the Reversibility of Stacking-Sequence Changes in Layered Intercalation Electrodes" ACS Nano Letters, 2017, DOI: 10.1021/acs.nanolett.7b03989

15. Li, H; Tang, H; Ma, C; Bai, Y; **Alvarado, J**; Radhakrishnan, B; Ong, S.P; Wu, F; Meng, Y.S "Understanding the Electrochemical Mechanisms Induced By Gradient Mg2+ Distribution of Na-rich $Na_{3+x}V_{2-x}Mg_x(PO_4)_3$/C for Sodium ion Batteries" (submitted)

ABSTRACT OF THE DISSERTATION

Investigating and Optimizing Interfacial Properties of Electrode Materials for Lithium-ion and Sodium-ion Batteries

by

Judith E. Alvarado

Doctor of Philosophy in Materials Science and Engineering

University of California, San Diego, 2017

Professor Ying Shirley Meng, Chair

The current commercial lithium ion battery utilizes “host-guest” electrodes that allow for the intercalation of lithium between the crystal lattice of the anode and cathode materials. The lithium ions are transported through the electrolyte medium during the charge/discharge process. Given their success, lithium ion batteries have now penetrated the electric vehicle market and large scale grid storage, which require batteries with much higher energy densities. To meet this

demand, alternative anode and cathode chemistries are required. Consequently, this will put high strain on the electrolyte which will decompose at both low and high potentials to form a passivation layer known as the solid electrolyte interphase (SEI).

Herein, the fundamental reduction mechanism of fluoroethylene carbonate (FEC) is investigated as an additive for conventional electrolytes to improve the SEI formation on various silicon anodes using a series of advanced spectroscopic and microscopic techniques. For the first time, the direct visualization of the SEI generated on the silicon nanoparticle is investigated by scanning electron microscopy and its chemical composition by electron energy loss spectroscopy. The SEI is further investigated on lithium metal anode. Highly concentrated bisalt ether electrolytes form a SEI that is dominated by salt decomposition rather than solvent decomposition, which enables high lithium metal cycling efficiencies.

At high potentials the electrolyte oxidizes on the cathode to form the cathode electrolyte interphase (CEI). With the discovery of 5V cathode materials, a new electrolyte is required. Therefore, sulfone based electrolytes are studied as potential high voltage electrolyte. Combined with lithium bis(fluorosulfonyl) imide, this solvent-salt synergy addresses the traditional performance issues that develop at the interface of high voltage cathodes.

The factors that affect the cycling performance of cathode materials for lithium ion batteries are also seen in sodium ion batteries. Atomic layer deposition (ALD) is widely used to improve the cycling performance, coulombic efficiency of batteries, and to maintain electrode integrity for LIBs. Therefore, this approach is used to understand the effect of Al_2O_3 ALD coating on P2-$Na_{2/3}Ni_{1/3}Mn_{2/3}O_2$ cathodes, which lowers the cathode impedance and improves particle morphology after cycling. Improving the electrode-electrolyte interface is critical to the development of next generation high density energy storage systems.

Chapter 1. Motivation and Outline

The unprecedented warming trend over the last decade due to human activities has raised concerns, sparking a global effort to combat climate change. One way is to place stringent emissions requirements on industries that rely heavily on the burning of fossil fuels , another is to decrease our dependence on fossil fuels altogether; specifically, to move away from oil as our main source of energy for transportation. Therefore, we require alternative "green" energy that is efficient, reliable, inexpensive, and energy dense in order to spearhead the electric vehicle (EV) revolution and to reduce greenhouse gases that lead to global warming.

Given their vast success in the portable electronic market, lithium ion batteries are the logical energy source to power EVs. The market for hybrid EVs has expanded in recent years, and EVs are now mass produced by nearly every major automotive manufacturer. Though hybrid EVs still rely on the partial use of fossil fuels, consumers have embraced the improvement over the traditional combustion engine. Increasingly, the demand for more environmentally friendly transportation continues to grow, prompting the desire for fully electric vehicles. The current intercalation chemistry in commercial lithium ion batteries has enabled some automotive companies to make fully electric vehicles commercially available. By connecting battery packs consisting of hundreds of cells in series and in parallel, the energy can be combined to increase the energy density, thereby further improving the driving range.[1] However, the driving range of the battery pack still remains a barrier for purchase, as consumers' biggest fear is to become stranded without power. This driving anxiety is a major driving force for researchers to develop new high energy density batteries that, when combined in a battery pack, can increase the energy density to 500 Wh/kg, which subsequently increases the driving range exponentially.

As researchers seek alternative high energy cathode and anode materials to improve the overall energy density of lithium ion batteries, the electrolyte must also be considered. The beauty of the current lithium ion battery is that the electrolyte forms a stable passivation layer known as the solid electrolyte interphase (SEI), which is ionically conductive and electronically insulating. This prevents the battery from undergoing self-discharge and also contributes to the long term cycle life. Therefore, during electrochemical cycling, the electrode-electrolyte interface is vital to the success of the next generation lithium ion batteries.

On the anode side, graphite is a ubiquitous anode found in all commercial lithium ion batteries due to its stable SEI and structure. However, the relatively low theoretical capacity of 372 mAh/g has prompted researchers to seek anode alternatives with a significantly higher capacity to increase the cell's energy density. Anodes such as silicon and lithium metal with a theoretical capacity of 4200 mAh/g and 3860mAh/g, respectively, have yet to reach the commercial market due to their inherent challenges, one of which is the SEI formation and evolution.

A similar process occurs on the cathode. During electrochemical cycling, the electrolyte oxidizes and forms a passivation layer known as the cathode electrolyte interphase. The development of $LiNi_{0.5}Mn_{1.5}O_4$ (LNMO) spinel, $LiCoPO_4$ (LCP), and the layered Li-Ni-Mn-Co oxides (NMC) form a new class of high voltage materials which put significant strain of the current carbonate based electrolytes that are stable to 4.5V.[2] Therefore, cycling the abovementioned cathodes to 4.7V and even 5V will continuously decompose the electrolyte, further adding to the commercial setbacks. It is imperative to solve the high voltage electrolyte stability and to improve the cathode-electrolyte interface.

The combination of next generation anode and cathode materials is governed by the stability of the electrolyte and its interface. Understanding and engineering the SEI can further increase the reliability of lithium ion batteries for portable electronics and electric vehicles.

Another way to further reduce global warming is to consider energy storage systems for large scale power applications. The demand for lithium has brought concerns regarding its abundance, cost, and political mining location.[3] Therefore, lithium ion batteries are not suitable for grid storage applications where cost plays a major factor. Sodium, on the other hand, overcomes all the shortcomings of lithium and has a redox potential of -2.71V which is slightly higher than that of lithium ($E^0_{Li+ / Li}$ = -3.04 V versus standard hydrogen electrode). Given the similarities of sodium to lithium, similar approaches can be taken to sodium ion batteries in order to reach the maturity of lithium ion batteries. In particular, layered transition metal oxides can be used as cathode materials for sodium ion batteries, which also suffer from similar shortcomings in the case of lithium ion batteries. The same characterization techniques used in lithium ion batteries to study electrode-electrolyte interface can be applied to further design and optimize the cathode interface to improve the cycling performance of layered oxide cathodes for sodium ion batteries.

Although researchers have studied the electrode-electrolyte interface on anode and cathode materials, the development of next generation chemistries warrants the formation of new electrolytes that can improve the electrode stability. Therefore, my PhD research mainly focuses on the investigation and development of electrode-electrolyte interface. A fundamental understanding of the SEI can aid in improving one of the factors that contributes to the longevity of lithium and sodium ion batteries.

My PhD thesis consists of nine chapters, including this motivation (**Chapter 1**). **Chapter 2** provides a general introduction to all of the lithium ion battery components. It also introduces layered transition metal oxide cathode materials for sodium ion batteries. **Chapter 3** briefly introduces advanced characterization tools that I used in my research including x-ray photoelectron spectroscopy, time-of-flight secondary ion mass spectroscopy, and scanning transmission electron microscopy (STEM) coupled with electron energy loss spectroscopy (EELs). In **Chapter 4,** the fundamental reduction mechanism of FEC is investigated on amorphous silicon thin films to determine how the additive improves the silicon anode performance. **Chapter 5** further investigates the effect of FEC on composite silicon anode. For the first time, the direct visualization of the SEI on silicon nanoparticles is demonstrated by STEM. The chemical composition is investigated to understand how binder and conductive additive affect the SEI. **Chapter 6** discusses the role of electrolyte formulations to yield high efficient lithium plating and a SEI dominated by salt decomposition. High concentrated salt ether electrolytes in this section have the ability to cycle cathodes to 4.4V. **Chapter 7** focuses on alternative high voltage electrolytes for lithium ion batteries. The unique properties of the sulfone electrolyte are explained. **Chapter 8** explains the improvement of the cathode electrolyte interphase on P2-$Na_{2/3}Ni_{1/3}Mn_{2/3}O_2$ via atomic layer deposition of aluminum oxide. **Chapter 9** summarizes the overall work and ideas for future research.

Chapter 2. Introduction to Lithium Ion Batteries

2.1. Over all Function of Lithium-ion Batteries (LIBs)

Lithium ion batteries (LIBs) can be categorized as an electrochemical energy storage system. Figure 2.1. shows the components and working principle of a LIB. The anode, cathode, electrolyte, and polymer membrane separator enable the LIB to function. The basic working principle of the commercial LIB requires the electrodes to undergo an oxidation reaction and a reduction reaction simultaneously. During the charge process, the lithium ions embedded in the crystal structure of the cathode are transported though the electrolyte medium, which then permeate the inert polymer separator. The ions pass through the solid electrolyte interphase and intercalate in between the anode (graphite) sheets. Concurrently, electrons move from the cathode to the anode through aluminum and copper current collectors which generate an electric current. Since the chemical potential of lithium is higher in the anode than it is in the cathode, the electrochemical energy is stored. The reverse process occurs in the discharge state. The stored electrochemical energy is released, producing electric energy which allows one to power his or her portable electronics. Herein, all of the major battery components will be discussed in more detail.

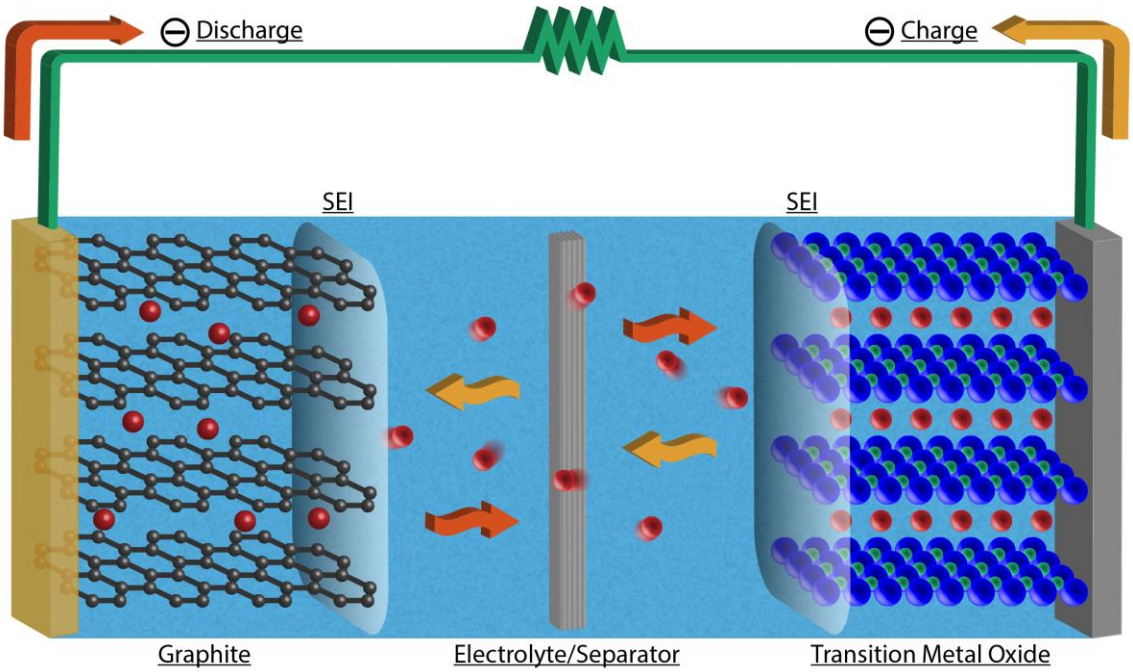

Figure 2.1. Schematic of the working mechanism of a LIB.

2.2. Anode Materials for LIBs

The development of the rechargeable lithium battery was hindered by the anode due to safety concerns. To combat the inherit issues of the previous generation, Sony developed a safer alternative by switching the anode to an insertion material, coined as "the rocking chair technology".[4,5] This revolutionized the portable electronic industry. Since their inception, improvement to energy density has been gradual, making it difficult to match the staggering growth of computing technology and electric vehicles. Therefore, researchers are seeking alternative anodes with higher theoretical capacity to increase the energy density of LIBs, as demonstrated in Figure 2.2. Herein, anodes for LIBs will be further discussed.

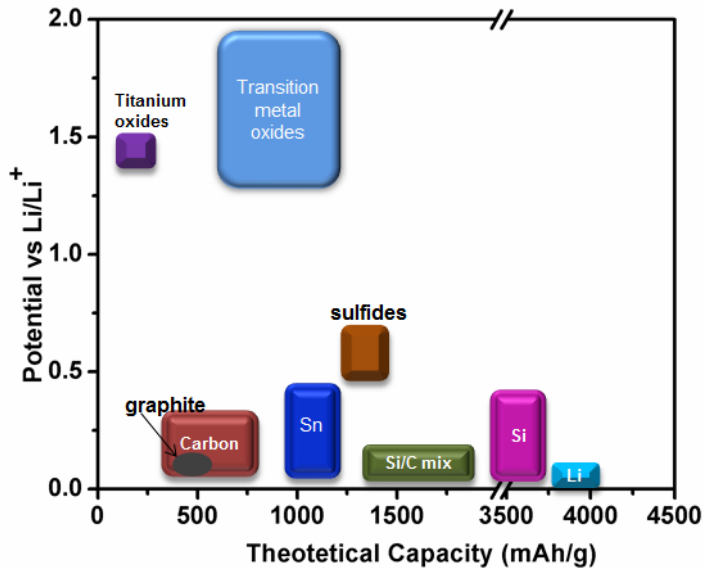

Figure 2.2. Theoretical Capacity of various anode materials for LIBs.

2.2.1. Graphite/Carbons

Graphite anode is known as the model anode because of its structural stability, high conductivity, long cycle life, and safety. The low cost and abundant nature makes it the perfect candidate for mass production. During the discharge process, lithium ions are intercalated between the graphite sheets. The reversible reaction is as follows:

$$C_6 + Li^+ + e^- \leftrightarrow LiC_6 \qquad (1.1)$$

Upon lithiation, the graphitic anode has a relatively low volume change of 10%, accommodating the Li ions with ease in its structure.[6] Its 2D mechanical structure allows for fast Li ion diffusivity and mechanical strength. Intercalating lithium at a relatively low potential yields a gravimetric capacity of 372 mAh/g and a volumetric capacity of 756 mAh/cm^3. The success of graphite anodes is also due to the formation of a stable passivation layer that only occurs with specific electrolytes; this will be discussed later in this chapter. Without the proper protective layer, graphite suffers from exfoliation, which occurs when the electrolyte is also intercalated

into the structure causing significant cell failure. Yet, the current commercial LIB graphite has overcome all the abovementioned obstacles by demonstrating a high coulombic efficiency, thus allowing LIBs to cycle hundreds of times.

The quest to increase the theoretical capacity of graphite has prompted researchers to seek alternative structures to the planer graphite. Carbon nanotubes (CNTs), an allotrope of graphite, are good candidates. Their theoretical capacity varies from 300-600 mAh/g, which is much higher than the current commercial anode.[7] Their unique cylindrical tube offers high conductivity, rigidity, and tensile strength. During the discharge state, the Li ions are intercalated in between the nanotube channels. However, it suffers from low first cycle coulombic efficiency. During the charge process, the cathode does not recover all of the Li ions that were inserted in the CNTs. Although they are not susceptible to exfoliation, more research is required to solve the first cycle irreversibility. Hard carbons are also less prone to exfoliation because of their small disordered orientation grains. Within the grains, there are nanovoids that reduce volume expansion and increase gravimetric capacity. However, the exposed graphitic grains exacerbate the decomposition of the electrolyte which causes low coulombic efficiency. The high hysteresis and capacity fade makes hard carbon unsuitable for commercialization. If graphite works extremely well, albeit with lower gravimetric capacity, there is no point in switching to other problematic carbon anodes for a small gain in gravimetric capacity.

2.2.2. Silicon Alloy

Lithium has the potential to alloy with a myriad of materials—aluminum, tin, germanium, and silicon, to name a few.[8] Alloys are highly sought after as next generation anode materials because of their high gravimetric and volumetric capacities, two to ten times higher than that of graphite. Contrary to graphite, alloys have a higher onset voltage which makes it less

susceptible for lithium plating during electrochemical cycling. The abundance of the alloy materials make this a cost effective anode which would help the production cost. Given all of the positives, alloy anode materials face two main challenges that hinder their commercialization: 1) mechanical degradation; and 2) chemical degradation.

For example, silicon suffers from severe mechanical strain because during lithiation, four Li atoms are incorporated into one silicon atom, which generates its high gravimetric capacity of 3579 mAh/g. Consequently, the material undergoes a 300% volume expansion. Upon delithiation, the silicon anode is unable to maintain its structural integrity, causing the silicon particles to crack (shown in Figure 2.3.).

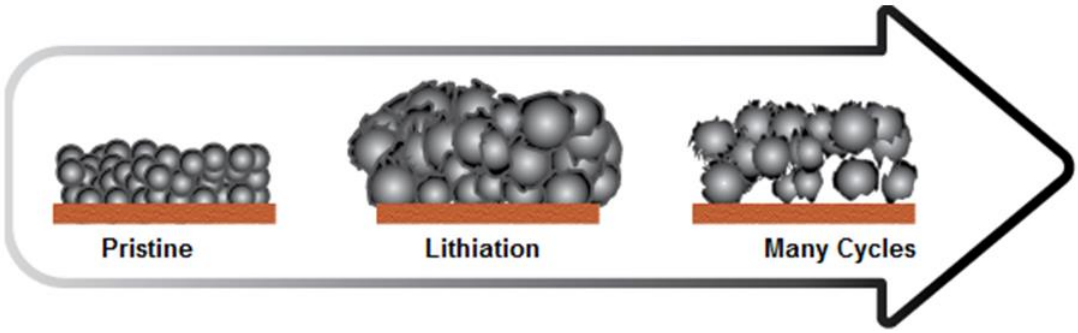

Figure 2.3. Schematic of the mechanical strain that occurs to during the lithiation process of silicon to form $Li_{15}Si_4$.

As a result, it causes mechanical breakdown and loss of electrical contact between the silicon and the current collector, thereby causing severe capacity loss and electrode in activity. To mitigate the volume expansion, researchers have focused their efforts on nanostructured silicon because there is a strong correlation between size and fracture. *In-situ* transmission electron microscopy (TEM) demonstrated that silicon nanoparticles with a diameter of 150 nm or less were able to withstand full lithiation without cracking.[9] Silicon nanowires with an average diameter of 85 nm expanded vertically in the <112> direction during lithiation and maintained their structure upon delithiation.[10] One key observation is that crystalline silicon transforms to an amorphous state

after the first cycle. TEM further illustrated that in the first lithiation process, the silicon has two phases: the core remains crystalline while the outer edges are amorphous.[11] This forms a sharp two phase bounder within the particle which adds to the mechanical strain. Therefore, researchers have also focused on using amorphous silicon thin films and microstructures to avoid the drastic change within the material.[11–13]

To minimize the delamination of silicon after repeated cycling, polymeric coatings have been widely used.[14] Self-healing polymer coatings have been proven to minimize electrode cracking, maintain the particles intact, and increase the capacity retention of silicon anodes.[15] Even after 100 cycles, the electrode has over 2000 mAh/g of capacity with a coulombic efficiency above 99%.[16] Molecular layer deposition was used to coat the entire electrode and to improve the capacity retention of silicon composite electrodes. The flexible alucone coating improves the mechanical stability of silicon nanoparticles with 900 mAh/g capacity after 100 cycles.[17]

Although several approaches have been made to make silicon anodes more mechanically stable, the solutions have led to side effects. Downsizing to nanostructures increases the surface area of the active material which subsequently increases the chemical instability with the electrolyte. As soon as the electrolyte makes contact with silicon, it quickly begins to decompose. This process is exacerbated throughout electrochemical cycling as shown in Figure 2.4.

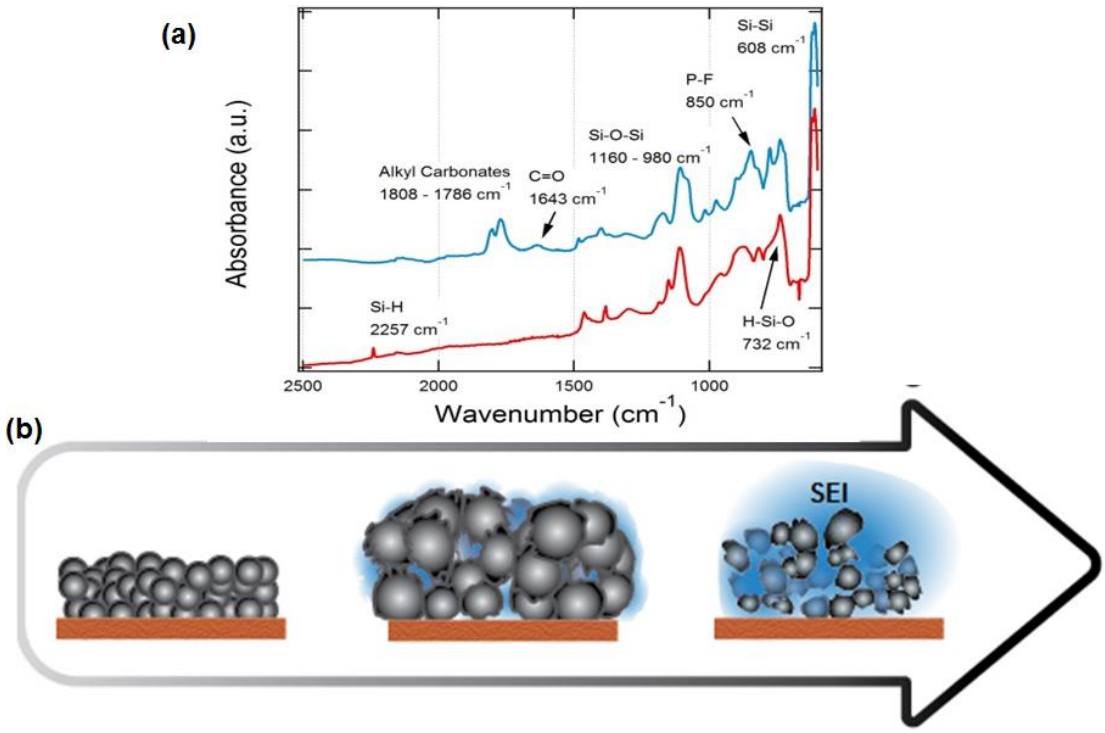

Figure 2.4. (a) FTIR of etched silicon wafer (red) compared to etched silicon wafer that was exposed to the carbonate electrolyte (blue). (b) Schematic of the solid electrolyte interphase growth (SEI) over prolonged cycling.

The decomposition of the electrolyte on silicon is known as the solid electrolyte interphase (SEI). Over prolonged cycles, fresh silicon is exposed to the electrolyte causing the SEI to continuously grow as shown in Figure 2.4b. The combination of the mechanical and chemical instability has hindered the commercialization of a pure silicon anode. However, combining silicon with graphite or in carbon host structures[18,19] has revitalized silicon as a potential anode. For commercial applications, silicon may be implemented to increase the energy density of LIBs, albeit in limited percentage. The current motivation is to test silicon in full cell applications to determine its feasibility.[20–22] Major research and development is currently ongoing to solve this issue.

2.2.3. Lithium Metal

Lithium metal is seen as the ultimate anode for LIBs due to its extremely high theoretical energy density (3860 mAh/g) and low negative redox potential (-3.04 V *vs.* standard hydrogen electrode). Making Li metal a ubiquitous anode is the key in propelling energy storage and conversion systems. It is one of the key components that will further the development of next-generation high-energy batteries such as Li-S, Li-O_2, and high energy density (500Wh/kg) batteries for the automotive industry.

However, the continuous growth during electrochemical cycling, the incompatibility with the electrolyte, and the large safety concerns have prevented its implementation. In the plating state, lithium ions nucleate on the surface of the copper foil and then propagate. However, inhomogeneous conduction pathways form branch-like Li morphology known as dendrites. The dendrites continue to grow throughout electrochemical cycling, puncturing through the separator and reaching the cathode. This ultimately leads to a short circuit which is largely due to the electrolyte.

During electrochemical plating of Li metal, the potential is driven more negative, reducing the electrolyte anode surface (Cu or Li metal for a symmetrical cell) to form the SEI. In an ideal case, once the SEI forms it should not change during electrochemical cycling. However, just as in the case of the Li-alloy anodes, the SEI on Li metal is tremendously unstable. The parasitic SEI continues to consume the electrolyte, forming “hot spots” which are highly conductive pathways where Li ions are more prone to plate, shown in Figure 2.5.[23]

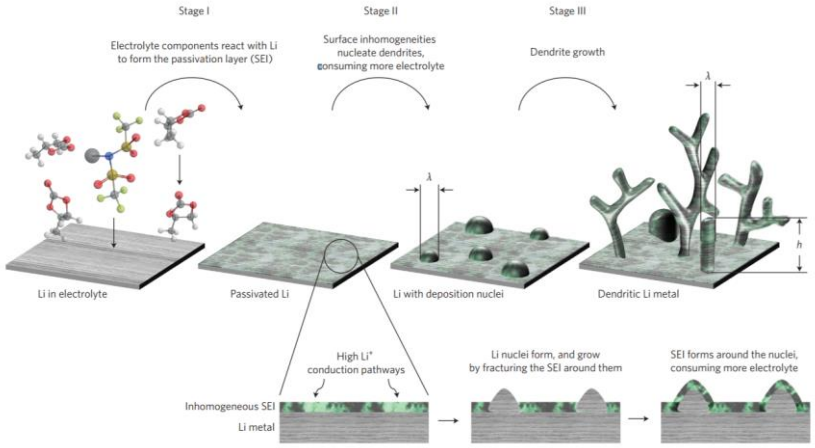

Figure 2.5. Schematic of the various stages of dendrite growth.[23]

In the event of preventing Li metal dendrite formations during electrochemical cycling, polymer electrolytes gained much attention because they act as a physical barrier between the anode and cathode, thus avoiding the penetration of dendrites to cathode as well as transporting Li ions during electrochemical cycling. Monroe proposed a model that takes into consideration the modulus of the electrolyte-separator and the surface tension of lithium metal deposition kinetics to determine that dendrites can be prevented if the shear modulus of polymer electrolytes are twice that of Li metal.[24] The self-healing electrostatic shield mechanism has demonstrated the prevention of dendrite formation. Cesium ions coat the surface of the lithium metal, forming an electrostatic shield that repels the incoming lithium ions and forms a uniform barrier that prevents the branch-like morphology.[25,26] This research has further inspired others to develop ways to prevent dendrite formation.[27] Very recently, the Battery 500 Consortium was created by the Department of Energy which aims to develop a 500 Wh/kg battery for the electric vehicle market. The multidisciplinary team from academia, national labs, industry are working together to enable the lithium metal anode to meet the energy demand.

2.3. Transition Metal Oxide Cathode Materials for LIBs

Similar to anodes, cathodes must also possess excellent performance, a long lifespan, and excellent structure stability to host the lithium ions during cycling. The development of higher capacity anodes (silicon and lithium) encourages researchers to focus their efforts on new cathode materials since cathodes only have about half of the gravimetric capacity of graphite. Therefore, cathode materials also play a critical role in improving the energy density of LIBs. This section focuses on the development of lithium transition metal oxide cathodes.

2.3.1. Layered Metal Oxides

Much of the success of LIBs is due to lithium cobalt oxide ($LiCoO_2$), a transition metal oxide cathode, developed by Goodenough's group in the 1980s.[28,29] The cathode provided a voltage of approximately 4V which was coupled with graphite and commercialized by Sony in the 1990s. Although $LiCoO_2$ played an important role in the commercialization of LIBs, there are several issues associated with the material. First, cobalt (Co) is toxic and expensive, which increases the cost of the overall battery. Second, the low theoretical capacity of 120 mAh/g inherently limits the energy density of the battery for electric vehicle applications. Third, the structure stability is compromised if 50% of the lithium ions are removed during delithiation.

The cost was alleviated by switching Co with other inexpensive transition metals such as nickel and magnesium. The attempt to synthesize $LiNiO_2$ proved to be challenging; as result, the combination of Ni and Mn was developed ($LiNi_{0.5}Mn_{0.5}O_2$).[30] However, the Li/Ni disorder caused severe capacity fade due to the structure instability. To stabilize the structure, Co was reinstated to form what we now know as NMC (lithium nickel manganese cobalt oxide ($LiNi_xMn_yCo_zO_2$). This new class of materials has high capacity, high operating potential, and

good rate capability.[31] Altering the TM ratio can further increase the gravimetric capacity and operating voltage but leads to structure failure and electrolyte incompatibilities.[32,33]

Lithium excess layered oxides is another cathode that has the potential to meet the high energy demands. Its high gravimetric capacity (above 300 mAh/g) is significantly higher than that of the current commercial cathode $LiNi_{0.8}Co_{0.15}Al_{0.05}O_2$ (NCA, ~200mAh/g).[34] Although it has a high capacity, the material suffers from poor first cycle coulombic efficiency, structure reordering, and chemical instabilities with the electrolyte. The oxygen evolution that occurs in the first cycle is irreversible and contributes to form an unstable passivation layer on the cathode surface.[35,36] Therefore, surface modifications have been applied to improve the stability.[37,38] Oxygen activities have been proven to alter the surface and bulk properties of lithium excess cathodes which affect the transport kinetics.[39,40] Furthermore, this material suffers from voltage fading, poor rate capability, and safety concerns due to the oxygen evolution. Researchers continue to improve lithium excess cathodes with the hope of solving all the abovementioned problems.

Similar to lithium excess materials, $LiNi_{0.5}Mn_{1.5}O_4$ (LNMO) and $LiCoPO_4$ (LCP) also have inherit challenges that need to be addressed before reaching commercialization. Both cathodes have high operating potential close to 5V, thus putting them in a category of their own. Long term cycling causes these materials to have capacity fade due to structure instability and electrolyte decomposition.[41] The passivation layer formed on these cathodes are not stable because the electrolytes continue to decompose at such high voltages[2,42]; this will be discussed further in the next section.

2.4. Electrolytes for LIBs and The Solid Electrolyte Interphase Formation (SEI)

Electrolytes are found in all electrochemical energy storage and conversion devices. The role of the electrolyte is to serve as a transport medium for the transfer of charges. In LIBs, the transfer of charges is in the form of lithium ions that are transferred between the anode and the cathode.[2] The electrolyte solutions consist of salts dissolved in (an) aqueous or nonaqueous solvent(s). Electrolytes for LIBs should follow a few basic requirements: 1) wide voltage range; 2) wide temperature range; 3) high dielectric constant; 4) low viscosity; and 5) low or no flammability. However, meeting all of these requirements proves to be a difficult task.

2.4.1. Surface film formation

During electrochemical cycling, the electrolyte reduces on the anode to form the solid electrolyte interphase (SEI). This occurs in the initial cycle and serves as a protective layer on the graphite anode to prevent further decomposition of the electrolyte. The ideal SEI is an ionic conductor and an electron insulator which avoids self-discharge. It is crucial to have a stable SEI because it is known to affect the anodes structure stability and performance, as demonstrated by Peled.[43,44] Otherwise, the parasitic SEI continues to consume the electrolyte, forming various decomposition products that continue to evolve from primary to secondary, and even tertiary reactions. Moreover, if there are contaminates in the electrolyte such as water, carbon dioxide, or oxygen, it can cause further alteration in the SEI. The electrolyte also oxidizes on the cathode and forms the cathode electrolyte interphase that also protects the cathode from continuous electrolyte decomposition. Figure 2.6 shows a schematic of the relative electrode and electrolyte electron energies in an aqueous medium, but can also be applied to other electrolytes. The

energy separation (E_g) of the highest occupied molecular orbital (HOMO) and the lowest occupied molecular orbital (LUMO) is deemed as the electrolyte stability window. The anode (μ_A) and cathode (μ_C) each have a specific potential during the open circuit voltage. Once current is applied, the potential of the anode and cathode shift beyond the HOMO and LUMO of the electrolyte, causing it to decompose. However, this can be alleviated by finding additives that will decompose before the solvent to form a protective layer on either the anode[45,46] or the cathode.[32,47,48]

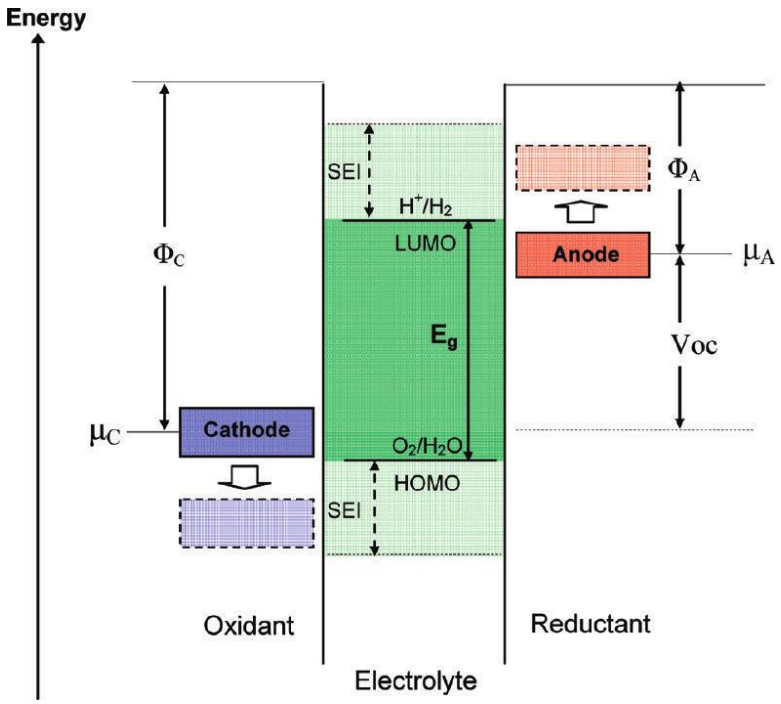

Figure 2.6. Schematic of the electrolyte voltage stability compared to the anode and cathode potentials.[49]

2.4.2. Solvents

There are several types of electrolytes available for use, each serving its purpose to fulfill a need in high voltage and low voltage applications. Carbonate based electrolytes are widely

used in commercial batteries and are the only solvents that have a wide enough voltage window for high voltage applications. However, this class of solvents is problematic and forms unstable SEI on lithium and silicon anodes during electrochemical cycling. Lithium metal interfacial chemistry research began in the late 1970s, where the investigation of solvent chemical decomposition products and their effects on passivation film was recognized.[50] This spurred the research interest of electrode-electrolyte interface in lithium primary and secondary batteries that we know of today. Commonly used carbonate based electrolytes (ethylene carbonate (EC), propylene carbonate (PC), dimethyl carbonate (DMC), diethyl carbonate (DEC), ethyl methyl carbonate (EMC)) primarily decompose to form lithium alkyl carbonates (RCO_3Li), lithium alkoxides (RCOLi), and lithium carbonate (Li_2CO_3).[51–54] Zhaung and coworkers further enhanced the understanding of actual chemical compounds found in the SEI after Li metal plating, where lithium ethylene dicarbonate forms through a single electron reduction of EC to became a primary SEI component.[55] Whereas the primary decomposition products of DMC are lithium methyl carbonate, lithium oxalate and lithium methoxide.[56] The carbonate decomposition products continue to evolve and can further react with other contaminants such as water and carbon dioxide to alter the SEI composition, exponentially increasing its complexity.[57] This inherently leads to poor coulombic efficiency and can potentially lead to cell failure. Moreover, their voltage window renders them unfit to cycle 5V cathodes.

2.4.3. Salts

Not only does the solvent play a critical role in the SEI formation, the lithium salts also participate—these could have either detrimental or positive effects on cycling efficiency. Altering the lithium salts is seen as a direct way to optimize the electrolyte. Figure 2.7

demonstrates the structures of the reviewed salt systems. A myriad of lithium salts have been studied in carbonate based electrolytes, primarily by Aurbach.[58]

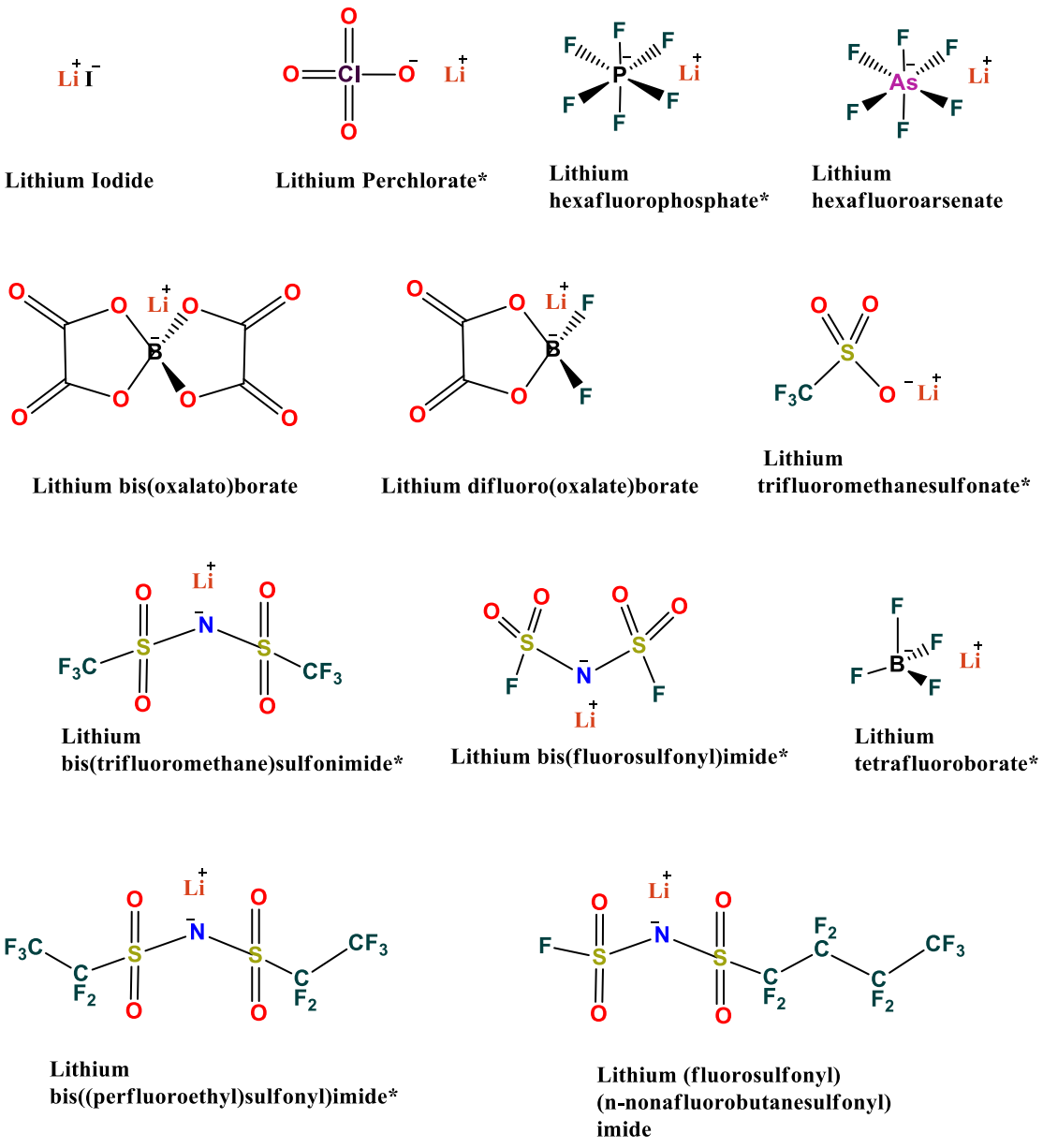

Figure 2.7. Commonly studied salts for lithium ion batteries and for Li metal cycling.

The next step is to uncover an electrolyte combination that has the potential to be stable at high voltages, is less flammable, and produces little to no gas generation. Electrolyte reviews have already demonstrated that researchers are steering in the right direction.[59]

Chapter 3. Advanced Characterization Tools

3.1. X-ray Photoelectron Spectroscopy (XPS)

XPS is a surface characterization technique that yields chemical information of materials. It has the ability to measure elemental composition, chemical states, and electronic states of each element within the materials of interest. This is achieved by using photons of a specific energy that excite a core level electron to the vacuum level, shown in Figure 3.1.

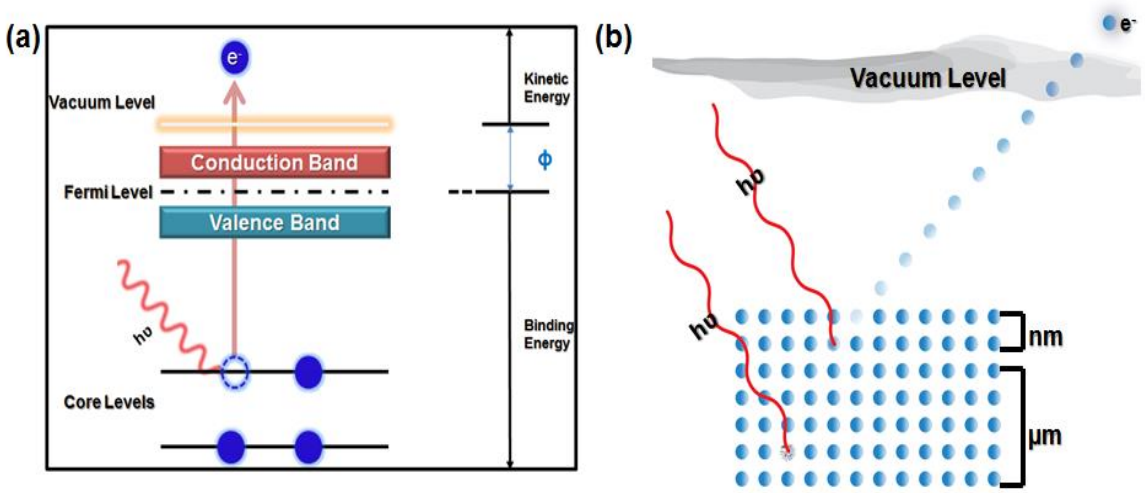

Figure 3.1. (a) Energy diagram of the core level electron excitation. (b) Schematic representation of ejected electrons to the vacuum level.

This ejected electron has a kinetic energy (K.E) that is equaled to the phonon energy minus the binding energy (B.E) minus the work function of the instrument (eq 3.1).

$$K.E = h\upsilon - B.E - \phi_{sp} \qquad \text{(eq. 3.1)}$$

The surface ejected electrons are filtered using the hemispherical (electron energy) analyzer which disperses the emitted electrons depending on their kinetic energy. The intensity for related energy is recorded by the detector (Figure 3.2) and is presented in an energy spectrum of the

intensity versus binding energy. All of these steps must be completed in an ultra-high vacuum to avoid gas phase collisions and contamination of the analyzed surface.

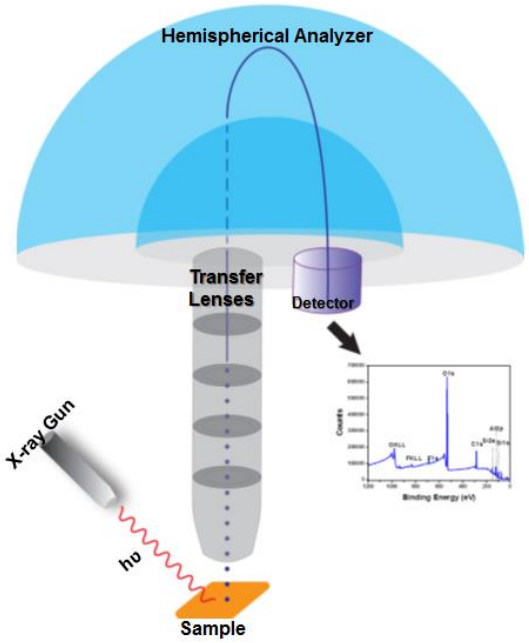

Figure 3.2. Schematic of the internal function of the XPS.

Here, binding energy of the excited electron is unique and dependent upon the bonding environment, giving each element its own fingerprint region.

This technique is extremely surface sensitive because it uses low energy x-ray sources (Mg K_α:1253.6 eV, Al K_α: 1486.6 eV) that can excite the core level electrons. The core level electrons must travel an average distance without losing energy; this is known as the inelastic mean free path (λ). The intensity of the emitted electrons decay as a function of distance as demonstrated by the Beer Lambert Law (eq 3.2):

$$I_s = I_0 e^{-\frac{d}{\lambda sin(\theta)}} \qquad \text{(eq 3.2)}$$

When the takeoff angle is 90° (Figure 3.3) and the distance traveled is equal to 3λ, 95% of the signal intensity comes from depths between 0 and 3λ. Therefore, with electron energies of 50-2500 eV, the inelastic mean free path is 5 nm, making XPS a reliable surface characterization technique.

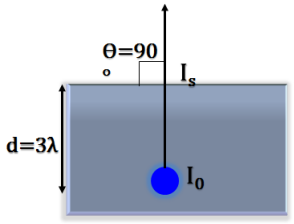

Figure 3.3. Schematic representation of the inelastic mean free path for emitted electrons.

The chemical shifts of core levels are due to the change in the local binding environment. The directions of the shifts are dependent on the potential of the nucleus and repelling interactions of the surrounding electrons. Therefore, a higher energy shift can be due to a change in oxidation state or electronegativity.

The surface sensitivity and penetration depth make XPS a suitable technique to study the SEI of battery electrodes. However, it is critical that one uses anoxic and anhydrous methods to transfer battery electrodes as the SEI is extremely sensitive to water and air. In my PhD work, all of the samples were transferred at ultra-high vacuum to avoid any contamination and to properly characterize the SEI.

3.2. Time-of-Flight Secondary Ion Mass Spectroscopy (TOF-SIMS)

TOF-SIMS is an extremely surface sensitive characterization technique that is widely used in a myriad of research fields (biology, chemistry, physics, materials science). Time of flight is a key component because ion fragments with similar energies but different masses travel at different speeds, which allows isotopes to be properly identified. A yield of secondary ions from the sample surface is bombarded with a low current pulsed beam. The electrostatic field accelerates the excited secondary ions to the flight detector (1.5 mm away from surface). As expected, the ions with less weight travel significantly faster than do the heavy ions, which allows for even light elements to be detected (H, He, Li). The flight technique can separate species with similar mass fragments as close as 0.001 a.m.u. Secondary ion spectroscopy is an analytical technique that measures the mass of the ejected secondary ions from the sample surface. Combined, this technique can detect both surface and bulk chemical composition with ultra-high sensitivity in the parts-per-billion (concentration) for elemental detection and for a few atomic layers for surface films. The ionized functionalities can be analyzed by molecular surveys, elemental maps, surface imaging, and sputter depth profile.

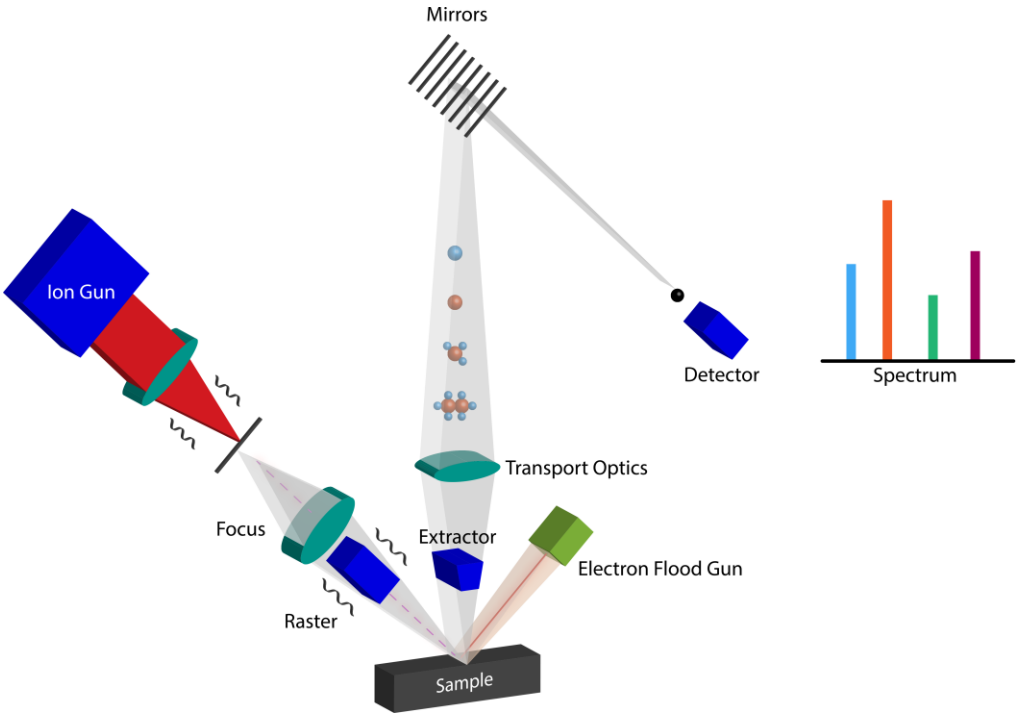

Figure 3.4. Schematic representation of TOF-SIMS.

For my research, I used a dual primary ion beam to analyze the solid electrolyte interphase of amorphous silicon, shown in Figure 3.4. First, the surface is bombarded with Cs^+ via a pulsed ion beam to remove molecules from the very outermost surface of the sample. Then, Bi_3^{2+} cluster is used to accelerate fragmented species into the flight tube to determine the mass by measuring the exact time at which the fragments reach the detector. Previously, Ar^+ primary ions were used as an excitation source, but when energy potential is in the range of keV, it can cause detrimental effects to the sample.[60] The surface of the sample can exhibit nonelastic processes, Coupling a low energy sputter source such as Cs^+ with the polyatomic Bi_3^{2+} cluster as the analysis source, we are able to maximize the yield and minimize sample damage.[61] More importantly, the samples are transferred from the XPS in ultra-high vacuum to the TOF-SIMS instrument to avoid contamination from the ambient environment.

3.4. Scanning Transmission Electron Microscopy (STEM)-Electron Energy Loss Spectroscopy (EELS)

Figure 3.5 shows a schematic of the STEM configuration. The electron beam with an energy of 100 keV is focused through a series of condenser lenses (shown in green) to form a small atomic scale probe that passes through the objective lens.[62] The objective lens provides the final demagnification step, where aberrations dominate to restrict the aperture size and to not blur the probe. The beam current used during analysis is governed by the objective aperture. Unlike TEM, STEM utilizes scan coils that raster the focused electron beam into a narrow spot probe over the sample. The angular dark field detector configuration optimizes the electron detection. The transmitted electrons that leave the sample at high angles with respect to the optic axis are referred to angular dark field mode. Conversely, electrons that leave at high angles are referred to bright field mode. The electrons pass through the electron spectrometer to generate a magnified image.

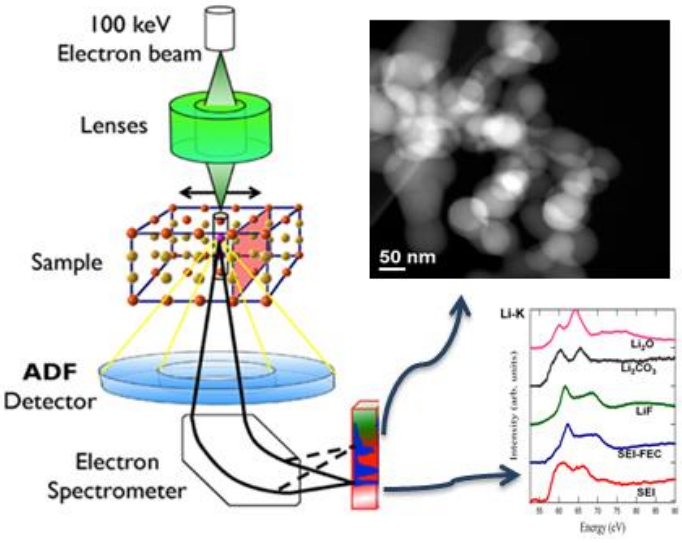

Figure 3.5. Schematic representation of the working mechanism of STEM-EELS.

While focusing the beam in STEM, the electrons could be elastically scattered when it comes into contact with the sample. Here, the electron beam loses energy and is bent in the electron spectrometer through a small angle.[63] This energy distribution provides substantial information pertaining to chemical bonding, charge transfer, and valence states which is the principle of EELS.

This powerful technique has been recently introduced to study cathode materials for lithium-ion batteries.[9, 30] However, this technique poses challenges when characterizing beam sensitive materials; in particular, for lithium-silicate alloys and the SEI. The electron dose causes beam damage when the SEI and lithium-silicate alloys material are exposed for long periods of time at high energy, as demonstrated in Figure 3.6. However, beam damage can be prevented by spreading out the electron dose in a large area as to not affect the sample. The total electron dose used in our EELS spectrum experiments is 620 e/Å^2 and the critical electron dose to study the SEI composition is 800 e/Å^2, which is highlighted in Chapter 5.

.

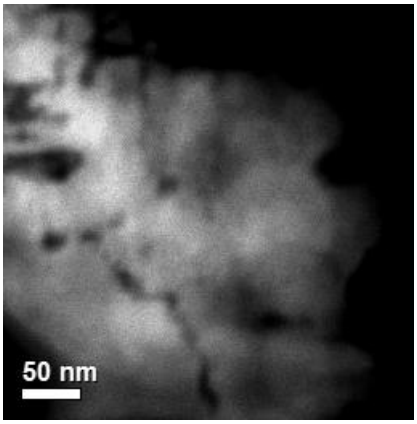

Figure 3.6. ADF-STEM image of the delithiated Si after long exposure time with a high energy beam.

Chapter 4. The Effect of Fluoroethylene Carbonate as an Additive on the Solid Electrolyte Interphase on Silicon Lithium-ion Electrodes

4.1. Introduction

Silicon-lithium alloys have been the subject of intense research as a negative electrode active material in lithium-ion batteries (LIBs). The high theoretical gravimetric capacity of lithiated silicon has motivated this research; however, major challenges remain for the implementation of silicon in commercial devices. Upon lithiation, silicon undergoes a volume expansion of about 300%. This causes mechanical breakdown and loss of electrical connection between the active material and the current collector, in turn causing lost capacity and electrode inactivity.[64,65] Using nanostructured electrodes, the mechanical pulverization of the Si active material has largely been mitigated.[10,18,19,66,67] For example, Si nanoparticles with a diameter less than ~150 nm can accommodate the strain of full lithiation without fracturing.[9,64,68–70] Additionally, a wide range of electronically conductive binders and electrode coatings have been developed to address the pulverization of the overall composite electrode structure.[71,72] Unfortunately, nano-structures and complicated architectures generally lead to low tap (volumetric) density electrodes with extremely high surface areas. Such high surface area electrodes exacerbate capacity losses (and diminish electrode cycle life) through parasitic surface reactions.[73] Moreover, in a composite electrode, the conductive additive and binder also participate in surface reactions, making it difficult to isolate the effects of each electrode component on particular surface chemistries.[74]

Because interfacial chemistry on next generation negative electrode materials like silicon is not well understood, rational design and control of new battery architectures is not possible.[70,75] The traditional electrolyte, $LiPF_6$ salt in diethyl carbonate (DEC) and ethylene carbonate (EC), 1:1 by % wt., is unstable at normal battery cycling potentials (lithiation and

delithiation below 1.0 V vs. Li/Li^+). During the lithiation process, a portion of the Li ions is consumed, as the electrolyte is reduced to inactive side products in parasitic reactions. Some of these parasitic reactions form insoluble products that result in a solid electrolyte interphase (SEI) which coats the negative electrode's surface.[43,54,76] The SEI components are generally electronically insulating in nature and passivate (to some degree) the active material's surface from further solvent reduction. As a result, the SEI hinders further progression of the parasitic reactions to minimize the capacity loss due to irreversible sequestration of lithium-ions. Therefore, SEI stability directly relates to the loss of capacity in LIBs. Incomplete passivation of the electrode surface truncates the battery cycle life because of the continued consumption of lithium throughout electrochemical cycling.[77–79]

For silicon, one of the more successful strategies for dealing with the capacity loss associated with electrochemical cycling and continuous electrolyte decomposition has been the use of battery electrolyte additives such as co-solvents and co-salts. Of these, fluoroethylene carbonate (FEC) has been very successful at extending battery cycle life. Its unique performance has made it a standard additive in the literature for almost all silicon electrodes.[45,80–82] As discussed above, cycle life is linked to SEI stability; however, the connection between SEI stability and FEC is still not well understood. Calculations by Balbuena and co-workers have suggested that the kinetically fast reduction of FEC to neutral radical carbonate and fluoride anion leads to rapid formation of LiF in the SEI.[83–85] On the other hand, previous work has proposed that polycarbonates such as polymeric fluorocarbonate and polymeric vinylene carbonate are formed during the reduction of FEC, and play a role in stabilizing the SEI or promoting Li-ion transport during electrochemical cycling.[45,80,86,87]

To understand how the inclusion of FEC in the electrolyte affects SEI structure and its evolution, we attempt to reconcile the differing accounts by: (1) using mechanically stable amorphous Si (*a*-Si) thin film electrodes as a model system and (2) extending previously developed anoxic and anhydrous analytical characterization techniques of silicon electrodes.

As shown by Lucht, Abraham and co-workers, model systems free of binder and conductive additives are important for understanding the chemical composition of the SEI.[88–91] Li and coworkers have shown that direct current (DC)-sputtered *a*-Si thin film electrodes with a film thickness below the critical dimension of 150 nm or less are mechanically stable during their formative cycles.[12] To limit the irreversibility due to mechanical pulverization, we use a model system of binder-free and conductive additive-free 50 nm thick DC-sputtered *a*-Si thin films on copper foil. Unlike crystalline silicon, *a*-Si experiences much less strain and mechanical deterioration with cycling because of reduced lattice mismatch associated with the sharp two-phase silicon lithiation mechanism.[13,92] By using a stable model system, we can better relate the addition of FEC co-solvent directly with the electrochemical results and surface properties such as SEI stability, structure, and chemical makeup.

To accurately characterize and understand how the inclusion of FEC in the electrolyte affects SEI structure and evolution, we extend previously developed anoxic and anhydrous XPS[61,93,94] and TOF-SIMS[61,95] measurement techniques to our model system. In much of the previous experimental work on SEI formed from electrolytes with FEC,[45,80,86,91] there was no discussion of the known effects of exposing SEI to ambient conditions.[93,94] However, Xu, et al.[96] has used a special-built airtight transfer system to avoid air exposure during sample analysis. Although similar sample preparation precautions were taken in our study, Xu, et al. used nanoparticle composite electrodes. As previously mentioned, it is widely accepted that both

conductive additive and binder contribute to the SEI formation, therefore, it is difficult to solely isolate the decomposition products formed from the electrolyte. Ultimately, their findings suggest that FEC containing electrolyte preserves electrode integrity by preventing particle agglomeration, cracking, and influence the salt dissolution reaction. Building on this work and others, we discuss the differences between the electrode cycled in EC/ DEC versus EC/DEC/FEC using a model system. Characterization by XPS and TOF-SIMS depth profiling elucidates the reaction pathways that lead to thicker SEI, increased LiF formation, Li_2O formation, and increased silicon surface reactivity.

4.2. Experimental

50 nm a-Si thin film substrates were fabricated by direct current (DC) sputtering. Thin films sputtered onto rough copper foil were repeatedly lithiated and delithiated (cycled) to understand the structure of the SEI resulting from electrolyte containing FEC. The electrodes where then analyzed by TOF-SIMS and XPS, closely following methods described previously for anoxic and anhydrous characterization with minimal exposure to oxygen and water.[61,93]

4.2.1. Silicon Materials

Amorphous silicon thin films (50 nm) were fabricated by DC sputtering from an un-doped Si target (99.999%) and deposited on battery grade copper foil. In order to calibrate the TOF-SIMS depth profiling experiments, a-Si 50 nm films were sputtered on Si wafers. For these samples, a metallic layer of 200 nm Cu (99.999%) and 200 nm Ti (99.995%) was deposited on Si wafer as the current collector followed by 50 nm a-Si film. All sputtering was carried out under pure argon atmosphere (99.9995%). A quartz crystal microbalance was used to monitor the film thickness. The films were exposed to air prior to battery assembly.

4.2.2. Electrochemistry

The *a*-Si thin films were assembled into 2032 coin cells, using a Celgard (C480) polyprolylene separator (Celgard Inc., USA), 1 M $LiPF_6$ electrolyte solutions (battery grade, BASF) including traditional 1:1 (wt%) EC:DEC, (hereafter "EC/DEC") and a blend of 45:45:10 (wt%) EC:DEC:FEC, (hereafter "EC/DEC/FEC"), with lithium metal as the counter electrode. The electrochemical cells were assembled in a glove box purged with high purity argon (99.9995%) and maintained with oxygen and water vapor levels at or less than 5 ppm. After assembly, the electrochemical properties of the two-electrode cells were measured on an Arbin battery cycler in galvanostatic mode. The open circuit voltage of the coin cells was monitored for 1.5 hours then the cells were charged and discharged between 2.0 to 0.05 V, with a current density of 21 $\mu A/cm^2$, which is approximately C/2 rate at room temperature. Additionally, electrochemical impedance spectroscopy (EIS) measurements were carried out with AC frequencies from 0.01 to$1x10^6$ Hz on galvanostatic cycled *a*-Si electrodes in lithiated and delithiated states, as described above. In a classical three-electrode cell, the voltage can be applied and measured between the working and reference electrode, and current is collected on the counter electrode. However, in this study, the impendence was collected in a half cell (pseudo three-electrode cell) using a Solatron 1287 Potentiostat after first lithiation, first delithiation, and 100 cycles delithiation. After the EIS measurements were taken, an equivalent circuit model was fit to the data to analyze the reactions that took place using Z view software (v. 3.4a, Scribner Associates, Inc.).

4.2.3. Surface Analysis

After electrochemical cycling, the cells were disassembled in the glove box, then transferred to the ultra-high-vacuum environment using a reduced oxidation (ROx) interface

designed for transferring air-sensitive samples. The ROx has methods and figures of merit to determine if the samples are ever exposed to additional traces of oxygen and water greater than those experienced in the glove box environment, even during pump-down. The methods and components of the ROx are described in further detail in the Supporting Information and elsewhere.[61,93,97]

X-ray photoelectron spectroscopy (XPS) was performed using a Kratos Ultra DLD XPS. Analysis of the spectra closely followed previous work, with fitting performed by CasaXPS software (version 2.3.15, Casa Software Ltd.);[61,93] an example fit is given in the Supporting Information.

Time-of-flight secondary ion mass spectrometry (TOF-SIMS) data were collected using an ION-TOF GmbH TOF.SIMS 5, again closely following previous work.[61] TOF-SIMS depth profiling experiments were performed by a dual ion beam interrogation of the surface, alternating between an analysis beam (primary) (Bi_3^{2+} ions) and sputtering beam (secondary) (Cs^+ ions). Full spectra from 1 to 1000 amu were acquired in negative ion mode at pressures between 5×10^{-8} and 9×10^{-9} mbar, with mass resolution was better than 8000 ($m/\Delta m$).

TOF-SIMS spectra were analyzed with the ION-TOF software package (version 6.3). Mass calibration used a set of only inorganic peaks.[98] After depth profiling, samples were removed from the TOF-SIMS and sputtering craters where analyzed by optical profilometry (Veeco, NT9100 Optical Profiler). Additional samples for calibration were fabricated by DC sputtering *a*-Si thin films on metalized silicon wafer (discussed in more detail in the Supporting Information). Sputtering times and crater depths were used to determine sputtering rates for both the SEI layer and the wafer by a linear fit of the sputtering depth versus sputtering time data. The resulting sputtering rates were used to transform sputtering time into depth using a simple two-

layer sputtering model.[61,99,100] A homemade script executed in the iPython nootbook interpreter environment using the numpy, scipy, and pandas libraries, organized and transformed the data from the time domain to depth.[101–104] The Si^- mass fragment signal was used to define the relative contributions of each sputtering rate in the transition between the SEI and the silicon active material. The outer surface of the silicon active material was defined to be where Si^- intensity was halfway between its maximum and minimum signal values.

4.3. Results and Discussion

4.3.1. Galvanostatic Cycling of a-Si Thin Film Electrodes

In order to understand the effects of FEC, SEI formed from the EC/DEC and EC/DEC/FEC electrolyte systems were compared. To form the SEI, thin film electrodes underwent controlled lithiation (discharge) and delithation (charge) by constant applied current while measuring the voltage, as described above. Figure 4.1 shows representative charge/discharge curves for three particular cycles taken from electrodes that were cycled 100 times. The applied current drove lithium-silicon alloy formation as well as decomposition of the electrolyte via parasitic reactions – some of which resulted in the formation of the SEI. It is common practice to plot the charge applied to the system in terms of the mass of active material ("capacity"), where one can observe how much of the active material is used during electrochemical cycling. However it is important to note that some charge is consumed during the formation of the parasitic side reactions, which should not be interpreted as used active material.

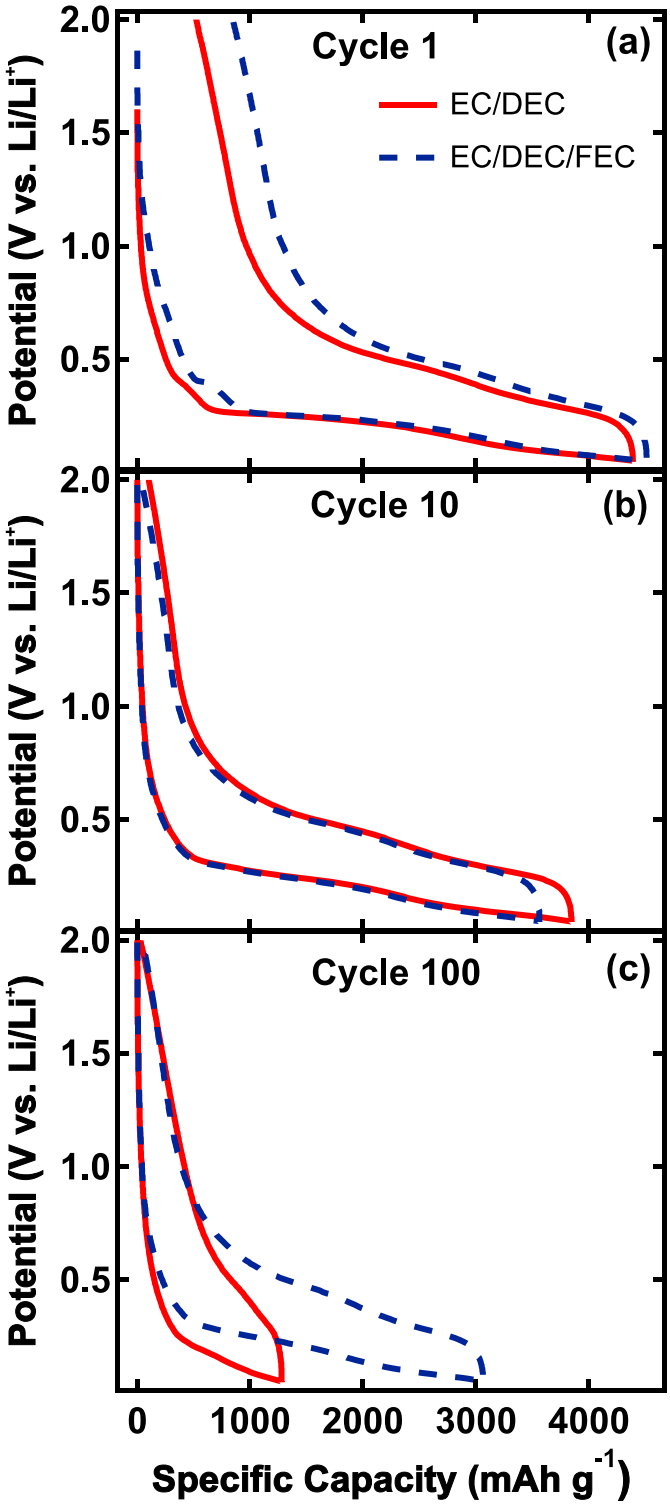

Figure 4.1. Voltage profiles of half cells taken during the (a) first cycle; (b) tenth cycle; (c) one hundredth cycle. Cells were cycled with EC/DEC (solid red line) and EC/DEC/FEC (dashed navy line) electrolytes.

In addition to using the integrated current applied during cycling to determine capacity, the mass loading of silicon deposited on the copper foil was also used. Using the mass loading per half-inch electrode (11.65 μg cm^{-2}), the capacity for the lithiated thin film cycled with the EC/DEC was calculated to be 4446.2 mAh/g and the electrode cycled with EC/DEC/FEC electrolyte was calculated to be 4525.84 mAh/g.

The voltage profiles include two curves, the left-most solid and dashed curves indicate the lithiation of the material and the right-most indicate the delithation of the material. Regions in the voltage profiles where capacity changed more rapidly than the voltage were defined as voltage plateaus. These plateaus are also observed as peaks shown in differential capacity plots, also known as $dQdV^{-1}$ plots or pseudo-cyclic voltammograms, shown in the Figure 4.2. In the first lithiation (Figure 4.1a), plots resulting from both electrodes have a small plateau at 0.42 V vs. Li/Li^{+}. This plateau diminishes to the point of being unobservable by the tenth cycle (Figure 4.1b). Based on the potential at which this reaction takes place and previous work, we attribute this behavior to the reduction/lithiation of native oxide layer on the electrodes.[105–108]

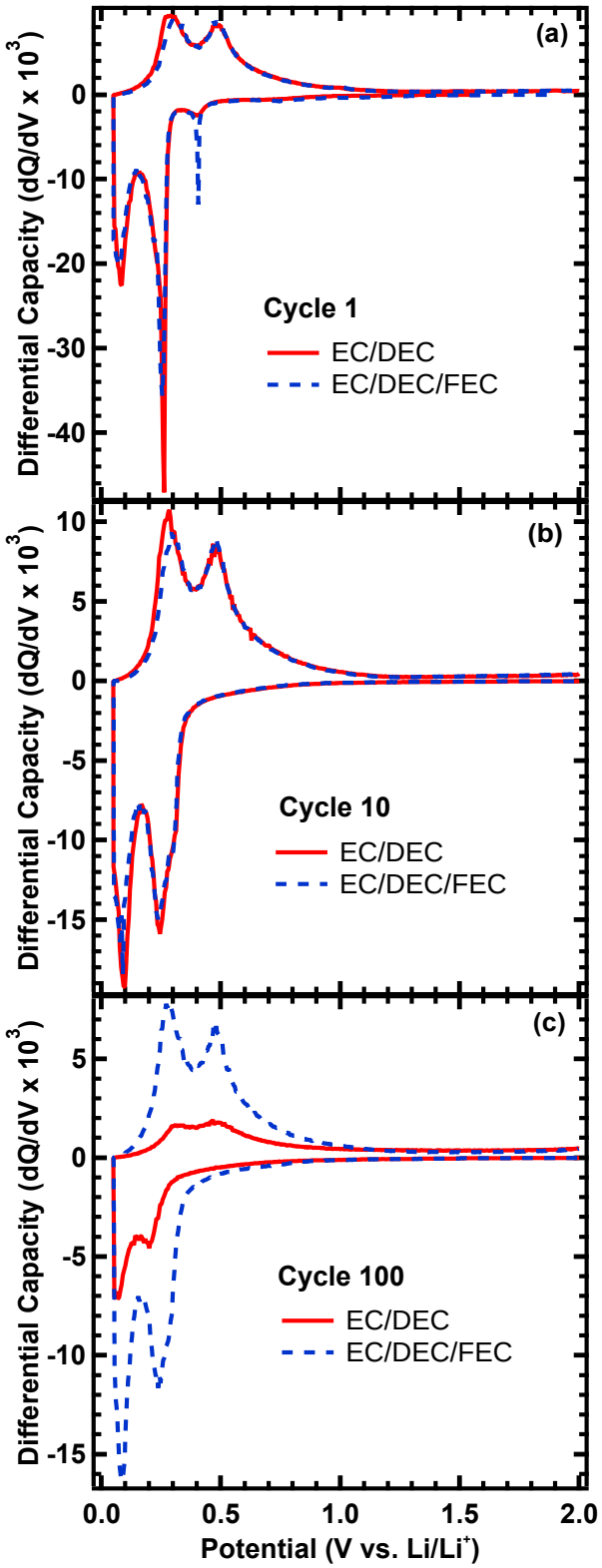

Figure 4.2. $dQdV^{-1}$ plots for half cells during the (a) first cycle; (b) tenth cycle; (c) hundredth cycle. Cells were cycled in EC/DEC (solid red line) and EC/DEC/FEC.

Lithiation and delithation reactions that took place during the first cycle for both electrodes (Figure 4.1a) are shown in the plateaus at 0.262 V and 0.076 V during reduction and at 0.285 V and 0.488 V during oxidation. There is a slight decrease in the potential of the first lithiation reaction between the first and hundredth cycle (Figure 4.1c) for both electrodes cycled in both electrolytes. However, the shift to less positive potential for lithiation and more positive potential for delithation is greater for the electrode cycled in EC/DEC, indicating an increase in over-potential with continued cycling. We attribute this behavior to increased resistance to ionic transport in the SEI, for reasons discussed in more detail below. Conversely, the lithiation plateaus hardly shift between the tenth and hundredth cycle for the electrode cycled in EC/DEC/FEC.

More qualitatively, the plateaus for the electrode cycled in EC/DEC (solid red line) deform from Figure 1a to 1c. The profile changes to poorly defined potentials at 100 cycles in Figure 1c. The electrode cycled in EC/DEC/FEC (dashed navy line) displayed similar behavior in the first cycle (Figure 4.1a) and hardly any change is observed between the tenth and hundredth cycle (Figures 4.1b and c). This indicates that the free energy required to lithiate is more poorly defined after 100 cycles for the electrode cycled in EC/DEC relative to the electrode cycled in EC/DEC/FEC. This could be due to the transport properties of each respective SEI, or a degradation in the active material caused by repeated cycling (i.e., no clear phase equilibrium between lithiated and delithiated silicon).

Figure 4.3 shows the evolution of the specific capacity and Columbic efficiency for electrodes cycled in each electrolyte system described above. As previously mentioned, by noting the x-axis value obtained at the end of each half cycle, an empirical estimate of the storage capacity of the *a*-Si thin film electrodes can be found. This capacity is shown for each

half cycle in Figure 2a. The ratio of the two capacity values is the Coulombic efficiency (CE), a measure of the irreversibility of the reactions that participate in each cycle, shown in Figure 2b.

In Figure 4.3a, we note that the electrode cycled with EC/DEC exhibited higher capacity up to the 37th cycle, compared to the electrode cycled in EC/DEC/FEC. However, with the exception of the first cycle, the electrode cycled with EC/DEC/FEC had superior capacity retention and CE (Figure 4.3b) compared to the electrode cycled with EC/DEC. The electrode cycled in EC/DEC continued to lose capacity in each cycle until 100 cycles were reached, while the electrode in EC/DEC/FEC maintained its capacity for the first 40 cycles, and then decreased gradually thereafter.

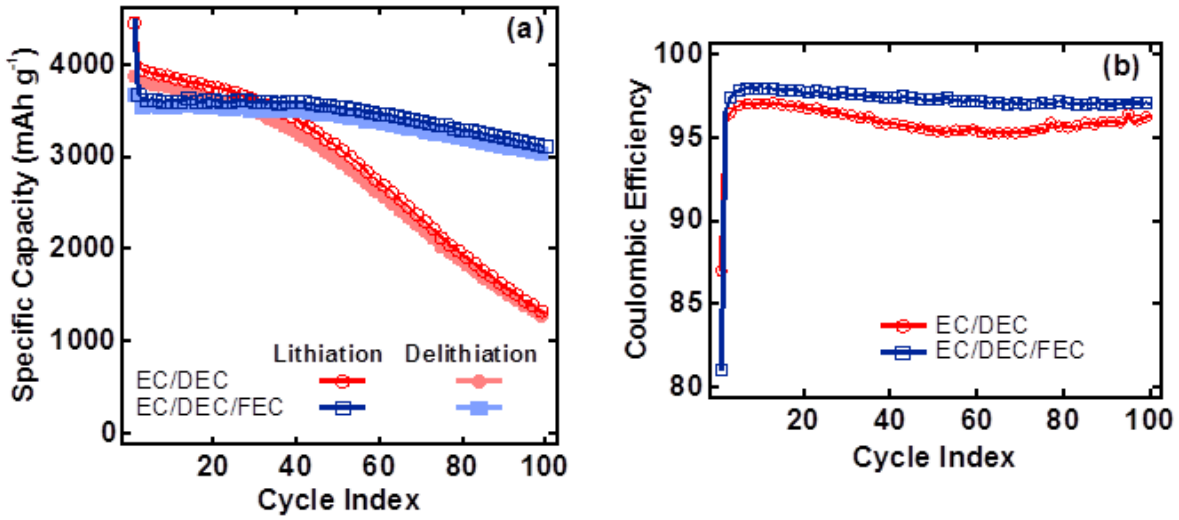

Figure 4.3. (a) Specific capacity versus cycle at ~C/2 rate and (b) Coulombic efficiency as a function of cycle for *a*-Si thin film electrodes galvanostatically charged and discharges in EC/DEC (red circles), and EC/DEC/FEC (navy squares).

The electrodes were not pre-cycled in anyway; therefore, the information from the first cycle reports on the formation of the SEI in both of the electrolytes used. After the first delithiation, the electrode cycled in EC/DEC had a capacity of 3867.3 mAh/g, while the electrode cycled in EC/DEC/FEC had a capacity of 3665.21 mAh/g. Upon delithiation neither

electrode returned to 0.0 capacity (Figure 1a) at the nominal open circuit voltage of 2.0 V. This was due to electrons measured during reduction and lithiation that were not recovered upon oxidation and delithiation. As a result, in the first cycle the electrode cycled in EC/DEC had a CE of 86.95% and the electrode cycled in EC/DEC/FEC had a CE of 80.96% (Figure 4.3b).

After the tenth lithiation (Figures 4.1b and 24.3a), despite having a lower initial theoretical capacity, the electrode cycled with EC/DEC showed higher capacity (3858.5 mAh/g) compared to the electrode cycled in EC/DEC/FEC (3597.2 mAh/g). However, even though the capacity of the electrode cycled in EC/DEC was higher, its CE was lower compared to the electrode cycled in EC/DEC/FEC (Figure 4.3b).

By the one-hundredth cycle (Figure 4.1c), the electrode cycled in EC/DEC/FEC maintained a capacity above 3000 mAh/g while the electrode cycled in EC/DEC suffered from severe capacity fade (down to 1252 mAh/g). The relative performance of the two electrolytes is in good agreement with the previous results shown in the literature, where the addition of FEC to the electrolyte improves capacity retention and CE over prolonged cycles.[45,80–82,91]

We attribute the observed difference in loss of capacity between the electrodes to surface processes and not mechanical degradation. We can deduce that changes in capacity are due to surface properties because of the mechanical stability of both thin-film electrodes, which do not show delamination or mechanical failure (see Figure 4.4). As a result, discrepancies in the amount of CE decrease experienced by the electrodes must come from: (1) continued progression of electrochemical parasitic reactions and incomplete surface passivation of the *a*-Si electrodes by the SEI, and/or (2) lithium retained in the active material, e.g., as a reduced silicon-lithium oxide (Li_xSiO_y).[105–109]

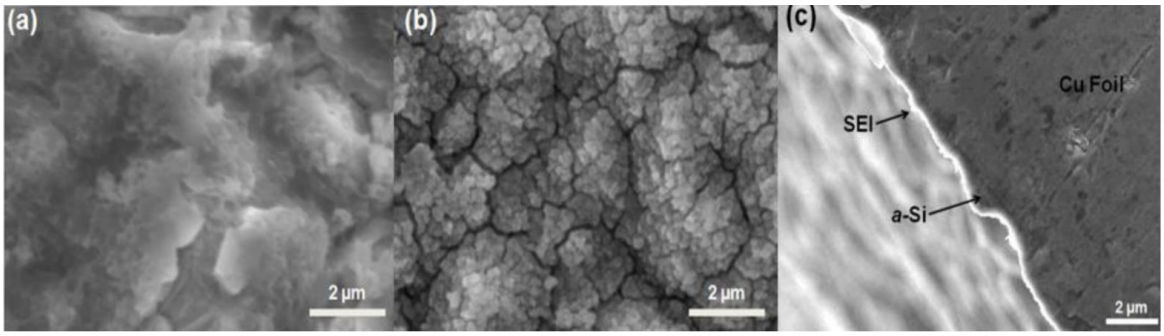

Figure 4.4. SEM images of electrodes after 100 cycles in (a) EC/DEC, (b) EC/DEC/FEC, and (c) cross-section image of EC/DEC electrode. All electrodes demonstrate high mechanical integrality without substrate liftoff.

Before we look at the electrochemical evidence for differences in the SEI formation and stability in the electrode/electrolyte systems, we will consider what is already known about EC/DEC/FEC blends in comparison to EC/DEC. Previous work suggested that the chemical composition and evolution of the SEI is controlled by the reaction kinetics of: (1) the initial reactants, such as the electrolyte and additives, and (2) the initial, insoluble, parasitic reaction products.[43,74,110,111] According to Balbuena and coworkers, density functional theory (DFT) calculations predict that FEC selectively decomposes over DEC and EC by a comparatively high rate. The reduction mechanism follows a one electron lithium-assisted reduction of the fluoromethyl group to fluoride and neutral radical carbonate to form LiF as a main reduction product.[83–85] Scheme 4.1 shows reactions that produce LiF and either ethylene and carbonate as products (Reaction 4.1) or alternately alkoxy products (Reaction 4.2). Nie, Abramham, Lucht *et al.* have also established the prominence of LiF in SEI derived from FEC reduction compared to other carbonate solvents.[91]

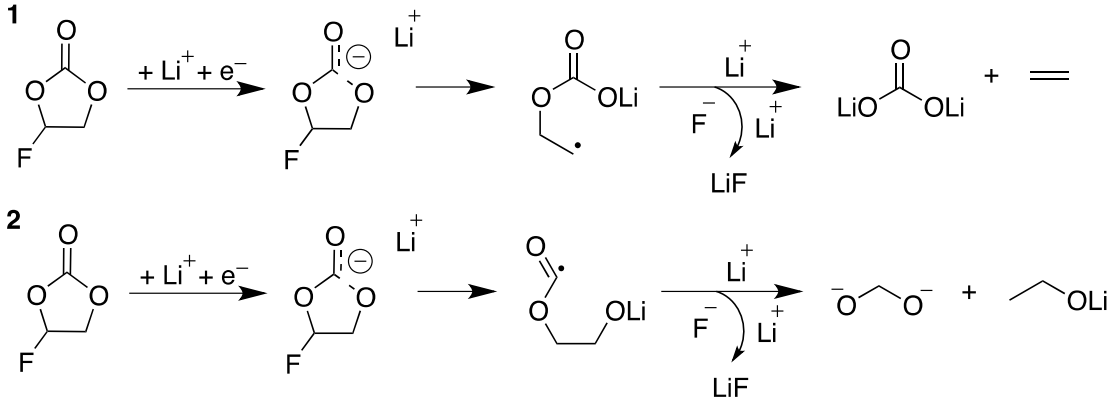

Scheme 4.1. Reaction 4.1; Electro-reduction of fluoroethylene carbonate to form lithium fluoride, lithium carbonate and ethylene and Reaction 4.2; Electro-reduction of fluoroethylene carbonate to form lithium fluoride, methylenedioxyl ion (or alternately carbon dioxide) and lithium ethoxide.

In the first cycle we observe that EC/DEC/FEC has worse CE than EC/DEC (Figure 3b). If more charge and lithium are consumed in the first cycle when the electrode is cycled in EC/DEC/FEC versus an electrode cycled in EC/DEC, then this suggests that the reduction rate is greater for FEC than EC.[96] Therefore, the addition of FEC to the electrolyte generates a large amount of LiF in the first cycle. This further suggests that the reduction reactions of all carbonates below 1.0 V Li/Li^+ are in a kinetically limited regime where the rate-limiting step involves the carbonate species reduction and not charge transfer to the solvent. Because we are comparing surfaces of similar area while maintaining mechanical stability, we are able to detect this shift in the SEI formation reactions, which was not observed in previous work.

The direct electrochemistry observations in the first cycle also support the idea that the difference in CE between the two electrolyte systems is due to SEI formation in the first cycle. We observed a larger increase in "capacity" above ~0.5 V vs. Li/Li^+ in the electrode cycled in EC/DEC/FEC during the first cycle (Figure 4.1a, dashed navy line). Since there is no electrochemical processes related to the lithiation of the electrode at these potentials, the

electrode cycled in EC/DEC/FEC must have consumed more charge during the formation of the SEI prior to the actual lithiation of the electrode.

These results are in contrast to previous literature, where it has been shown that adding FEC to a carbonate based electrolyte improves the initial CE. This result has been observed even on conductive additive and binder free electrodes such as *a*-Si thin films, nanowires, and nanoparticles.[45,86,87,90] Nakai *et al*. and Nie *et al*. both observed roughly equal CE between electrodes cycled in EC/DEC/FEC and EC/DEC electrolytes. However, Nakai *et al*. used relatively thick, ~2 μm *a*-Si thin film electrodes. The use of such thick electrodes makes it difficult to attribute the difference in CE to surface reactions and not other factors related to mechanical stability.[12] It is also difficult to compare electrodes made with nano-structured active material because of the inhomogeneity in surface area of each electrode when made on a laboratory scale. Here, the small change in porosity and particle packing can have a large effect on the SEI and lithiation rate of the active material.[73] In the present work, we use thin films grown during the same deposition event, in order to obtain a relatively controlled surface area and morphology from electrode to electrode.

Because the electrode cycled in EC/DEC/FEC shows better CE after the first cycle, we propose that the SEI formed during electrochemical cycling is better at passivating the surface from further reactions. To better understand the mechanisms of SEI formation and how the SEI from the two electrolytes differs, we turn to surface analytical techniques.

4.3.2. Surface Analysis by XPS and TOF-SIMS Depth Profiling

The complex and coupled nature of the parasitic surface reactions makes it difficult to directly observe their products and reduction mechanisms. Here the structure and chemistry of the SEI is determined by surface analysis via XPS and TOF-SIMS (Figures 4.5 and 4.6) *post hoc*

and *ex-situ,* avoiding environmental contamination by water vapor or oxygen, which can be detrimental to the SEI. By studying the SEI composition on a model system, we gain insights into the reduction mechanism of EC/DEC/FEC from its SEI structure via both XPS and TOF-SIMS depth profiling.

DC sputtered *a*-Si electrodes with SEI formed in both electrolytes underwent the following galvanostatic experiments: (1) a single lithiation event, (2) one complete lithiation and delithiation cycle, and (3) one hundred cycles. Each electrode surface was characterized first by XPS analysis, then by dual-beam TOF-SIMS depth profiling.

The XPS assignments (Figure 4.5) follow a careful self-consistent fitting model and are similar to previously reported results for SEI formed on other silicon model systems.[61,93] The identified chemistries included organics such as aliphatic carbon ("C sp^3"), alkoxy groups (ethers and alkoxides labeled "RCO"), carboxyl groups (carboxylates, esters) and/or oxalates (all labeled "ROCO"), and carbonic esters and/or ionic carbonate salts ("RCO_3"). Inorganic functionalities include lithium fluoride ("LiF"), and fluoro- and phosphoro- oxides ("$P_xO_yF_z$"). Lithium signal that could not be attributed to lithium fluoride is labeled "Li-X," which may include alkyl lithium, inorganic lithium oxide, and lithium phosphoro-oxy-fluoride compounds. Additionally, lithium included in the Li-X functionalities, as well as oxygen attributed to $P_xO_yF_z$ may in fact be part of lithium-silicon oxide (Li_xSiO_y) following the work of Philippe *et al*., Martin *et al*., and Radvanyi and co-workers.[105–108] A small, yet detectable amount of lithium oxide ("LiO_x") was observed in one experiment and will be discussed in more detail below. It can be difficult to distinguish between hydroxide, peroxide, and oxide compounds by XPS; therefore, the LiO_x assignment includes all of these functionalities.

It should be noted that due to the mean-free path of the photo-excited electrons, the compositions measured by XPS are only representative of the outer-most ~10 nm film thickness of the SEI.

TOF-SIMS assignments (Figure 4.6) follow the work by Schroder *et al*.[61] and only represent a small subset of marker species used to identify the layered structure of the SEI. Determining the complete chemistry of the SEI from secondary mass fragments in an inhomogeneous, poorly controlled, mixed inorganic/organic interface is outside the scope of this work.[61,95,112] In lieu of comparing different functionalities directly (e.g., relative concentrations of organic and inorganic species), the depth profiles consist of the signals of particular secondary ion mass fragments normalized to each fragment's maximum measured intensity. Identifying the maximum intensity allows us to discuss the structure of the SEI in terms of intermixing strata and micro-phases consistent with the kinetic stability theory of the SEI summarized by Peled and Golodnitsky.[43] Accordingly, we use the C_2H^- mass fragment as a marker for organic species (with H^- shown to provide context for the fragmentation of these species). The PO^- and LiF_2^- are markers for the inorganic compounds such as $P_xO_yF_z$ and LiF species. LiO^- is also present and we have attributed its source to a mixture of LiO_x species as well as Li_xSiO_y formed during reduction of the native oxide present on the electrodes.

All mass fragments are plotted as a function of depth, with 50% of the maximum (steady state) Si^- fragment signal taken as the surface of the electrode. It should also be noted that the depth profiles are plotted on their own differing x-axis to highlight each ion's changing signal with depth. Additionally, when discussing the ion signals it is important to remember that the overlapping intensities are the result of multiple factors, including knock-in, recoil, and interfacial roughness effects.[61]

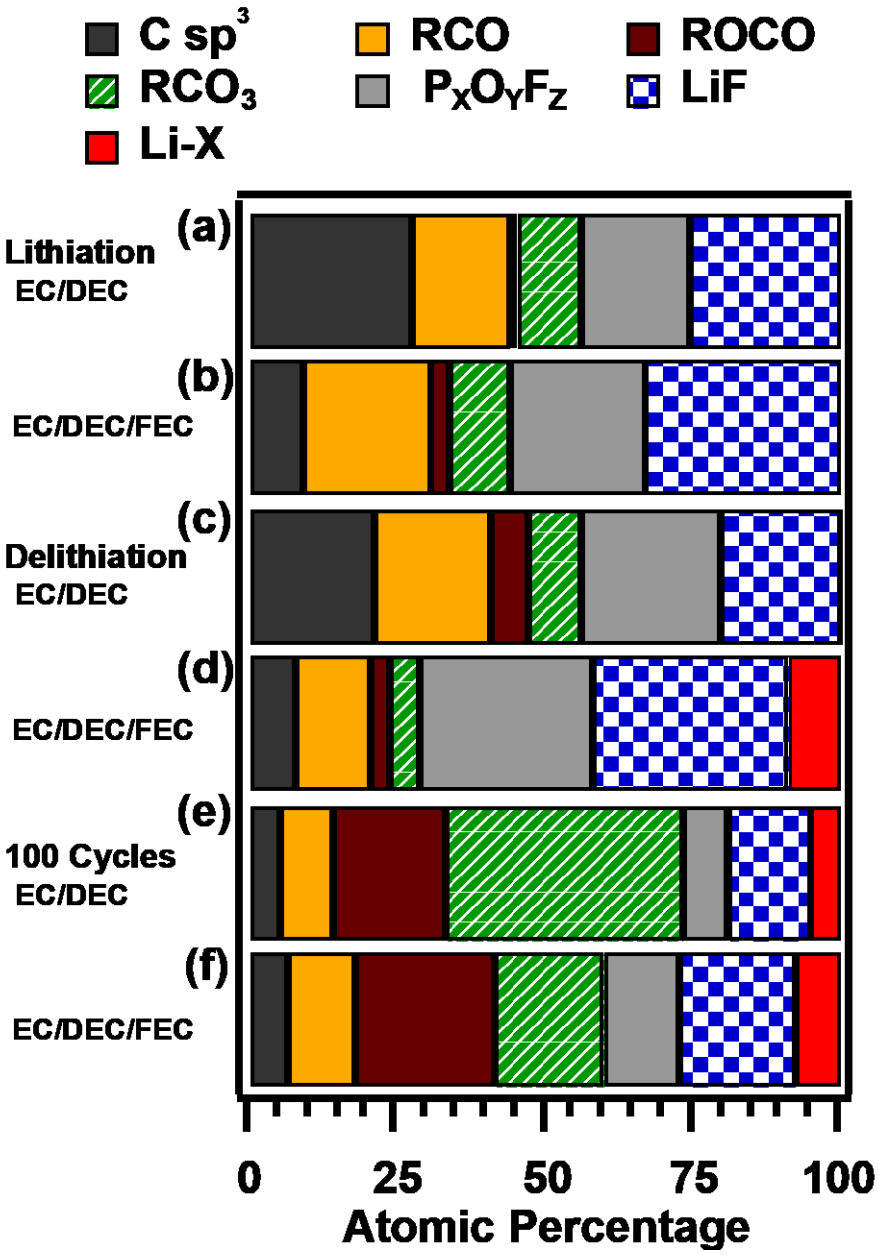

Figure 4.5. Relative composition of the 10 nm outer SEI after: first lithiation (a and b); first delithiation (c and d); and 100 cycles in the delithiated state (e and f). The layer resulted from and was in fluid communication with EC/DEC (a, c, and e) and EC/DEC/FEC (b, d, and f).

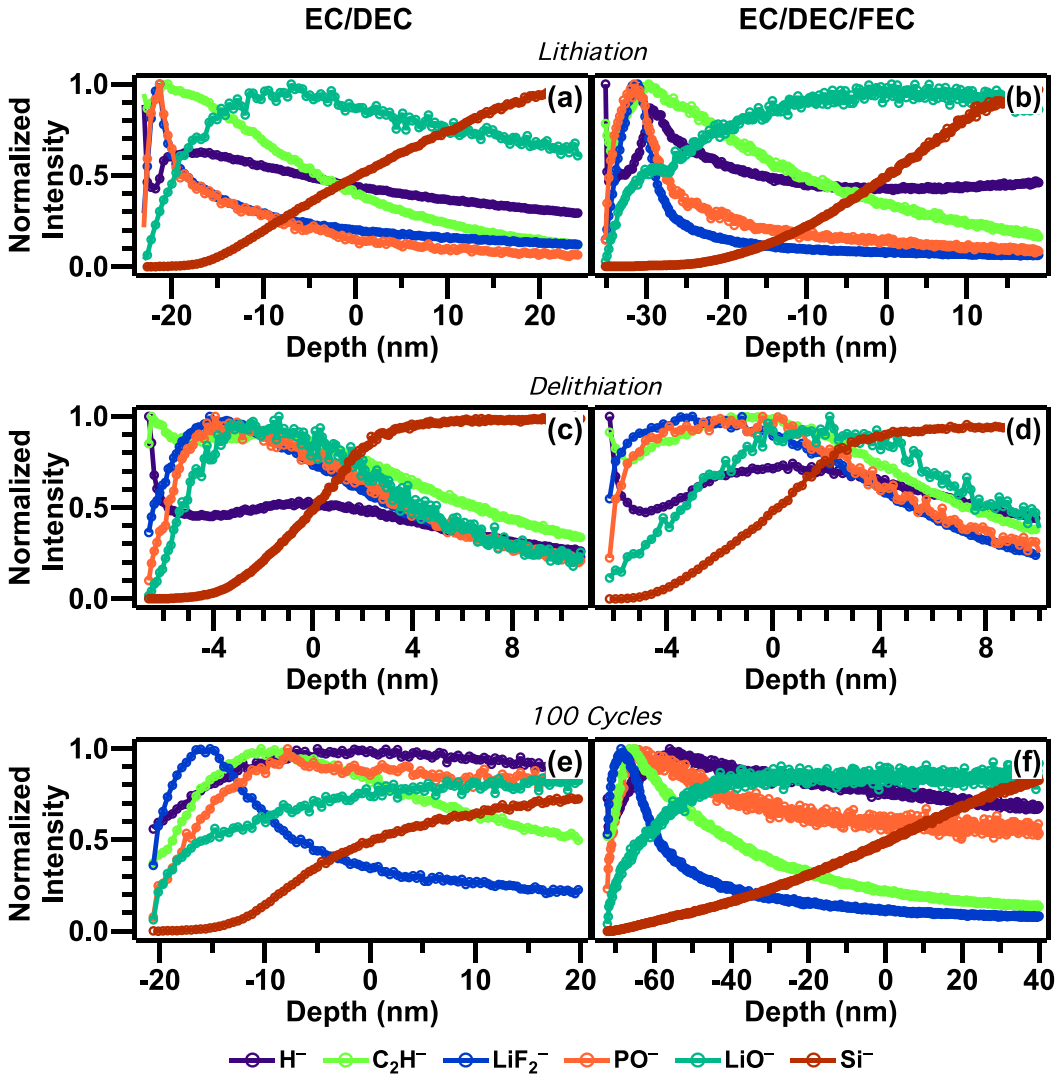

Figure 4.6. TOF-SIMS depth profiles of SEI resulting from both EC/DEC (left column) and EC/DEC/FEC (right column) electrolytes that have undergone (a) and (b) galvanostatic lithiation; (c) and (d) one full cycle of galvanostatic lithiation and delithation; and (e) and (f) 100 galvanostatic cycles. It should be noted that each subfigure is plotted on its own x-axis; the thickness of each SEI varies significantly as it evolves and each is on their own scale to better see the changes in the secondary ions' normalized signal. Negative depths are above the surface of the *a*-Si electrode, and positive depths go below the surface.

Comparing the lithiated electrodes (Figures 4.5a, 4.5b, 4.6a, and 4.6b), we observe changes in the chemical composition and stratification consistent with the calculations done by Balbuena and co-workers. First, from the XPS, the SEI resulting from the EC/DEC/FEC

electrolyte had increased concentration of inorganic species (Figure 4.5b), specifically LiF (Reactions 1 and 2). Although not shown in Figure 3b, the SEI formed from EC/DEC/FEC after initial lithiation was the only sample we observed with appreciable LiO_x species (0.01 percent of the atoms probed). Of the organic species present from the reduction of EC/DEC/FEC electrolyte, there was less aliphatic carbon, as well as more alkoxy and carboxyl compounds compared to the EC/DEC electrolyte SEI. This is consistent with what would be expected from Reaction 2 if the computationally predicted FEC reduction preferentially occurred over the EC reduction. Additionally, recent work by Martinez de la Hoz, et al.,[113] has suggested that salt decomposition products such as the $P_xO_yF_z$ species, LiF and LiOx all result from multiple step reduction reactions. Significant among these findings is that phosphorus species form very stable oxide and P-Si species on the surface of the active material. In addition to PO^- ion having a high TOF-SIMS cross-section, the detection of these species close to the surface in the delithiated electrodes (Fig. 4c-f) is in line with these predictions.

With regards to the structure of the SEI, TOF-SIMS depth profiles (Figures 4.6a and 4.6b) show that after the initial lithiation, EC/DEC/FEC produced a thicker SEI (35.1 nm), compared to the SEI formed in EC/DEC (23.1 nm). Additionally, EC/DEC/FEC produced a thicker stratum of LiF. In these electrodes, taking the stratum of SEI containing LiF to be where LiF_2^- signal was greater than 50% of its maximum intensity, this layer was ~4 nm in the SEI derived from EC/DEC (Figure 4.6a) versus ~7 nm (Figure 4.6b) from EC/DEC/FEC. The SEI structure was substantially similar in terms of the ordering of each marker species' maximum intensity for both electrolytes. Both SEI had overlapping inorganic (PO^-, LiF_2^-) and organic (C_2H^-) mass fragment signals far from the electrodes surface (50% of maximum of the Si^-) with lithium oxide/hydroxide and Li_xSiO_y close to the to the electrodes' surfaces.

The SEI that resulted from both EC/DEC and EC/DEC/FEC evolved significantly during delithiation. XPS showed that more inorganic species and more LiF specifically, remained after delithation for the EC/DEC/FEC SEI (Figure 4.5c and 4.5d). This suggests that the reactions in EC/DEC/FEC that formed the SEI during lithiation were more inorganic, irreversible, and stable. From the TOF-SIMS depth profiles (Figures 4.6c and 4.6d), we observe that the SEI resulting from both electrolyte systems were of similar thicknesses: 6.6 nm for EC/DEC and 6.1 nm for EC/DEC/FEC. This information, combined with the known higher concentration of LiF in the outer ~10 nm of the SEI further suggests that there is a more dense layer of LiF formed on the surface of the electrode cycled in EC/DEC/FEC.

There are, however, two structural differences: (1) SEI formed from EC/DEC had a thicker organic stratum on top of the inorganic species compared to the SEI formed from EC/DEC/FEC; and (2) there is a thicker stratum of LiO^- species in the depth profile of the electrode cycled in EC/DEC than the electrode cycled in EC/DEC/FEC. To explain (2), we examine Figures 4c and 4d, where LiO^- fragments primarily result from Li_xSiO_y species, as LiO_x species may be oxidized during delithation.[61] This implies that there is less Li_xSiO_y on the electrode cycled in EC/DEC/FEC. The simplest explanation for this observation is that the FEC reduction leads to the formation of a radical organic anion and fluoride ion (similar to the Reactions 4.1 and 4.2) and then reacts with native oxide present on the surface, following Reaction 4.3.

$$SiO_X + xF^- \rightarrow SiF_X + (x/2)O_2 \qquad (4.3)$$

This hypothesis is further supported by previous work done by Schroder *et al.*[61] where reactive ion etched silicon produced SEI morphology and chemistry comparable to that of the SEI produced by EC/DEC/FEC after initial lithiation (Figures 4.5b and 4.6b). Below, we will

further discuss the importance of this reaction with regards to SEI composition and function after 100 cycles in the delithiated state, and silicon surface reactivity.

After 100 cycles, we assume the SEI to be in an approximate steady-state and the differences in chemistry and structure of the SEI to be the result of the different electrolytes. The SEI produced by EC/DEC has much more carbonate and less carboxyl and/or oxalate species. More importantly, this electrode contains much less inorganic species, especially LiF. The TOF-SIMS depth profiles (Figure 4.6e and 4.6f) show that EC/DEC/FEC actually produced a much thicker SEI (72.3 nm compared to 20.6 nm). The overall structure of both SEI; however, are very similar in terms of the relative location of maximum signal for each of the marker species. The strata in both SEIs are arranged with LiF near the surface of the SEI, intermixed with organic and then PO^- containing species and then LiO^- near the surface of the electrode. LiF strata thicknesses are comparable, but EC/DEC/FEC did produce a thicker layer of 11.5 nm vs. 13.2 nm. The layer of lithium oxide (LiO^-) species found close to the surface of each electrode produced the biggest difference in thickness between the SEI cycled in the different electrolytes. These results are very much in line with recent predictions by Balbuena and co-workers who examined computationally the effects of multiple competing reduction reactions and found Li_2O and P-O species to be important stable SEI products.[113]

Our results are in conflict with some of those previously reported, especially those that claim the presence of poly-fluorocarbonate (poly FEC), poly-(vinylene carbonate) (polyVC), and –CHF-OCO_2 type compunds.[45,86,87,96] In some cases, it is unclear where the direct evidence for poly FEC originates in these reports. While it is possible to assign peaks in the C 1s and F 1s spectra to C-F bonds, our fitting procedure was able to account for all oxidation states of carbon by the oxygen signal detected. Qualitatively, the F 1s of the SEI produced by EC/DEC and

EC/DEC/FEC in the region that would be assigned to C-F do not look particularly different, making it difficult to justify why C-F bonds should be assigned. In other cases, the detection of C-F bonds may be due to the investigated samples having polyvinylidene fluoride (PVdF) binder, decomposed PVdF binder and/or exposure to air and water. This makes it difficult to determine the origin of these species.

Schroder *et al*.[93] have shown that limited exposure to ambient atmosphere (i.e., oxygen gas, and water vapor) dramatically changes the XPS results. We reproduce these results with SEI formed from EC/DEC/FEC that were exposed to ambient conditions in the Supporting Information (Figure S3). The literature that reports "limited" exposure does not take into account the time when a sample is loaded into an instrument during pump down when the environment around the sample is contaminating. During this time there is continuous exposure to gaseous water vapor and oxygen until the sample antechamber reaches UHV conditions, which with off-gassing of high surface area materials may be on the order of hours. As a result, these samples are always exposed to ppm oxygen and water higher than a glove box environment, which is a large determining factor in the irreproducibility and/or inaccuracy of the results.[74,93,94]

We have shown that compared to the SEI formed in the traditional electrolyte, SEI formed from EC/DEC/FEC is consistently thicker during cycling and contains more LiF. Moreover, SEI formed from EC/DEC/FEC included different organic species after initial formation that evolved to contain much less carbonate species after 100 cycles, compared to the SEI formed from EC/DEC. Additionally, the SEI from EC/DEC/FEC comprised more lithium oxide and lithium fluoride species near the electrode after 100 cycles.

4.3.3. EIS of SEI Formed With and Without FEC

To determine how the differing chemical composition of the SEI affects its function, we carried out a series of electrochemical impedance spectroscopy (EIS) experiments. EIS is a standard analytical technique used to provide information on lithium ion migration through surface films, charge transfer, phase transition, and solid state diffusion.[45,46,114] In particular, we use EIS to study the resistance associated with lithium ion migration through the SEI.

Figure 4.7 shows the changes in the impedance spectra of the *a*-Si thin films in a two electrode system after the first lithiation, first delithiation, and 100 cycles in the delithiated state. Figure 5a shows Nyquist plots for electrodes cycled in EC/DEC and EC/DEC/FEC after first lithiation. A Nyquist plot shows the real part of the measured impendence versus its imaginary component over a range of AC frequencies. In order to quantitatively and qualitatively analyze the impedance spectra, we turn to a model circuit of the elementary reactions that occur during electrochemical cycling (Figure 5d). The model accounts for the uncompensated ohmic resistance of an *a*-Si electrode (R_Ω), the double layer capacitance of the electrode/electrolyte interface (CPE_f), resistance due to the surface reactions on the electrode (R_f), the double-layer capacitance (CPE_{dl}), the charge transfer resistance (R_{ct}),_and the impedance due to solid state diffusion processes, known as the Warburg impedance (Z_w).[45,81,115–117] It is widely accepted in the case of battery negative electrodes that the semi-circle traces (Figures 5a, 5b, and 5c) generated at high frequency and the associated resistance R_f are due to lithium-ion migration through multilayer surface films.[45,114,118] At low frequencies, linear trends in high impedances are observed, which are attributed to the Warburg impedance (Z_w) of the electrode and are due to the solid-state lithium diffusion through the Li-Si alloy material.[114,118,119]

The major difference in the EIS between the electrodes cycled in EC/DEC and EC/DEC/FEC is the resistance of the surface films, R_f. However, since this was conducted in a two electrode cell, the impedance measurement also includes the lithium metal. The EIS data for the lithiated electrodes were fit to calculate an R_f of 0.120 kΩ and R_{ct} of 0.489 kΩ for the electrode cycled in EC/DEC/FEC, while the electrode cycled in EC/DEC had a lower R_f of 0.067 kΩ and a R_{ct} of 0.481 kΩ. After the first delithiation both electrodes had an increase in impedance: the electrode cycled with EC/DEC/FEC had an R_f of 0.276 kΩ and R_{ct} of 0.926 kΩ, while the electrode cycled in EC/DEC had a lower R_f of 0.021 kΩ and a R_{ct} of 0.785 kΩ. The increased impedance for the electrode cycled in EC/DEC/FEC electrolyte correlates with the work conducted by Xu, C *et al*.[96]

We find that the EIS data supports the idea that the FEC produces a dense, thick, LiF-dominant SEI on the first cycle. Overall, the SEI from EC/DEC/FEC was thicker, it exhibited decreased performance in terms of overall resistance to lithium transport after initial formation. However, by compared SEI thickness to resistance in SEI produced by different methods, Lu, Harris, *et al.* found that thicker SEI often had more inorganics and lower resistance per unit length (depth resistivity).[120] Even though the measurements came from different electrodes, we can estimate that EC/DEC/FEC produced an SEI on the order of 29.5 Ω/nm vs. 35.5 Ω/nm for EC/DEC.

EIS had previously been carried out on electrodes cycled for 30 and 100 cycles.[45,81] Both studies suggested that the impedance of the SEI derived from EC/DEC/FEC had lower surface film resistance. After 100 cycles, we found EC/DEC/FEC produced an R_f of 0.012 kΩ and a R_{ct} of 0.021 kΩ, while EC/DEC produced an R_f of 0.121 kΩ and a R_{ct} of 0.148 kΩ, consistent with these results. As we note above, a thicker, more inorganic SEI may be more conductive per unit

thickness. This helps explain how EC/DEC/FEC produced a thicker SEI on the electrode after 100 cycles (in the delithiated state), but nevertheless its R_f was smaller and the electrode showed well-defined plateaus in the charge/discharge curves (Figure 4.1c).

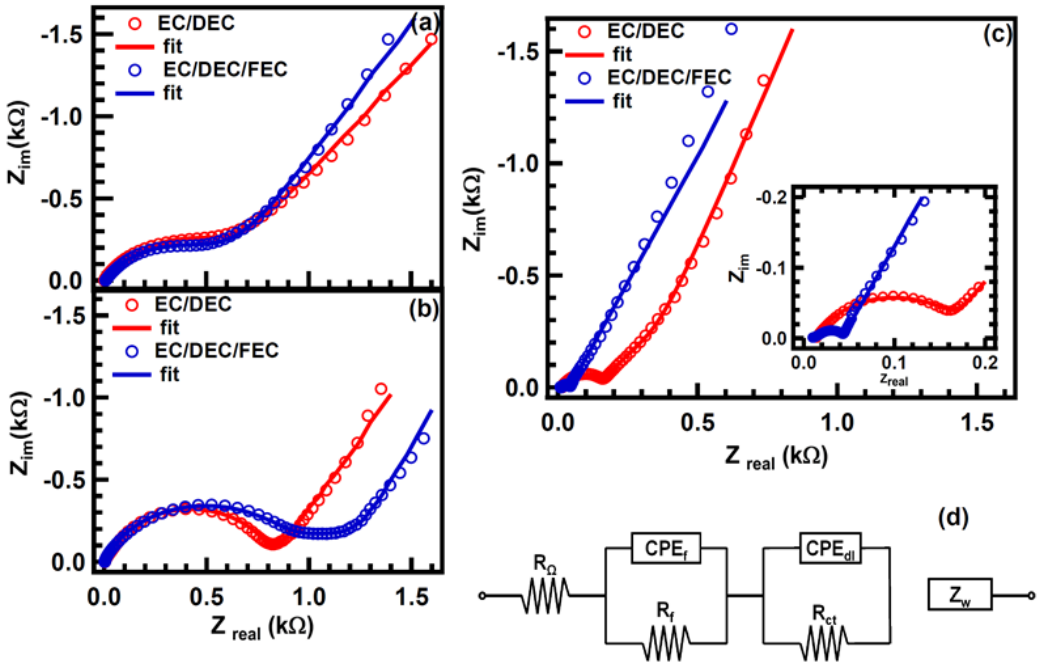

Figure 4.7. Impedance spectra of half-cells after the initial lithiation (a), delithiation (b), and 100 cycles in the delithiated state (c) for 1 M $LiPF_6$ in EC/DEC (red), and EC/DEC/FEC (navy). An inset in (c) shows a more detailed view of the impedance behavior at low resistances and high applied frequencies. An equivalent circuit (d) is used to model the reactions on the *a*-Si electrode varying the electrolyte. The fits for the data for each electrode are shown as solid lines.

First, FEC reduces to form fluoride anions near the surface of the electrode, but previous work has failed to consider surfaces with native oxides. It is well known that F^- reacts with SiO_x suboxides and we suggest that F^- generated near the electrode is very likely to react with species other than lithium. Looking at Figures 4.6c and 4.6d, the LiO^- signal from SiO_x and Li_ySiO_x species indicate a thicker oxide layer on the interface cycled in EC/DEC than the electrode cycled in EC/DEC/FEC (previously discussed). This data is consistent with the data shown by

Nakai *et al.*[87] However, they suggested that an electrolyte not containing FEC somehow oxidized the silicon surface, without suggesting a mechanism or providing supporting evidence for their conclusion. We propose that fluoride ion etching is a more likely and is a simpler explanation. Moreover, there is no reason to infer, *a priori*, that oxidation of the surface takes place under reducing conditions (lithiation).

Previous work has suggested that Li_ySiO_x is a very compact and kinetically stable protective coating of the electrode; however, it is also electronically and ionically insulating. As a result, etching the surface should improve *a*-Si conductivity.[61,105,106,108] Intentional removal of silicon oxide on model wafer electrodes in previous work lead to formation of a thick Li_2O layer, consistent with the kinetic stability model of SEI structure.[43,61] The increased LiO^- in TOF-SIMS depth profiles of the electrodes cycled in EC/DEC/FEC after initial lithiation (Figures 4.6b) and after 100 cycles (Figure 4.6d), further supports the hypothesis that etching Reaction 3 takes place.

The removal of Li_ySiO_x may also lower interfacial resistance, which helps explain the SEI resistance observed in the EIS after 100 cycles. Additionally, the lack of Li_ySiO_x reduces the irreversible lithium sequestration associated with this oxide layer and explains some of the increased CE that results from EC/DEC/FEC electrolyte.

The formation of LiF at the electrode surface is also important in understanding the transport properties of the SEI, the passivation of the surface, and the SEI evolution. As we have discussed, the elevated concentration of LiF in the SEI (Figure 4.5b) results from the direct, fast, electrochemical reduction of FEC is the evidence for the occurrence of Reactions 4.1 and 4.2 (Scheme 4.1). In contrast, the electrodes cycled in EC/DEC have only an indirect path to LiF formation through thermal decomposition (Reaction 4.4):[121–123]

$$Li^{+}_{(sol)} + PF_6^{-}{}_{(sol)} \rightarrow PF_{5\,(sol)} + LiF_{(s)} \qquad (4.4)$$

In addition, the solubility of LiF in liquid carbonates is very low,[124–126] so the formation of LiF is self-perpetuating and drives further precipitation (Reaction 5):

$$Li^{+}_{(sol)} + F^{-}_{(sol)} \rightarrow LiF_{(s)} \qquad (4.5)$$

For EC/DEC, the formation of LiF is reliant on the resistance at the interface of the electrode to drive the thermal decomposition of $LiPF_6$. As a result, LiF formation in EC/DEC is preceded to some extent by decomposition of the solvent into organic species to form electronically or ionically insulating species. In EC/DEC/FEC, LiF formation occurs by electroreduction concurrently with formation of the organic SEI species. LiF is known to be more kinetically stable product under reduction compared organic SEI products, so LiF may remain stable close to the electrode surface.[43,44] Therefore, the SEI resulting from EC/DEC/FEC has a more direct path to forming kinetically stable species than EC/DEC, as a result there is less evolution of the SEI (and improved CE) with additional cycling.

The reduction of FEC to form fluoride ions has a big impact on the desolvation of lithium ions and the transport of lithium through the SEI. Through the common ion effect, saturated solutions of LiF lower the free energy barrier to desolvate (precipitate) other lithium-containing species. As a consequence, the solubility (S_{Li2O}) of Li_2O decreases with lithium fluoride concentration in solution, following Equation 4.1:

$$S_{Li_2O} = \sqrt[3]{\frac{K_{SP}}{4}} = \sqrt[3]{\frac{[O]([Li]_{Li_2O} + [Li]_{LiF})^2}{4}} \qquad \text{(eq 4.1)}$$

In this way, LiF formation is also coupled to Li_2O. The formation of lithium oxide and/or hydroxide species on the surface of the electrode is important for two reasons. First, we propose

that it improves Li-ion transport though the SEI. Second, the formation of the species has been shown to be quasi-reversible and therefore sequesters lithium to a lesser degree than other SEI species.

Schroder *et al.*[61] have already shown that lithium oxide species formation is quasi-reversible via oxidation reactions that take place when *a*-Si electrodes were delithiated (Figure 4d). The formation of the lithium oxide is due to electrolyte decomposition,[61] which is detrimental to the long-term life of the cell; however, the quasi-reversibility of the reaction helps to explain why the electrode cycled in EC/DEC/FEC has less lithium sequestration (and thus higher CE). It is difficult to gauge the importance of this degradation mechanism because results related to silicon electrodes that experience catastrophic failure after long term cycling are rarely published (because this is a negative result). Furthermore these results are often attributed *de facto* to mechanical failure of the active material or binder in composite electrodes.[127] However, the degradation of the electrolyte due to continued reduction into lithium oxide might also explain this behavior.

4.4. Conclusion

Using amorphous silicon thin film model systems and anoxic, anhydrous surface analysis techniques, we have investigated the effect of FEC co-solvent in promoting a stable SEI formation. Galvanostatic cycling of the *a*-Si thin film electrodes in electrolytes with and without FEC and 1 M $LiPF_6$ salt resulted in significant difference in the CE, consistent with prior work. It was demonstrated that cycling the electrodes in the FEC-containing electrolyte lowered CE on the first cycle; however, every cycle after showed better capacity retention, and CE.

The SEI that resulted from both of these electrolytes was characterized by anoxic and anhydrous XPS and TOF-SIMS. XPS showed that FEC lead to an SEI with increased

concentrations of inorganic species, specifically LiF. Moreover, the organic species present in the SEI contained less aliphatic carbon, in comparison to the composition of the traditional electrolyte SEI. These results are consistent with calculations conducted by Balbuena and co-workers, which suggests a kinetically fast formation of neutral radical carbonate and fluoride via a ring opening mechanism leading to the rapid formation of LiF. The TOF-SIMS depth showed that the SEI was thicker in the electrode cycled with FEC-containing electrolyte.

Both the XPS and TOF-SIMS depth profiles showed evidence of fast reduction kinetics of FEC. Subsequent formation of F^- affected the electrodes: (1) improving silicon's conductivity via silicon native oxide etching, (2) changing the solubility of lithium, which lead to (3) quasi reversible lithium sequestration and (4) improved Li-ion transport through the SEI via a shuttling mechanism. The style of analysis presented in this work can be further applied to understanding how SEI formation changes with other additives and on surface coatings.

With regards to SEI Li-ion transport, it has been suggested that inorganic species have preferable properties compared to organic species. One justification of this idea is that inorganic SEI species tend to have Li-ions bound in ionic bonds that facilitate hopping-type transport mechanisms. High concentrations of LiF relative to organic species has already been shown, in simulation, to promote rapid Li transport by Jorn, *et al*.[128]

We propose Li_2O has improved transport properties over organic species because of its ionic nature. This hypothesis is consistent with the ideas put forth by Jorn *et al.* and would explain the improved transport properties observed by EIS in Figure 4.7c. Moreover, the oxidative instability of Li_2O leads to desolvated lithium near the electrode's surface. This desolvated lithium, combined with the low solubility of lithium in and near the SEI, leads to an abundance of free lithium. These conditions facilitate a shuttle mechanism, decoupling the

process whereby lithium leaves the electrolyte and enters the electrode, improving lithiation kinetics.

Chapter 4, in full, is a reprint of the material “The Effect of Fluoroethylene Carbonate as an Additive on the Solid Electrolyte Interphase on Silicon Lithium-ion Electrodes” as it appears in the Chemistry of Materials, Schroder, K; Alvarado, J; Yersak, T.A; Li, J; Dudney, N; Webb, L; Meng, Y.S; Stevenson, K.J, 2015, 27, 5531. The dissertation author was the co-primary investigator and author of this paper. All the electrochemical tests were performed by the author except for the TOF-SIMS data analysis and interpretation. Both Schroder and the author designed and analysed, and wrote the results.

Chapter 5. Direct Visualization of the Solid Electrolyte Interphase and Its Effects on Silicon Electrochemical Performance

5.1. Introduction

Silicon is regarded as a potential candidate for next generation anode material for lithium ion batteries (LIBs). The high theoretical gravimetric energy density of silicon-lithium is attributed to the alloying reaction that occurs during the lithiation state, resulting in a high specific capacity (3579 mAh/g for $Li_{15}Si_4$), which is ten times greater than the current commercial graphite anode. However, the material undergoes severe mechanical stress and strain due to the volume expansion (300%), typical for lithium alloying reactions, which leads to active material cracking, pulverization, and contact loss with the current collector. In order to mitigate the mechanical degradation processes, clever nanomaterial design of silicon (i.e. particles, wires, core shell) have proved to accommodate the large volume expansion during lithiation.[19,45,80] Lui, Xiao *et al.* demonstrated that silicon cracking and fracture is dependent on the Si particle size, ultimately, determining that below 150 nm crystalline Si particles can endure the mechanical strain of full lithiation.[9] Moreover, Gu, Meng *et al.* observed a two phase lithiation process resulting in mechanical stability improvement for Si nanoparticles (NP) ranging from 60 to 100 nm in size, validating the critical cracking size.[129] Though researchers have improved the volume expansion and active material contact to the current collector, the Si anode still suffers from electrolyte chemical degradation caused by the formation of an unstable solid electrolyte interphase (SEI). As a result of the continuous volume expansion, the unstable SEI continues to consume and trap lithium ions as well as electrolyte during electrochemical cycling.[11,130] Both the mechanical and chemical degradation of Si causes rapid capacity failure and poor Columbic efficiency (CE) during electrochemical cycling. Thus several challenges must be resolved in order to realize the pragmatic application of Si based anodes for LIBs.

Previous work has reduced the SEI effects by: (1) a series of backend coatings; (2), varying binders and conductive additives; and (3) modifying the traditional carbonate based electrolyte.[17,46,131,132] Of these, altering the electrolyte composition by the addition of electrolyte additives has successfully improved the chemical degradation of Si anodes. In particular, the addition of fluorethylene carbonate (FEC) to conventional 1M $LiPF_6$ in ethylene carbonate (EC): diethylene carbonate (DEC) electrolyte has successfully improved the cycling stability and CE of various Si anode types. Though many researchers have used FEC, little is known on how it improves the SEI formation and its morphology. In response, a series of recent publications have investigated the SEI formation process using advanced surface characterization techniques. Yet contradicting studies regarding to the reduction mechanism of FEC have caused researchers to propose differing accounts, where some studies claim that FEC reduces to vinylene carbonate which then self-polymerizes to form either polycarbonates or a poly(alkene).[45,86] While Balbuena *et al.* used computational methods to study the decomposition of FEC and demonstrated that the most probable decomposition mechanism for FEC occurs via a ring opening reaction to form F^-, CO_2^{2-} and $CHOCH_2$. These reduction products can then react further to form LiF, RCOLi, and Li_2CO_3. This work agrees that a possibility to the stabilization of Si's SEI is due to the substantial formation of LiF in the initial cycle as a result of the fast FEC reduction. Schroder, Alvarado *et al*. used a-Si thin film to reconcile the differing accounts of the FEC reduction mechanism, composition, and morphology.[11] Their results determined that the electrode cycled in (10 wt.%) FEC additive forms SEI components that can help facilitate lithium ion transport through the SEI despite being thicker and denser in structure. Xu e*t al*. used Si NP composite electrode to determine the effect of FEC at different state of charge in the initial cycle and as a

function of depth, suggesting that FEC aids the preservation of the electrode by forming a uniform dense SEI improving the cycling performance.[130]

The notion that FEC forms a protective uniform SEI has been speculated and proposed by scanning electron microscopy (SEM) and transmission electron microscopy (TEM).[45,80,87,91] These studies use BF-TEM images mainly to study the volume changes after cycling, not focusing on surface morphology Etacheri, *et al*. observed the Si nanowires after 30 cycles using TEM; however, they mainly focus on volume expansion of the Si nanowires after cycling by BF-TEM images with low spatial resolution not in the SEI morphology evolution.[45] Nie *et al*. monitored the Si NP's morphology using TEM and SEI elemental composition by EDX.[90] However, they claimed that the morphology of the SEI changes throughout electrochemical cycling, yet the TEM images do not clearly demonstrate this phenomenon. This is largely because BF-TEM images are not sensitive to the Z-contrast; therefore, how FEC improves the SEI stability in the initial cycles has been proposed but not well characterized by microscopic techniques. Therefore, more work needs to be done in order to determine how FEC affects the SEI-Si NP interface and electrochemical performance given that the SEI formation is found to be heavily influenced by surface chemistry and surface area. It is hypothesized that the rapid decomposition of FEC forms a uniform conformal coating around Si NPs reducing the rate at which the electrolyte decomposes,[130] preventing the Si NPs from being exposed to the electrolyte after initial lithiation and delithiation. Conversely, the electrodes cycled in a conventional electrolyte (EC/DEC) suffer from a porous heterogeneous SEI. This hypothesis has yet to be observed using proper single particle microscopy techniques; therefore, we aim to validate this hypothesis by coupling annular dark field scanning transmission microscopy imaging (ADF-STEM) with electron energy loss spectroscopy (EELS) to provide comprehensive

insights into the SEI morphology evolution and observe its evolution throughout progressive electrochemical cycling.[133] Using Z-contrast ADF-STEM images can display the SEI morphology evolution with high-spatial resolution, while EELS analysis is used to correlate the morphology evolution with the chemistry changes throughout electrochemical cycling. For the first time, we discuss the SEI structural differences in the Si NP composite electrodes cycled with EC/DEC and EC/DEC/FEC (FEC 10 wt %) using STEM techniques. Furthermore, the chemical composition of the SEI using a linear scan by EELS can elucidate the chemical composition of the SEI from the bulk of the active material to the surface (SEI-Si np interface). STEM techniques poses many challenges such as the organic compound's instability under electron beam exposure [134,135] and local area probing which limits the statistical analysis. Therefore, we have taken several measures to overcome these difficult challenges, which will be discussed in a greater detail later. One of which is to use XPS and Helium Ion Microscopy (HIM) surface sensitive techniques to further validate the STEM/EELS results to give a macroview of the SEI composition and morphology. Herein, we demonstrate how utilizing a suite of characterization tools can be a powerful approach to obtain critical information of the SEI morphology and chemical composition for Si NP composite electrodes.

5.2. Experimental

5.2.1. Battery Preparation and Electrochemical Cycling

Silicon electrodes were prepared by coating a slurry of silicon Nano powder (NP) (average particle size of around 60 nm, Alfa Assar), KetjenBlack (Kjundo), and sodium carboxymethyl cellulose (CMC-Na, DS = 0.9, Mw = 250000, Sigma Aldrich) with a mass ratio of 2:1:1 onto thick rough copper foil (battery grade). First Si NP and KetjenBlack were ball milled for 20 min. The powder was added to a CMC water solution and placed in the

homogenizer to mix. The slurry was casted on the Cu foil using a doctor-blading. The electrode was dried at 80 °C under vacuum for 12 h. The electrodes were punched and had a mass loading 0.5 mg of Si per cm^2. The coin cells were assembled in an argon- filled glovebox (Micromeritics ASAP 2010, H_2O < 0.1 ppm). The electrochemical half-cells were assembled using 2032 coin cells, polymer separators (Celgard), 1 mm thick lithium foil, 1 M $LiPF_6$ electrolyte solutions (battery grade, BASF) including traditional 1:1 (wt. %) EC:DEC (ethylene carbonate: diethyl carbonate), and a blend of 45:45:10 (wt. %) EC/DEC/FEC (fluoroethylene carbonate). The approximate 100 uL of electrolyte was used in each cell. Half-cells were cycled in galvanostatic mode (0.05 V–1.0 V vs. Li) at room temperature and a C/20 rate for the first cycle and a C/10 rate for all subsequent cycles on an Arbin battery cycler.

5.2.2. Surface Analysis-X-ray photoelectron spectroscopy (XPS)

After electrochemical cycling, the cells were disassembled in the glovebox and washed with DEC to remove excess lithium salt. The washed electrodes were then transferred to the ultrahigh-vacuum environment using a reduced oxidation (ROx) interface designed for transferring air-sensitive samples. The ROx has methods and figures of merit to determine if the samples are ever exposed to additional traces of oxygen and water greater than those experienced in the glovebox environment, even during pump-down. The methods and components of the ROx are described in further detail in our previous publication.[19] X-ray photoelectron spectroscopy (XPS) was performed using a Kratos Ultra DLD XPS. Analysis followed similar methods used in previous work.[20,21] All XPS measurements were collected with a 300 μm by 700 μm spot size without using a charge neutralizer during acquisition. Survey scans were collected with a 1.0 eV resolution, followed by high-resolution 0.05 eV, 1 second scans of the carbon 1s, oxygen 1s, lithium 1s, silicon 2p, fluorine 1s, and phosphorus 2p regions.

Fits of the XPS spectra were performed with CasaXPS software (version 2.3.15, Casa Software Ltd.) to estimate the atomic compositions and chemical species comprising the SEI. All fitting followed a self-consistent method similar our previous publication.[20,21] All SEI species were assumed to be electronically insulating and were therefore fitted with linear backgrounds and with Voight functions composed of 15% Lorentzian and 85% Guassian following previous work.[22–27] Initial peak fits were made of the spectra using a Levenberg–Marquardt least-squares algorithm, and atoms in the same functionality were assumed to be stoichiometric. The resulting spectra were then refit and all spectra were shifted relative to the binding energy of the carbon 1s sp^3 oxidation state (assigned to 284.8 eV) to compensate for any charging during the measurement. The sum of the areas under the peaks were then used to determine relative composition of the outer-most ~10 nm of the SEI.

5.2.3. Helium Ion Microscopy (HIM)

Helium ion microscopy was performed using a Carl Zeiss Orion Plus System operating at 30kV acceleration voltage and using 0.2-0.4 pA beam current. The base pressure in the analysis chamber was kept at $1x10^{-7}$ torr. No beam induced sample damage was observed.

5.2.4. Scanning Transmission Electron Microscopy (STEM)

The electrochemical cells were disassembled in an argon-filled glovebox, and the silicon electrodes were washed in DEC. The electrodes were then scraped to produce a fine powder and then placed on a TEM lacy carbon film supported on a copper grid. The TEM samples were loaded on a vacuum transfer holder and transferred to the TEM to avoid any contamination from air or water. Annular dark field scanning transmission electron microscopy (ADF-STEM), and electron energy loss spectroscopy (EELS) were recorded at 197 kV with a JEOL-2010F microscope equipped with a Gatan-200 imaging filter (GIF) spectrometer. The energy resolution

of the EELS spectra measured from the full width at half magnitude (FWHM) of the zero-loss peak (ZLP) was 0.9 eV. In addition, a collection angle (β) of 20 mrad and a convergence angle (α) of 10 mrad were used for the acquisition of EELS spectra.

5.3. Results and Discussion

5.3.1. Electrochemical Results

The discharge capacity and Coulombic efficiency (CE) of the Si NP composite electrodes cycled with EC/DEC and with EC/DEC/FEC are shown in Figure 5.1. The electrodes were cycled within the potential range of 0.05-1V at C/20 for the first cycle and at C/10 for prolonged cycling. Under these galvanostatic conditions the Si NP composite transformed into lithium-silicon alloy and the electrolyte decomposed to form SEI. The electrodes were discharged by applying a constant current until the voltage reached 50 mV to avoid the $Li_{22}Si_5$ alloy phase.[136] It is found that the EC/DEC electrolyte is reduced at 0.8V; however, the FEC is reduced at a higher voltage consistent previous work.[11,130] The CE and specific capacity of the electrode with EC/DEC/FEC electrolyte has a slightly lower CE and specific capacity than the electrode cycled with EC/DEC after first cycle, however, the CE improves after prolonged electrochemical cycling. This behavior is most likely due to the reduction of the FEC in the first cycle to form F^- that could react with several components within the SEI such as etching the native oxide layer [61] and also form LiF. The reduction process of FEC also generated Li_2CO_3, along with other organic products. This is consistent with all previous reports demonstrating that the FEC additive improves the performance of Si anodes after prolonged cycling.[11,45,86,130,137] Thereby further proving that the FEC reduction stabilizes the Si NP composite interface by forming a rapid uniform coating (compact SEI).

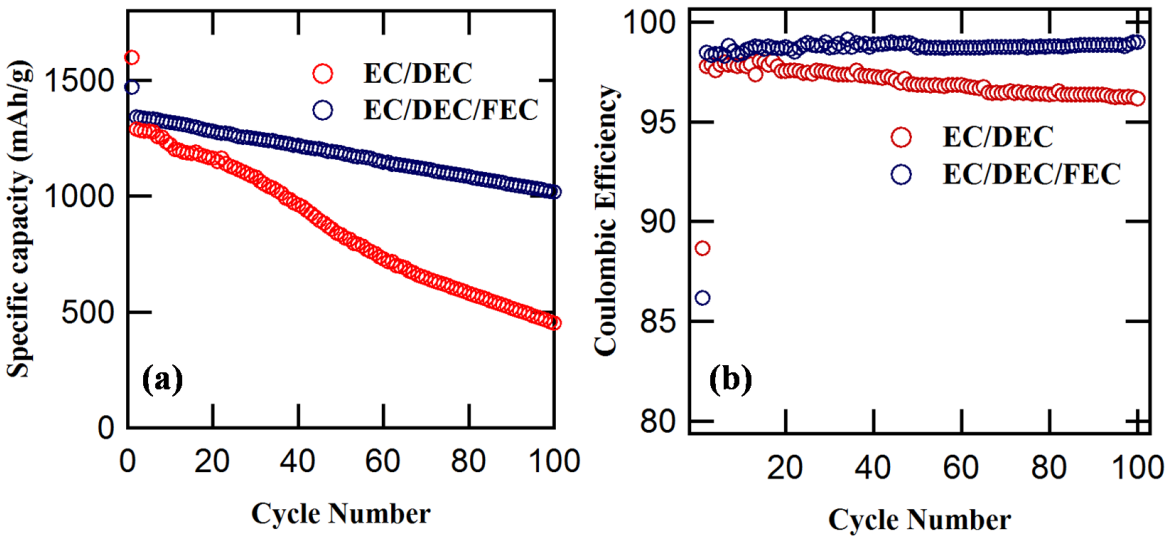

Figure 5.1. Electrochemical cycling performance of the Si nanocomposite electrode with EC/DEC and EC/DEC/FEC at C/10 rate, (b) Coulombic efficiency as a function of cycle number for Si NP with EC/DEC and EC/DEC/FEC.

5.3.2. Surface Characterization

Helium ion microscopy (HIM) was used for the first time to study the changes in surface morphology of Si NPs after the initial lithiation and 100 electrochemical cycles (delithiated state) at the submicron scale. HIM images of the pristine Si (as casted electrode) and the cycled samples are presented in Figure 5.2. The surface morphology of the pristine particles (Figure 5.2(a)) is very smooth and can be easily distinguished. However, it can be clearly seen that the surface morphology changed significantly upon cycling, clearly showing a surface morphology change between the electrode cycled in EC/DEC and EC/DEC/FEC (Figure 5.2(b and c)). This is largely due to the difference in electrolyte decomposition products associated with the electrodes in distinct electrolytes. However, Si NPs composite electrode contains inhomogeneity in active surface area and small change in porosity and particle packing can have a large effect on the SEI formation. The surface of the electrode cycled in EC/DEC is rougher than that of the electrode cycled in EC/DC/FEC after one cycle. After 100 cycles, both electrodes demonstrated an

increase in surface roughness, which can be attributed to the growth of SEI. To further validate the HIM images a combination of characterization techniques such as STEM-EELS and XPS were used to study the morphology and chemistry evolution of SEI throughout electrochemical cycling.

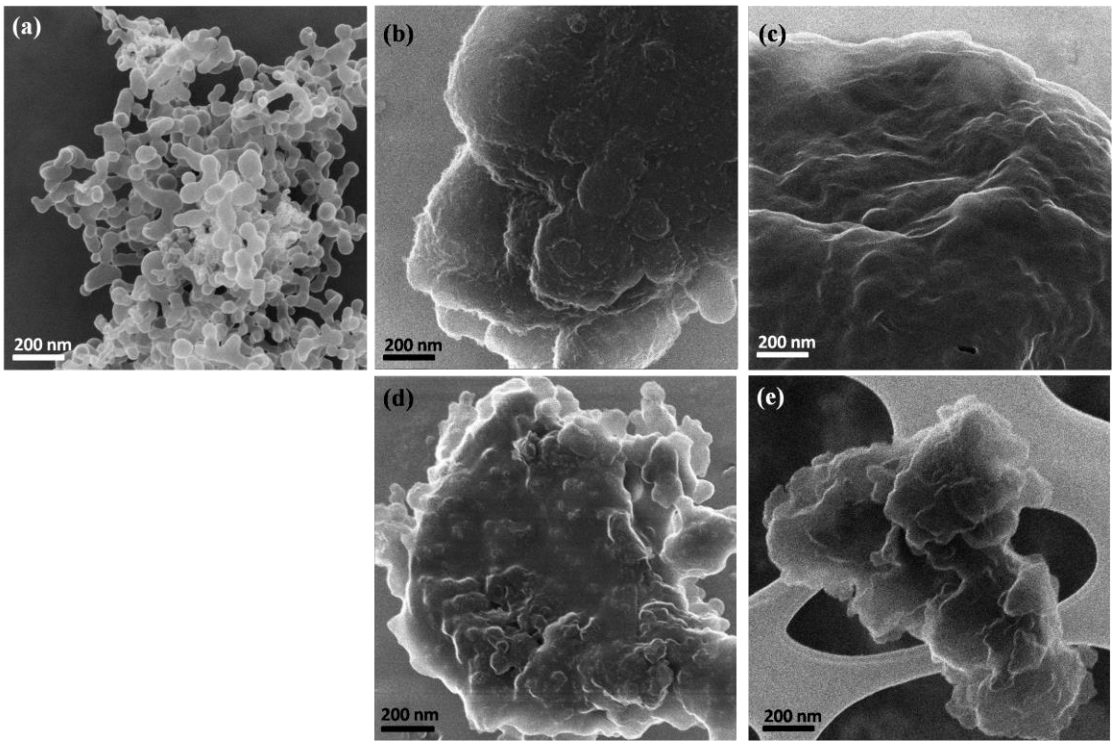

Figure 5.2. Helium ion microscope images of the (a) pristine Si, (b) lithiated Si cycled in EC/DEC after one cycle, (c) lithiated Si cycled in EC/DEC/FEC after one cycle, (d) lithiated Si cycled in EC/DEC after 100 cycles, and (e) lithiated Si cycled in EC/DEC/FEC after 100 cycles.

It was found that organic compounds and lithium containing compounds are vulnerable to electron beam exposure because of knock on displacement, radiolysis and heating effects.[138,139] Conclusively, in this work the electron dose and spatial resolution were optimized during STEM experiments to minimize the electron beam damage to the SEI and Li_xSi compounds. In this regard, the electron beam was spread throughout ADF imaging and EELS spectra acquisition.

The acquisition time was reduced to mitigate the electron dose and prevent beam damage (Figure 5.3). Moreover, we lowered the sample temperature to LN_2 temperature to further reduce the beam damage by limiting the diffusion process.[140] The ADF-STEM image of the pristine Si with an average particle size of about 60 nm is shown in Figure 5.4(a). The crystalline structure of Si can be confirmed from the EELS spectrum (Figure 5.4(b)).[141] As the average particle size of Si is less than 150 nm, the Si NP can withstand the strenuous lithiation process; therefore, in the first few cycles the Si degradation (Figure 5.1) can largely be attributed to the changes in the surface properties of Si (SEI formation). This allows us to mainly focus on the interfacial chemistry and morphology changes of the cycled Si NP electrodes (SEI) that are associated with the addition of FEC to the traditional electrolyte. The ADF-STEM image of the lithiated Si cycled in EC/DEC is shown in Figure 5.5 (a). Important changes after lithiation can be observed, especially the expansion of the lithiated crystalline Si particles. EELS spectrum of the lithiated Si (Figure 5.5 (c)) confirms the formation of amorphous Li_xSi alloys (the enlarged Li-K EELS spectrum is shown in the upper right corner of the Figure 5.5 (c)).[142] However, after delithiation, the Li-K edge disappears (Figure 5.5(c)) suggesting the full delithiation of Si NP. The particle size becomes smaller (Figure 5.5(b)) and transforms from crystalline to amorphous Si, which is confirmed by the EELS spectrum (Figure 5.5(c)). The regions with low contrast at the edge of the cycled electrodes can be observed in the ADF images (Figure 5.6 (a and b)). This region is ascribed to the presence of SEI, which is mostly composed of organic compounds (with lower atomic number).[133,143] Based on the STEM images (Figure 5.6), the electrode cycled with EC/DEC/FEC has an SEI that uniformly coats the entire Si NP in a dense thick film, whereas the electrode cycled with EC/DEC has an inhomogeneous porous SEI. Furthermore, EELS scanning profile was performed from the outer surface toward the bulk of these samples (along the

indicated line in the Figure 5.6 (a and b)) to study the chemical changes from the bulk of the particle to SEI. It is worth noting that Si was not detected in the SEI layer for both samples (outer most surface of Si) based on our EELS spectra results, clearly demonstrating that we are solely focusing on characterizing the chemical composition of the SEI.

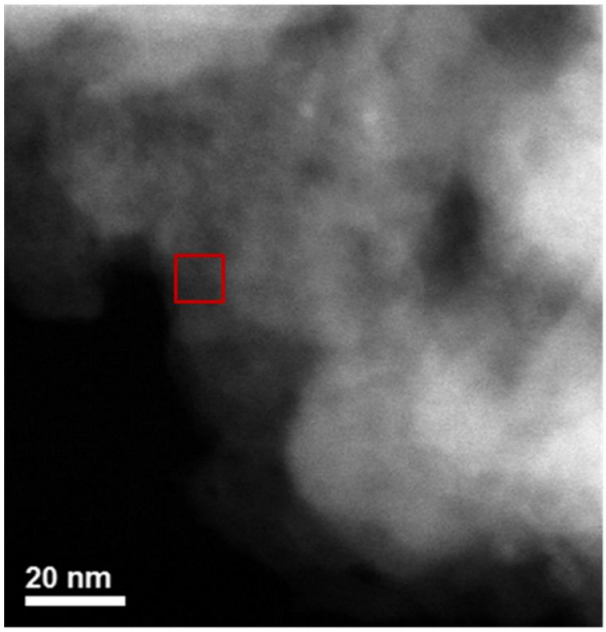

Figure 5.3. ADF-STEM image of the lithiated electrode cycled in EC/DEC after 5 cycles. The region of interest for EELS acquisition is shown is marked by square.

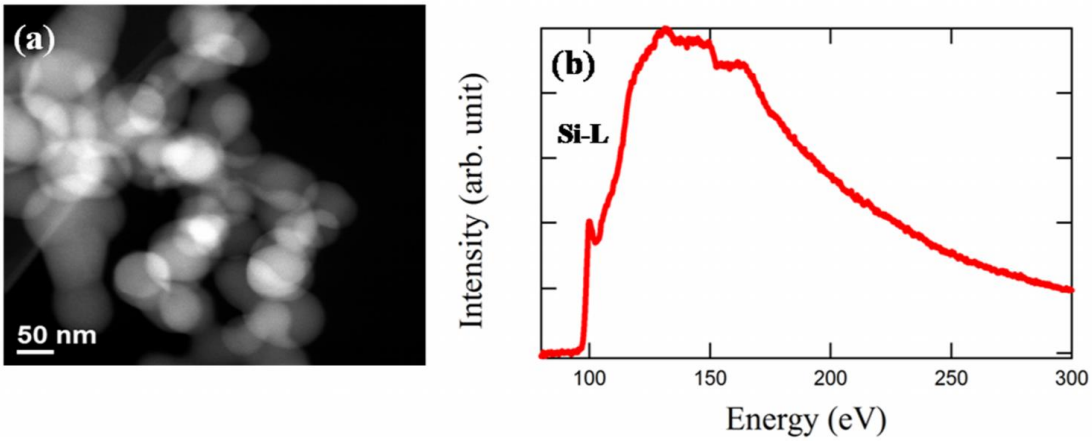

Figure 5.4. ADF-STEM image of the pristine Si electrode, (b) EELS spectrum of the pristine Si showing the presence of crystalline Si-L edges.

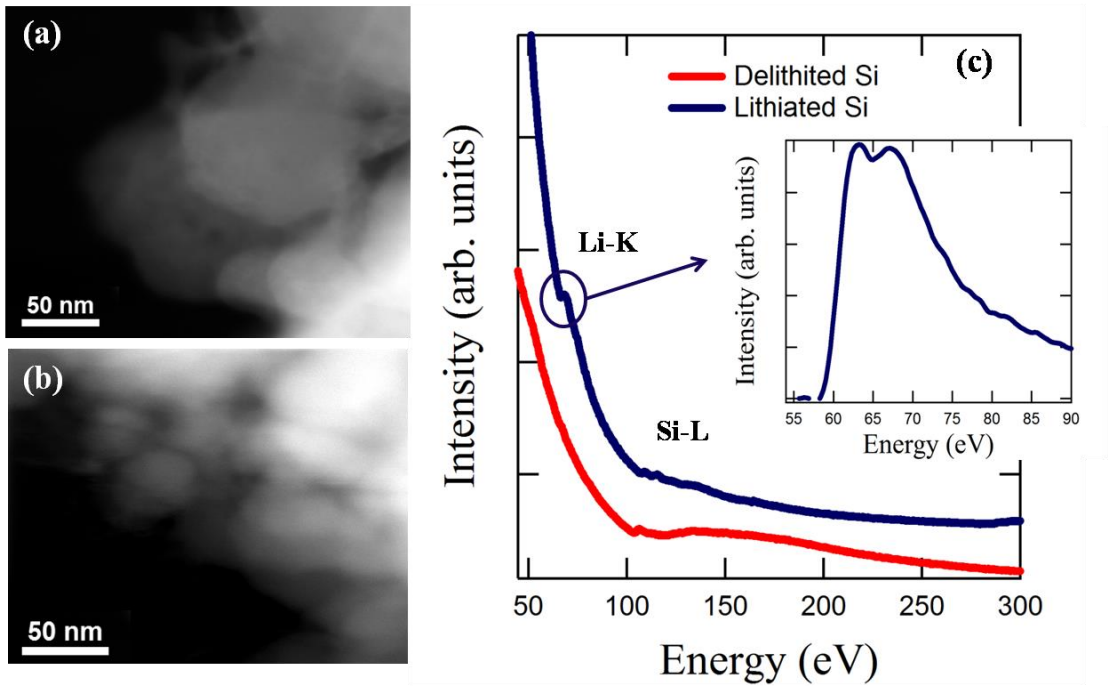

Figure 5.5. ADF-STEM image of the (a) lithiated, (b) delithiated Si, and (c) EELS spectra of the first lithiated and delithiated Si with EC/DEC. The enlarged Li-K EELS spectrum is shown in the upper right.

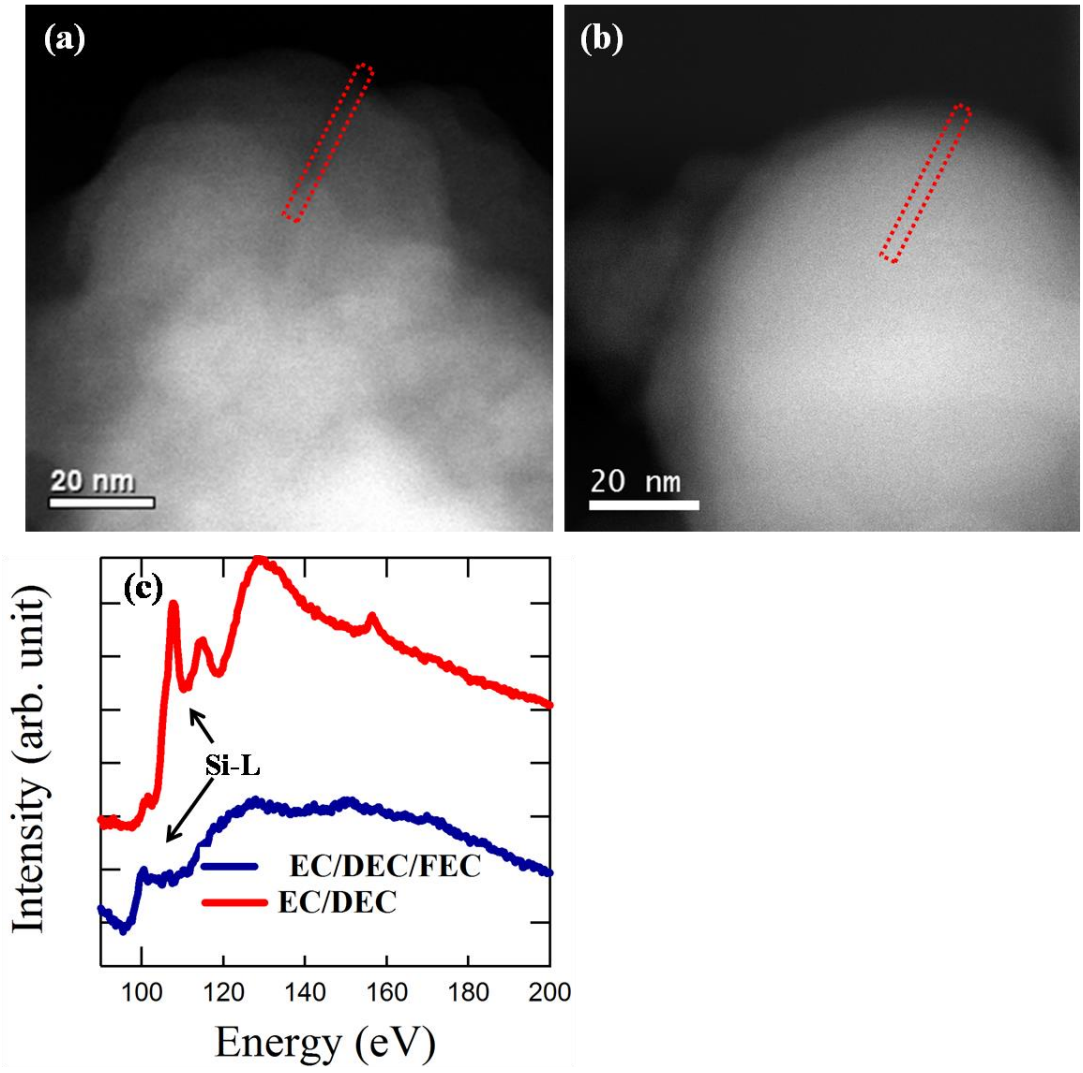

Figure 5.6. ADF-STEM image of the lithiated Si after one cycle cycled in (a) EC/DEC (b) EC/DEC/FEC, and (c) corresponding EELS spectra from the surface of both electrodes.

Interestingly, the interfacial chemistry of the lithiated electrode cycled in EC/DEC varied significantly from the electrode cycled in EC/DEC/FEC (Figure 5.6(c)), where more lithium silicon oxide alloys are present. The distinct peak shifts towards higher energy for Si-L edge, implies the change in oxidation state of Si.[144] The Si-L fine structure from the surface of the lithiated electrode cycled in EC/DEC/FEC is attributed to amorphous Li_xSi, however, the Si–L fine structure from the surface of the lithiated electrode with EC/DEC corresponds to Li_xSiO_y

(Figure 5.6(c)).[144] This indicates that the lithiated Si cycled with EC/DEC is covered in a native oxide. These results directly correlate with our previous work, where we propose the reduction mechanism of FEC through a rapid ring opening mechanism, forming fluoride anion.[11] The fluoride anion then undergoes competing reactions to either form HF or LiF (see Scheme 5.1, reaction 5.1 and 5.2). The formation of HF then will etch the native oxide layer causing the formation of less Li_xSiO_y in the electrode cycled with EC/DEC/FEC in the first cycle, which correlate with our previous findings.[11,61]

$$SiO_X + xF^- \rightarrow SiF_X + (x/2)O_2 \quad (5.1)$$

$$Li^+ + PF_6^- \leftrightarrow PF_5 + LiF \rightarrow LiF + Li_xPF_y \quad (5.2)$$

$$PF_5 + H_2O_{(trace)} \rightarrow POF_3 + 2HF$$

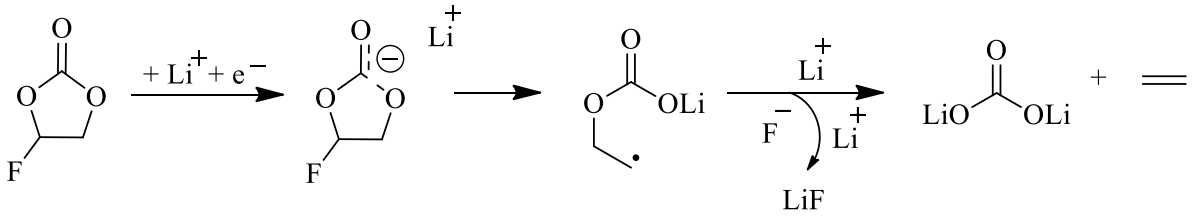

Scheme 5.1. Electrochemical reduction of FEC via a ring opening mechanism to produce lithium fluoride, lithium carbonate, and ethylene.

Thus, the interfacial chemical and morphology evolution between the two electrodes (cycled in EC/DEC and EC/DEC/FEC) can be one of the major factors that lead to electrochemical performance differences. Several researchers have confirmed the existence of silicon oxide layer on the Si electrode, once lithiated its surface (SiO_x) is transformed to Li_xSiO_y which leads to the high impedance and low specific capacity retention.[145,11] It is established that silicon oxide layer has lower flexibility than that of amorphous silicon,[145] consequently, the higher flexibility of the

amorphous Li_xSi can endure large volume expansion of silicon upon cycling and maintain the particle integrity. In addition, as the oxide layer on the Si NPs is insulating, it reduces the lithium ion transport and increases the charge transfer impedance, therefore, reducing the cycling properties. This oxide layer consumes Li-ion during lithiation which leads to low specific capacity.[145,11] We further investigated the evolution of Li_xSiO_y and SEI with progressive cycling for the electrodes cycled in EC/DEC and EC/DEC/FEC (1 cycle, 5 cycles and 100 cycles).

Accordingly, we probed the interfacial chemical changes of the electrodes cycled in EC/DEC and EC/DEC/FEC to further understand the role of FEC in oxide layer evolution with cycle number (Figure 5.7). Figure 5.7 (a) compares the Si-L EELS spectra from surface and bulk of the Si electrodes cycled in EC/DEC after various cycle numbers, where there were no significant changes observed in Si-L edge after progressive cycling. All the Si–L edge taken from the surface of the cycled electrodes in EC/DEC at different cycle numbers correspond to Li_xSiO_y and the Si-L edge from the bulk can be assigned to the Li_xSi. However, the surface and bulk of the Si cycled in EC/DEC/FEC after one cycle corresponding to Li_xSi. After 5 cycles, two out of 15 acquired EELS spectra (from various regions) demonstrated the existence of Li_xSiO_y which is shown in dashed line graph in Figure 5.7(b). Meanwhile, the EELS results from the surface of the cycled electrode with EC/DEC/FEC after 100 cycles, only represent the Li_xSiO_y compound. This is most likely due to the, reduction in effects of FEC decomposition compounds as well as an increase in Li_xSiO_y content after 100 cycles. Accordingly, the Si-L edge from the bulk of the electrode cycled in EC/DEC after 100 cycles shows two additional peaks (marked in Figure 5(a)) corresponding to the infiltration of the native oxide layer (Li_xSiO_y) into the bulk. These results show the increase of native oxide layer with extending cycle number for both

electrodes due to further electrolyte reaction with the surface of the electrode. Meanwhile, the diffusion of the oxide layer into the bulk was only found for the electrode cycled in EC/DEC after 100 cycles. This suggests that FEC limits the increase of oxide layer (Li_xSiO_y) with progressive cycling (100 cycles). This may attribute to the improved cycling performance of the electrode cycled in EC/DEC/FEC compared to the electrode cycled in EC/DEC. The increase of Li_xSiO_y was also reported in a recent work indicating that the presence of Li_xSiO_y in high amount for the Si anode (EC/DEC) after 100 cycles lead to capacity fading.[135]

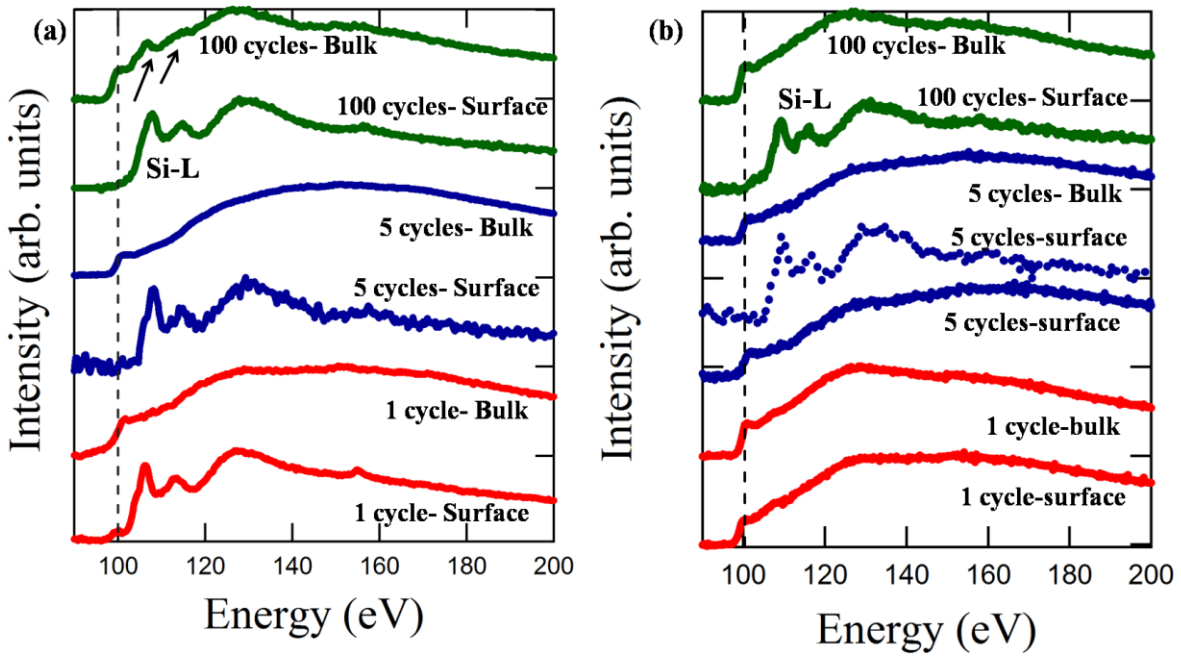

Figure 5.7. Si-L EELS spectra of the Si NP half cells with (a) EC/DEC, and (b) EC/DEC/FEC at various cycle numbers. The dashed line graph showing the presence of Li_xSiO_y at the surface of the electrode with EC/DEC/FEC after 5 cycles, which is only observed for 2 of the EELS spectra out of 15, acquired EELS spectra.

ADF-STEM image (Figure 5.8 (a)) and the corresponding Si-L and Li-K EELS maps were acquired from the lithiated Si samples cycled in EC/DEC (Figure 5.8(b and c)) to determine the distribution of Li_xSi and SEI composition. The bright contrast in the image is associated with

high Si content; however, the grey regions demonstrate rich Li content in the SEI, which is found on the outer most surface of the particle and further confirms the presence of the SEI. Figure 6(d-i) shows the ADF-STEM images of SEI with progressive cycling, where the electrode cycled in EC/DEC after the first delithiation forms an inhomogeneous porous SEI. Moreover, this SEI is intermixed with silicon particles with increasing cycle number (up to 100 cycles). Conversely, the electrode cycled in EC/DEC/FEC is covered with a dense and uniform SEI and the silicon particle integrity is preserved which was hypothesized by Xu *et. al*.[130] Here for the first time we present a comparative study to directly visualize the effects of FEC on SEI morphology in the first few cycles (1, 5, cycles) using STEM-EELS. Surprisingly, the same phenomenon was not observed after 100 cycles for the electrode cycled in EC/DEC/FEC. The SEI has similar morphology properties to the electrode cycled in EC/DEC, which is also consistent with the HIM images, previously mentioned.

The EELS spectra from the lithiated Si cycled in EC/DEC and EC/DEC/FEC after 1 cycle are compared with the possible reference compounds resulting from the electrolyte decomposition including LiF, Li_2CO_3, and Li_2O (Figure 5.9).[143,146] A comparison of the Li-K, C-K, O-K, and F-K edges taken from SEI cycled with EC/DEC indicate that the SEI mainly contains Li_2CO_3, which is due to EC reduction. However, the electrodes cycled in EC/DEC/FEC ~~are~~ mainly contains LiF according to Li-K and F-K edge fine structures (Figure 5.9 (a and d)). This is formed as a result of the FEC decomposition and salt dissolution which decomposes at a much higher voltage than that of EC/DEC, therefore, limiting the degradation of EC/DEC which is consistent with previous results.[11,145] Figure 5.9(a) compares where the Li-K edge of the SEI generated by EC/DEC and EC/DEC/FEC. The SEI generated by adding of FEC shows the formation of Li_2O, which can occur when the electrolyte reacts with the SEI. Based on our EELS

results, we did not observe SEI chemical changes for the electrodes with EC/DEC and EC/DEC/FEC after prolonged cycling (up to 100 cycles). These results are in agreement with the previous results.[130] It is necessary to note that in spite of using the low electron dose, electron beam damage may still preclude the detection of low content organic and inorganic compounds. As such, a surface sensitive XPS technique was utilized to further understand the SEI chemistry changes upon cycling for the electrodes cycled in EC/DEC and EC/DEC/FEC.

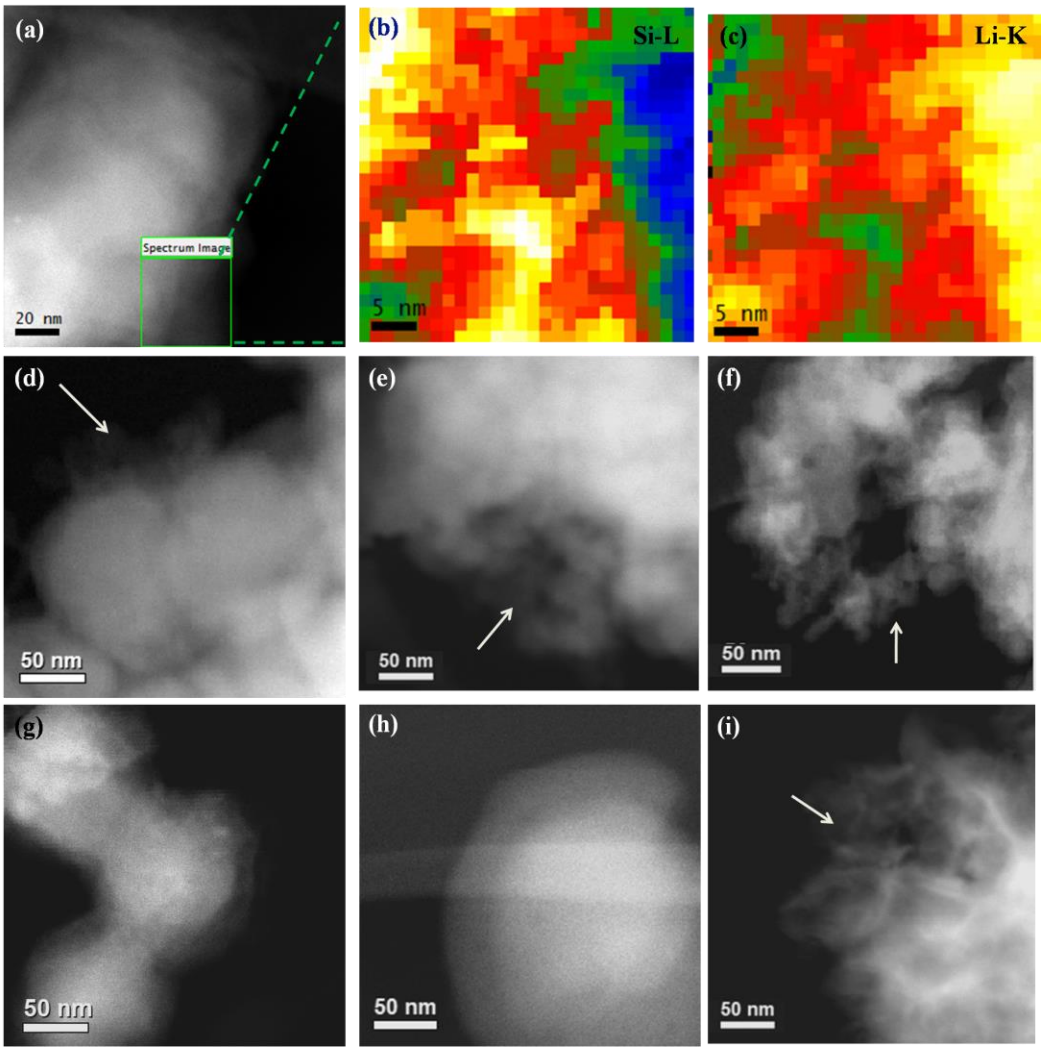

Figure 5.8. (a) ADF-STEM image of the delithiated Si EC/DEC after 5 cycles and the corresponding EELS mapping of (b) Si-L, and (c) Li-K. ADF-STEM images of the lithiated Si (d) after 1 cycle, (e) after 5cycles, (f) after 100 cycles and the lithiated Si containing FEC, (g) after 1 cycle, (h) after 5 cycles and (i) after 100 cycles.

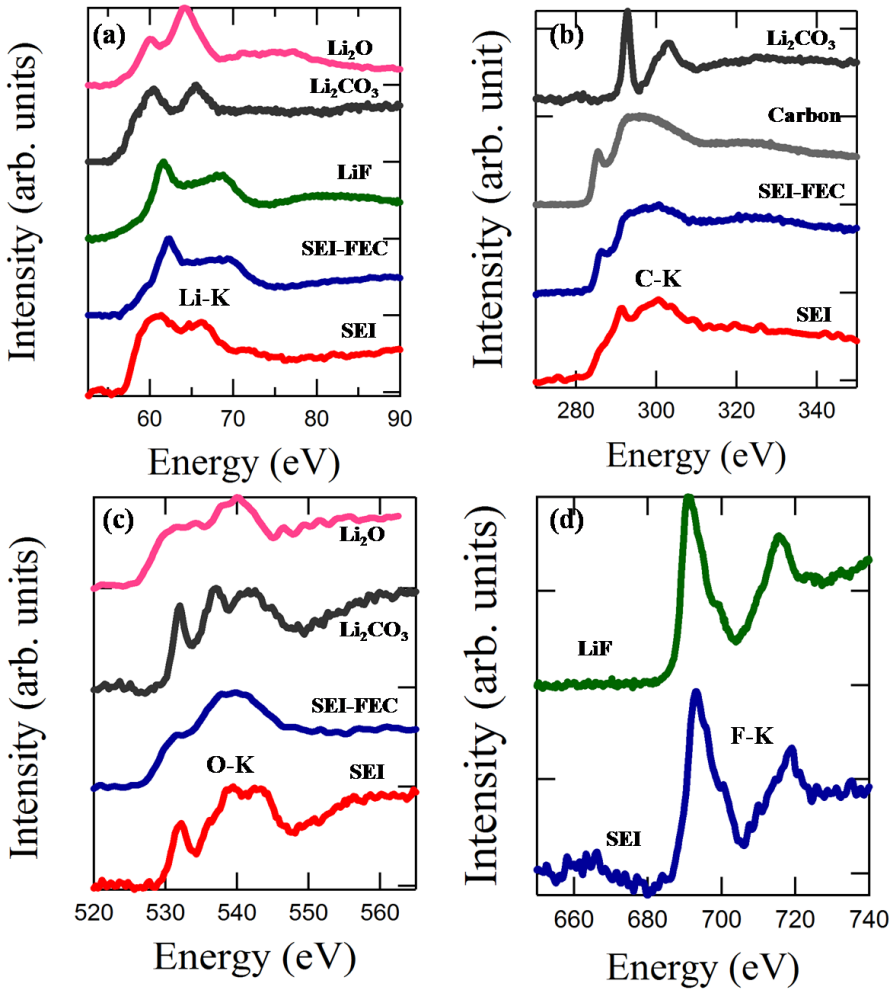

Figure 5.9. Comparison of SEI layer EELS fine structure in the lithiated Si after 1cycle with reference compounds for (a) Li K-edge, (b) C-K edge, (c) O-K edge, and (d) F-K edge. SEI for the electrode cycled in EC/DEC shown in red (SEI) and electrode cycled in EC/DEC/FEC shown in blue (SEI-FEC).

5.3.3. XPS data supporting EELS data

Figure 5.10 demonstrates the relative composition of the first 10 nm of the SEI of electrodes cycled with EC/DEC (a, c, and e) and EC/DEC/FEC (b, d, and f). The XPS analysis was performed after the first lithiation (a and b), first delithiation, and 100 cycles in the delithiated state (e and f).

The special resolution and detection limit of STEM EELS makes it difficult to determine the atomic composition of the parasitic electrolyte decomposition products over a large area. Given that EELS is a local technique, XPS was used as a complementary surface characterization technique to obtain a better understanding of the SEI using a large area scan (300 x 700 μm). Post hoc and *ex-situ* XPS was used to avoid any environmental contamination by water vapor or oxygen which can alter the SEI composition, as demonstrated by Schroder *et al*.[61] and our previous work.[11] By studying the SEI composition via anoxic and anhydrous XPS, we can gain insights as to how EC/DEC/FEC affect the cycling performance of composite, avoiding any contamination.

The highly stable Si composite electrodes cycled with both electrolytes generated an SEI by galvanostatic electrochemical cycling. The XPS assignments follow a meticulous self-consistent fitting model previously used for Si anode types (shown in the supporting information).[93] Figure 5.10 shows a bar graph demonstrating the relative compositions of the SEI for electrodes cycled with EC/DEC and EC/DEC/FEC deduced from the XPS peak fittings. The inelastic mean free path of the photoexcited electrons limits the detection depth to 10 nm; therefore, Figure 8 demonstrates the outer most surface composition of the SEI generated by two electrolyte types. In our previous work, amorphous Si thin films (without binder or conductive additives) were used to clarify the FEC reduction mechanism and determine how FEC improves the SEI in the initial cycles,[11] however, this study focuses on determining the SEI morphology and chemical composition of the SEI in a composite electrode, which is how a Si electrode would be used in a real battery configuration. The previous model system study was used to decipher the convoluted SEI generated by a composite electrode because the binder and conductive additive contribute to the rapid SEI formation.

The atomic percentage of all the electrodes investigated is shown in Figure 5.10. Organic species are labeled C sp^3 for alphatic carbon and may include adventitious carbon, ROR for alkoxy groups (ethers), ROCO for carboxyl groups (carboxylates, esters), and RCO_3 for carbonic esters and ionic carbonate salts. Ionic carbonate salts are difficult to deconvolute by XPS because of their similar binding energies and functional group (Li_2CO_3, $ROCO_2Li$). Therefore, when discussing RCO_3 it is likely that both these reduction products are being detected. The high resolution XPS spectra and peak fittings can be found in the supporting information. Inorganic species include lithium fluoride (LiF), fluoro-phosphoro-oxides ($P_xO_yF_z$), and LiX (which could include alkyl lithium and lithium phosphoro-oxy-fluoride). Additionally, it is difficult to distinguish ionic lithium ions bound to organics such as carbonic esters and lithium alkoxides, also labeled LiX. As demonstrated, we observed little to no Si 2p signal for all cycled electrodes. Therefore, the SEI generated in the initial lithiation was much thicker than 10 nm given the Si 2p signal.

We propose that the variations in the SEI composition are explained by kinetics of the competing FEC versus EC reduction products perpetuated by the 60 nm Si particles. Though 60 nm crystalline Si particles help mitigate the volume expansion[129] (below the critical cracking limit), the surface area is increased which promotes the rapid SEI formation.[105,130,147,148] In the first lithiation step, we find the electrode cycled with EC/DEC contained approximately 21.2% organic functionalities and the SEI formed by EC/DEC/FEC contained approximately 18% organic functionalities. In our case, it is difficult to fully assign the C sp^3 carbon solely to SEI moieties because our electrode contains conductive carbon and binder which contribute to the signal as in our previous work.[11] Therefore, the atomic percentage of organic functionalities is solely based on ROR and ROCO species found in the SEI. The SEI comprised of 32% and 8%

(atomic percent) carbonate species for the electrodes cycled with EC/DEC and EC/DEC/FEC, respectively making it difficult to properly quantify the organic SEI species. These results are consistent with the EELS data analysis, validating that the data is not the result of beam damage. Furthermore, the SEI generated from EC/DEC contains a higher concentration of ROCO and ROR (esters, ethers, carboxylates) 14.2 % and 7%, respectively. Where the electrode cycled with EC/DEC/FEC contains 6% ROR and 12% ROCO. Here, the formation of ROCO is more profound which may be attributed to the reduction mechanism of FEC while the electrode cycled with EC/DEC forms more ROR reduction products as a result of the EC and DEC decomposition. In the SEI generated by EC/DEC shows a higher concentration of RCO_3 functionalities (~ 31%) while the SEI generated by EC/DEC/FEC has less (~8%). This is due to the reduction potential and reaction kinetics, where FEC is more likely to form less carbonate based functionalities. It is widely accepted that FEC decomposes at higher reduction potential; therefore, the electrode cycled with EC/DEC/FEC contains 50% LiF whereas the electrode cycled with EC/DEC contains 12% LiF. Given that the EC/DEC electrolyte's only source of fluoride anion comes from the salt ($LiPF_6$), the indirect path of LiF formation through the reversible thermal decomposition of the salt (Reaction 2).[120,125,147] As a result, the electrode cycled with EC/DEC/FEC contains two reaction pathways to generate LiF. Furthermore, the high surface area of the 60 nm Si nanoparticles further increases decomposition kinetics of the SEI.[73] Here, we find no evidence of C-F bonds which is still a heavily disputed conclusion as a result of the FEC decomposition mechanism. However, determining the reduction mechanism of FEC is beyond the scope of this work because the analysis was carried out using a composite electrode containing binder and conductive additive which affect the SEI composition. Here, we are

focusing on the morphology of the SEI over prolonged cycles using STEM and EELS and XPS is used to observe the chemical composition of the SEI to validate the EELS results.

In addition to LiF, the electrode cycled with EC/DEC/FEC contains more $P_xO_yF_z$ which is a function of multiple step reaction,[83] which form very stable oxides on the surface. These results are consistent with our previous study where the FEC containing electrolyte produced a higher concentration of $P_xO_yF_z$. Our findings are consistent with previous results, where and FEC containing electrolyte produces a more inorganic SEI in the initial lithiation (Equation 2).

After delithiation, the SEI composition is consistent, where there is no major peak shift or appearance of new compounds (supporting information). However, for the electrode cycled with EC/DEC contains less RCO_3 and more ROR and ROCO functionalities generating an SEI consisting of 92% atomic percent. The LiF and $P_xO_yF_z$ species form 8% of the total SEI consistent with the EELS results. The more organic species in the SEI forms a porous, "cloud" like SEI morphology. Therefore, more electrolyte decomposes as a result of the exposed Si surface that leads to poor electrochemical performance. Conversely, the electrode cycled with EC/DEC/FEC has little change in SEI composition (in terms of atomic percentage), where the LiF and $P_xO_yF_z$ species form ~ 52% of the SEI composition. If we compare this percentage to the first lithiated percentage (~70%), it demonstrates that the SEI formed is much more stable. Initially, EC/DEC/FEC forms a uniform dense coating (SEI) because of the fast reduction kinetics if FEC compared to EC.[149] Therefore, there is little change in the SEI composition in the first lithiated and delithiated state.

After 100 cycles, the SEI composition of both electrodes looks very similar which is consistent with the STEM images. The SEI formed from EC/DEC/FEC has more organic species than in the first cycle. There is a slightly more LiF and less RCO_3 moieties than the SEI

generated from EC/DEC. Since there is only 10 wt.% FEC additive and its rapid reduction kinetics in the first few cycles (even to 5 cycles), over prolonged cycles the FEC will eventually be depleted. This was first hypothesized in our previous work and is confirmed in this work. Therefore, LiF forms in the initial cycles forming a protective coating around the Si NP and after prolonged cycles the EC decomposition products dominate the SEI composition. As shown in the STEM images, after 100 cycles the SEI morphology is identical for both electrolytes, which is consistent with the XPS results. Furthermore, a more inorganic SEI is brittle and can crack easily, therefore, after prolonged cycling this layer will become mechanically unstable, exposing fresh Si surface forming a more organic SEI.

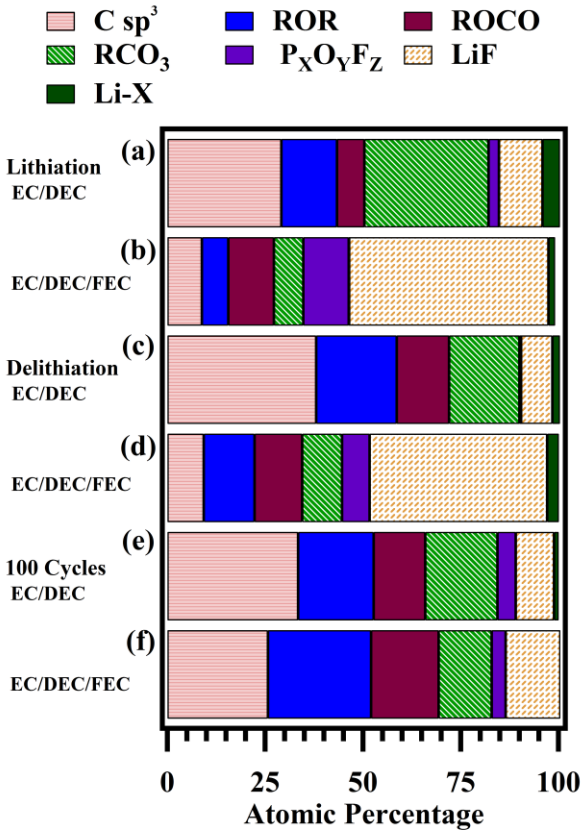

Figure 5.10. Relative composition of the SEI at Si NPs after (a,b) first lithiation, (c,d) first delithiation, and (e,f) 100 cycles in the delithiated state. The layer resulted from and was in fluid communication with EC/DEC (a,c,e) and EC/DEC/FEC (b,d,f).

5.4. Conclusion

A comprehensive study of the effects of FEC on the Si electrochemical changes discovers new insights to the significance of SEI morphology and chemical changes that occur during electrochemical cycling using STEM/EELS analysis. Specifically, the direct visualization of SEI morphology evolution obtained for both electrode systems reveals that the electrode cycled in EC/DEC/FEC is covered with a uniform and stable SEI mainly for the first few cycles while the SEI of the electrode cycled in EC/DEC forms a porous and inhomogeneous SEI right away. The stable SEI formation can contribute to the improvement in electrochemical performance of Si NP electrode. Furthermore, according to the STEM-EELS profile results, less oxide layer (Li_xSiO_y) is found in the initial cycle on the Si electrode cycled with EC/DEC/FEC. Our XPS results provide a much larger length scale for the SEI chemical changes after cycling, which demonstrated that the electrode cycled in EC/DEC has a higher atomic percentage of Li_2CO_3 consistent with the EELS results. On the other hand, the electrode cycled in EC/DEC/FEC contained fewer carbonate species and more LiF, also correlating well with the STEM/EELS analysis. Thus, we propose two main reasons as the effects of FEC which result in the electrochemical improvements: (1), FEC decomposition products eliminate the Li_xSiO_y layer, and (2), the initial formation of homogeneous and dense SEI on the Si NPs. Therefore, the chemical composition formed with FEC additive is not the sole reason for improved capacity retention with cycling of Si electrode but the SEI density and morphology also plays a critical role in electrode stability. However, the mechanical property of such a dense SEI film may not be most ideal if large amount of lithiation/delithiation occurs upon long term cycling. Further investigation on how SEI morphology and composition changes with the degrees of lithiation/delithiation in the electrode cycled with EC/DEC/FEC can provide critical information for further improving and developing Si anodes as well as electrolyte additives.

Chapter 5, in full, is a reprint of the material "Direct Visualization of the Solid Electrolyte Interphase and Its Effects on Silicon Electrochemical Performance" as it appears in Advanced Materials Interfaces, Sina, M; Alvarado, J; Shobukawa, H; Alexander, C; Manichev, V; Feldman, L; Gustafsson, T; Stevenson, K; Meng, Y.S, 2016, 1600438. The dissertation author was the co-primary investigator and author of this paper. All the experiment parts were performed by the author except for the HIM and STEM EELS analysis.

Chapter 6. Bridging the Gap: Electrolytes for Efficient Coupling of Lithium Metal Anodes with Next Generation Cathodes

6.1. Introduction

The development of Sony's lithium-ion battery and its subsequent proliferation revolutionized the electronics industry. However, with the growing demand for high energy density batteries for the emerging electric vehicle market there is revitalized interest in lithium metal anodes—once deemed unsafe due to dendrite formation. The greatest strengths of lithium metal as a negative battery electrode are also its major weaknesses. First, it has the lowest electrochemical reduction potential compared to the current graphite anode, which increases cell voltage compared to other negative electrode materials, but this comes at the cost of extreme reactivity with the electrolyte. Second, as the lightest metal and as a pure active material, lithium offers a tremendous theoretical specific capacity of 3,860 mAh g^{-1}, but suffers from dendrite formation during cycling. This makes the formation of a stable solid electrolyte interphase (SEI) extremely difficult and introduces significant safety and reliability concerns due to dendrite formation and subsequent cell shorting. Mitigating these issues have proven to be challenging and more research is required to solve the low cycling efficiency and to prevent dendrite formation.

In conventional Li-ion batteries the efficiency, cycle life, and rate capability of the cell is dictated by the SEI, which forms between the anode and the electrolyte. The miracle of the current commercial Li-ion battery SEI is that it is a conformal, self-limited film composed of reduced electrolyte components that allows lithium transport without conducting electrons, which would otherwise lead to further parasitic reactions. For lithium metal anodes, the anode-electrolyte interface is in a stronger reducing environment which undergoes significant volume

changes, leading to continuous exposure of the highly reactive surface, generating inhomogeneities in the SEI and corresponding irregularities in the current density distribution that lead to dendritic Li growth. Thus, stabilizing the Li SEI is currently one of the greatest challenges that researchers face. A variety of approaches have been proposed including: 1) host structures for Li[150–152]; 2) physical barriers to prevent dendrite formation such as polymer [153]and solid state electrolyte[154–157]; 3) flexible coatings[158]; and 4) electrolyte engineering[159,160].

One of the most promising and economically viable approaches is *in situ* tuning of the interphase chemistry with different electrolyte solvent/co-solvent combinations. It has taken researchers over 40 years to increase the plating/deplating efficiencies from 80% to 98.5%, cycling at 0.5mAh/cm^2 in Li versus Cu cells. This significant jump in efficiency was achieved by moving away from highly reactive solvents (carbonate based electrolytes) to systems that are more cathodically stable and by changing the lithium salt chemistry pioneered by Aurbach et al. [58,159,161]The morphology of plated Li metal is dependent on a variety of factors associated with the salt, including the degree of dissociation, the strength of solvation, and the cathodic stability, all of which are associated with the SEI.[162,163]In some cases, increasing the salt concentration has also shown to be a viable method for improving the homogeneity of the SEI.[159,164] Suo and coworkers coined the term "solvent-in-salt", based on the concept of "polymer-in-salt", where a super high concentration of lithium salt outweighs the molar ratio of the solvent (or polymer).[165] The vast improvements of highly concentrated electrolytes (above 3M) have been extended to single solvent systems for lithium sulfur and high voltage lithium ion batteries (LNMO vs graphite), demonstrated by Kim and coworkers[166] and Yamada and coworkers[167], discoveries which may change the outlook of single solvent electrolytes. For example, highly concentrated (5M) LiFSI in 1, 2 Dimethoxyethane (DME) improved the Li metal cycling efficiency in Li

symmetrical cells and in electrochemical performance of Li-S system.[166] Qian et al. further examined highly concentrated 4MLiFSI-DME electrolyte for Li metal cycling to achieve 99.1% and 98.4 efficiency at 0.2 mA/cm^2 and 4 mA/cm^2 current for over 500 cycles (Li vs Cu coin cell) without evidence of dendrite formation, thus making it the best performing electrolyte to date.[168] Despite these significant developments, researchers have yet to achieve the 99.9% benchmark required for widespread commercialization of Li metal anodes. Bisalt combinations further alter the SEI, generally promoting more inorganic interphases which in turn increase the Li metal cycling efficiency. A 1M combination of LiTFSI (0.5M):LiFSI (0.5M) in 1,3-dioxolane (DOL)/DME solvent reduced dendrite formation and improved the plating efficiency to 99% at 0.25mA/cm^2.[169] This increases the LiF concentration without increasing the salt content, thus lowering the cost of the electrolyte. Still, the abovementioned reports demonstrate that non-aqueous electrolytes with LiFSI as the primary salt component generally exhibit the highest plating efficiencies, even exceeding $LiPF_6$ and $LiAsF_6$ in carbonate solvents with additives.

Though there have been recent advancements in Li metal plating efficiencies, researchers have a limited understanding of how the electrolytes affect the Li metal nucleation, growth mechanism, and fine nanostructure. This is largely due to the beam sensitivity of Li metal which limits the possible characterization techniques used. *In-situ* optical cells are widely used to investigate the Li metal growth mechanism.[170,171] However, understanding the real behavior of the Li growth mechanism is challenging because it is difficult to detect the Li nucleation at the nanoscale and to mimic the stack pressure to that of a coin cell which would have altering morphology. Therefore, to further understand the initial plated Li metal morphology, researchers must consider alternative techniques to enable high resolution imaging of plated Li metal while avoiding sample damage. Cryogenic (cryo) techniques have been widely applied to study

proteins, ribonucleic acid, and macromolecules because they allow high resolution imaging of sensitive material and have revolutionized structural biology imaging.[172–174] Recently, our group was the first to develop cryogenic transmission electron microscopy (cryo-TEM) to elucidate the nanostructure of deposited Li metal while avoiding beam damage. Our group has extended the cryogenic capability to focused ion beam (cryo-FIB). For the first time, we present cross sectional images of deposited Li metal to accurately investigate the density and morphology of electrochemically plated Li metal.

While it is already a colossal challenge to develop electrolytes that allow for efficient plating/deplating of Li, next generation lithium metal batteries will also have a cathode that demands a voltage stability window beyond the upper limit offered by previously published systems (> 4.5V). While the state-of-the-art ether electrolyte (4M LiFSI in DME) has been tested in half cell and anode free configurations versus lithium iron phosphate cycled to 3.8V[175], an ether-based system has yet to be paired with nickel rich cathodes (4.4V), which offer significantly enhanced metrics for energy density. Inspired by previous work, we investigate highly concentrated bisalt electrolytes to expand the voltage window of ether electrolytes and cycle $LiNi_{0.6}Mn_{0.2}Co_{0.2}O_2$ (NMC-622) in both half cell and anode free cell configurations to 4.4V. Finally, we demonstrate that bisalt electrolytes can potentially facilitate the use of Li metal anodes for rechargeable lithium metal batteries by forming a predominantly inorganic SEI that enables safe and reversible Li metal operation during electrochemical cycling. We characterize this SEI and the underlying lithium using a specialized cryo-FIB setup to minimize sample damage while gaining information on the density, morphology, thickness, and surface chemistry (SEI) of the Li metal. Together, these results provide a comprehensive look at the performance

improvements garnered by the bisalt approach and the mechanism responsible for this enhancement.

6.2. Experimental Section

6.2.1. Electrolyte preparation

The electrolytes were prepared using Lithium bis(fluorosulfonyl) imide (LiFSI Oakwood Products, Inc.-battery grade (>99%)), Lithium (trifluoromethanesulfonyl) imide (LiTFSI BASF-battery grade), lithium hexafluorophosphate ($LiPF_6$ BASF-battery grade), dimethoxyethane (DME, BASF-battery grade), ethylene carbonate (EC, BASF-battery grade), and ethylmethyl carbonate (EMC, BASF-battery grade). All lithium salts were dried under vacuum for 24 hours and the solvents were dried using molecular sieves for 72 hours prior to making the electrolytes (moles of salt/volume of solvent). Seven salt-solvent electrolyte compositions were used in this work: 4.0M LiFSI-DME, 4.0M LiFSI:2.0M LiTFSI-DME, and 1.0M $LiPF_6$ EC: EMC (3:7 wt). All electrolyte solvents and solutions were stored and handled in an argon-filled Vacuum Atmospheres Nexus One glovebox with measured levels of O_2 and H_2O < 1ppm.

6.2.2. Electrolyte Characterization

A three electrode Swagelok cell containing Li metal as the counter and reference electrode with platinum metal disk (0.5 inch diameter) as the working electrode was used for all LSV measurements. A glass fiber separator (*Whatman QMF*) was included to avoid cell shorting, and the cells were filled with 300 uL of electrolyte. The experiments were carried out on a single channel Gamry Potentiostat (*Reference 3000*), sweeping from OCV to 6V at $5mVs^{-1}$. Experiments were conducted three times for each electrolyte to ensure reproducibility.

Electrolyte conductivity κ of the electrolytes were measured with a Solartron potentiostat at selected temperatures within a Tenney Jr. environmental chamber. The conductivity cells consist of a pair of platinum−iridium electrodes. The cell constants of a nominal value of 0.1 cm^{-1} were calibrated with a standard KCl solution of 111 mS cm^{-1} nominal value. The temperature measurements ranged from 60 to -10°C in 10 degree decrements.

6.2.3. Electrochemical Testing

Copper foil was cut into ½ inch diameter disks (1.27cm^2) and washed in 1.0M HCl solution for 10 minutes. The Cu disks were rinsed with deionized water (three times) and acetone (three times), dried under vacuum for 12 hrs. The washed Cu foil was assembled in the coin cell as the working electrode while the Li metal (1.5mm thick, FMC Corp) was the reference and counter electrode. Asahi Kasei C5 was used as the separator and soaked in 120 µL of electrolyte. The cells were first discharged until they reached an area capacity of 0.5mAh/cm^2 and charged until reaching 1.0V (all at various currents).

All composite electrodes (lithium iron phosphate and lithium nickel manganese cobalt oxide (622) were coated on 20 µm thick aluminum foil. These electrodes were provided by the CAMP Facility at Argonne National Laboratory. All electrodes were punched to 9/16" diameter (1.6 cm^2 area) and assembled in 2032 coin cells (*Hohsen Corp.*) Asahi Kasei C5 was used as the separator and soaked in 120µL of the desired electrolyte. Li metal (9/16'' diameter) was used as the counter and reference electrode. In the case of anode free cells, Cu foil disks (5/8 in diameter) were used as the counter electrode. All half cells were cycled at C/3 for both charge and discharge without a formation cycle—in a Maccor battery cycler. The anode free cells were cycled at C/10 during charge cycle and C/3 during the discharge state.

The experiment was conducted in a pseudo-three electrode cell with the copper foil as the working electrode and the Li metal as the reference/counter electrode. The cell was measured from OCV to -0.1V at $2mVs^{-1}$ for three scans using Solartron 1287 potentiostat at room temperature.

6.2.4. Sample Investigation using SEM, XPS, cryo-FIB

The deposited Li metal on Cu foil was disassembled and washed with anhydrous DMC in the glovebox. The sample was mounted on the SEM sample holder in the glovebox then imaged using ZEISS Aurgia SEM with an ES2 detector at 5 kV.

Following cycling, all coin cells were disassembled in an argon-filled *Vacuum Atmospheres* Nexus One glovebox (H_2O < 1 ppm, O_2<1ppm). The electrodes were rinsed with anhydrous dimethyl carbonate and dried in vacuum at room temperature to evaporate any residual solvent. The samples were transferred to a *PHI* Versaprobe III XPS system using a sealed vacuum transfer capsule enabling rigorous air/moisture exclusion, as to not alter the surface chemistry. The XPS was operated using Al anode source at 15 kV with a 100 μm x 100 μm spot size and charge compensation was provided by the PHI charge neutralization system to eliminate differential charging. Survey scans were collected with a pass energy of 224 eV and a 1.0 eV step size followed by high-resolution scans with a pass energy of 26 eV and a step size of 0.05 eV. Peak fitting was performed using CasaXPS software (version 2.3.15, Casa Software Ltd.), using 70/30 Gaussian/Lorentzian line shapes on a linear background. Quantification was performed using peak area corrections to account for the photoionization cross section of each element and the instrument geometry. All spectra were shifted relative to the binding energy of the carbon 1s sp^3 (assigned to 284.5 eV) to compensate for any off-set during the measurement.

The deposited Li metal on Cu foil were disassembled and washed with anhydrous DMC in the glovebox. The samples were mounted on the SEM sample holder in the glovebox then transferred to a FEI Helios NanoLab Dualbeam. The stage was cooled with liquid nitrogen to ≤-180 °C. Sample cross-sections were exposed using 5 nA ion beam current and 100 ns dwell time and cleaned twice at 0.5 nA and 0.3 nA respectively. SEM images were taken with an ETD detector at 5 kV.

6.3. Results and Discussion

6.3.1. Electrochemical Analysis

The newly developed electrolytes were examined first by cyclic voltammetry, shown in Figure 6.1. The cells were cycled in a Li versus copper (Cu) coin cell configurations, were the Li metal works as both the counter and reference electrode. In Figure 6.1a, the insert is a magnified image of the CV from 2.5V to 0.2V, which demonstrate small current peaks from the electrolyte decomposition. However, since we have a bisalt electrolyte system it is difficult to decipher the peaks that correspond to each Li salt. Therefore, CV's were run for each Li salt at a slower sweep rate (Figure 6.1b) to properly determine the decomposition peaks. Figure 6.1b shows the effect of 4M LiFSI-DME on Li metal cycling, a small peak at 2.4V and a large peak at 1.25V is attributed to LiFSI decomposition which was previously demonstrated by Kim et al at 60°C in the same solvent system.[166] In the case of LiTFSI, it produces decomposition peaks at 2.0V and 1.44V. This demonstrates that both Li salts participate in the SEI formation.

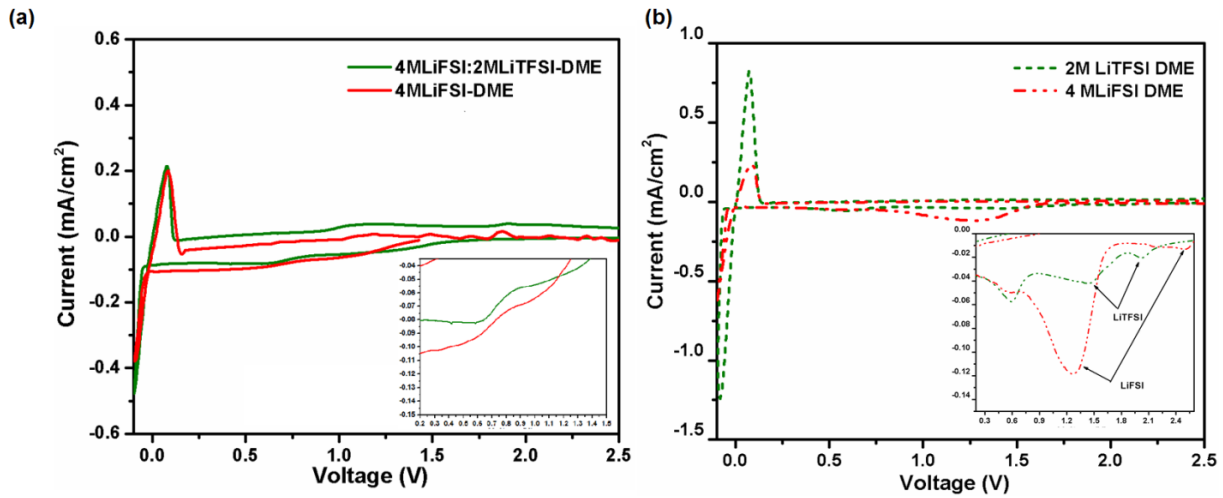

Figure 6.1. (a) Cyclic Voltammetry of 4MLiFSI-DME (red) and 4MLiFSI:2MLiTFSI-DME (green) at 1mV /sec. Insert is a magnified image of CV to determine decomposition peaks. (b) Cyclic Voltammetry of 4MLiFSI-DME (red-dashed line) and 2MLiTFSI-DME (green-dashed line) at 0.2 mV /sec. Insert is a magnified image of CV to determine decomposition peaks of each lithium salt.

The stability of Li metal during galvanostatic plating/deplating cycling was examined in Li versus Cu coin cells. The conventional electrolyte (Gen II, 1.2 M $LiPF_6$ (3:7) ethylene carbonate (EC): ethylmethyl carbonate (EMC)) efficiency was compared to DME electrolytes (4MLiFSI-DME and 4MLiFSI:2MLiTFSI-DME). The cells were cycled at 0.5 mA/cm^2 to an areal capacity of 0.5 mAh/cm^2. The voltage profiles at different cycle numbers are shown in Figure 6.3. The Coulombic efficiency (CE) can be calculated by taking the areal capacity ratio of deplated Li from the Cu to the plated Li. Gen II electrolyte has a first cycle efficiency of 55% which then increases to 80% until the 85th cycle. As expected, the carbonate electrolyte capacity decreases significantly after 100 cycles (Figure 6.2a). Conversely, the DME electrolytes have a notable increase in initial efficiency and in subsequent cycles. Figure 6.2b compares the state-of-the-art 4MLiFSI-DME to our bisalt electrolyte formulation (4MLiFSI:2MLiTFSI-DME). As shown in the literature, the cell cycled with 4MLiFSI-DME quickly reaches 98.5% and maintains stably cycling for 200 cycles.[168] Although the bisalt DME electrolyte takes 20 cycles to reach

98.2%, the cycling stability increases to compete with the state-of-the-art ether electrolyte. 4MLiFSI:2MLiTFSI-DME electrolyte has the ability to cycle Li with efficiency between 98.5 and 98.7%. It is no surprise that carbonate electrolytes have poor cycling performance because of their high reactivity to Li metal. [176,177]

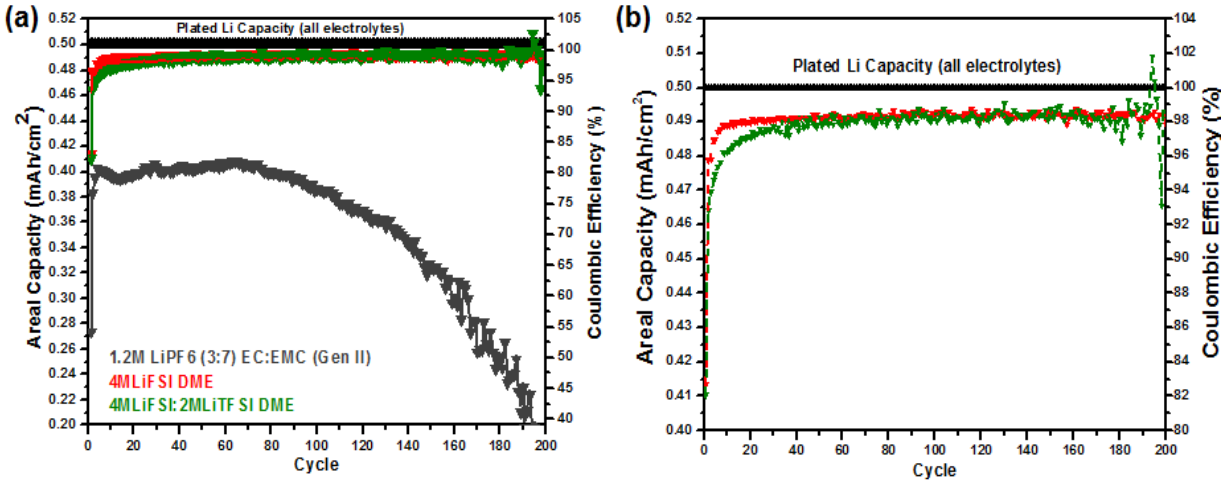

Figure 6.2. Galvanostatic cycling of lithium versus Cu at 0.5mA/cm^2 comparison of the conventional electrolyte to ether solvent electrolytes (a) and zoomed in image (b).

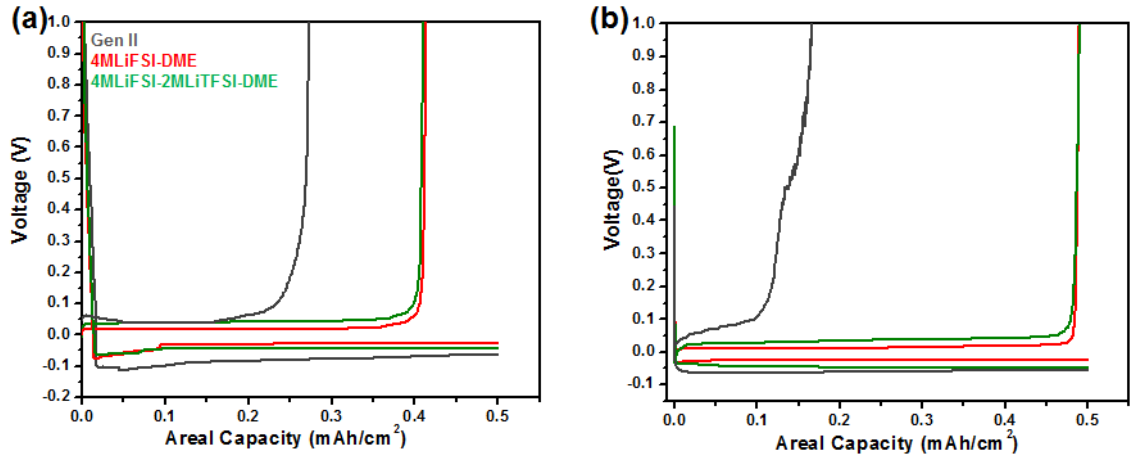

Figure 6.3. Voltage profiles of Li versus Cu coin cells in Gen II (grey), 4MLiFSI-DME (red),4MLiFSI-DME (red), and 4MLiFSI:2MLiTFSI-DME (green), after (a) first cycle and (b) 100 cycles.

Recent computation results demonstrate that ether solvents have a lower reactivity towards Li metal and have shown to have slower dendrite formation.[161,170] The most widely used solvent mixture to examine the plating and stripping efficiency Li metal is DOL:DME (1:1) mixture. The most widely used solvent mixture to examine the plating and stripping efficiency of Li metal is DOL:DME (1:1) mixture. DOL is known to be a good passivation agent with low viscosity (η:0.6 mPa/s) and has a good dielectric constant (ε: 7.1), while DME improves the solvation (donor number: 20) and solubility of the lithium salt with low viscosity (η:0.455 mPa/s).[178] Recently, Miao and coworkers proposed a new solvent combination that reduces the dendrite formation and improves the cycling efficiency of Li metal.[179] However, the cycling efficiency still lingers at 98% when cycled at 0.25 mA/cm^2, which is problematic for commercial applications that require higher efficiencies and rate capabilities. Although the electrochemical efficiencies seem promising, ether electrolyte formulations can only cycle low voltage cathodes for lithium-sulfur and Li-ion batteries. To date, there has not been an ether based electrolyte that has been pushed to its limits.

6.3.2. Li Metal Morphology

Figure 6.4 shows the important role that the electrolyte plays on Li metal plating morphology and packing density. As expected, Gen II electrolyte produces needlelike dendrites in the first plating state. These results are consistent with previous results, which cause catastrophic cell failure.[163,180] Conversely, the Li metal morphology produced from 4MLiFSI-DME follows similar morphology as presented previously by Qian et al.[168,175] Figure 6.4c shows the large Li particle morphology when cycled with 4MLiFSI:2MLiTFSI-DME. Both high concentrated DME electrolytes have uniform, closely packed Li metal particle morphology without dendrite formation. It is difficult to determine if the Li metal morphology is consistent

from the top view SEM, therefore alternative techniques were applied in order to elucidate the Li metal packing density.

To investigate the cross section of the Li metal morphology, previous reports rely heavily on SEM. However, this requires either physically cutting the electrode with scissors or focusing on the outer edge of the electrode to determine the area where the Li metal is deposited on the copper (Cu) foil. There are several issues associated with these methods. First, when scissors are used to cut the Li metal deposited on Cu foil, the sample will be damaged during preparation. As a result, the SEM image is not a true representation of the Li metal deposition packing density, as the Li metal will inevitably be compressed during the cutting process. Secondly, imaging the outer edge of the Li deposited on Cu foil to determine film thickness and packing morphology can lead to incorrect assumptions. This is due to the non-uniform current density distribution during Li metal deposition which causes heterogamous Li metal film deposition.[181,182] As a result, the packing density can be different when comparing the outer edge morphology to that in the center of the electrode due to the sharp increase in local current.[183] And third, tilting the SEM stage to obtain a cross section image makes it difficult to focus on the Cu foil and deposited Li metal interface. To further improve Li metal cycling efficiency, we need to understand how electrolytes affect the nucleation growth and packing density at the Cu-Li metal interface. For the first time, we utilize cryogenic-focused ion beam (cryo-FIB).

Cryo-FIB overcomes all the shortcomings of traditional SEM cross section images. Cooling the samples below -180°C prevents local melting and re-deposition during cross-sectional milling of the deposited Li metal, thereby obtaining a true representation of the cross sectional image (see supporting information). Figure 6.4 d-f demonstrates the deposited Li metal on Cu foil packing density. Additional images are shown in supporting information, which

demonstrate consistent results. When Gen II electrolyte is used, the cross section image demonstrates a needlelike Li metal morphology, highlighted by the red arrows (Figure 6.4d). The large void space between the Li metal and the Cu foil propagates throughout, generating a thickness of ~5μm. It is this large porosity in the Li deposition that causes parasitic side reactions, eventually forming an unstable SEI. With 4MLiFSI-DME, the porosity in deposited Li is reduced, with no observe dendritic Li; however, small pores are present closer to the Cu interface, highlighted by the white arrow (Figure 6.4e). Nonetheless, the use of 4MLiFSI-DME increases the Li metal packing density with an average thickness of ~4 μm. The use of 4MLiFSI:2MLiTFSI-DME dramatically reduces the porosity of Li metal deposition and plating thickness to ~2.5 μm. This electrolyte plates dense Li metal, especially at the Li-Cu interface (Figure 6.4f). This demonstrates that the synergy between LiFSI and LiTFSI helps generate a SEI that promotes even Li nucleation and deposition. As a result, the trend persists until the desired capacity is reached.

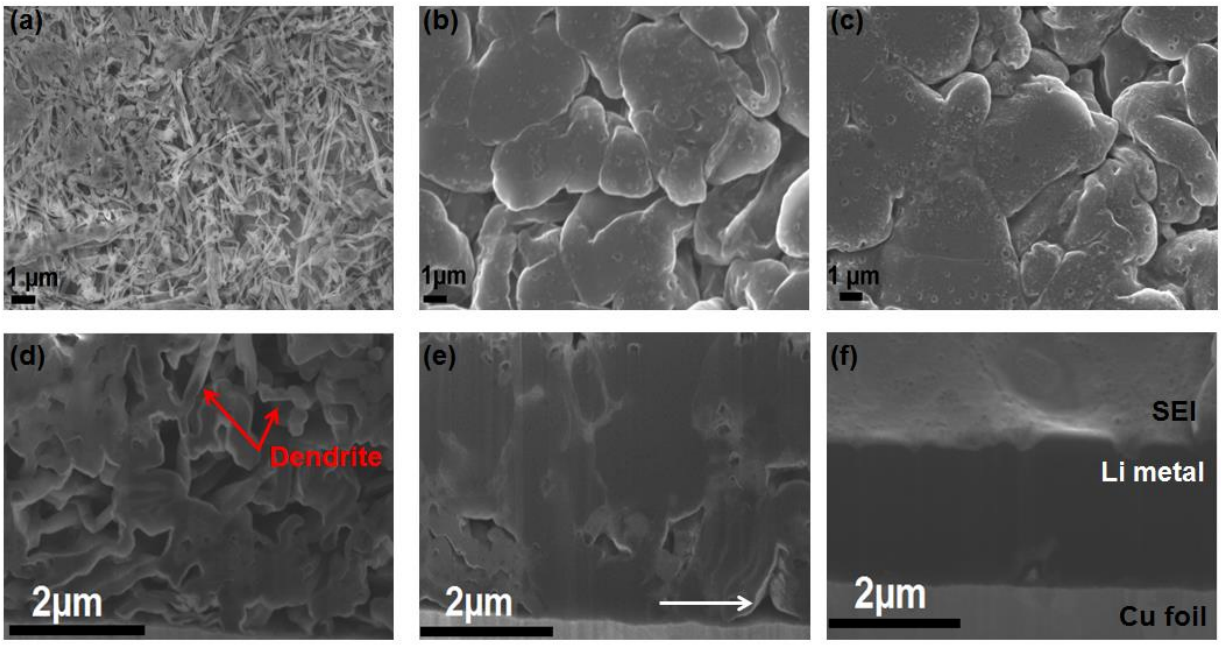

Figure 6.4. Top view SEM images of the initial lithium plated morphology and their corresponding Cryo-FIB cross sectional cuts when cycled in (a, d) Gen II, (b, e) 4MLiFSI- DME, and (c,f) 4MLiFSI:2MLiTFSI-DME.

6.3.3. SEI Investigation by XPS

The electrochemical cycling and plating pack density of Li metal in DME electrolytes demonstrate that the initial SEI formation is critical for high efficiency Li metal cycling. The SEI generated by the Gen II electrolyte has been extensively studied by various spectroscopic techniques, which clearly indicate that Gen II is not a suitable electrolyte for lithium metal batteries.[58,184,185] More importantly, the plated Li metal on Cu foil shows that the Li metal porosity (demonstrated by cryo-FIB, Figure 6.4 d) allows for the Li metal to be continuously exposed to the electrolyte; this inevitably results in an unstable SEI. In recent years, the SEI generated by the decomposition of 4MLiFSI-DME electrolyte has been studied by computation and XPS. However, the addition of LiTFSI to 4MLiFSI-DME requires further investigation. Figure 6.5a shows the C1s spectra for all electrolytes, where the SEI generated by Gen II

electrolyte is dominated by solvent (EC:EMC) decomposition forming ethers (CO, 286.6 eV), esters (OCO, 288.6 eV), and carbonates (CO_3, 289.9eV) functionalities. The SEI generated by 4MLiFSI-DME also has similar functionalities that are associated with the decomposition of the DME solvent. The addition of LiTFSI demonstrates that the salt is actively participating in the SEI formation where CF_3 and CF_2 are found at 293.2 eV and 291 eV, respectively. As a result, the more electronegative environment causes a significant shift in CO peak (286.9eV) and OCO (289.1 eV), which is demonstrated by the dashed line.

This is further validated by the fluorine 1s spectra in Figure 6.5b. There is a slight LiF peak shift to higher binding energy when comparing Gen II (684.8 eV) and 4MLiFSI-DME (684.9 eV) to 4MLiFSI:2MLiTFSI-DME (685.3 eV). Peaks associated with the LiFSI and LiTFSI decompositions are found at 688.8eV for CF_3 and 687.8 eV for compounds containing S-F, which is consistent with previous reports.[166,169] The O1s region shows that Li_2O is present in the cells cycled with Gen II and 4MLiFI-DME. The O1s region for Gen II cells also shows correlation with the C1s region scan (CO: 531.4eV, OCO: 530.5 eV, CO_3: 532.1 eV). The salt decomposition products ($Li_xO_yPF_z$: 533.3eV) also correlate well with the F1s region scan. The LiTFSI and LiFSI salt decomposition products, particularly S-O containing functionalities, are present between approximately 532 eV to 533 eV. The high electronegative environment of the SEI generated by 4MLiFSI:2MLiTFSI-DME is further demonstrated by the higher binding energy peak shift of the S-O salt decomposition peak. The SEI generated by the bisalt electrolyte promotes the formation of a more dense and uniform Li metal deposition that decreases the void space between the Li metal and Cu. This allows for better contact of the Li to the Cu, which may avoid Li metal disconnect during rigorous electrochemical cycling.

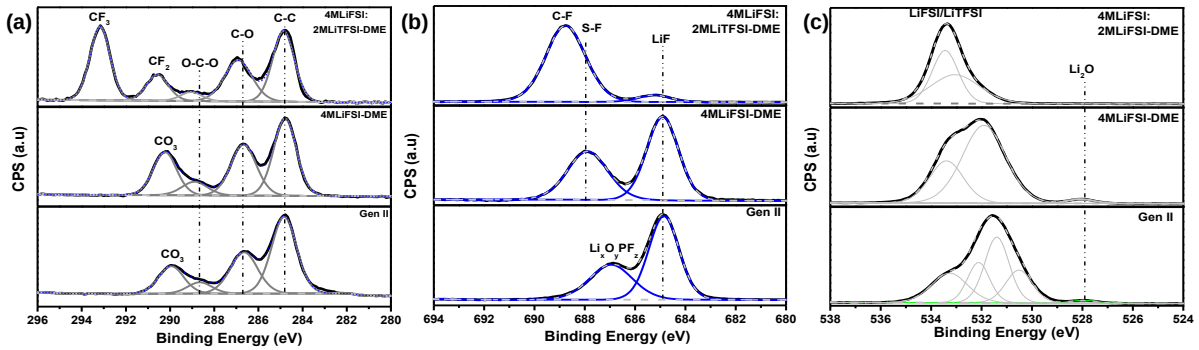

Figure 6.5. Region scans of (a) carbon 1s, (b) fluorine 1s, (c) oxygen 1s on plated lithium metal after the first cycles.

6.3.4. Electrolyte Oxidative Potential

It is widely accepted that ether based electrolytes have low oxidation stability (approx. 4V).[1] When ether electrolytes are used in an actual cell, the oxidation potential is even lower as a result of the catalytic surface of various cathode materials.[186] Therefore, the applications for ether based electrolytes are limited to lithium air[187], lithium sulfur[188], and low voltage lithium ion cathodes such as lithium iron phosphate (LFP). New ether electrolyte formulations are typically tested against LFP and sulfur battery cathodes.[166,179] Although Qian and coworkers determined that high concentrated ether (4MLiFSI-DME) electrolytes have a higher oxidation potential than do low concentrated electrolytes (1MLiFSI-DME), they only tested the electrolyte using LFP in half cell and anode free cell configurations.[168,175] The oxidative stability of our bisalt electrolyte was examined using linear sweep voltammetry (LSV), shown in Figure 6.6. Consistent with Qian and coworkers, we observe a 4.4V oxidation potential for 4MLiFSI-DME electrolyte.[20] The bisalt electrolyte has an oxidative potential of 5V which is greater than the Gen II base line (4.8V). Similar to the "water-in-salt" and "water-in-bisalt",[189,190] our bisalt electrolyte experiences a similar effect in improving the oxidation potential as a result of higher Li ion concentration compared to 4MLiFSI-DME electrolyte. As a result, the solvent has less of an

effect on the oxidation potential. All of the electrolytes were tested using LFP as our cathode (half cell configuration), shown in Figure 6.7a.

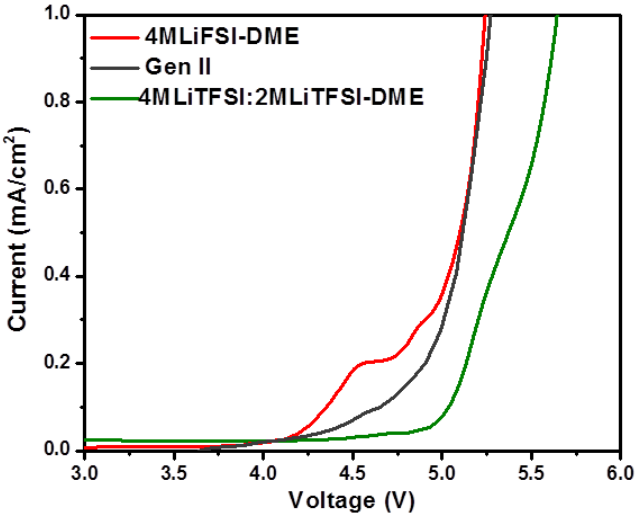

Figure 6.6. Linear sweep voltammetry using a three electrode cell of Gen II (grey), 4MLIFSI-DME (red), and 4MLiFSI:2MLiTFSI-DME (green).

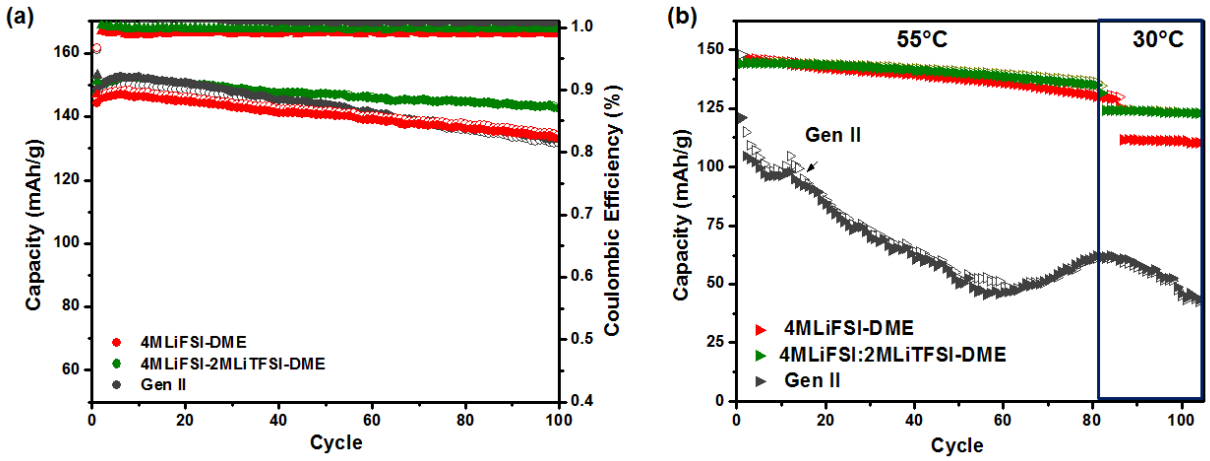

Figure 6.7. Cycling performance of (a) lithium iron phosphate (LFP) at 30°C and (b) lithium cobalt oxide half cells at 55°C and 30°C when cycled with 4MLIFSI-DME (red), 4MLiFSI-4MLiTFSI-DME (green), and Gen II (grey).

Given the LSV results, all electrolytes were used to cycle lithium cobalt oxide (Figure 6.7b) at both 55°C and 30°C (at C/3). First, the cells are cycled at 55°C to 4.2V for 80 cycles. The Gen II electrolyte is unable to handle high temperature cycling. Conversely, both ether electrolytes have negligible capacity fade. When the temperature decreases to 30°C, the Gen II electrolyte continues to lose capacity, which is likely due to the poor thermal stability of $LiPF_6$ and CO_2 gas generation.[191] The cell cycled in 4MLiFSI-DME has a large drop in capacity with temperature change, ranging from 130 mAh/g at 86 cycles when cycled at 55°C to 111.5 mAh/g at 30°C. On the other hand, the cell cycled with 4MLiFSI:2MLiTFSI-DME has a slight drop in capacity from 134.2 mAh/g (86 cycles, 55°C) to 124.1 mAh/g for the remaining cycles at 30°C. This demonstrates that our high concentrated bisalt electrolyte has good thermal stability, leveraging the properties from both lithium salts. As a result, it can cycle lithium cobalt oxide to 4.2V without serious voltage decay both at high and room temperature.

6.3.5. Rigorous Half Cell and "Anode Free" Cell Tests of $LiNi_{0.6}Mn_{0.2}Co_{0.2}O_2$

Until now, researchers had not tried cycling $LiNi_{0.6}Mn_{0.2}Co_{0.2}O_2$ (NMC-622) with ether electrolytes due to their low oxidation potential. Based on our LSV study, we know that our bisalt electrolyte oxidizes at a much higher potential than 4.0V. All of the electrolytes were further pushed to cycle the next generation high nickel content cathodes, NMC 622, to 4.4V at C/3 in a half cell configuration. All of the cells have stable cycling until 100 cycles; however, the Gen II electrolyte fades quickly afterwards. The cell cycled in 4MLiFSI-DME failed after 100 cycles which is attributed to the oxidation potential of the electrolyte. Given that the oxidation potential of 4MLiFSI–DME is at 4.4V, the electrolyte continues to oxidize at every cycle. This prevents it from forming a stable passivation layer on the cathode. Remarkably, the bisalt

electrolyte outperforms all of the electrolytes. Even after 200 cycles, the cell has a 70% capacity retention with a CE of 99.8%.

Pioneered by Qian and coworkers, the "Anode Free (AF)" cell configuration consisted of LFP vs. Cu.[175] Here, the Li ions are directly plated on the Cu foil at negative potential, testing the true performance of the electrolyte in the cell. Brown et al., demonstrated that the anode free system is useful to study the effect of vinylene carbonate on the SEI formation.[192] Inspired by the abovementioned works, AF cells with NMC-622 were used to test all electrolytes (Figure 6.8b). It is known that the performance of Li metal plating and striping in AF and half cell configurations improve substantially with variable rate cycling, where the Li metal is plated at a slow rate and stripped at a fast rate.[175,193] Therefore, our AF cells were plated at C/10 and delithiated at C/3 to obtain the highest efficiency cells. Consistent with the literature, the cell cycled with Gen II electrolyte quickly fades with no remaining capacity after 30 cycles.[175] On the other hand, the bisalt (4MLiFSI:2MLiTFSI-DME) outperformed the state-of-the-art ether electrolyte (4MLIFSI-DME) with initial CEs of 80.5% and 78%, respectively. After 55 cycles, the cell cycled with 4MLiFSI-DME had a discharge capacity of 54.8 mAh/g and a CE of 97.3% compared to 89.9 mAh/g and CE of 99.1% for the cell cycled in the bisalt electrolyte. We acknowledge that we have not solved all of the issues with Li metal. Given that we still have capacity fade in both cell configurations, additional work will be required in order to solve the remaining issues.

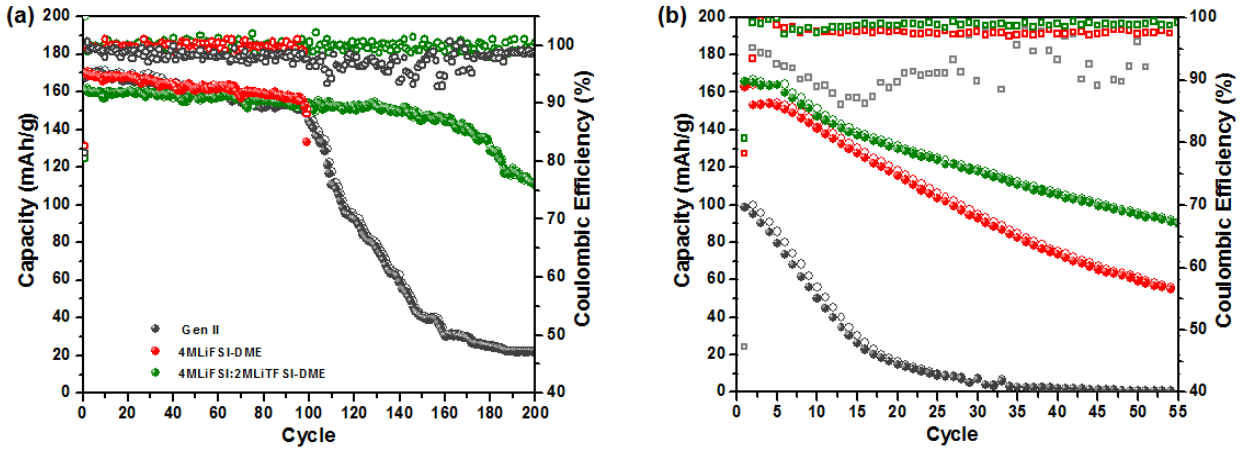

Figure 6.8. Cycling performance of (a) NMC-622 half cell cycled at C/3 and (b) "Anode Free" Cu versus NMC-622 cycled at C/10 for the charge state and C/3 in the discharge state.

6.4. Conclusion

High concentration ether bisalt electrolytes (4MLiFSI:1MLiTF-DME, 4MLiFSI:2MLiTFSI-DME) were used to test the efficiency of lithium plating and deplating. With plating efficiencies between 98.5-98.7% at 0.5mA/cm^2, they prove to be comparable to the state-of the-art 4MLiFSI-DME. The increase in salt concentration increases the oxidation potential from 4V to 4.7V for the 6M bisalt ether electrolyte. As a result, the electrolyte was tested in a half cell and "Anode Free" configuration with NMC-622. The 6M bisalt electrolyte outperformed all of the electrolytes achieving stable CE above 99%. This was achieved by forming an inorganic SEI composed of S-O functionalities, LiF, Li_2O, and CF compounds which act as a protective layer on the Li metal surface. Generating a uniform SEI dominated by salt decomposition products forms uniform Li metal plating on the Cu surface. The fundamental findings in this work yield a pathway to develop new electrolyte formulations for stable Li metal batteries.

Chapter 6, in full, is currently being prepared for submission for publication “Bridging the Gap: Electrolytes for Efficient Coupling of Lithium Metal Anodes with Next Generation Cathodes” Alvarado, J; Schroeder, M; Borodin, O; Lee, J-W; Wang, X; Wynn, T; Zhang, M; Xu, K; Meng, Y.S. The dissertation author was the co-primary investigator and author of this paper. All of the experiment parts were performed by the author except for the Cryo-FIB.

Chapter 7. Solvent-Salt Synergy Offers Fresh Pathway to Unlock Next Generation Li-Ion Chemistries

7.1. Introduction

Since the initial commercialization of lithium ion batteries (LIBs) more than 25 years ago, the energy demands of portable electronic devices have rapidly outpaced the deliverable performance metrics of state-of-the-art battery systems. This already widening gap is further strained by the recent surge in development and adoption of large-scale energy storage applications including electric vehicles and smart electric grids. These systems bring requirements for energy/power densities, cycle life, low cost, and improved safety to challenging new levels. An assortment of energy dense, high voltage positive electrode materials including $LiNi_{0.5}Mn_{1.5}O_4$ (LNMO) spinel, $LiCoPO_4$ (LCP), and high Ni-content layered Li-Ni-Mn-Co oxides (NMC) offer promising theoretical performance metrics as long as the challenges—primarily arising from shortfalls of currently available electrolytes that are almost exclusively based on carbonate esters—can be addressed.

The first of these challenges has troubled Li-ion battery development from the start: achieving reversible lithium intercalation at extreme potentials (from 0V vs. Li/Li^+) while preventing persistent decomposition of electrolyte solvents and anions. The key enabler of this process in commercial Li-ion cells is the interphase at anode/electrolyte junction: the solid-electrolyte-interphase (SEI)[194], which forms and functions as a result of self-limited decomposition reactions of electrolyte components and ultimately dictates the reversibility and kinetics of lithium intercalation.[2,59] This process is extremely sensitive to the electrolyte composition (solvent, salt and its concentration). Despite extensive investigation of many aprotic solvents and additives, only ethylene carbonate (EC) and a few other "enablers" (vinylene

carbonate (VC)[195], fluoroethylene carbonate (FEC)[11], (4R,5S)-4,5-difluoro-1,3-dixolan-2-one (DiFEC)[196], methylene-ethylene carbonate (MEC)[197], prop-1-ene-1,3-sultone (PES)[198], and succinic anhydride (SA))[199] have been reported to exhibit this behavior. Aside from this limited group, most other electrolyte systems (particularly non-carbonate systems) demonstrate similar electrochemical behaviors of varying degrees to systems based on propylene carbonate (PC), undergoing extensive parasitic surface reduction processes and exfoliating the graphitic structure.

The second major challenge has emerged more recently with the development of high voltage cathode materials such as LNMO and LCP, which operate at >4.5 V vs. Li and offer greater energy density at the cost of exposing electrolytes to more aggressive electrochemical conditions. The performance of these electrodes in conventional carbonate-based electrolytes suffers from extensive degradation at or above 4.4V due to continuous oxidation processes, which evolve CO_2, consume active material, and increase cell impedance[200]—parasitic effects that are all accelerated at higher temperatures.[201–205] Many electrolyte systems with superior anodic stability such as those based on nitriles, sulfones, ionic liquids, and fluorinated carbonates have been investigated for use with high-voltage cathodes, but often struggle to form a suitable anode SEI, leading to excessive reductive decomposition and exfoliation of graphite anodes. The few well known SEI-forming additives that can address this issue in carbonate systems are often anodically unstable against those high voltage cathode surfaces, and as a result, are unable to repair/reform SEI in a carbonate-free media.

Here, we report an electrolyte formulation that reconciles both of these challenges. High purity tetramethylene sulfone (TMS), or sulfolane (SL), a highly polar aprotic solvent with wide temperature and voltage stability windows was used as bulk electrolyte solvent without

additives, and lithium bis(fluorosulfonyl)imide (LiFSI) serves as both the conducting salt and SEI forming agent.[206] This solvent-salt combination exhibits a unique synergy, establishing stability at the anode-electrolyte interface with an SEI primarily formed by FSI^- anion and providing high voltage stability at the cathode-electrolyte interface via intrinsic anodic stability of the solvent and salt.

7.2. Experimental

7.2.1. Electrolyte Preparation

The electrolytes were prepared using LiFSI (Oakwood Products, Inc.-battery grade), $LiPF_6$ (BASF-battery grade), propylene carbonate (PC, BASF-battery grade), ethylene carbonate (EC, BASF-battery grade), ethylmethyl carbonate (EMC, BASF-battery grade), and tetramethylene sulfone (SL, Sigma Aldrich-98% purity). Given the quality of the sulfolane (SL) and its slightly yellow-brown color, it was purified.[207] The resulting material is a sticky white solid at room temperature that melts at 28.6°C to form a clear liquid. The carbonate solvents (PC, EMC, EC) were dried using molecular sieves and the salts were dried under vacuum at 60C for 12 hours to remove any residual water. Six salt-solvent electrolyte compositions were used in this work: 1.0m LiFSI-SL, 3.25m LiFSI-SL, 1.0m LiPF6-SL, 1.0m LiFSI-PC, 4.0m LiFSI-PC, and 1.2m $LiPF_6$ EC: EMC (3:7 wt%) (all formulated in the glovebox).

7.2.2. Electrolyte Characterization

Electrolyte conductivity κ of the electrolytes were measured with an Agilent E4980A precision LCR meter at selected temperatures within a Tenney Jr. environmental chamber, controlled and automated with an in-house computer program. The conductivity cells consist of a pair of platinum−iridium electrodes and a Pyrex cell body that can be sealed with a ground-glass

stopper. The cell constants of a nominal value of 0.1 cm−1 were calibrated with a standard KCl solution of 111 mS cm−1 nominal value. The temperature measurements ranged from 85 to -20°C in 5 K decrement, stopping at each for an hour of thermal equilibration before taking a measurement. After the measurement at a set temperature, readings from five thermocouples placed near the conductivity cells were recorded and averaged to give the actual temperature for the conductivity values. Each conductivity measurement consisted of an impedance scan from 20 Hz to 2 MHz with an amplitude of 10 mV, from which a $Z'Z''$ plot was made and κ was evaluated from the impedance curve. This followed parameters from our previous publication.[208]

7.2.3. Graphite Half Cell Experiments

The graphite electrodes contained 91.83% Gelon G15 MCMB with 2 wt% C45 conductive additive and 6 wt% Kureha 9300 binder, and were coated on 10 μm thick Cu foil. These electrodes were provided by the CAMP Facility at Argonne National Laboratory. These electrodes were punched to 9/16" diameter (1.6 cm^2 area) and assembled in 2032 coin cells (*Hohsen Corp.*) with *Celgard* 3501 separators soaked in various electrolytes (1m, 3.25m LiFSI SL, 1m $LiPF_6$ SL, and 1.2m LiFSI ethylene carbonate (EC): ethylmethyl carbonate (3:7 wt%)) and a 1.5 mm thick, 0.5" diameter Li metal counter-electrode (*FMC Corp.*). Cell assembly was carried out in a dryroom (dew point < -75°C). After resting for 12 hours, the coin cells were cycled in a 30° environmental chamber with a *Maccor* battery cycler. The galvanostatic cycling protocol included upper and lower voltage limits of 2.0V and 0.05V, respectively, for a formation cycle at C/20 followed by 4.5 cycles at C/5 until the end of the sixth discharge (lithiated graphite). Cells that exhibited exfoliation/decomposition behavior without reaching the lower limit (i.e. 1.0m PF_6 PC) were discharged at C/20 for 80 hours for consistency in the XPS analysis. The cell configuration was also used for cyclic voltammetry experiments on Solartron

potentiostat. Here the Li metal acts as the counter electrode and reference electrode, while MCMB anode is the working electrode. The experimental parameters included sweeping the voltage from OCV to 0.05V at 0.05mVs^{-1}, for a total of three CV cycles.

7.2.4. Full cell Experiments

The $LiMn_{1.5}Ni_{0.5}O_4$ electrodes contained 84% Gelon G15 MCMB with 8 wt% C45 conductive additive and 8 wt% Kureha 1120 binder, and were coated on Al foil. These electrodes were provided by the CAMP Facility at Argonne National Laboratory. These electrodes were punched to 9/16" diameter (1.6 cm^2 area) with a areal loading of 14.7 mg cm^{-1} and assembled versus MCMB anode with a mass loading of 6.44 mg cm^{-1} in 2032 coin cells (*Hohsen Corp.*) with glass fiber (*Whatman QMF*) separators soaked in various electrolytes (3.25m LiFSI SL, and 1m $LiPF_6$ SL, 1.2m $LiPF_6$ EC: EMC (3:7 wt%). Cell assembly was carried out in a dryroom (dew point < -75°C). After resting for 12 hours, the coin cells were cycled in a 30°C and 55°C environmental chamber with a *Maccor* battery cycler. The galvanostatic cycling protocol included upper and lower voltage limits of 4.85V and 3.5V, respectively, for a two formation cycles at C/20 followed by 300 cycles at C/5.

7.2.5. Linear Sweep Voltammetry

A three electrode Swagelok cell containing Li metal as the counter and reference electrode, with platinum metal disk (0.5 mm diameter) as the working electrode. The glass fiber separator (*Whatman QMF*) to avoid the cell from shorting, with 300 uL of electrolyte. The experiments were carried out on a single channel Gamry Potentiostat (*Reference 3000*), sweeping from OCV to 6V at 2mVs^{-1}. Experiments were conducted three times for each electrolyte to ensure reproducibility.

7.2.6. Cyclic Voltammetry and Impedance Measurements

The experiment was conducted in a two electrode coin cell with the MCMB graphite anode as the working electrode and the Li metal as the reference/counter electrode. The cell was measured from OCV to 0.05V at $0.05mVs^{-1}$ for three scans using Solartron 1287 potentiostat at room temperature.

Impedance measurements were measured in the same coin cell using a Gamry Potentiostat (*Reference 3000*). The MCMB half cells were first lithiated at C/20 until 0.05V and left to rest for four hours until the cells reached OCV. The impedance was measured using 10mA AC potential from 0.1 Hz to 1MHz versus open circuit potential. The cells were then delithiated at the C/20 until 2V. The cell was allowed to reach OCV and the impedance measurement was taken. After the impedance measurements were taken, an equivalent circuit model was fit to the data to analyze the reactions that took place using Z view software (v. 3.4a, Scribner Associates, Inc.).

7.2.7. XPS sample Preparation/Analysis:

Following cycling, all coin cells were disassembled in an argon-filled *Vacuum Atmospheres* Nexus One glovebox (H_2O < 1 ppm, O_2<1ppm). The electrodes were rinsed with anhydrous dimethyl carbonate and dried in vacuum at room temperature to evaporate any residual solvent. The samples were transferred to a *PHI* Versaprobe III XPS system using a sealed vacuum transfer capsule enabling rigorous air/moisture exclusion, so the electrode surface chemistry is believed to be unaltered. The XPS was operated using Al anode source at 15 kV with a 100 μm x 100 μm spot size and charge compensation was provided by the PHI charge neutralization system to eliminate differential charging. Survey scans were collected with a pass

energy of 224 eV and a 1.0 eV step size followed by high-resolution scans with a pass energy of 26 eV and a step size of 0.05 eV. Peak fitting was performed using CasaXPS software (version 2.3.15, Casa Software Ltd.), using 70/30 Gaussian/Lorentzian line shapes on a linear background. Quantification was performed using peak area corrections to account for the photoionization cross section of each element and the instrument geometry. All spectra were shifted relative to the binding energy of the carbon 1s sp^3 (assigned to 284.5 eV) to compensate for any off-set during the measurement.

7.2.8. Infrared Spectroscopy

All FTIR spectra were collected in an attenuated total internal reflection (ATR) geometry using a Nicolet 6700 (Thermo Scientific) spectrometer with a diamond ATR assembly (single bounce, 45°, Specac Ltd.). All spectra were the average of 64 scans collected at a resolution of 2 cm^{-1}. LabSpec5 curve fitting software was used to fit spectra to mixed Gaussian-Lorentzian functions.

7.2.9. Molecular Modeling

QC calculations were performed using the g09 Gaussian package including implicit solvent SMD solvation model with SL parameters (ε=42.5, ε_∞=2.194) was employed in all calculations. The composite methodology G4MP2 was utilized for small complexes because it was previously demonstrated to accurately predict ionization energies, electron and proton affinities and enthalpies of formation with the mean absolute deviations of 0.73-1.29 kcal/mol. Less expensive M05-2X/6-31+G(d,p) density functional theory (DFT) calculations were performed for examining the reactions in larger complexes. Oxidation and reduction potentials were calculated according to Eq. 1and 2, in which the value of the potential vs. an electron at rest

in vacuum was converted to the Li/Li^+ scale by subtraction of 1.4 V as previously discussed. The shift factor of 1.4 V dependents on the nature of the solvent and salt concentration giving rise to uncertainty of 0.1-0.3 V for predicted values.

$$E^0_{oxidation}(M) = [\Delta G_e + \Delta G^0_S(M^+) - \Delta G^0_S(M)]/F - 1.4 \quad (7.1)$$

$$E^0_{reduction}(M) = -[\Delta G_e + \Delta G^0_S(M^-) - \Delta G^0_S(M)]/F - 1.4 \quad (7.2)$$

where ΔG_e is the ionization free energy or electron affinity in gas-phase at 298.15 K; $\Delta G_S(M^+)$, $\Delta G_S(M^-)$ and $\Delta G_S(M)$ are the free energies of solvation of the oxidized, reduced and initial complexes, respectively, and F is the Faraday constant.

7.3. Results and Discussion

7.3.1. Electrolyte Characterization

Electrolytes with concentrations of 1.0m (mol kg^{-1}) and 3.25m LiFSI in SL were prepared for temperature-dependent conductivity measurements. The data shown in Figure 7.1a, with 1.0m $LiPF_6$ in EC/EMC (3:7) (Gen II) for comparison[209], indicates the LiFSI-SL system exhibits approximate conductivities of 2-3 mS cm^{-1} depending on the concentration, less than an order of magnitude lower than the standard carbonate formulations despite viscosity penalties associated with the solvent and increased salt concentration. Part of the conductivity penalty is compensated by the higher apparent Li^+-transference number (t^+) estimated from ion self-diffusion coefficients. The pfg-NMR (and MD simulations) yield t^+=0.48 (0.48 MD) for 1 m LiFSI-SL and 0.58 (0.65 MD) for 3.25 m LiFSI that are higher compared to the previously reported values for

mixed carbonates t^+=0.24-0.34 for $LiPF_6$/(EC/DEC)[210] and $t^+ \approx 0.4$ for $LiPF_6$/(EC:DMC).[211] Interestingly, at 3.25m MD simulations and pfg-NMR predict that the Li^+ diffusion is not only faster than diffusion of the FSI^- anion but also is faster than diffusion of SL solvent, suggesting that the Li^+ cation moves via solvent and anion exchange in 3.25m LiFSI-SL. More detailed analysis of MD trajectories showed that during one Li^+-SL residence time, a Li^+ moves 6.4 Å and 7.4 Å for 1m and 3.25m LiFSI-SL, respectively. These distances are similar to the size of the SL molecule and FSI^- anion. Thus, a Li^+ cation exchanges on average one solvent and anion from its solvate shell as its moves their size, further confirming the importance of solvent and anion exchange contributions to the Li^+ diffusion. In contrast, MD simulations predict that in EC:DMC (1:3) doped with 1M $LiPF_6$, the Li^+ cation moves much longer distance of 11.4 Å before it exchanges a DMC solvent in its solvating shell, showing a larger contribution of the Li^+ vehicular transport with DMC. While enhancement of the exchange mechanism with increasing salt concentration was previously discussed for concentrated electrolytes,[212–214] dominance of the exchange contribution is clear even in the low concentration 1m LiFSI-SL electrolyte. Examination of the lower temperature behavior of the 1m LiFSI-SL shows that it becomes supercooled 15 °C lower than 3.25m LiFSI-SL, but was slower to recover when reheated. Otherwise, no hysteresis was observed over the measured temperature range, indicating relatively fast kinetic processes.

These electrolytes were also characterized with differential scanning calorimetry (DSC) to establish a suitable temperature window of operation. Shown in Figure 7.1b, the carbonate baseline exhibited endothermic behavior until 175°C at which point the DSC cell ruptured due to overpressure from gas generation. Conversely, the 3.25m LiFSI-SL persisted to >280°C before

rupturing, suggesting less gas generation occurred over the majority of this extended temperature range, though the exothermic peaks above 200°C do suggest some chemical reactivity.

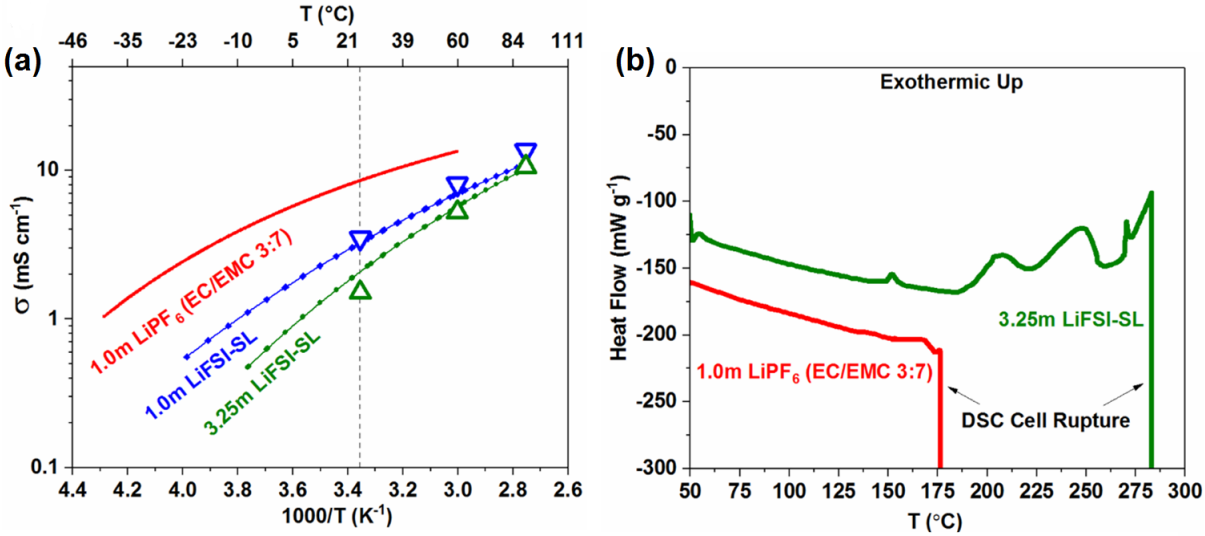

Figure 7.1. (a) Temperature-dependent conductivity data for 1.0m and 3.25m LiFSI in SL as compared to 1.0m $LiPF_6$ in EC/EMC (3:7) (Gen II). Open triangles indicate MD calculated values for the LiFSI-SL electrolytes (b) DSC heat flow measurement of LiFSI-SL electrolytes with Gen II for comparison.

FTIR measurements were conducted on SL-FSI at various salt concentrations to study the Li^+-solvation behavior. Due to large amounts of spectral overlap, the solvation behavior was studied utilizing only two regions of the spectra containing features assigned primarily to the structure of SL molecule. The first is the SO_2 twist in SL, located at ~445 cm^{-1}.[215,216] This region can be deconvoluted into two components (dashed lines, Figure 7.2a). The feature centered at 440 cm^{-1} corresponds to the SO_2 twist of non-solvating SL molecules in the electrolyte, and was confirmed by comparison to pure SL (Figure S1a). The broader feature at 450 cm^{-1} corresponds to the SO_2 twist of SL molecules coordinated with Li^+. With this deconvolution, the fractional area of both components can be tracked as a function of LiFSI concentration (Figure 7.2b). As expected, when LiFSI concentration increases so does the fraction of SL molecules participating

in the solvation of Li^+. In Figure 7.2b (blue), the fraction of free SL from MD simulations is also shown for comparison, and is in excellent agreement with the FTIR analysis. The average solvation number (N_S) of Li^+ is typically determined from the relation[217]:

$$\frac{A_{SL(Li)}}{A_{SL(Li)}+A_{SL(Free)}} = N_S \frac{c_{(Li)}}{c_{(SL)}}, \qquad (7.3)$$

where $A_{SL(Li)}$ and $A_{SL(Free)}$ are the integrated area intensities of the bands for the SL coordinated by Li^+ and free SL not coordinated by Li, respectively, c(Li) and c(SL) are the concentrations of the lithium cations and SL. This relation assumes that only one Li^+ can participate in the SL coordination forming contact ion pairs (CIP). Solvation numbers obtained from this CIP model are shown in Figure 7.1b (green), indicating a drop from an average of 3.7 to 1.8 of SL per Li^+ as salt concentration increases from 1m to 3.75 m. When this model (eq. 7.3) is applied to MD data, quite similar solvation numbers are obtained. However, when the Li^+ solvation numbers are calculated directly from MD simulations by analysis of the Li^+ solvation shell instead of using eq. 7.3, significantly higher values were obtained. The discrepancy between direct calculation and CIP model prediction (eq. 7.3) is attributed to formation of extended short-lived aggregates where Li^+ bridges multiple SL molecules, as opposed to the single Li-SL CIP model. Therefore, a standard technique for extracting solvation numbers should not be used for solvents with multiple solvating groups, such as SL, that would allow multiple Li^+ coordinating a solvent. MD simulations also predicted the extent of ion aggregation. The LiFSI-SL electrolyte at 1m is largely dissociated (61% free SL) and 33% of contact ion pairs (CIPs), while the 3.25m LiFSI-SL contains 47% of the FSI-Li CIPs and 43% of aggregates where FSI is coordinated by multiple Li^+. The FSI^- aggregation state is important for LiF reduction and electron stabilization.[218]

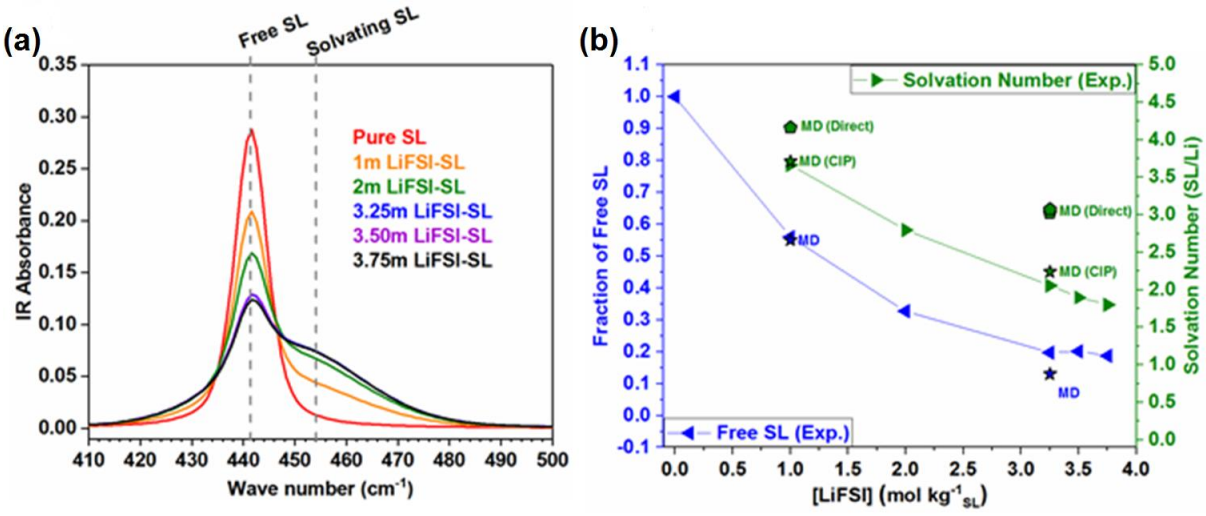

Figure 7.2. (a) FTIR spectra of sulfolane's SO_2 twist over a sweep of LiFSI concentrations. (b) The fractional area of the free sulfolane (blue) and solvation number (green) as a function of concentration according to FTIR measurements and MD simulations.

7.3.2. Cathodic Stability and Anode/Electrolyte Characterization

7.3.2.1. Electrochemical Testing

Sulfolane exhibits many attractive properties as an electrolyte solvent including excellent oxidative and high temperature stability, high dielectric constant, and stability toward lithium metal.[207] Unfortunately, selective separator wettability, electrolyte viscosity, and the inability to independently for a suitable SEI on graphite have hindered its use as the primary electrolyte solvent.[219,220] Given the importance of the SEI on anode operation and ultimately the full cell performance, we tested the proposed LiFSI-SL electrolytes in graphite-Li half cells with propylene carbonate-based electrolytes for comparison, as shown in Figure 7.3. In contrast to prior beliefs about SL-based electrolytes, the proposed LiFSI-SL electrolytes exhibit excellent galvanostatic cycling performance in graphite half cells, with a first cycle coulombic efficiency (CE) of 85.9% for 1m LiFSI-SL and 89.9% of 3.25m LiFSI-SL. Especially in the latter case, a capacity of ~300 mAh/g is achieved for graphite, approaching the theoretical limit allowed by

the stage I graphite intercalation (LiC_6, 372 mAh/g). The CE quickly increases to 99.8% for both high and low salt concentrations (Figure 7.3b).

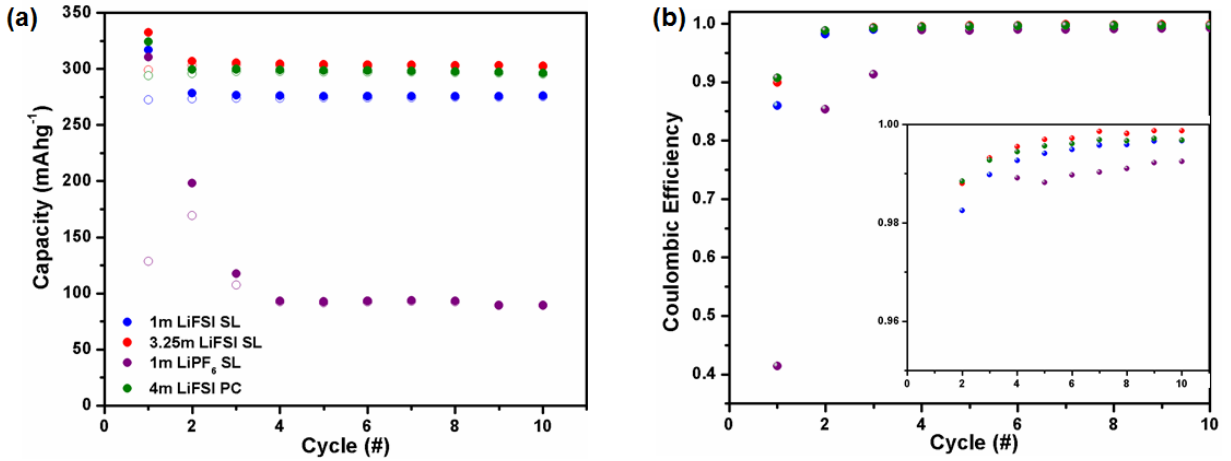

Figure 7.3. Galvanostatic cycling of MCMB half cells (a) and coulombic efficiency (b) comparison for propylene carbonate and sulfolane electrolytes.

Conversely, 1m LiFSI-PC exhibits severe graphitic exfoliation due to sustained electrolyte decomposition (Figure 7.4b). Interestingly, increasing the salt concentration to 4m LiFSI in PC stabilizes the graphite anode with a new interphasial chemistry, and achieves an initial CE of 90.7% (Figure 7.4b). This is consistent with the work reported by Nie et al,[221,222] and this performance improvement is attributed to the participation of the salt anion in the interphasial chemistry. Thus, graphite exfoliation is avoided in the LiFSI-SL system, regardless of salt concentration, while the PC system only operates reversibly at high salt concentrations. To further detail the effect of salt anion versus that of solvent, SL and PC electrolytes with 1m $LiPF_6$ were tested under identical conditions. Consistent with the literature,[223] the PC electrolyte decomposes and exfoliates graphite, while SL-$LiPF_6$ system reversibly cycles half of the graphite capacity, suggesting intrinsic differences in the behavior/properties of these two solvents, and more specifically the resulting Li^+-solvation structures.

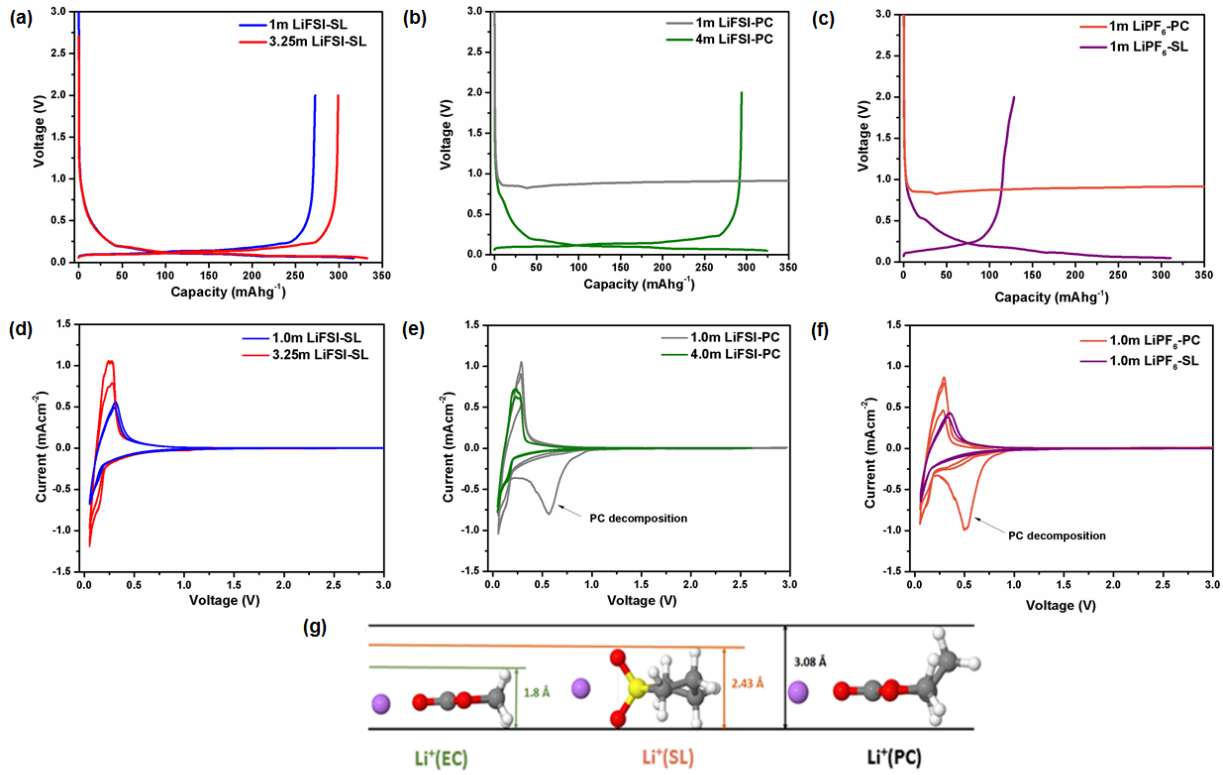

Figure 7.4. Galvanostatic cycling (a-c) and cyclic voltammetry (d-f) of MCMB graphite half cells at (a, d) 1.0m and 3.25m LiFSI SL, (b, e) 1.0m and 4.0m LiFSI PC, and (c, f) 1.0m $LiPF_6$ PC and 1.0m $LiPF_6$ SL. (g) Li-EC, Li-SL, and Li-PC co- intercalant structures with relative dimensions.

While the precise mechanism of graphite exfoliation is still unsettled, the generally established cause is the excess strain generated by co-intercalation of the electrolyte solvent with Li^+ before an SEI is completely formed to enable Li^+ desolvation.[224–226] Logically, larger co-intercalates generate greater strain and more extensive exfoliation, leading to significant performance deterioration. This trend is supported by Figure 7.4g, which compares the dimensions of EC-Li, SL-Li, and PC-Li co-intercalants structures. As an intermediate in size between the EC-Li (1.8Å) and PC-Li (3.08Å), the SL-Li (2.43Å) co-intercalate likely generates less strain in the graphite compared to PC-Li, but more than EC-Li, suggesting the intermediate interphasial behavior for SL between the two solvents, as reflected by the behavior observed in

Figure 7.4f at low salt concentrations. Of course, this explanation does not adequately address the reversible behavior observed for the 4m LiFSI-PC and both LiFSI-SL systems, because the stability/instability of these intercalants against subsequent electrochemical reduction and the consequent products' adhesion to electrode surface would also determine whether the fate of a graphitic structure being either exfoliated or protected. These reduction products will ultimately define the chemistry, morphology and quality of the resulting SEI.

For the $LiPF_6$-based systems, the kinetic onset[227] for significant salt reduction and LiF generation generally occurs within the same potential range as reduction of PC and SL molecules (0.4-0.6V vs. Li/Li^+, see supporting information for more details), despite the fact that slow $LiPF_6$ salt reduction was observed[228] and predicted by QC calculations[229] to take place at higher potentials. This means Li-solvent co-intercalants have most likely entered and strained the graphitic structure before the sufficient amount of PF_6^- is reduced and can significantly contribute to SEI formation. Conversely, LiFSI reduction is energetically favorable at higher potentials, starting around 2.4 V vs. Li/Li^+ according to QC calculations (Figure 7.5), the experiments in this work (Figure 7.6), and previous studies with other solvents.[218] This will drive anion decomposition at higher potentials, potentially resulting in formation of an inorganic SEI prior to Li cointercalation and the onset of exfoliation. While this effect enables the LiFSI-SL system across all concentrations tested, higher concentrations appear to be a necessary condition for reversible operation of the LiFSI-PC system. We attribute this high concentration requirement for the PC system to two effects: 1) the highly concentrated LiFSI-PC electrolyte is expected to further reduce the solubility of reduction products[230] such as LiF, thus making an SEI denser, and 2) raising concentration increases the populations of CIPs and aggregates needed to promote FSI decomposition at higher potentials, thus reducing the fraction of co-intercalants and

minimizing graphitic strain. It is worth noting that the effect of $LiPF_6$ concentration was not further explored because of its room temperature solubility limit at 1.5 m. Notably, these findings add a significant caveat to the works by Yamada et al.[231,232], which suggest that significant concentrations of LiFSI are necessary for universalization of the graphite electrode reaction in solvents other than EC, including sulfones.

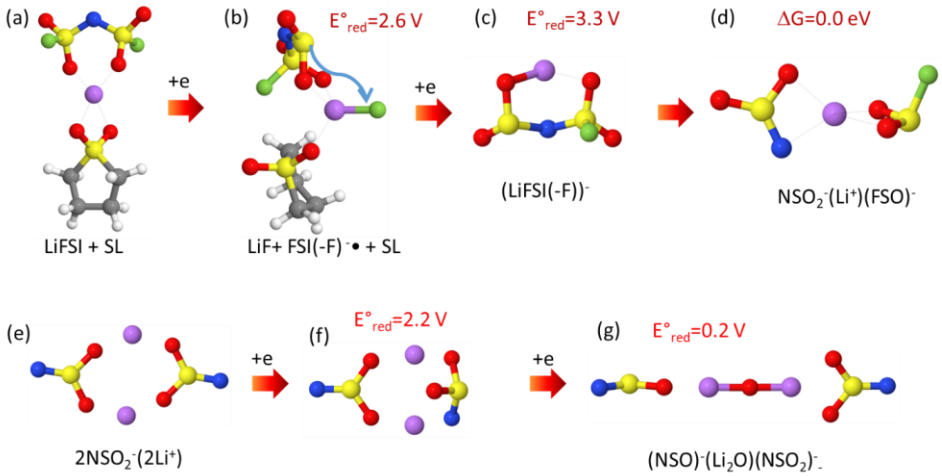

Figure 7.5. Reduction pathway and associated stepwise energetics from G4MP2 QC calculations for the formation of Li_2O from LiFSI and SL using SMD(SL) implicit solvent model for (a-b) and previous results[8] (c-g) using SMD(ether) model.

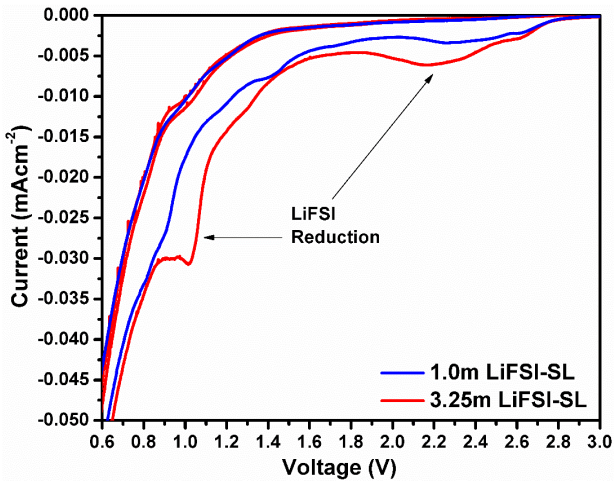

Figure 7.6. Magnified CV of Figure 7.4d which shows the decomposition peaks of LiFSI.

Electrochemical impedance spectroscopy (EIS) was conducted on Li-MCMB graphite half-cells containing these electrolyte systems (Figure 7.7, Table 7.1 and 7.2). The measurements took place in the same cell to not disturb the natural cycling environment. Impedance spectroscopy produces a Nyquist plot which reveals real part of the measured impendence versus its imaginary component over a range of AC frequencies. A circuit was modeled after the reactions that occur during electrochemical cycling, to properly quantitatively analyze the data. The model accounts for the uncompensated Ohmic resistance of electrolyte (R_{Ω}), the double layer capacitance of the electrode/electrolyte interface (CPE_{sf}), resistance due to the surface reactions on the electrode (R_f), the double-layer capacitance (CPE_{dl}), the charge transfer resistance (R_{ct}), and the impedance due to solid state diffusion processes, known as the Warburg impedance (Z_w). After the first lithiation (Table 7.1), a lower internal cell resistance was obtained for SL electrolytes as compared to the cells cycled in 4 m LiFSI-PC. The stark difference in these cells arises after the first delithiation (Table 7.2), during which cells with SL maintain a low charge transfer resistance (R_{CT}) (4.25Ω for 1m LiFSI and 13.55Ω for 3.25 m LiFSI), as compared 123.7Ω for 4m LiFSI-PC. The very minor dependence of R_{CT} on concentration and lithiation state for the LIFSI-SL electrolytes supports the presence of an efficiently formed, stable and ionically conductive SEI which enables the reversible lithium intercalation/de-intercalation observed experimentally.

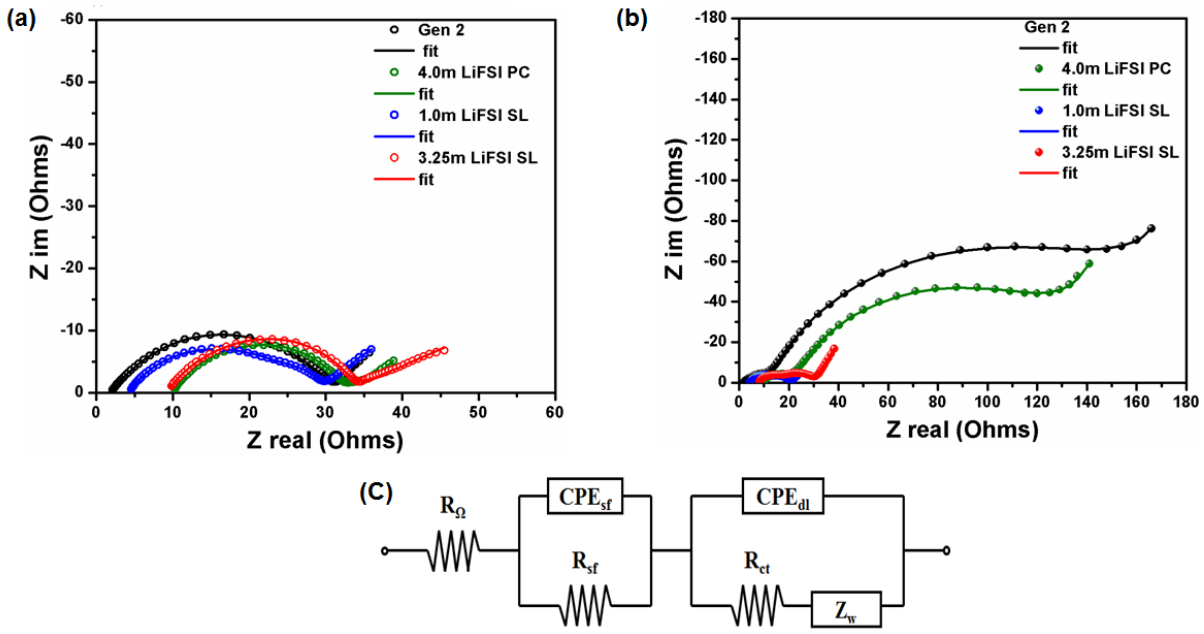

Figure 7.7. Electrochemical impedance spectroscopy measurements of cycled MCMB graphite half cells at the (a) lithiated and (b) delithiated state of charge. (c) Corresponding equivalent circuit used to fit the Nyquist plot.

Table 7.1. Impedance values after the lithiated state.

Symbol	**Gen II**	**4.0m LiFSI PC**	**1.0m LiFSI SL**	**3.25m LiFSI SL**
R_Ω	1.804	9.991	4.275	9.382
R_{sf}	19.77	12.19	21.78	8.619
R_{ct}	9.766	8.935	3.202	14.43
Chi value	3.63×10^{-5}	1.44×10^{-5}	4.49×10^{-5}	9.73×10^{-5}

Table 7.2. Impedance values after the delithiated state.

Symbol	Gen II	4.0 m LiFSI PC	1.0 m LiFSI SL	3.25m LiFSI SL
R_{Ω}	1.768	9.47	4.147	7.86
R_{sf}	12.09	13.04	11.16	9.515
R_{ct}	167.9	123.7	4.257	13.44
Chi value	1.47×10^{-4}	4.84×10^{-5}	7.20×10^{-5}	1.06×10^{-5}

7.3.2.2. SEI Investigation

MCMB graphite electrodes were galvanostatically cycled to the fifth lithiated state in order to ensure that a stable SEI had formed, and the electrodes were subsequently extracted from the cells and analyzed with XPS. Rigorous protocols were followed in order to prevent air exposure as described in the experimental section.

Although SL has been considered as a potential solvent platform for high voltage systems, to our knowledge there has been no experimental effort to determine its decomposition products on the negative electrode. Figure 7.8a shows the normalized O1s spectra for the electrodes cycled in SL- and PC-based electrolytes at both low and high salt concentrations. Both LiFSI-SL electrolytes show a large peak at 532.2 eV, which is associated to the S-O bond potentially resulting from either SL or FSI^- decomposition. Furthermore, these electrodes also share a common peak at 528.38 eV corresponding to lithium oxide (Li_2O).[74,120,233–235,184] For 1.0m LiFSI-PC, the typical decomposition products of carbonates are found at 531.7 eV (C-O),

532.4 eV (O-C=O), and 533.1 eV (CO_3) (Figure 7.7c and f), but there is no Li_2O peak. At 4.0m concentration, however, it does exist, revealing the concentration-dependence of Li_2O-formation. To determine its origin (anion (FSI^-) or solvent (SL)), graphite half cells were cycled with two reference electrolytes 1.2m LiFSI-EC:EMC (3/7 v/v) to test the anion-dependent surface chemistry independent of SL, and 1.0m $LiPF_6$-SL to test the solvent-based surface chemistry independent of the FSI^- anion. The cell with the LiFSI-carbonate electrolyte displayed signatures of Li_2O in the SEI (Figure 7.8), while the SL containing $LiPF_6$ did not, indicating Li_2O-formation originates from LiFSI decomposition. QC calculations also show an energetically favorable pathway to Li_2O formation as a result of LiFSI reduction (Figure 7.5) and previous work.[236–238] The identification of Li_2O in the SEI formed by LiFSI systems cannot be found in any published literature as of today. Nie et al. studied the role of LiFSI on the SEI formation using EC, but did not report any Li_2O on the graphite surface.[131] Philippe and coworkers showed that when LiFSI was used to cycle a silicon anode, the presence of Li_2O resulted from the reaction between Li^+ and SiO_2, instead of salt decomposition.[148] Though experimentally researchers have not directly observed Li_2O from LiFSI decomposition, we confirmed that Li_2O is a decomposition product of LiFSI and may be a critical component responsible for the many merits of LiFSI-based electrolytes reported so far.

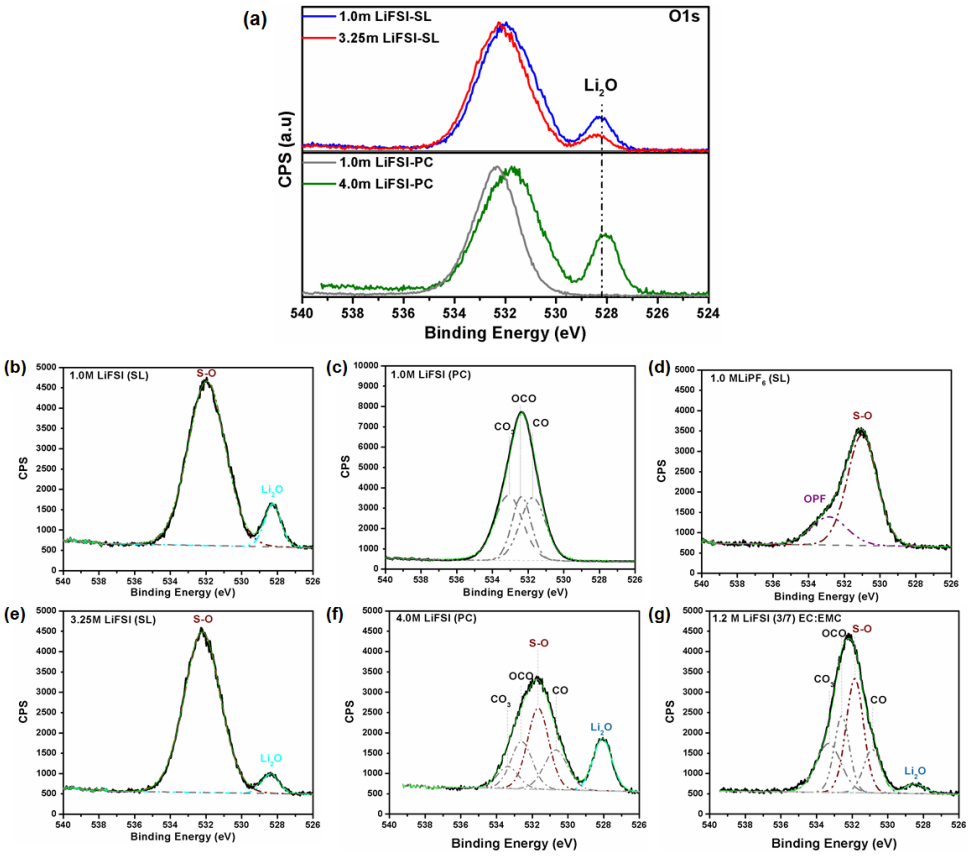

Figure 7.8. Normalized oxygen comparison between LiFSI-SL and LiFSI-PC. (b-g) XPS oxygen 1s spectra of various electrolytes.

The F 1s spectra were normalized by using the electrode's PVDF binder as reference to quantify F-containing SEI decomposition products. The large peak at 685 eV corresponds to LiF due to the LiFSI reduction—seen in both SL and PC electrolytes (Figure 7.9). This is expected since both computational and empirical measurements propose rapid defluorination of LiFSI to form LiF under reducing conditions.[166,239,240] The relative concentration of LiF and PVDF is vastly different for each electrolyte solvent and concentration. For electrodes cycled in both low and high concentration LiFSI-SL electrolytes, the percent concentration of LiF to PVDF were ~96.60 % and 3.40%, respectively. Conversely, the electrode cycled with 1.0m LiFSI-PC has 86.71%

LiF and 13.29% PVDF. This ratio increases only slightly in the case of high concentration (4.0m LiFSI-PC, LiF: 91.84%, PVDF: 8.16%). The detailed fits are shown in the Supporting Information without count normalization. These results indicate that LiFSI-SL electrolytes lead to an SEI strongly based on the FSI^- anion, with a significant presence of inorganic species including Li_2O and LiF, while PC-electrolytes, especially at low concentration, still consist of a significant portion of solvent reduction products.

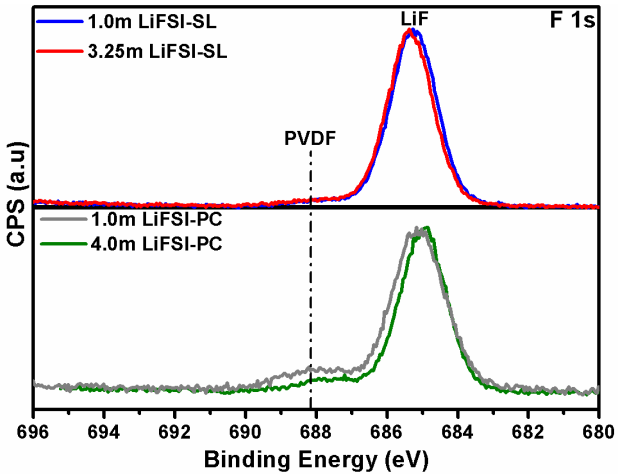

Figure 7.9. Normalized fluorine 1s comparison between LiFSI-SL and LiFSI-PC.

We propose that SEI formation is initiated at high voltages (> 2 V vs. Li/Li^+) as a result of LiFSI reduction, leading to LiF and eventually Li_2O formation that constitute the initial SEI products.[236–238] SL reduction occurs at the later stages of the formation cycle at ~0.5 V, contributing to the SO_2-rich SEI that is consistent with QC results (Figure 7.5). As expected, the SEI surface chemistry appears to be a key factor in improving the electrochemical window and cycling stability as compared to the PC electrolytes.

7.3.3. Oxidative Stability and 4.85V $LiNi_{0.5}Mn_{1.5}O_4$/MCMB Graphite Full Cell Performance

The oxidative stability of SL has been examined previously with both experimental measurements and theoretical calculations,[241–243] which collectively suggest a decomposition threshold at or above 5.0V vs. Li. While the instability of the anion in an electrolyte can significantly suppress the anodic stability of the entire electrolyte,[229] Wang et al. recently demonstrated that LiFSI can also be successfully applied to high voltage systems (4.6V LNMO).[167] The linear sweep voltammograms conducted with a three electrode cell (platinum: working electrode, Li metal: counter and reference electrode) (Figure 7.10) support these previous reports, as both 1.0m and 3.25m LiFSI-SL electrolytes show decomposition current densities below 0.02 mA cm^{-2} beyond 5V as compared to the 1.2m $LiPF_6$ (EC/EMC 3:7, Gen II) baseline, which approaches this threshold at platinum electrode potentials as low as 4.4V vs. Li/Li^+.

QC calculations predicted the oxidation stability of the SL(FSI^-) complexes, surrounded by implicit solvent with SL parameters, to be 4.65 V vs. Li/Li^+ (Figure 7.10(a and b)) as a result of H-transfer during oxidation from SL to nitrogen of FSI. This oxidation process is attributed to the initial small peak observed in the LSV around 4.5 V (Figure 7.10e). The importance of accounting for the H-transfer during oxidation by cathode surfaces has been previously highlighted for the carbonates and ether/FSI complexes[243,244] but does not agree with previous suggestions by Wang et al.[167], which advise that H-transfer does not occur in the SL-based electrolytes. In the concentrated regime when all SL molecules are coordinated by Li^+, QC calculations predict that the oxidation potential for the LiFSI-SL complexes significantly increases from 4.6 V to 5.5 V (Figure 7.10(c and d).

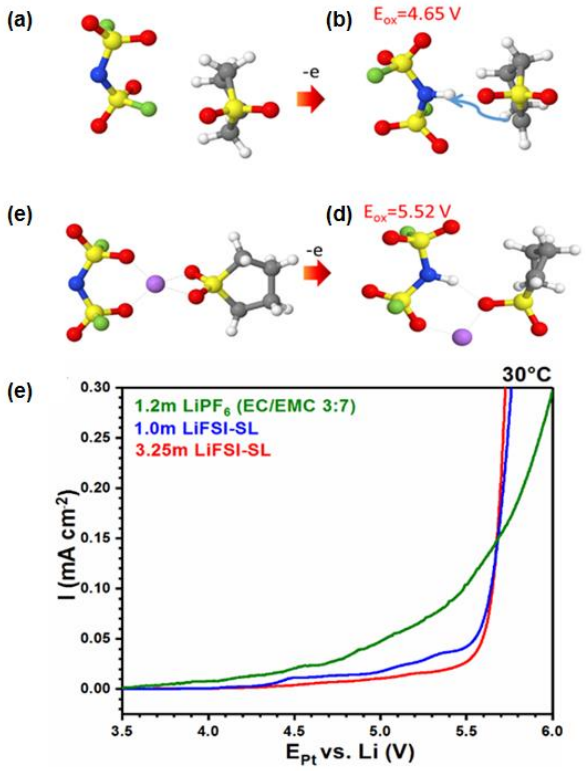

Figure 7.10. Oxidation potential (E_{ox}) (vs. Li/Li^+) from G4MP2 QC calculations with clusters surrounded by SMD(SL) implicit solvent model (a-d) and linear sweep voltammetry experimental results of LIFSI-SL and Gen II electrolytes (e).

LNMO presents an operating voltage that exceeds the anodic stability of most carbonate-based electrolytes. To rigorously confirm the high voltage stability of LiFSI-SL electrolytes observed in the anodic linear sweep voltammetry measurements, full Li-ion cells constructed with LNMO-MCMB configuration were assembled and tested. Galvanostatic cycling at room temperature (Figure 7.11a) indicate that the baseline electrolyte (Gen II) suffers a severe decline in capacity starting around 150 cycles, while the high concentration LiFSI-SL system exhibits relatively stable capacity retention for more than 250 cycles. These results are further illustrated by the voltage profiles of select cycles (Figure 7.11c,d). The advantage in stability of the 3.25m LiFSI-SL system is even more pronounced at elevated temperatures (Figure 7.11b). At 55°C, Gen II becomes even more unstable, yielding only a single cycle with little discharge capacity,

while the SL system maintains more than 50% of its original discharge capacity after more than 90 cycles under the harsh condition of high voltage and temperature conditions. This is a significant realization for an additive-free electrolyte comprised of a single solvent and a single salt, suggesting that this system is a strong platform for optimization via future additive/co-solvent studies.

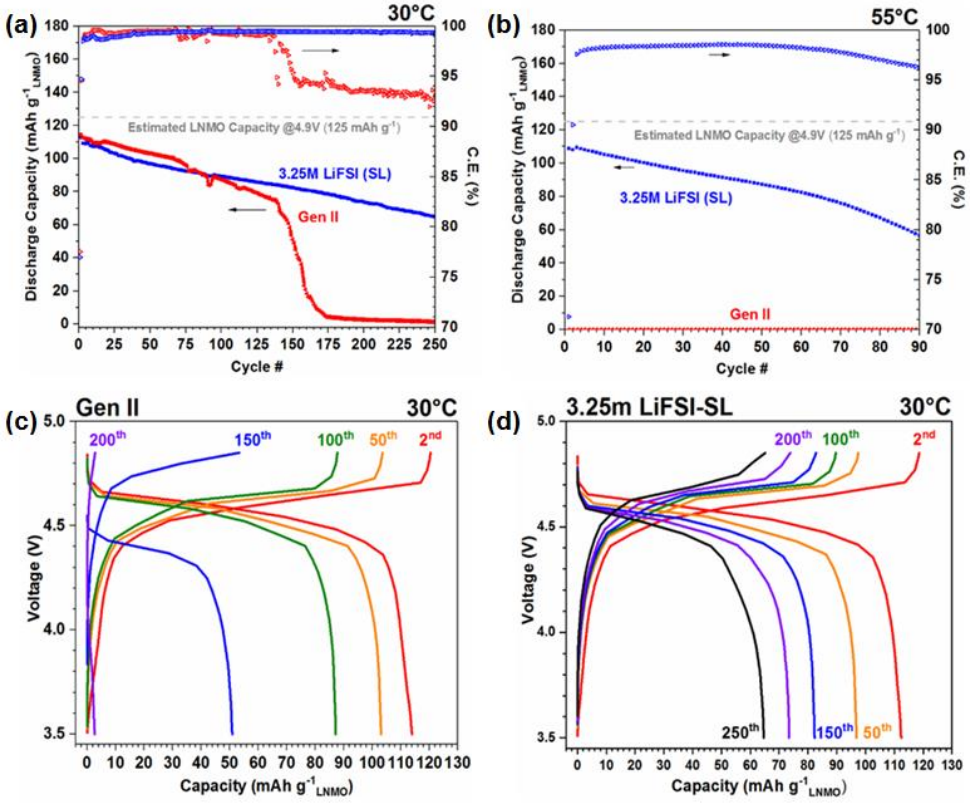

Figure 7.11. Galvanostatic cycling capacity for Gen II and 3.25m LiFSI-SL at 30°C (a), 55°C (b). Selected voltage profiles for each electrolyte at 30°C (from a) are shown in c and d, respectively.

The safety of the system was preliminarily evaluated by differential scanning calorimetry (DSC) using cathode and anode electrode fragments recovered from cycled LNMO-MCMB full cells in presence with a small volume of the as-prepared Gen II or 3.25m LiFSI-SL electrolyte (Figure 7.12). The low thermal stability of Gen II electrolyte was clearly indicated by the early

cell rupture at low temperature when charged LMNO reacts with the carbonate. Conversely, the SL electrolyte mixture with the charged cathode exhibits no major thermal event until the cell was stopped around 225°C during an exothermic process, suggesting the electrolyte is stable at high temperatures even in the presence of the typically highly reactive charged cathode surfaces. This is in part due to the high thermal inertness of both salt (LiFSI) and solvent (SL), as compared to the thermally sensitive $LiPF_6$ and carbonate solvents.[20].

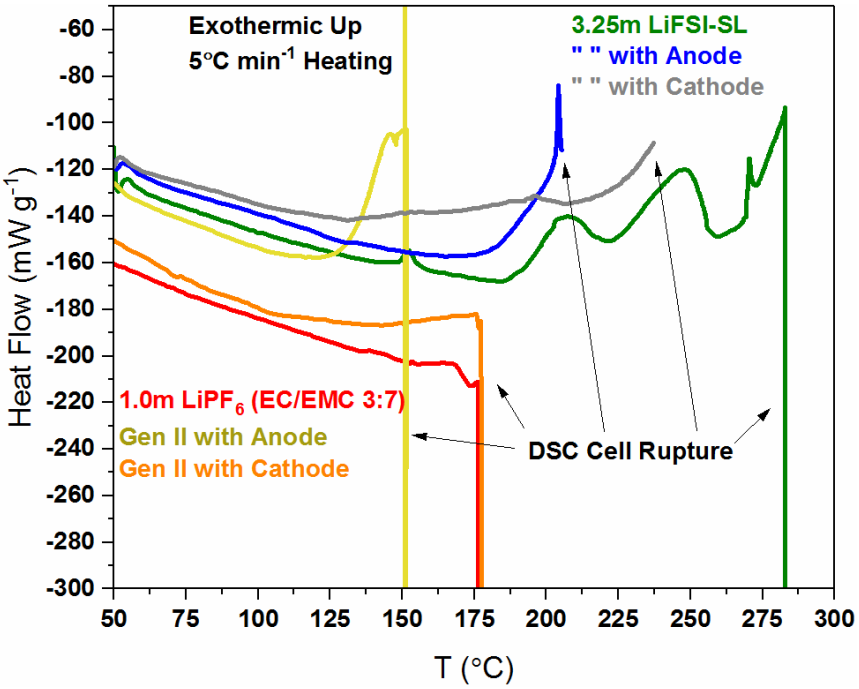

Figure 7.12. DSC plots of 3.25m LiFSI-SL and Gen II electrolytes with anode and cathode cell fragments in the charged state.

7.4. Conclusion

In this work we have introduced an electrolyte system that offers a promising new pathway toward enabling high voltage Li-ion batteries. With graphite, despite the absence of conventional carbonates, formulations of LiFSI in SL exhibit highly reversible intercalation behavior across all concentrations tested, despite a previous lack of success with SL-based

electrolytes. We attribute this behavior to the formation of an SEI strongly based on the unique FSI^- anion chemistry and the early onset of the LiFSI reduction that results in a favorable passivation layer formation that strips solvent from its solvation shell upon entering graphite. Full cell testing of this system indicates excellent high voltage and high temperature stability for a two component system, opening the door to future co-solvent and additive studies for further optimization. Excellent compatibility of the concentrated LiFSI-SL electrolyte with the high voltage spinel electrode is attributed to high oxidation potential of SL complexed with Li and polymerization of SL with low gas-generation for SL molecules not complexed by Li. These results suggest that the LiFSI-SL system is a safe, simple starting point for exploring promising successors to conventional Li-ion battery electrolytes.

Chapter 7, in full, is currently being prepared for submission for publication "Solvent-Salt Synergy Offers Fresh Pathway to Unlock Next Generation Li-ion Chemistries" Alvarado, J; Schroder, M; Borodin, O; Gobrogge, E; Olguin, M; Ding, M; Meng, Y.S.; Xu, K. The dissertation author was the co-primary investigator and author of this paper. All of the experiment parts were performed by the author except for the full cell electrochemistry data, FTIR experiments, conductivity measurements, and computational analysis. The experimental design and electrolyte formulations were generated from Marshall Schroder and the author.

Chapter 8. Improvement of the Cathode Electrolyte Interphase on P2-$Na_{2/3}Ni_{1/3}Mn_{2/3}O_2$ by Atomic Layer Deposition

8.1. Introduction

The commercialization of the rechargeable lithium ion battery (LIB) in the early 1990s[4] by Sony propelled the development of portable electronics. Technologies that once seemed impossible are now ingrained in modern society and have become a part of everyday life. This is largely due to the components within the battery that allow lithium ions to intercalate/deintercalate between the carbon anode and transition metal oxide cathode through the electrolyte, making it a high gravimetric energy density system.[245–247] As consumers become more aware of the global climate change, the applications for LIBs are extended to power hybrid and plugin electric vehicles,[5] however, using LIBs as a ubiquitous energy storage and conversion system could increase the demand for lithium, causing exorbitant prices of Li resources.[3] Therefore, researchers have focused their efforts on finding alternative systems that could replace LIBs in specific applications. Sodium ion batteries (NIBs) research was first investigated in the mid 1970s, where the sodium analog to lithium transition metal oxides were first reported.[248,249] In the recent decade, NIB research has significantly increased given the above-mentioned concerns with LIBs. NIBs offer several advantages over its lithium counterpart, given that the demand for sodium is much lower than lithium and it is more abundant.[250] Overall, the cost of manufacturing NIBs can be lower than that for LIBs[3],which can be attributed to the ability to use aluminum as the current collector for both the anode and cathode—eliminating the use of Cu, a heavier and more expensive material.[251] Though NIBs will unlikely reach the energy density of LIBs because of sodium's increased atomic mass and reduced electrochemical potential of 2.71V (Li=3.01V), it could be an alternative for large grid storage applications where cost plays a more significant role.[252,253]

Within the last decade several advancements have been made on the anode for NIBs where hard carbon, sodium titanate, tin oxide, and tin sulfide (few of several anode chemistries) have been extensively studied.[254–257] Given that in a full cell the cathode has higher mass fraction than the anode and operates at a higher potential–increasing the capacity in NIBs requires more exploration on high voltage cathode materials.[258] Layered transition metal cathode materials (Na_xTMO_2) are of particular interest because of their high operating voltage, specific capacity, and synthesis yield.[253,258,259] This class of cathode materials can be classified by their crystal structure stacking: P2, O2, P3, and O3.[260] The first letters "P" and "O" correspond to where the alkali metal lies within the crystal structure–either in the prismatic or octahedral site. The number is related to the number of repeating Na layers within the unit cell. Of these classes of materials, P2- $Na_{2/3}Ni_{1/3}Mn_{2/3}O_2$ has been extensively studied due to its high specific capacity (173 mAh/g) and high operating voltage (up to 4.5V). Lu et al. demonstrated that Na-ions can reversibly intercalate and deintercalate using *in-situ* X-ray diffraction (XRD), albeit, undergoing detrimental phase transformation concurrently.[261] Lee and Xu et al. determined via synchrotron XRD and first principles calculations that the long voltage plateau above 4.22V corresponds to a O2 phase transformation.[262] While the material has a Na content of 1/3 to 2/3, P2 phase is the lowest energy state but when the Na content falls to zero then O2 phase becomes the lowest, causing poor capacity retention[262,263] However, this can be combated by lowering the operating voltage from 4.5 to 4.1V, eliminating the phase transformation and increasing the rate capability (Capacity at 1C = 85% Capacity at C/20). This is not a perfect solution because it sacrifices a large amount of energy by lowering the specific capacity from 174 to 90 mAh/g. Researchers have used doping (Li, Mg, and Zn) to maintain the high operating voltage and capacity, while reducing and or eliminating the phase transformation.[264–267] However, the cathode operating

potential may also cause the electrolyte to decompose forming the cathode electrolyte interphase (CEI) which may also participate in the capacity degradation. Despite that doping improves the cycling stability of P2- $Na_{2/3}Ni_{1/3}Mn_{2/3}O_2$ class of materials, researchers have failed to address the carbonate based electrolyte instability above 4.2 V.[59]

Forming a protective layer that allows Na-ions to diffuse through the layer and reduce the electrolyte decomposition is one possible way to improve the electrolyte-electrode interface. Atomic layer deposition (ALD) is used in a variety of applications as a coating technique, in particular for battery electrodes. Several advantages in using ALD are: 1) conformal coating, it has the ability to coat various irregular materials, 2) controllable coating thickness down to angstroms or monolayers, and 3) apply to a wide range of coating materials (Al_2O_3, TiO_2, ZnO, HfO_2).[268] For this reason, ALD has largely been adopted for coating LIB electrodes and shown to improve cycling performance.[269–275] Considering the success on LIBs, researchers have adopted ALD coating for NIB anode materials. Zhao and coworkers have shown improved cycling performance of disodium terephthalate by Al_2O_3 ALD coating.[276] Recently, Han et al used ALD to coat Al_2O_3 on tin nanoparticles to elevate volume expansion in the anode.[277] Few reports have reported the use of ALD coatings as cathode materials for NIBs.[278] Liu et al demonstrated the effect of wet chemical Al_2O_3 coating on P2-$Na_{2/3}Ni_{1/3}Mn_{2/3}O_2$ cathode for NIBs.[279] The issues with wet chemistry coating are that it is not able to control the coating thickness, it is difficult to have a conformal coating, and it can introduce contamination during the process. Although there is an improvement in capacity retention with this method, it is challenging to determine what percentage it played in improving the cycling performance when the electrode was only cycled to 4.3V, which partially avoids the phase transformation (full phase transformation occurs at 4.5V). Moreover, both coating works mainly focused on the electrochemistry to showcase the effect of

ALD and wet chemical coating of Al_2O_3 on P2-cathode materials. Understanding the ALD coatings for P2-cathode materials for NIBs is still in its infancy; there is a need to understand how ALD coatings improve the cycling performance by investigating the electrode-electrolyte interface. Since NIB chemistry behaves differently than LIB chemistry, it is likely that the cathode electrolyte interphase can be composed of different components.

Herein, we compare uncoated P2-$Na_{2/3}Ni_{1/3}Mn_{2/3}O_2$ (NaNiMnO) composite electrode to an ultra-thin Al_2O_3 ALD coated electrode. Rigorous electrochemical characterization demonstrates the positive effect of ALD coating on the composite electrode. For the first time, X-ray photoelectron spectroscopy is used to elucidate to the factors that influence the chemical composition of the cathode electrolyte interphase (CEI) which enhances the coulombic efficiency and cycling performance (from 2-4.5V), by decreasing the impedance of the cycled P2-NaNiMnO cathode with ALD coating.

8.2. Experimental

8.2.1. Materials Preparation

The $Na_{2/3}Ni_{1/3}Mn_{2/3}O_2$ material was synthesized by co-precipitation method following our previous published work.[262] A stoichiometric amount of the precursors, $Mn(NO_3)_2 \cdot 4H_2O$ and $Ni(NO_3)_2 \cdot 6H_2O$, were dissolved in deionized water. The transition metal nitrate solutions were titrated into a stoichiometric NaOH solution using a peristaltic pump at rate of 10 ml/hr. The solution was stirred slowly to insure homogeneity. The co-precipitated solid $M(OH)_2$ was centrifuged and washed with deionized water (three times). The co-precipitated material was dried in the oven to remove excess water and was ground with a stoichiometric amount of Na_2CO_3. The material was precalinated at 500°C for 5 h and calcinated in a pellet form at 900 °C for 14 h in a 50 ml porcelain crucible. Electrodes were made by a slurry containing 80 wt% of

active material (based on the total mass of the P2-$Na_{2/3}Ni_{1/3}Mn_{2/3}O_2$ composite), 10 wt% of polyvinylidene fluoride (PVDF), and 10 wt% acetylene carbon black in n-methyl-2-pyrrolidone. The slurry was casted on aluminum foil and dried in a vacuum oven at 80 °C.

8.2.2. Aluminum Oxide Atomic Layer Deposition (ALD)

The electrode casted on aluminum foil was coated with aluminum oxide (Al_2O_3) using atomic layer deposition (Beneq TFS200). The deposition of Al_2O_3 required the use of trimethylaluminum (TMA) as precursor and water as reactor. The carrier gas was nitrogen in 300 mbar and the reaction temperature was 150 °C. The deposition rate was 1.1A per cycle. The coating thickness on the electrodes was controlled through the number of cycles performed.

8.2.3. Electrochemical Test

The uncoated and ALD coated P2-$Na_{2/3}Ni_{1/3}Mn_{2/3}O_2$ electrodes were assembled in 2032 coin cells using a glass fiber GF/F (Whatman) filter separator soaked in 1 M $NaPF_6$ in propylene carbonate electrolyte (PC). Battery assembly was carried out in an MBraun glovebox (H_2O < 0.1ppm). Galvanostatic discharge and charge at various current densities were performed using an Arbin BT2000 battery cycler. Additionally, electrochemical impedance spectroscopy (EIS) measurements were carried out with 10 mV perturbation and the AC frequencies from 0.01 to$1x10^6$ Hz on galvanostatic cycled electrodes at OCV, first cycle and 100 cycles. The electrodes were assembled in a three electrode Swagelok ® cell, where the active material was the working electrode and Na metal served as the counter and working electrode. The three electrode cells were then cycled using above mentioned conditions. This allows for proper isolation of working electrode impedance. A Solatron 1287 Potentiostat was used to measure the impedance at different states of charge and discharge. After the EIS measurements were taken, an equivalent

circuit model was fit to the data to analyze the reactions that took place using Z view software (v. 3.4a, Scribner Associates, Inc.).

8.2.4. Materials Characterization

The morphology of the as-synthesized material and post-electrochemical cycling was characterized by a Philips XL30 environmental scanning electron microscope (ESEM) equipped with an energy dispersive x-ray detector (EDX) operating at 10 kV. Transmission electron microscopy (TEM) images were taken with a FEI 200 kV Sphera Microscope. Samples for TEM were prepared by focused ion beam (FEI Scios DualBeam FIB/SEM), following the procedure from our previous work.[280] Samples were thinned within 100 nm. During FIB thinning process, only 5 kV voltage and 7 pA current were applied to the sample when the sample thickness is within 200 nm. This measure can minimize the beam-induced damaging within only within 10 nm.[281] A lift-out procedure with optimized FIB fabrication conditions was conducted on the coated ALD electrode and loaded on the Omni Probe grid (Ted Pella) which is needed to retain the electrochemical activity of the nanobattery. Image J was used to determine the ALD coating thickness on the entire electrode.

8.2.4.1. X-ray Photoelectron Spectroscopy (XPS)

After electrochemical cycling, the cells were disassembled in the glovebox and washed with DEC to remove excess sodium salt. XPS was performed at the Laboratory for Electron and X-ray Instrumentation using a Kratos AXIS Supra. In order to avoid air exposure, the samples were prepared in the glovebox connected to the XPS. Samples were transferred from the glove box to the XPS from an argon atmosphere to an ultra-high vacuum greater than 10^8 torr. The XPS was operated using Al anode source at 15 kV. All XPS measurements were collected with a 300 μm by 700 μm spot size without using a charge neutralizer during acquisition. Survey scans

were collected with a 1.0 eV step size followed by high-resolution scans with a step size of 0.05 eV, for carbon 1s, oxygen 1s, sodium1s, fluorine 1s, nickel 2p, manganese 2p, aluminum 2p, and phosphorus 2p regions.

Fits of the XPS spectra were performed with CasaXPS software (version 2.3.15, Casa Software Ltd.) to estimate the atomic compositions and chemical species comprising the cathode electrode interphase. All species were fit using a Shirley background. The resulting spectra were then refit and all spectra were shifted relative to the binding energy of the carbon 1s sp^3 (assigned to 284.8 eV) to compensate for any off-set during the measurement.

8.3. Results and Discussion

8.3.1. Aluminum Oxide ALD Coating Characterization

Inspired by ALD cathode coatings on LIB cathode materials, we coated classical P2-$Na_{2/3}Ni_{1/3}Mn_{2/3}O_2$ (P2-NaNiMnO) cathode with aluminum oxide (Al_2O_3) by ALD. The phase pure crystalline P2-NaNiMnO material is validated by the rietveld refinement (Figure 8.1). It is widely accepted that both binder and conductive additive contribute to the surface reactions caused by the instability of the electrolyte at high voltages.[282] To combat these issues, ALD was used to coat Al_2O_3 on the P2-NaNiMnO composite electrode surface. The deposition temperature occurred at 150°C to prevent the chemical decomposition of the PVDF binder, ensuring that a stable electrode is used. Figure 8.2 shows the SEM images of the as synthesized electrode material and the ALD coated electrode. EDS mapping was used to show that Al_2O_3 coating is uniform throughout the electrode and did not affect the electrode morphology. Since the entire electrode was coated, it is important to distinguish the amorphous ALD coating from the amorphous conductive carbon. First, a section of the electrode was cut using focused-ion beam

(FIB) to allow proper characterization of the top of the electrode. If FIB is not used and the coating thickness is characterized by scrapping the electrode and loading the material on the TEM grid for imaging, one is unable to distinguish the amorphous material, leading to improper ALD thickness characterization (Figure 8.3). Figure 8.4 shows a uniform ALD coating of 1nm on the P2-NaNiMnO particle. The higher resolution TEM image (Figure 8.4 (b)) gives a detailed view of the amorphous layer to the crystalline active material, a uniform ALD coating of 1nm on the P2-NaNiMnO particle.

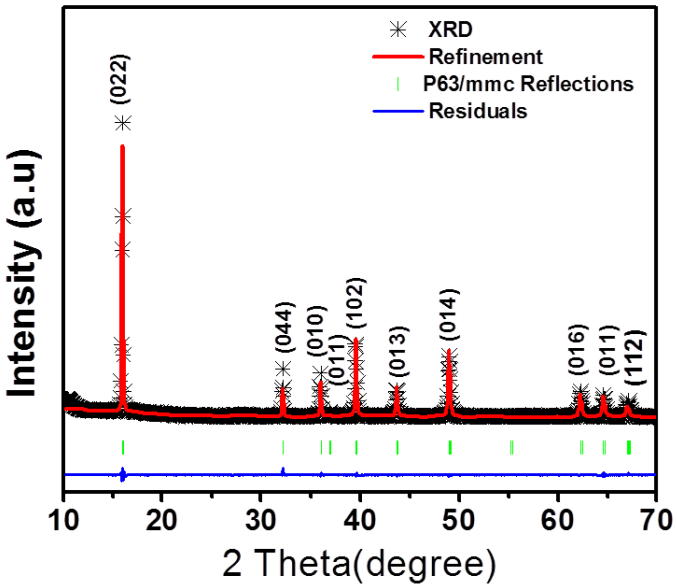

Lattice parameters: a=b=2.8878, c=11.1595 Rwp: 2.37 Rp: 6.07
Figure 8.1. XRD refinement results for the as-synthesized P2-$Na_{2/3}Ni_{1/3}Mn_{2/3}O_2$ (P2-NaNiMnO) cathode.

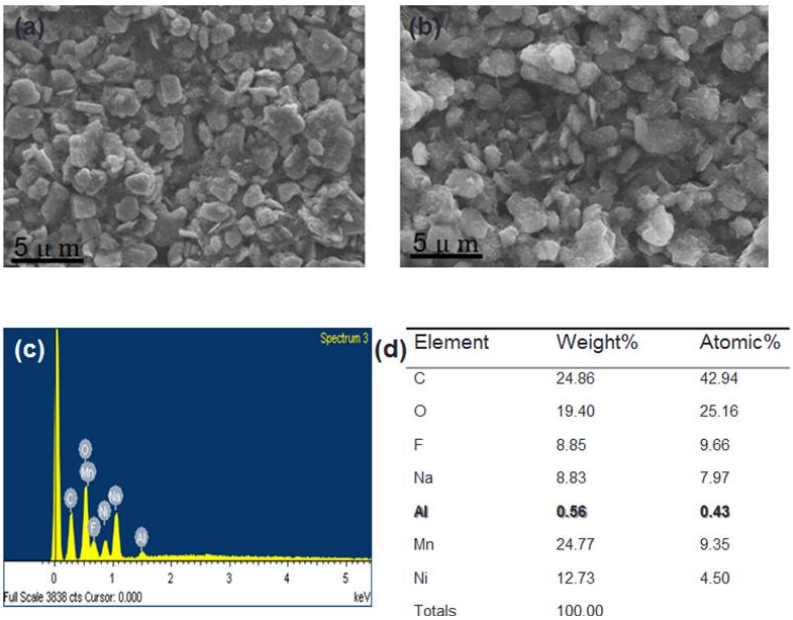

Element	Weight%	Atomic%
C	24.86	42.94
O	19.40	25.16
F	8.85	9.66
Na	8.83	7.97
Al	**0.56**	**0.43**
Mn	24.77	9.35
Ni	12.73	4.50
Totals	100.00	

Figure 8.2. (a) SEM image of ALD coated P2-NaNiMnO particle, and (b) SEM image coated P2-NaNiMnO electrode without conductive additive demonstrating the ALD coating thickness effectively. (c) (d) EDX results of the percentage of different elements.

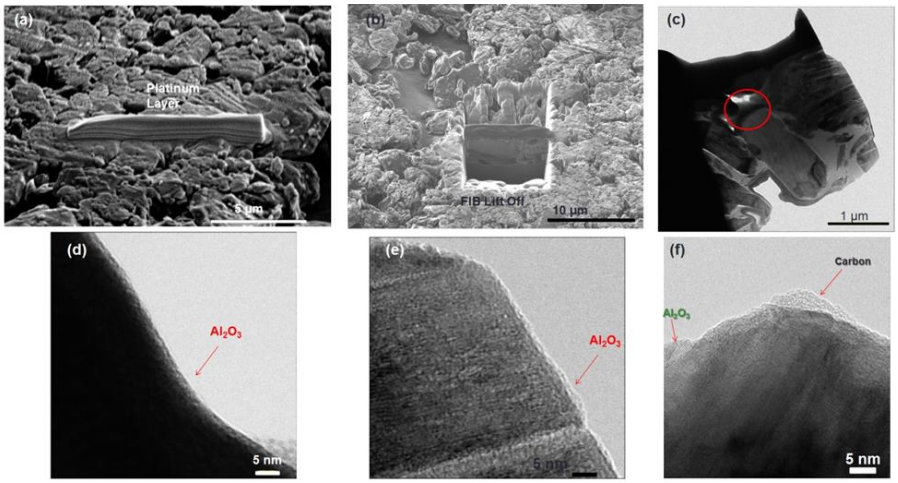

Figure 8.3. Preparation of electrode by Focused Ion Beam(FIB) (a)Platinum protecting layer deposited on P2-NaNiMnO electrode, (b) After Milling, (c) TEM picture of sample on Omni Probe, the red circle indicates where the TEM image are taken. (d) Dark field TEM image and (e) bright field TEM image of electrode. Image (f) demonstrates the TEM image without FIB preparation.

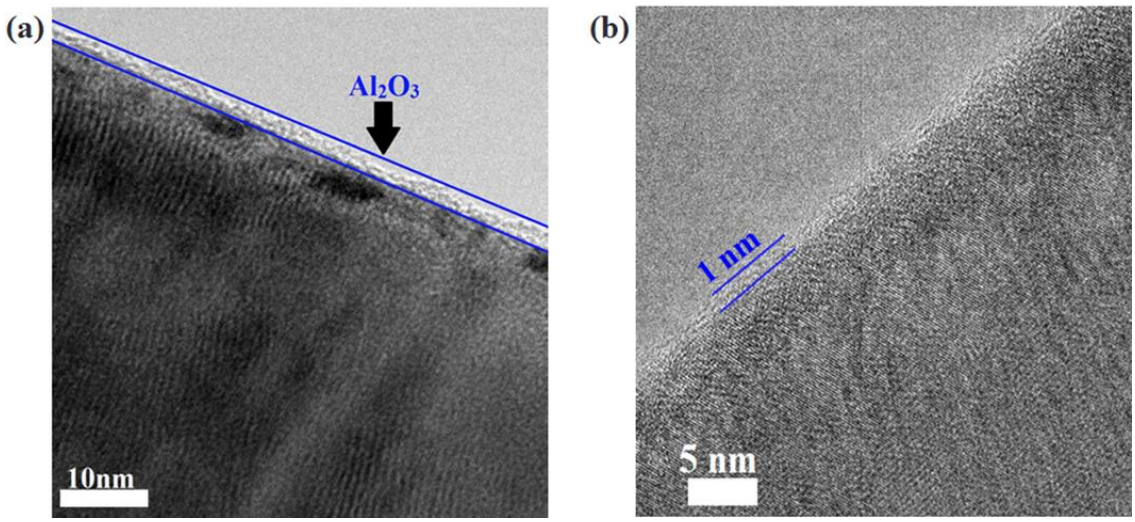

Figure 8.4. TEM images of the uncycled Al_2O_3 ALD coated $Na_{2/3}Ni_{1/3}Mn_{2/3}O_2$ composite electrode. (a) Low magnification image of coated pristine particle and (b) high magnification image determining the coating thickness of approximately 1 nm.

8.3.2. Galvanostatic Cycling Comparison of Uncoated and Al_2O_3 ALD Coated P2-$Na_{2/3}Ni_{1/3}Mn_{2/3}O_2$.

The uncoated and ALD coated P2-NaNiMnO electrodes were assembled into coin cells, then cycled in galvanostatic mode at C/20 rate. Figure 8.5 (a) highlights the materials first cycle voltage profiles, demonstrating the quintessential plateaus for this material.[262,283] The Al_2O_3 coated ALD electrode (blue), however, shows slight increase in the discharge capacity of 142.6 mAh/g compared to the uncoated electrode (134.6 mAh/g). More importantly, the P2-O2 phase transformation is evident in both electrodes in the charge state, demonstrating that ALD coating does not eliminate such a structure transformation. The differential capacity versus voltage profiles (Figure 8.5 (b)) shows five distinct dQ/dV peaks that correspond to the intercalation of Na-ions. The sharp peak at 4.20V is due to the P2-O2 phase transformation associated with this class of materials.[262] This peak is less intense in the Al_2O_3 coated electrode, owing to the strong binding of the coating to the surface of the material thus slightly reducing the phase

transformation and possibly forming the CEI. The coating does not eliminate the phase transformation but may aid in maintaining the particle integrity. Furthermore, a small peak at 2.98V (Figure 8.5 (b) insert) appears in the dQ / dV plots of the Al_2O_3 coated electrode, which is not shown for the uncoated sample in this work nor in the literature, it might be possible that this could be from the Al2O3 reacting during electrochemical cycling.

After repeated cycling, the material structure degrades as a result of the severe phase transformation (Figure 8.5 (c)). The ALD coated electrode still retains more of the structure properties at the 50^{th} cycle as demonstrated by the voltage plateaus. As shown, the coated electrode has a higher capacity of 92.3 mAh/g compared to the uncoated electrode capacity of 69.7 mAh/g. Given that the material has gone under repeated phase transformation, the dQ/dV of the 50^{th} cycle depicts that the peaks are no longer as sharp as they were in the first cycle. In Figure 8.5 (d), the peak at 2.98V persists after 50 cycles. Finally, it is obvious that Al_2O_3 ALD coating reduces the overall potential in the cell throughout electrochemical cycling. This is a common occurrence in Li-ion cathode electrodes when coated with an ALD type coating.[42,284] Though bulk Al_2O_3 is insulating in nature, the ultra-thin coating and amorphous nature reduce insulating effects at lower current density, allowing the transport of Na-ions through the film, yet its effects are still observed.

The electrochemical characterization of the uncoated and ALD coated P2-NaNiMnO electrodes are provided in Figure 8.6. The theoretical capacity of uncoated P2-NaNiMnO cathode material is 173 mAh/g due to the Ni redox reaction from Ni^{2+} to Ni^{4+} corresponding to the mole ratio of the Na-ions. Given that the coating is 1nm, which attributes to less than one percent of the total material weight, therefore, the coating weight is negligible. Both electrodes were cycled at constant current from 4.5 V to 2.3 V for 100 cycles. Figure 8.6 (a) demonstrates

the capacity versus cycle plot for the ALD coated and uncoated electrodes. The ALD coated electrode improves the capacity retention of P2-NaNiMnO—after 100 cycles, the cell exhibits a capacity of 77.43 mAh/g while the uncoated electrode has a capacity of 52 mAh/g. As expected the thin Al_2O_3 coating did not bring about drastic improvement in capacity retention because of the severe phase transformation that occurs above 4.2V. However, the coating does improve the capacity retention and may aid in other aspects of the electrochemical performance. By observing the value of the x-axis of each half cycle (Figure 8.5 (a), (c)), one can estimate the storage capacity of each electrode. Ultimately, the ratio of the two capacities is known as the coulombic efficiency (CE). This is one way to quantify the irreversibility of each cycle, shown in Figure 8.6 (b). We note that the thin coating improves the CE of the active material throughout electrochemical cycling. The first cycle CE for the ALD coated electrode is 91.6% and quickly reaches 99% in the fifth cycle. Conversely, the uncoated electrode exhibits a first cycle efficiency of 83.8% and 95.2% CE by the fifth cycle. Throughout electrochemical cycling, the uncoated electrode has an unstable CE as shown in Figure 8.6 (b). The CE fluctuates significantly while the ALD coated P2-NaNiMnO electrode maintains a stable CE, demonstrated by the flat curve. Comparing our previous work with the ALD coated LIB cathodes, we present similar effects.[285–287] Wise et al. demonstrated that an ultra-thin coating of Al_2O_3 can significantly improve the electrode-electrolyte interface, reducing the decomposition of the electrolyte on high voltage cathode materials.[288] The addition of the artificial Al_2O_3 CEI coating on P2-NaNiMnO active material enhances the interface by reducing the exposure of the electrolyte to the active material. The 1 nm Al_2O_3 ALD coating may help reduce the decomposition of the electrolyte by protecting the active material, PVDF binder, and conductive

carbon from reacting with the electrolyte; therefore, improving the CE throughout electrochemical cycling.

The electrochemical rate performance test is a good way to measure the kinetic property of the material at various charge and discharge rates. Here, the material is put under various stresses implemented through incremental current increase every few cycles. Figure 8.6 (c) compares the rate capability of the uncoated P2-NaNiMnO and Al_2O_3 ALD coated electrode. The rate performance begins at C/20, increases to 1C then returns back to C/20 after a 25 cycles period. The uncoated P2-NaNiMnO electrode exhibits inferior rate capabilities when increasing the rate from C/20 to C/10 then to C/5, and finally to C/2 compared to the ALD coated electrode. The disparity capacity increases at C/2, where the coated electrode has an average specific capacity of 105.6 mAh/g compared to 78.5 mAh/g for the uncoated electrode. Thus far, the coated electrode has outperformed the uncoated P2-NaNiMnO. However, at 1C the ALD electrode retains less capacity. Comparing our work to ALD coatings on the cathode materials for LIBs, the effect of thin Al_2O_3 ALD coatings on high voltage LIB cathode materials differ significantly. In some cases, the Al_2O_3 substantially improves the rate capability by preventing transition metal dissolution and reducing electrolyte decomposition.[42,286,287,289] Conversely, there are accounts that demonstrate the Al_2O_3 coating has lower capacity than the bare electrode at higher rates.[290] These effects are not ubiquitous with one type of active material; the high voltage lithium nickel manganese oxide, for example, has poor rate capability when coated with Al_2O_3.[285] Riley et al. clearly show that at higher rates from C/4 to 1C the ALD coated electrode has a lower capacity than the bare $Li(Ni_{1/3}Mn_{1/3}\ Co_{1/3})O_2$, which is attributed to the Al_2O_3 creating a barrier for ion mobility.[291] Although it is difficult to compare Al_2O_3 ALD coating on

various cathode materials in LIB due to electrode configuration, the above-mentioned cases can be applied to NIB coated cathode materials.

There are few works that have used Al_2O_3 as a protective layer for SIB cathode materials.[278,279] Kaliyappan and coworkers investigated a series of ALD Al_2O_3 coated electrodes with discrete thicknesses on P2-$Na_{2/3}(Mn_{0.54}Ni_{0.13}Co_{0.13})O_2$ and the effects on rate performance. They determined that a thinner coating outperforms the bare cathode while a thicker coating hinders the rate capabilities due to the insulating properties of Al_2O_3.[278] Our work directly opposes the notion that a thinner coating is better, given that our ultra-thin coating has a lower capacity at higher rates. Both electrode materials have similar voltage ranges (2-4.5V) and were cycled at similar rates. However, it is commonly agreed upon that P2 cathodes suffer from severe phase transformations and that doping cobalt into the P2-NaNiMnO cathode enhances the cycling performance. Therefore, the improvement in rate capability for thin ALD coating in P2-$Na_{2/3}(Mn_{0.54}Ni_{0.13}Co_{0.13})O_2$ is not only due to the coating effect, but also the improved stability as a result of cobalt doping. Our material demonstrated the true effect of Al_2O_3 ALD coating in a traditional P2-NaNiMnO without doping. Computation techniques are widely used to help validate experimental work or understand fundamental mechanisms that occur within a battery system during electrochemical cycling. Jung et al. used ab initio molecular dynamics calculations to investigate the sodiation through Al_2O_3 and compare it to Li-ions.[292] They conclude that Na-ion diffusion occurs much faster through Al_2O_3 compared to Li-ions even though the Na-ions are much larger, albeit the study was conducted through a crystalline Al_2O_3. However, the Al_2O_3 in our case is amorphous where we see that at fast rate (1C) the Al_2O_3 coated electrode has lower rate capability than the uncoated electrode, demonstrating that the diffusivity is subpar in the Al_2O_3 film.

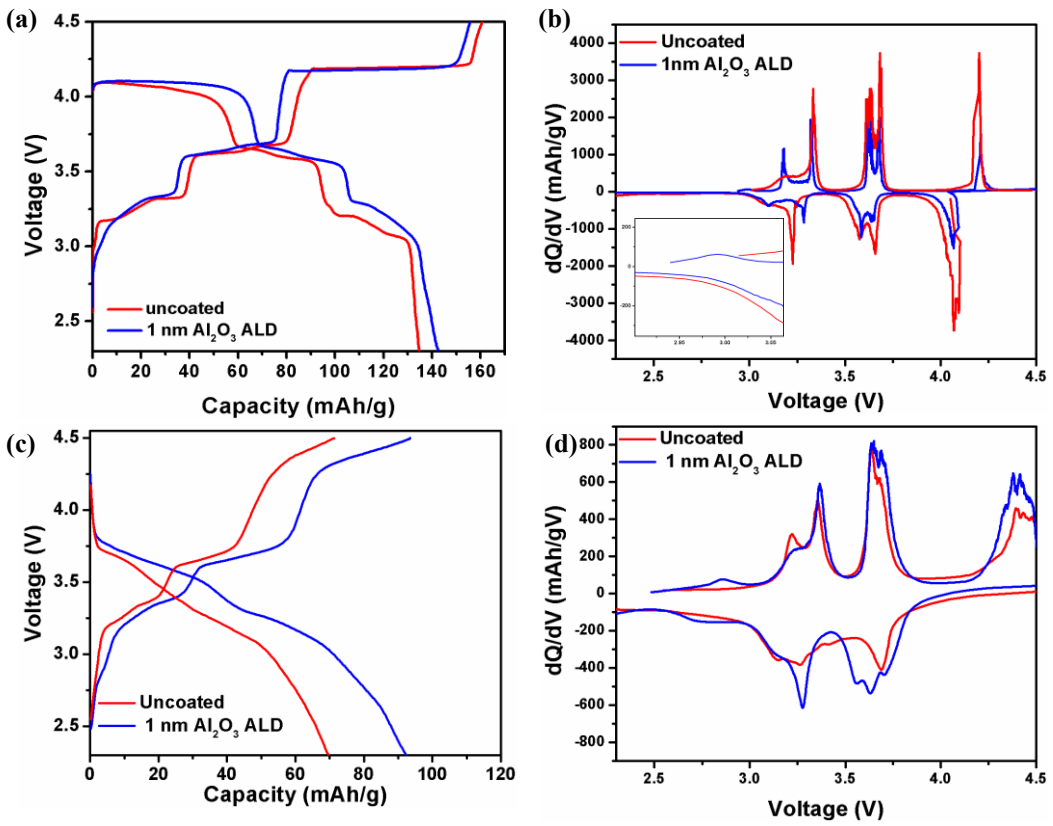

Figure 8.5. Voltage profiles and their corresponding differential voltage plots of uncoated and Al_2O_3 ALD coated electrodes at the (a, c) first cycle and (b, d) fiftieth cycle.

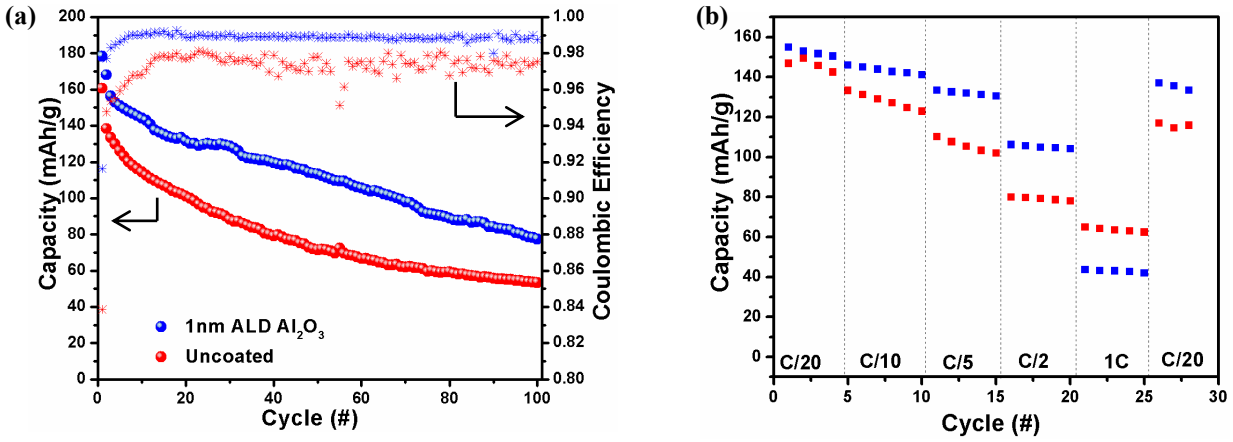

Figure 8.6. Galvanostatically cycled electrodes demonstrating (a) specific capacity versus cycle at C/20 rate and coulombic efficiency as a function of cycle number, and (b) rate capability plot for Al_2O_3 coated (blue) and uncoated (red).

8.3.3. Cathode Interfacial Resistance

Figure 8.7 shows the changes in the impedance spectra of the Al_2O_3 coated and uncoated P2-NaNiMnO electrodes cycled galvanostatically in a three electrode Swagelok® cell. Using a three electrode configuration allows us to hone in on the working electrode (P2-NaNiMnO cathode) impedance while eliminating the effects associated from the reference and working electrode (Na metal), demonstrated in Figure 8.8.[293] Previous reports failed to investigate the effect of the ALD coating on the cathode. They took into account the impedance of the sodium metal in addition to the coating which could lead to inaccurate impedance quantification.[278,279] Furthermore, there is a need to understand the effect of the Al_2O_3 coating. Figures 8.7 demonstrate the Nyquist plots for electrodes in the charged state after one cycle and 100 cycles. The Nyquist plots depicts the measured real versus imaginary impedance over a series of AC frequencies. We can quantitatively analyze the impedance spectra by a model circuit generated by several reactions that occur in the cell during electrochemical cycling (Figure 8.7 (c)). The model accounts for the ohmic resistance of the electrolyte (R_Ω), the double layer capacitance of the electrode/electrolyte interface (CPE_{sf}), resistance due to the lithium ion diffusion through the surface reactions on the cathode (R_f), the double-layer capacitance (CPE_{dl}), and the charge transfer resistance (R_{ct}).[11,42,115,285] Finally, the model accounts for the Warburg impedance (Zw) known as the impedance according to solid state diffusion of the Na-ion through the bulk of the active material.[286]

Comparing the uncoated and Al_2O_3 coated electrodes after the first cycle (cycled at C/20), both the R_{sf} and R_{ct} are significantly lower in the coated electrode (Table 8.1). After one cycle the uncoated P2-NaNiMnO has a surface film resistance of 878.8 Ω while the Al_2O_3 coated P2-NaNiMnO has an R_{sf} value of 182 Ω. The R_{ct} associated with the Na-ion diffusion through the

electrode-CEI interface is 3948 Ω for the uncoated electrode compared to 420 Ω for the coated electrode. After 100 cycles (cycled at C/20), the R_{sf} and R_{ct} increased significantly for the uncoated electrode compared to the coated electrode. The ultra-thin coating protects the surface of the electrode, reducing the effects that the binder and conductive additive have on electrolyte decomposition. Though Al_2O_3 is insulating in nature, the thin coating allows for Na-ions to diffuse through the coating film. Given that the surface film resistance increases slightly from the first cycle to the 100th cycle, the Al_2O_3 coating reduces the electrolyte decomposition at high potentials, forming a better CEI.[275,291] From Table 8.1, the charge transfer resistance increases significantly compared to the coated P2-NaNiMnO. This implies that the active material structure has degraded significantly during electrochemical cycling, as shown in Figures 8.5 and 8.6. Therefore, the ALD coating helps suppressing the structure instabilities associated with sodiation and desodiation.[270] To validate the effect of Al_2O_3 ALD coating, post cycling characterization is required.

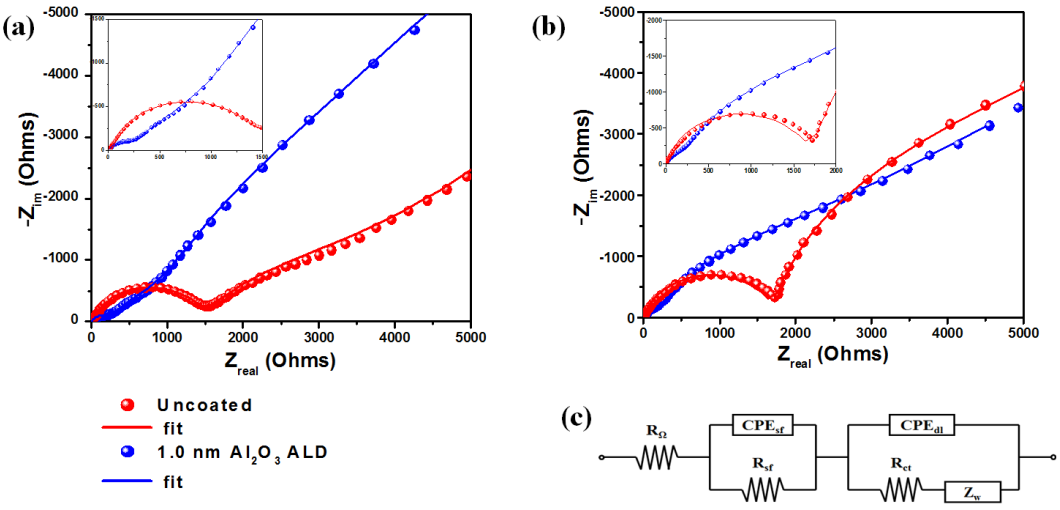

Figure 8.7. Nyquist plots of uncoated P2-NaNiMnO cycled electrodes (red) and Al_2O_3 coated cycled electrodes (blue) and uncoated (blue), at the (a) first cycle and (b) 100th cycle. The data was fit based on the circuit shown in (c).

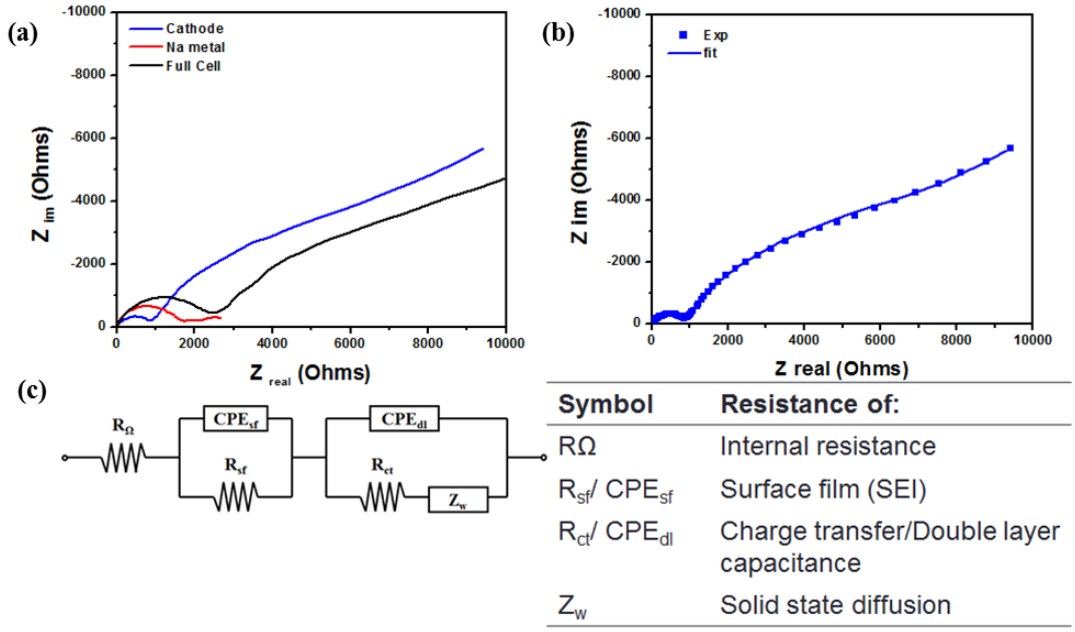

Symbol	Resistance of:
RΩ	Internal resistance
R_{Sf}/ CPE_{Sf}	Surface film (SEI)
R_{ct}/ CPE_{dl}	Charge transfer/Double layer capacitance
Z_W	Solid state diffusion

Figure 8.8. (a) EIS of the uncycled first cycle Nyquist plot of the full cell, cathode, Na metal. (b) Fitted Nyquist plot of the cathode using the equivalent circuit in (c). Equivalent circuit and table describes the symbol of the equivalent circuit.

Table 8.1. Impedance measurement values for coated and uncoated cycled electrodes.

Symbol	**Uncoated first cycle**	**100 cycles uncoated**	**1.0 nm Al_2O_3 first cycle**	**1.0 nm Al_2O_3 100 cycles**
R_Ω	3.5332	1.3676	8.701	1.414
R_{sf}	878.8	1723	182	230.5
R_{ct}	3948	5043	420	1300

8.3.4. *Ex-situ* Electrode Characterization

The above-mentioned electrochemistry has clearly demonstrated that the Al_2O_3 ALD coated electrode improves the cycling performance, CE, the surface film resistance, and charge transfer resistance. Part of the improvements can be attributed to particle stability; to examine this, SEM images were taken after 100 cycles at C/20 rate. The pristine electrode clearly shows the P2-NaNiMnO active material surrounded by acetylene black (Figure 8.9 (a)). After repeated slow cycling, the active material endures repeated sodiation and desodiation. As the Na-ions are extracted from the P2-NaNiMnO structure, the material compensates by the restructuring of the metal-oxide layer, causing the oxygen layer to glide to reduce the steric hindrance within the crystal structure.[259,262,264] Lu et al. proposed stacking faults occur as a result of the shift in oxygen-oxygen contact due to the instability of the metal oxide layer during sodium extraction.[294] Therefore, it is not surprising that the cycled uncoated P2-NaNiMnO demonstrated severe particle exfoliation. This is consistent with work done by Liu et al., where they investigated the failure mechanism of P2-NaNiMnO after 300 cycles at 1C using SEM and TEM.[279] Although this material undergoes an intercalation reaction mechanism, it can still exhibit stress and strain within the particle during electrochemical cycling. This is evident in our previous XRD study of the material, when the sodium concentration is less than 1/3, the oxygen layers are in direct contact leading to an electrostatic repulsion which directly expands the c parameter.[262] Conversely, the ALD coated electrode significantly reduces particle exfoliation after 100 cycles and only few particles showed signs of particle degradation. The notion that ALD coating can be used to maintain particle integrity has been demonstrated in alloying anodes (Si and Sn) for LIBs by holding the particle together after 300% volume expansion during repeated lithiation.[272,295,296] In their case, a thick ALD coating can improve the integrity of the

active material without forming a strong binding interaction between the coating and the active material. Since we applied an ultra-thin coating, it is speculated that the Al_2O_3 ALD coating forms Na-Al-O bonds to form a strong binding interaction that can reduce particle exfoliation. The detailed mechanism still requires more in-depth analysis. Having the ability to maintain electrode stability can be traced to the charge transfer resistance (Figure 8.7), which is the resistance associated with Na-ion diffusion through the surface of the active material through the SEI. To further understand how Na-ion kinetics is affected by ALD coating, it is needed to further investigate the effects of electrolyte decomposition on the P2-NaNiMnO particle surface both coated and uncoated.

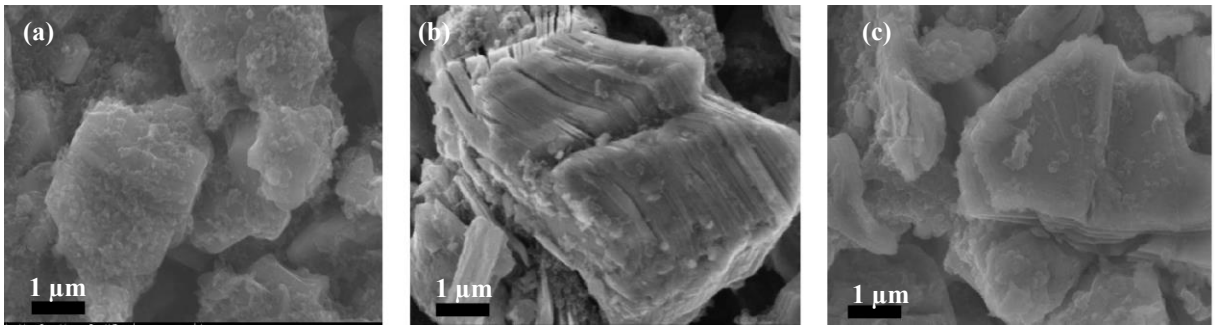

Figure 8.9. SEM images of (a) pristine uncoated and uncycled $Na_{2/3}Ni_{1/3}Mn_{2/3}O_2$ electrode, cycled electrodes after 100 cycles (b) uncoated and (c) Al_2O_3 ALD coated electrodes.

The surface of each electrode was analyzed before cycling (uncycled, not exposed to electrolyte) in addition to after the first charge to 4.1V, 4.5V, 5 cycles, and 100 cycles—avoiding air exposure as described in the experimental section. The elemental atomic percentage of the cycled electrodes is shown in Figure 8.10, where we can see the elemental evolution of the SEI throughout electrochemical cycling. Figure 8.11 demonstrates that the cycled electrodes are largely dominated by acetylene black at 284.4 eV. Before cycling, the electrodes have the signature peaks of the PVDF polymer binder at 285.5 eV (CH_2), 290.5 eV, and 292.7 eV (CF_2). Once the electrodes are cycled to 4.1V, the decomposition products of the PC electrolyte begin

to evolve, forming CO, OCO, CO_3 moieties for both uncoated and Al_2O_3 coated. After the electrodes are cycled to 4.5V, the PVDF peak corresponding to C-F_2 broadens due to the formation of sodium carbonate species. Prolonged cycling causes all peaks to shift to higher binding energy and form more CO components in the in the coated electrode, which is largely associated with ethers, esters, and oligomeric species of polyethylene oxide $(CH_2\text{-}CH_2\text{-}O)_n$ [297] from the PC electrolyte decomposition. These functionalities can also be seen in the O1s spectra (Figure 8.12). For the uncoated P2-NaNiMNO electrode, peaks indicative of lattice oxygen (529.3 eV), surface oxygen (531.2 eV), CO from the interaction between the conductive additive and active material (532 eV), and Na auger (536 eV)[298] are clearly demonstrated. In the coated electrode, the Al-O (531.9 eV) peak corresponding to Al_2O_3 ALD coating as well as all of the above-mentioned peaks are shifted slightly to higher binding energy, due to the interaction with the coating (lattice oxygen at 529.6 eV, surface oxygen at 531.6 eV, CO at 532.6, and Na auger at 536.9 eV). As the electrolyte begins to decompose at 4.1V and 4.5V we begin to see organic decomposition products in Figure 8.12 and Figure 8.13 as well as oxidative species that result from the $NaPF_6$ salt ($Na_xPF_yO_z$ around 534 eV) for both coated and uncoated electrodes. However, for the Al_2O_3 coated electrode, the $Na_xPF_yO_z$ peak broadens and increases throughout electrochemical cycling. Moreover, the Al-O peak associated with the coating is present even after 100 cycles as shown in Figure 8.14. Both the O1s spectra and Al 2p spectra show a shift to higher binding energy as the cycle number increases. This could be due to the strong biding interaction that the ALD coating has with the electrode influencing the formation of a different CEI with respect to the uncoated electrode, consistent with the shift in binding energies of the CEI functionalities and an increase in salt decomposition products. Furthermore, this demonstrates the robustness of the coating, also demonstrated in Figure 8.9, where the ALD

coated electrode preserves the active material integrity even after repeated cycling. Consistent with the literature, we see that as we continue to cycle the electrodes, the surface oxygen peak decreases indicative of a thicker CEI formation.[297] Although it seems that the coated electrode has more CEI formation, the atomic percentage of carbon and oxygen in the surface is less than that of the uncoated P2-NaNiMnO (Figure 8.10). The dashed line in Figure 8.12, guides the peak shift that occurs throughout electrochemical cycling, which is more prevalent in the coated electrode. When peaks shift to higher binding energies it signifies that the binding environment is more electronegative which can be further investigated by F 1s (Figure 8.13 (a)), P 2p (Figure 8.13 (b)), and Na 1s (Figure 8.15).

Given that the electrode is composed of 80% active material, 10% PVDF binder, and 10% acetylene black, the uncycled electrodes have a large peak corresponding to the C-F bond of the binder (F 1s at 687 eV). This peak persists throughout cycling and continues to dominate the signal. Consistent with both the F 1s and Na 1s, a NaF peak at 684 eV for the uncoated P2-NaNiMnO and 685 eV for the Al_2O_3 coated electrode are observed. This is due to the interaction between the active material and the PVDF binder. The Na surface reacts with the PVDF to form NaF from the dehydroflurination, generating HF and reacting with Na, similar to the LIBs.[299–301] This is more prevalent in the Al_2O_3 coated electrode because it is needed to use the water as a precursor to form the aluminum oxide coating, which causes the PVDF binder to react with water forming more HF. Eventually, the formation of more NaF in the uncycled coated electrode maybe one of the causes for prepping the electrode surface to promote the formation of a more inorganic CEI leading to higher initial CE and overall cycling performance compared to the uncoated electrode (Figure 8.6).

As we charge the electrodes to 4.1V, we begin to see the decomposition products form that result from the $NaPF_6$ salt. Similar to $LiPF_6$, the sodium salt is susceptible to a similar process (reaction 8.1-8.3)

$$NaPF_6 \leftrightarrow Na^+ + PF_6^- \quad (8.1)$$

$$PF_6^- + Na^+ \rightarrow NaF + PF_5 \quad (8.2)$$

$$PF_5 + H_2O_{(trace)} \rightarrow OPF_3 + 2HF \quad (8.3)$$

Contrary to the uncoated electrode, the ALD coated cycled electrode has an increase in NaF throughout prolonged cycling, exhibited in both Figure 8.13 (a) and Figure 8.15. NaF on its own is a highly resistive material and it can be assumed that this would hinder the CEI; however, Figure 8.7 and Table 8.1 indicates otherwise. As salt decomposes, it is likely that we are not generating a consistent NaF film, but rather discrete crystallites that allows for Na-ions to pass as seen in the case of LIB.[297,302] At 4.1V we begin to see the decomposition of the salt (Figure 8.13 (b)), which is largely dominated by $Na_xPF_yO_z$ moieties generated when sodium continues to react with the OPF products in scheme 3. Little Na_xPF_6 is found when the electrodes are charged to 4.1 and 4.5V; however, it was observed that the amount of Na_xPF_6 increases when the electrodes are cycled both 5 and 100 times. This is largely seen in the uncoated electrode which maybe one of the factors that increases the impedance of the electrode surface, as seen in Figure 8.7. The CEI generated from the coated electrodes is more inorganic causing the electrolyte decomposition functionalities to shift to a higher binding energy. Moreover, it is widely accepted that coating cathode materials for LIBs improves the stability of the electrode-electrolyte interface. In our case, it is likely that the Al_2O_3 ALD coating tends to enhance the interface by protecting the electrode from HF formation (scheme 3).[303] Therefore, the electrode is less likely to form less unwanted byproducts as a result, boosting the coulombic efficiency.

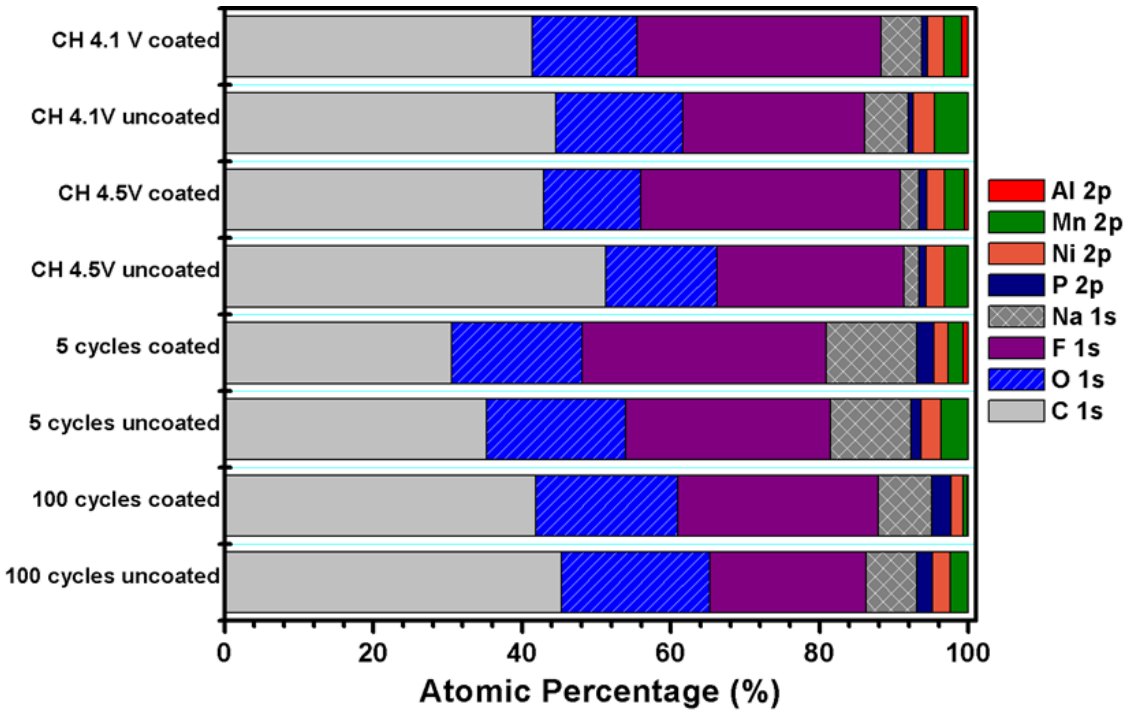

Figure 8.10. Elemental atomic percentage of the uncoated and ALD coated cycled electrodes at first charge 4.1V, 4.5V, 5 cycles, and 100 cycles.

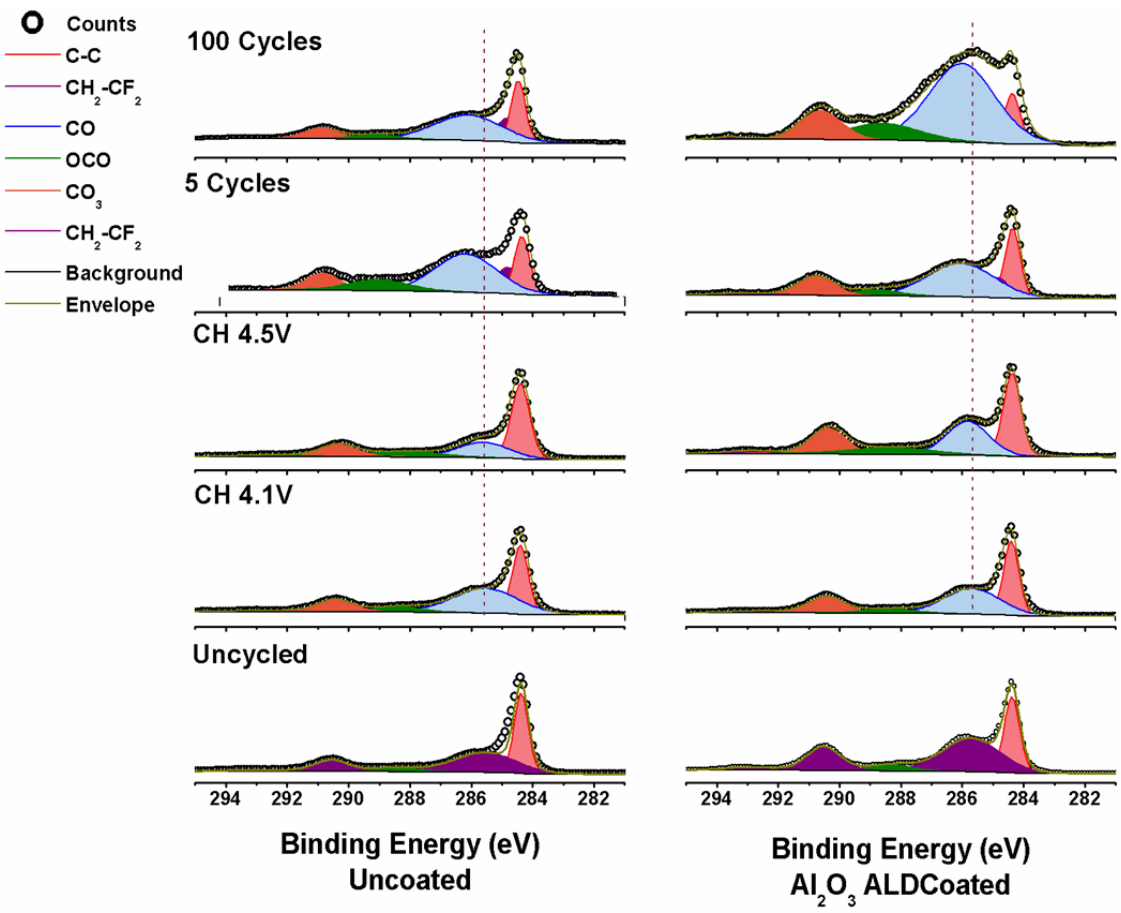

Figure 8.11. XPS C 1s regions of uncoated P2-NaNiMnO (left) and ALD Al_2O_3 coated (right) electrodes cycled to first charge 4.1V, 4.5V, 5 cycles, and 100 cycles.

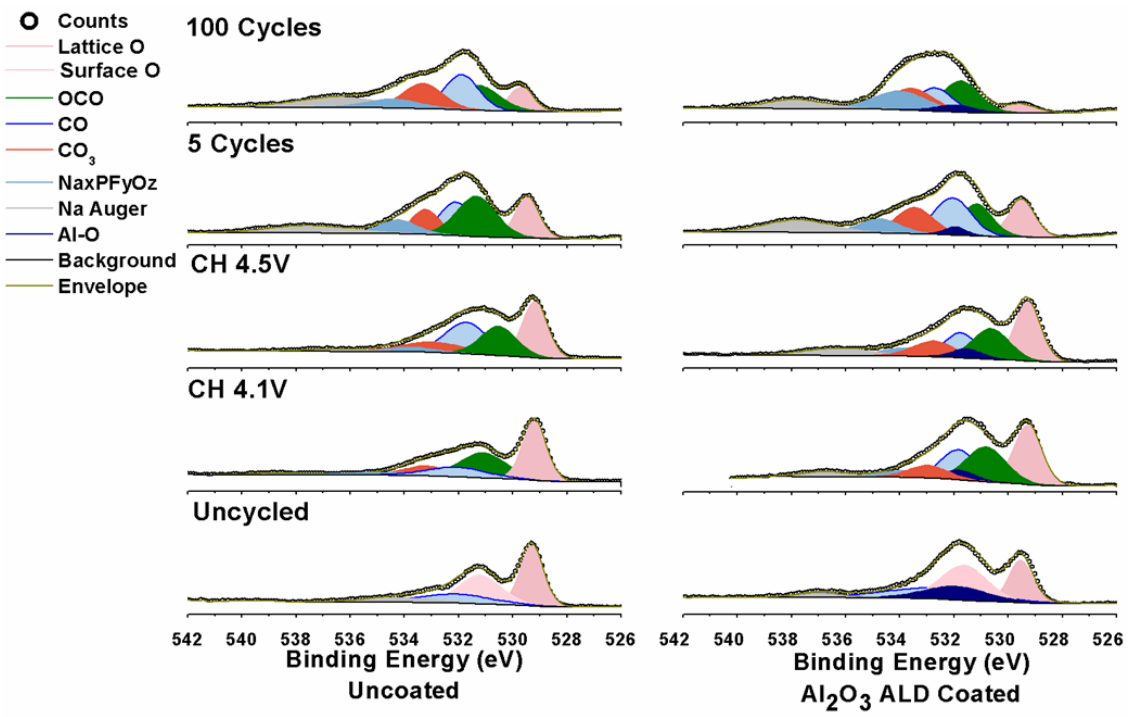

Figure 8.12. XPS O 1s regions of uncoated P2-NaNiMnO (left) and ALD Al_2O_3 coated (right) electrodes cycled.

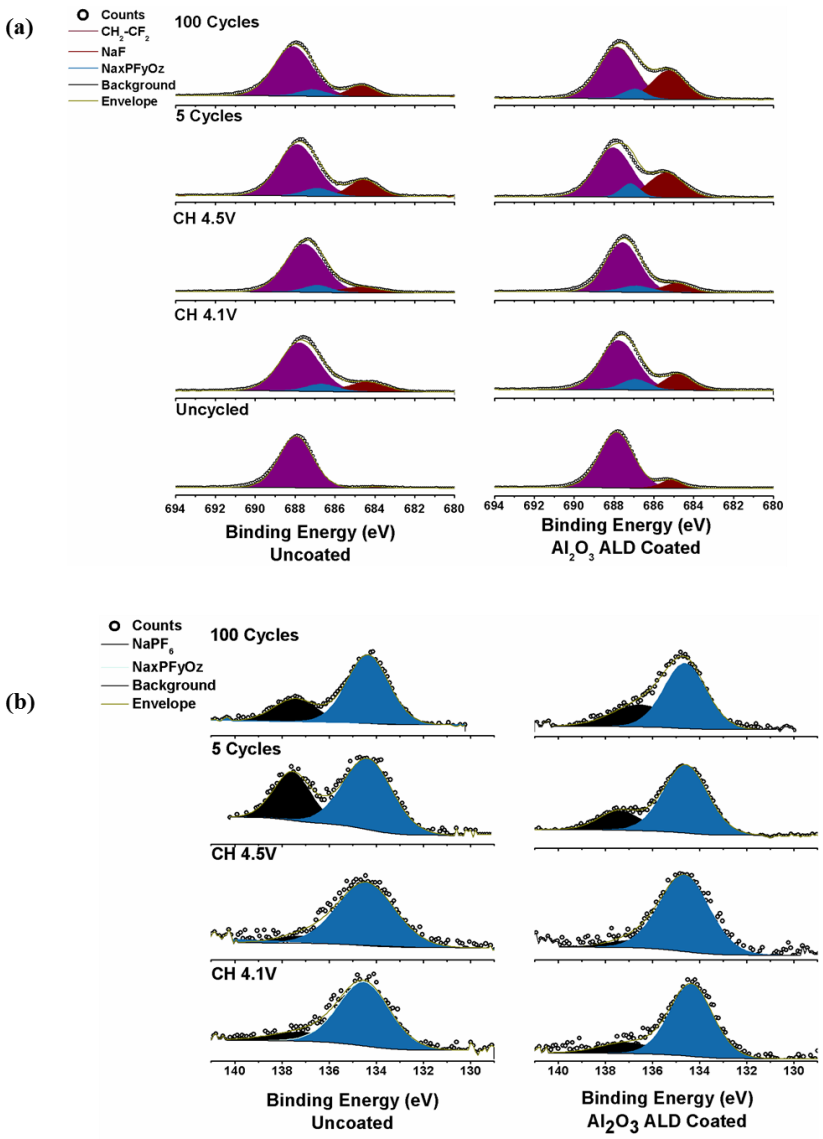

Figure 8.13. (a) XPS F 1s regions of uncoated P2-NaNiMnO (left) and ALD Al_2O_3 coated (right) electrodes cycled and (b) XPS P 2p region of ALD Al_2O_3 coated at to first charge 4.1V, 4.5V, 5 cycles, and 100 cycles.

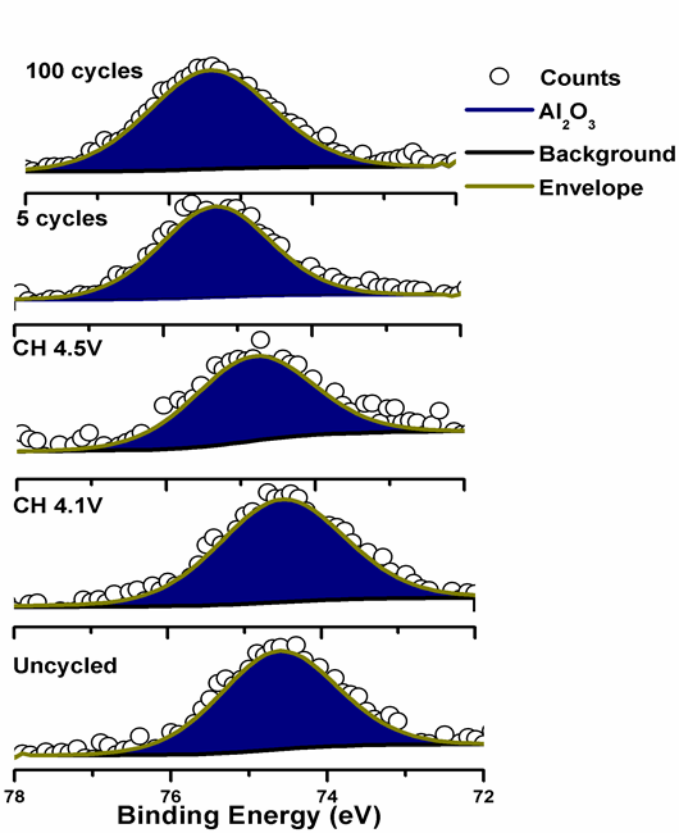

Figure 8.14. Elemental atomic percentage of the uncoated and ALD coated cycled electrodes at first charge 4.1V, 4.5V, 5 cycles, and 100 cycles.

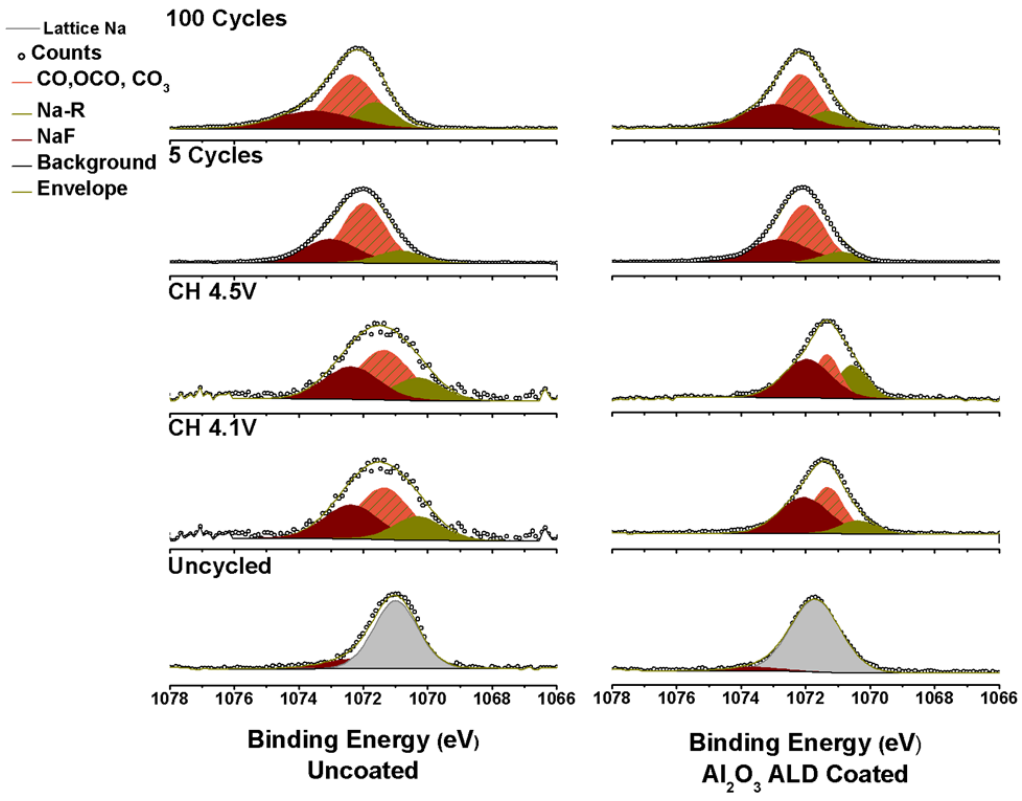

Figure 8.15. XPS Na 1s regions of uncoated P2-NaNiMnO (left) and ALD Al_2O_3 coated (right) electrodes cycled to first charge 4.1V, 4.5V, 5 cycles, and 100 cycles.

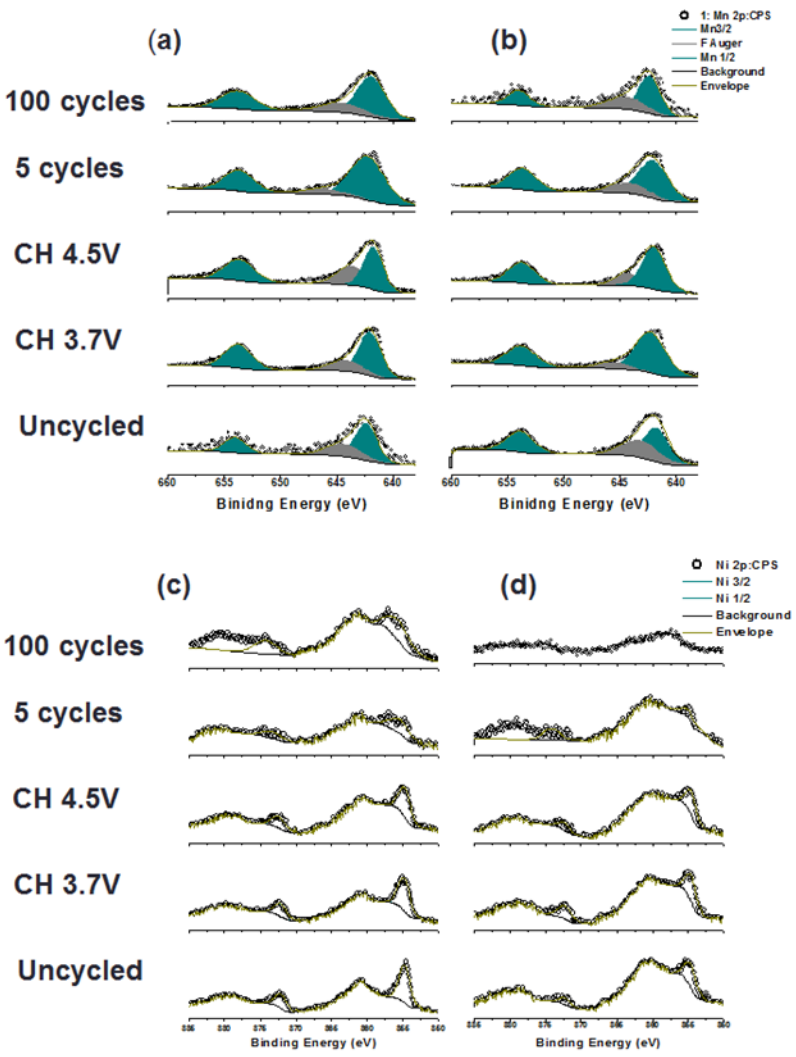

Figure 8.16. Nickel 2p region scan and fits of (a) uncoated P2_NaNiMnO and (b) ALD Al_2O_3 coated P2-NaNiMnO. Manganese 2p region scan and fits (c) uncoated and (d) coated electrode.

8.4. Conclusion

The comparison of a P2-$Na_{2/3}Ni_{1/3}Mn_{2/3}O_2$ electrode and Al_2O_3 ALD coated P2-$Na_{2/3}Ni_{1/3}Mn_{2/3}O_2$electrode was presented. The ALD coating drastically improved the initial and overall coulombic efficiency and cathode resistivity. The cathode electrolyte interphase was investigated by XPS, which determined that each electrode generated a different surface film. The uncoated electrode contained more organic species such as carbonates, esters, and alkoxyl functionalities, retained more residual salt, and formed less NaF. Conversely, the coated electrode forms large CO moieties that are associated with polymeric species such as polyethylene oxide, which play a critical factor in forming a more flexible CEI that can reduce the exfoliation of the P2-NaNiMnO particle (Figure 8.9). Furthermore, the coated electrode forms more NaF throughout cycling, which plays a vital role in the overall CEI. The CEI generated on the coated P2-NaNiMnO electrode enhances the Na-ion kinetics from the bulk of the material through the electrode film versus the uncoated electrode. We demonstrated that optimizing the P2- NaNiMnO surface is a vital parameter in improving the electrode electrolyte interface which facilitates the cycling performance of this class of materials.

Chapter 8, in full, is a reprint of the material “Improvement of the Cathode Electrolyte Interphase on P2-$Na_{2/3}Ni_{1/3}Mn_{2/3}O_2$ by Atomic Layer Deposition” as it appears in ACS Advanced Materials &Interfaces, Alvarado, J; Ma, C; Wang, S; Nguyen, K; Kodur, M; Meng, Y.S, 2017, 9 (31), 26518-26530. The dissertation author was the co-primary investigator and author of this paper. All the experiment parts were performed by the author except the FIB and TEM.

Chapter 9. Summary and Future Work

Rechargeable LIBs have reached a state of massive commercialization. Society is now highly dependent on LIBs to power numerous portable electronics and electric vehicles. Yet the energy density has only slightly increased, which is not yet sufficient to meet the energy demand. In order to meet this demand, stable materials and electrolytes must be studied. During electrochemical cycling, the electrolyte decomposes on the electrode to form the solid electrolyte interphase (SEI). The SEI plays a vital role in LIB cycling stability, performance, and safety. The focus of my thesis was to investigate additives, electrolytes, and protective coatings to improve the SEI. The physical and chemical properties were investigated with advanced characterization tools.

On the additive side, Fluoroethylene carbonate (FEC) was investigated as an electrolyte additive for silicon negative electrodes (Chapters 4 and 5). The SEI formed from $LiPF_6$-based carbonate electrolytes, with and without FEC were investigated on 50 nm thick amorphous silicon (a-Si) thin film electrodes and on composite Si electrodes. In contrast to previous work, anhydrous and anoxic techniques were used to prevent air and moisture contamination of prepared SEI films. This allowed for the accurate characterization of the SEI structure and its chemical composition by X-ray photoelectron spectroscopy (XPS) and time-of-flight secondary ion mass spectrometry (TOF-SIMS) depth profiling. Scanning transmission electron microscopy coupled with electron energy loss spectroscopy (STEM/EELS) gave insight as to how FEC affected the SEI evolution. In the first lithiation state, the electrode cycled without FEC formed a porous uneven SEI that contained mostly Li_2CO_3. However, the electrode cycled with the addition of FEC was covered in a dense and uniform SEI that mostly contained LiF. Surface

sensitive helium-ion microscopy (HIM) gave further insights to the SEI composition and its morphology. These results showed that the reduction of FEC led to the formation of fluoride ions and LiF, consistent with previous computational and experimental results. Surprisingly, we also found that these species decrease lithium-ion solubility and increase the reactivity of the silicon surface. We concluded that the effectiveness of FEC at improving the coulombic efficiency and capacity retention was due to fluoride ion formation from reduction of the electrolyte, which led to the chemical attack of any silicon-oxide and the formation of a kinetically stable SEI comprising predominately LiF and Li_2O.

In Chapter 6, electrolytes were investigated to improve the SEI on Lithium metal anodes. Lithium metal batteries are an enticing platform for matching the aggressively evolving energy and power demands for consumer electronics and electric vehicles. However, despite nearly a half-century of research efforts, serious barriers must be addressed before lithium metal anodes can deliver the efficiency and cycle life metrics that would warrant widespread adoption. Lithium bis(fluorosulfonyl) imide (LiFSI) was coupled with lithium bistrifluoromethanesulfonimidate (LiTFSI) at various concentrations to generate bisalt ether electrolytes. The plating/deplating efficiencies of lithium metal in the conventional carbonate based electrolyte and the current best performing high concentration ether electrolyte were compared to our bisalt ether electrolyte, which demonstrated remarkable improvements in efficiency and cycling stability. This behavior was observed in lithium versus copper cells, Li half cells, and “anode-free” full cell configurations with a few different cathode materials over their corresponding voltage ranges. Cryogenic-focused ion beam cross sectional milling after the initial plating state validated the dense Li metal morphology that resulted from the bisalt

electrolyte. XPS indicated that the solid electrolyte interphase was primarily composed of anion decomposition products, forming a more inorganic SEI.

In Chapter 7, a new sulfone solvent-LiFSI salt synergy was revealed which addressed the traditional performance issues of the current carbonate electrolytes at high voltages. Baseline characterization indicated that the system maintained good conductivity and stability over a wide temperature range while being nonflammable. Graphite half cell studies indicated that this rare carbonate-free system can rival the reversibility of conventional carbonate-based systems by forming a unique SEI which contained significant concentrations of LiF and Li_2O. The intrinsic stability and interface-dependent solvation behavior was elucidated by quantum chemistry calculations and molecular dynamics simulations. Our Sulfone-LiFSI electrolyte exhibits excellent high voltage and high temperature stability, which was demonstrated in $LiNi_{0.5}Mn_{1.5}O_4$ (LNMO) spinel full cell measurements.

In Chapter 8, Aluminum oxide (Al_2O_3) atomic layer deposition (ALD) surface coating was investigated to understand its effect on the SEI and electrode-electrolyte interface. ALD is known to improve the cycling performance, coulombic efficiency of batteries, and maintain electrode integrity. Therefore, the electrochemical performance of uncoated P2-$Na_{2/3}Ni_{1/3}Mn_{2/3}O_2$ electrodes was compared to ALD coated Al_2O_3 P2-$Na_{2/3}Ni_{1/3}Mn_{2/3}O_2$ electrodes. For the first time, XPS was used to elucidate the cathode electrolyte interphase (CEI) on ALD coated electrodes. The CEI contained less carbonate species and more inorganic species; this allows for fast Na kinetics, resulting in a significant increase in coulombic efficiency and a decrease in cathode impedance. Al_2O_3 ALD coating also enhanced the mechanical stability of the active material, which prevented particle exfoliation.

Given the abovementioned work, there is definitely room for improvement in all aspects of the battery. Therefore, for future work, I propose the improvement of the electrode-electrolyte interface in several ways. The first proposition is the modification of the electrolyte to chemically engineer the SEI. As mentioned in my thesis, a myriad of high voltage and high energy dense cathodes have been recently developed. However, their implementation in lithium ion batteries has been hindered due to instabilities with the electrolyte and/or the SEI. Currently, there are a few groups in the country that focus on the development of next generation electrolytes. There needs to be a push to completely alter the current carbonate based electrolyte. Recently, we determined that electrolytes without carbonate electrolytes are able to cycle high voltage cathodes. Sulfones and fluorinated ethers have also demonstrated high oxidation potential. Perhaps investigating electrolytes with functional groups containing nitrogen, sulfur, phosphorous, and lithium could generate a SEI that is more inorganic, less porous, and chemically stable. If accomplished, this could improve the battery cycling performance and safety.

The second proposition is the improvement of the electrode material stability. That includes improving particle coatings, surface coatings, and the current collector robustness. Electrode materials that undergo a morphology change during electrochemical cycling require a binder that maintains electrode tortuosity in order to avoid contact loss during cycling. This will further improve the overall electrode integrity. However, this is a difficult task because the material must be: 1) stable at high and low voltages; 2) mechanically robust; 3) stable against the electrolyte; 4) nontoxic, and; 5) inexpensive. Surface modification of the electrode or active material can greatly improve the performance of both cathode and anode materials. In particular, lithium rich cathodes exhibit oxygen activation in the first charge. Preventing the oxygen

evolution can significantly improve capacity retention. Coupling surface coatings with highly stable electrolytes can potentially mitigate oxygen gas evolution. This can subsequently improve the battery cycling efficiency while increasing the energy density of lithium ion batteries.

Finally, with the implementation of new lithium salts, the aluminum current collector has suffered significant corrosion. Therefore, I propose the implementation of surface modification of the Al current collector through *in-situ* electrochemical decomposition which could form a stable passivation layer on the Al to prevent the corrosion. This can be done by utilizing the advantages of various salts (dual salt electrolyte) which promote the stability of Al. Furthermore, an artificial surface treatment of the Al current collector before casting the electrode slurry could prevent corrosion at high voltages.

References

(1) Etacheri, V.; Marom, R.; Elazari, R.; Salitra, G.; Aurbach, D. .

(2) Xu, K. *Chem. Rev.* **2004**, *104* (10), 4303.

(3) Yabuuchi, N.; Kubota, K.; Dahbi, M.; Komaba, S. *Chem. Rev.* **2014**, *114* (23), 11636.

(4) Ozawa, K. *Solid State Ionics* **1994**, *69* (3), 212.

(5) Armand, M.; Tarascon, J.-M. *Nature* **2008**, *451* (7179), 652.

(6) Nitta, N.; Wu, F.; Lee, J. T.; Yushin, G. *Mater. Today* **2015**, *18* (5), 252.

(7) de las Casas, C.; Li, W. *J. Power Sources* **2012**, *208*, 74.

(8) Zhang, W.-J. *J. Power Sources* **2011**, *196* (1), 13.

(9) Liu, X. H.; Zhong, L.; Huang, S.; Mao, S. X.; Zhu, T.; Huang, J. Y. *ACS Nano* **2012**, *6* (2), 1522.

(10) Chan, C. K.; Peng, H.; Liu, G.; McIlwrath, K.; Zhang, X. F.; Huggins, R. A.; Cui, Y. *Nat. Nanotechnol.* **2007**, *3* (1), 31.

(11) Schroder, K.; Alvarado, J.; Yersak, T. A.; Li, J.; Dudney, N.; Webb, L. J.; Meng, Y. S.; Stevenson, K. J. *Chem. Mater.* **2015**, *27* (16), 5531.

(12) Li, J.; Dozier, A. K.; Li, Y.; Yang, F.; Cheng, Y.-T. *J. Electrochem. Soc.* **2011**, *158* (6), A689.

(13) Wang, J. W.; He, Y.; Fan, F.; Liu, X. H.; Xia, S.; Liu, Y.; Harris, C. T.; Li, H.; Huang, J. Y.; Mao, S. X. *Nano Lett.* **2013**, *13* (2), 709.

(14) Liu, W.-R. *Electrochem. Solid-State Lett.* **2005**, *8*.

(15) White, S. R.; Sottos, N. R.; Geubelle, P. H.; Moore, J. S.; Kessler, M. R.; Sriram, S. R.; Brown, E. N.; Viswanathan, S. *Nature* **2001**, *409* (6822), 794.

(16) Wang, C.; Wu, H.; Chen, Z.; McDowell, M. T.; Cui, Y.; Bao, Z. *Nat. Chem.* **2013**, *5* (12), 1042.

(17) Piper, D. M.; Travis, J. J.; Young, M.; Son, S.; Kim, S. C.; Oh, K. H.; George, S. M.; Ban, C.; Lee, S. *Adv. Mater.* **2014**, *26* (10), 1596.

(18) Yao, Y.; McDowell, M. T.; Ryu, I.; Wu, H.; Liu, N.; Hu, L.; Nix, W. D.; Cui, Y. *Nano Lett.* **2011**, *11* (7), 2949.

(19) Liu, N.; Wu, H.; McDowell, M. T.; Yao, Y.; Wang, C.; Cui, Y. *Nano Lett.* **2012**, *12* (6), 3315.

(20) Shobukawa, H.; Alvarado, J.; Yang, Y.; Meng, Y. S. *J. Power Sources* **2017**, *359*, 173.

(21) Jin, Y.; Li, S.; Kushima, A.; Zheng, X.; Sun, Y.; Xie, J.; Sun, J.; Xue, W.; Zhou, G.; Wu, J.; Shi, F.; Zhang, R.; Zhu, Z.; So, K.; Cui, Y.; Li, J. *Energy Environ. Sci.* **2017**, *10* (2), 580.

(22) Yim, C.-H.; Niketic, S.; Salem, N.; Naboka, O.; Abu-Lebdeh, Y. *J. Electrochem. Soc.* **2017**, *164* (1), A6294.

(23) Tikekar, M. D.; Choudhury, S.; Tu, Z.; Archer, L. A. *Nat. Energy* **2016**, *1* (9), 16114.

(24) Monroe, C.; Newman, J. *J. Electrochem. Soc.* **2005**, *152* (2), A396.

(25) Lin, D.; Liu, Y.; Cui, Y. *Nat. Nanotechnol.* **2017**, *12* (3), 194.

(26) Ding, F.; Xu, W.; Graff, G. L.; Zhang, J.; Sushko, M. L.; Chen, X.; Shao, Y.; Engelhard, M. H.; Nie, Z.; Xiao, J.; Liu, X.; Sushko, P. V.; Liu, J.; Zhang, J.-G. *J. Am. Chem. Soc.* **2013**, *135* (11), 4450.

(27) Pei, A.; Zheng, G.; Shi, F.; Li, Y.; Cui, Y. *Nano Lett.* **2017**, *17* (2), 1132.

(28) Mizushima, K.; Jones, P. C.; Wiseman, P. J.; Goodenough, J. B. *Mater. Res. Bull.* **1980**, *15* (6), 783.

(29) MIZUSHIMA, K.; JONES, P.; WISEMAN, P.; GOODENOUGH, J. *Solid State Ionics* **1981**, *3–4*, 171.

(30) Mohanty, D.; Li, J.; Nagpure, S. C.; Wood, D. L.; Daniel, C. *MRS Energy Sustain.* **2015**, *2*, E15.

(31) Fergus, J. W. *J. Power Sources* **2010**, *195* (4), 939.

(32) Arumugam, R. S.; Ma, L.; Li, J.; Xia, X.; Paulsen, J. M.; Dahn, J. R. *J. Electrochem. Soc.* **2016**, *163* (13), A2531.

(33) Wang, D. Y.; Xia, J.; Ma, L.; Nelson, K. J.; Harlow, J. E.; Xiong, D.; Downie, L. E.; Petibon, R.; Burns, J. C.; Xiao, A.; Lamanna, W. M.; Dahn, J. R. *J. Electrochem. Soc.* **2014**, *161* (12), A1818.

(34) Hy, S.; Liu, H.; Zhang, M.; Qian, D.; Hwang, B.-J.; Meng, Y. S. *Energy Environ. Sci.*

2016, *9* (6), 1931.

(35) Hy, S.; Su, W.-N.; Chen, J.-M.; Hwang, B.-J. *J. Phys. Chem. C* **2012**, *116* (48), 25242.

(36) Hy, S.; Felix, F.; Rick, J.; Su, W.-N.; Hwang, B. J. *J. Am. Chem. Soc.* **2014**, *136* (3), 999.

(37) Liu, H.; Qian, D.; Verde, M. G.; Zhang, M.; Baggetto, L.; An, K.; Chen, Y.; Carroll, K. J.; Lau, D.; Chi, M.; Veith, G. M.; Meng, Y. S. *ACS Appl. Mater. Interfaces* **2015**, *7* (34), 19189.

(38) Liu, H.; Huang, J.; Qian, D.; Hy, S.; Fang, C.; Luo, J.; Meng, Y. S. *J. Electrochem. Soc.* **2016**, *163* (6), A971.

(39) Qian, D.; Xu, B.; Chi, M.; Meng, Y. S. *Phys. Chem. Chem. Phys.* **2014**, *16* (28), 14665.

(40) Xu, B.; Fell, C. R.; Chi, M.; Meng, Y. S. *Energy Environ. Sci.* **2011**, *4* (6), 2223.

(41) Allen, J. L.; Thompson, T.; Sakamoto, J.; Becker, C. R.; Jow, T. R.; Wolfenstine, J. *J. Power Sources* **2014**, *254*, 204.

(42) Cho, H.-M.; Chen, M. V.; MacRae, A. C.; Meng, Y. S. *ACS Appl. Mater. Interfaces* **2015**, *7* (30), 16231.

(43) Peled, E.; Golodnitsky, D. In *Lithium-ion Batteries: Solid-Electrolyte Interphase*; Balbuena, P. B., Wang, Y., Eds.; World Scientific Publishing Company, 2004.

(44) Peled, E.; Golodnitsky, D.; Ardel, G.; Menachem, C.; Bar Tow, D.; Eshkenazy, V. In *MRS Proceedings*; 2011; Vol. 393, p 209.

(45) Etacheri, V.; Haik, O.; Goffer, Y.; Roberts, G. a.; Stefan, I. C.; Fasching, R.; Aurbach, D. *Langmuir* **2012**, *28* (1), 965.

(46) Chen, L.; Wang, K.; Xie, X.; Xie, J. *J. Power Sources* **2007**, *174*, 538.

(47) Ma, L.; Xia, J.; Dahn, J. R. *J. Electrochem. Soc.* **2014**, *161* (14), A2250.

(48) Xiong, D. J.; Petibon, R.; Nie, M.; Ma, L.; Xia, J.; Dahn, J. R. *J. Electrochem. Soc.* **2016**, *163* (3), A546.

(49) Goodenough, J. B.; Kim, Y. *Chem. Mater.* **2010**, *22* (3), 587.

(50) Solidfilms, T.; Dey, A. N.; Mallory, P. R. **1977**, *43*.

(51) Aurbach, D. *J. Electrochem. Soc.* **1987**, *134* (7), 1611.

(52) Peled, E. *J. Power Sources* **1983**, *9* (3), 253.

(53) Processes, L. D. **1996**, *143* (11), 1.

(54) Peled, E.; Ardel, G.; Golodnitsky, D. *J. Electrochem. Soc.* **1997**, *144* (8), L208.

(55) Zhuang, G. V.; Xu, K.; Yang, H.; Jow, T. R.; Ross, P. N. *J. Phys. Chem. B* **2005**, *109* (37), 17567.

(56) Zhuang, G. V.; Yang, H.; Ross, P. N.; Xu, K.; Jow, T. R. *Electrochem. Solid-State Lett.* **2006**, *9* (2), A64.

(57) Leung, K.; Soto, F.; Hankins, K.; Balbuena, P. B.; Harrison, K. L. *J. Phys. Chem. C* **2016**, *120* (12), 6302.

(58) Aurbach, D.; Zinigrad, E.; Cohen, Y.; Teller, H. *Solid State Ionics* **2002**, *148* (3–4), 405.

(59) Xu, K. *Chem. Rev.* **2014**, *114* (23), 11503.

(60) Nagy, G.; Lu, P.; Walker, A. V. *J. Am. Soc. Mass Spectrom.* **2008**, *19* (1), 33.

(61) Schroder, K. W.; Dylla, A. G.; Harris, S. J.; Webb, L. J.; Stevenson, K. J. *ACS Appl. Mater. Interfaces* **2014**, *6* (23), 21510.

(62) Nellist, P. D. .

(63) Hofer, F.; Schmidt, F. P.; Grogger, W.; Kothleitner, G. *IOP Conf. Ser. Mater. Sci. Eng.* **2016**, *109* (111), 12007.

(64) Mukhopadhyay, A.; Sheldon, B. W. *Prog. Mater. Sci.* **2014**, *63* (February), 58.

(65) Philippe, B.; Dedryveère, R.; Gorgoi, M.; Rensmo, H.; Gonbeau, D.; Edström, K. *Chem. Mater.* **2013**.

(66) Kim, H.; Han, B.; Choo, J.; Cho, J. *Angew. Chemie* **2008**, *120* (52), 10305.

(67) Magasinski, A.; Dixon, P.; Hertzberg, B.; Kvit, A.; Ayala, J.; Yushin, G. *Nat. Mater.* **2010**, *9* (4), 353.

(68) Xiao, X.; Liu, P.; Verbrugge, M. W.; Haftbaradaran, H.; Gao, H. *J. Power Sources* **2011**, *196* (3), 1409.

(69) Liu, X. H.; Zhong, L.; Huang, S.; Mao, S. X.; Zhu, T.; Huang, J. Y. **2012**, No. 2, 1522.

(70) Su, X.; Wu, Q.; Li, J.; Xiao, X.; Lott, A.; Lu, W.; Sheldon, B. W.; Wu, J. *Adv. Energy Mater.* **2014**, *4* (1), n/a.

(71) Liu, G.; Xun, S.; Vukmirovic, N.; Song, X.; Olalde-Velasco, P.; Zheng, H.; Battaglia, V. S.; Wang, L.; Yang, W. *Adv. Mater.* **2011**, *23* (40), 4679.

(72) Piper, D. M.; Travis, J. J.; Young, M.; Son, S.-B.; Kim, S. C.; Oh, K. H.; George, S. M.;

Ban, C.; Lee, S.-H. *Adv. Mater.* **2014**, *26* (10), 1596.

(73) Harris, S. J.; Lu, P. *J. Phys. Chem. C* **2013**, *117* (13), 6481.

(74) Verma, P.; Maire, P.; Novák, P. *Electrochim. Acta* **2010**, *55* (22), 6332.

(75) Balbuena, P. B. In *Proceedings of the 1st International Freiberg Conference on Electrochemical Storage Materials*; 2014; Vol. 82, pp 82–97.

(76) Aurbach, D. In *Advances in Lithium-Ion Batteries*; Schalkwijk, W. A., Scrosati, B., Eds.; Kluwer Academic Publishers: Boston, 2002.

(77) Deshpande, R.; Verbrugge, M. W.; Cheng, Y.-T.; Wang, J.; Liu, P. *J. Electrochem. Soc.* **2012**, *159* (10), A1730.

(78) Christensen, J.; Newman, J. *J. Electrochem. Soc.* **2004**, *151* (11), A1977.

(79) Christensen, J.; Newman, J. *J. Electrochem. Soc.* **2005**, *152* (4), A818.

(80) Markevich, E.; Salitra, G.; Fridman, K.; Sharabi, R.; Gershinsky, G.; Garsuch, A.; Semrau, G.; Schmidt, M. A.; Aurbach, D. *Langmuir* **2014**, *30* (25), 7414.

(81) BuddieáMullins, C.; Lin, Y.-M.; Klavetter, K. C.; Abel, P. R.; Davy, N. C.; Snider, J. L.; Heller, A.; Mullins, C. B. *Chem. Commun.* **2012**, *48* (58), 7268.

(82) Chockla, A. M.; Klavetter, K. C.; Mullins, C. B.; Korgel, B. A. *ACS Appl. Mater. Interfaces* **2012**, *4* (9), 4658.

(83) de la Hoz, J. M. M.; Balbuena, P. B. *Phys. Chem. Chem. Phys.* **2014**, *16* (32), 17091.

(84) Leung, K.; Rempe, S. B.; Foster, M. E.; Ma, Y.; Martinez del la Hoz, J. M.; Sai, N.; Balbuena, P. B. *J. Electrochem. Soc.* **2013**, *161* (3), A213.

(85) Ma, Y.; Balbuena, P. B. *J. Electrochem. Soc.* **2014**, *161* (8), E3097.

(86) Nguyen, C. C.; Lucht, B. L. *J. Electrochem. Soc.* **2014**, *161* (12), A1933.

(87) Nakai, H.; Kubota, T.; Kita, A.; Kawashima, A. *J. Electrochem. Soc.* **2011**, *158* (7), A798.

(88) Xiao, A.; Yang, L.; Lucht, B. L.; Kang, S.-H.; Abraham, D. P. *J. Electrochem. Soc.* **2009**, *156* (4), A318.

(89) Kang, S.-H.; Abraham, D. P.; Xiao, A.; Lucht, B. L. *J. Power Sources* **2008**, *175* (1), 526.

(90) Nie, M.; Chalasani, D.; Abraham, D. P.; Chen, Y.; Bose, A.; Lucht, B. L. *J. Phys. Chem. C* **2013**, *117* (3), 1257.

(91) Nie, M.; Abraham, D. P.; Chen, Y.; Bose, A.; Lucht, B. L. *J. Phys. Chem. C* **2013**, *117* (26), 13403.

(92) Liu, X. H.; Wang, J. W.; Huang, S.; Fan, F.; Huang, X.; Liu, Y.; Krylyuk, S.; Yoo, J.; Dayeh, S. A.; Davydov, A. V. *Nat. Nanotechnol.* **2012**, *7* (11), 749.

(93) Schroder, K. W.; Celio, H.; Webb, L. J.; Stevenson, K. J. *J. Phys. Chem. C* **2012**, *116* (37), 19737.

(94) Malmgren, S.; Ciosek, K.; Lindblad, R.; Plogmaker, S.; Kühn, J.; Rensmo, H.; Edström, K.; Hahlin, M. *Electrochim. Acta* **2013**, *105*, 83.

(95) Pereira-Nabais, C.; Światowska, J.; Rosso, M.; Ozanam, F.; Seyeux, A.; Gohier, A.; Tran-Van, P.; Cassir, M.; Marcus, P. *ACS Appl. Mater. Interfaces* **2014**, *6* (15), 13023.

(96) Xu, C.; Lindgren, F.; Philippe, B.; Gorgoi, M.; Björefors, F.; Edstrom, K.; Gustafsson, T. *Chem. Mater.* **2015**, *27* (7), 2591.

(97) Celio, H. Interface Designed with Differential Pumping and Built-in Figure of Merit Method to Monitor Chambers where Environmentally Sensitive Samples are Prepared and Transferred for Analysis. U.S. Patent App. Serial No. 14/445,650, 2014.

(98) Green, F. M.; Gilmore, I. S.; Seah, M. P. *J. Am. Soc. Mass Spectrom.* **2006**, *17* (4), 514.

(99) Elko-Hansen, T. D.-M.; Dolocan, A.; Ekerdt, J. G. *J. Phys. Chem. Lett.* **2014**, *5* (7), 1.

(100) Zimmerman, J. D.; Lassiter, B. E.; Xiao, X.; Sun, K.; Dolocan, A.; Gearba, R.; Vanden Bout, D. A.; Stevenson, K. J.; Wickramasinghe, P.; Thompson, M. E.; Forrest, S. R. *ACS Nano* **2013**, *7* (10), 9268.

(101) Perez, F.; Granger, B. E. *Comput. Sci. Eng.* **2007**, *9* (3), 21.

(102) van der Walt, S.; Colbert, S. C.; Varoquaux, G. *Comput. Sci. Eng.* **2011**, *13* (2), 22.

(103) Jones, E.; Oliphant, T.; Peterson, P. *SciPy: Open Source Scientific Tools for Python*; http://www.scipy.org/.

(104) McKinney, W. *Proc. 9th Python Sci. Conf.* **2010**, 51.

(105) Philippe, B.; Dedryvère, R.; Allouche, J.; Lindgren, F.; Gorgoi, M.; Rensmo, H.; Gonbeau, D.; Edström, K. *Chem. Mater.* **2012**, *24* (6), 1107.

(106) Radvanyi, E.; De Vito, E.; Porcher, W.; Jouanneau Si Larbi, S. *J. Anal. At. Spectrom.* **2014**, *29* (6), 1120.

(107) Martin, L.; Martinez, H.; Ulldemolins, M.; Pecquenard, B.; Le Cras, F. *Solid State Ionics* **2012**, *215*, 36.

(108) Radvanyi, E.; De Vito, E.; Porcher, W.; Danet, J.; Desbois, P.; Colin, J.-F.; Si Larbi, S. J.

J. Mater. Chem. A **2013**, *1* (16), 4956.

(109) Memarzadeh Lotfabad, E.; Kalisvaart, P.; Kohandehghan, A.; Karpuzov, D.; Mitlin, D. *J. Mater. Chem. A* **2014**, *2* (46), 19685.

(110) Peled, E.; Golodnitsky, D.; Menachem, C.; Bar-Tow, D. *J. Electrochem. Soc.* **1998**, *145* (10), 3482.

(111) Peled, E.; Golodnitsky, D.; Ardel, G.; Eshkenazy, V. *Electrochim. Acta* **1995**, *40* (13–14), 2197.

(112) Veryovkin, I. V.; Tripa, C. E.; Zinovev, a. V.; Baryshev, S. V.; Li, Y.; Abraham, D. P. *Nucl. Instruments Methods Phys. Res. Sect. B Beam Interact. with Mater. Atoms* **2014**, *332*, 368.

(113) Martinez de la Hoz, J. M.; Soto, F. a.; Balbuena, P. B. *J. Phys. Chem. C* **2015**, *119* (13), 7060.

(114) Cho, H.-M.; Meng, Y. S. *J. Electrochem. Soc.* **2013**, *160* (9), A1482.

(115) Chan, C. K.; Ruffo, R.; Hong, S. S.; Cui, Y. *J. Power Sources* **2009**, *189* (2), 1132.

(116) Wang, M. S.; Fan, L. Z. *J. Power Sources* **2013**, *244*, 570.

(117) Xiao, Y.; Hao, D.; Chen, H.; Gong, Z.; Yang, Y. *ACS Appl. Mater. Interfaces* **2013**, *5* (5), 1681.

(118) Aurbach, D.; Markovsky, B.; Weissman, I.; Levi, E.; Ein-Eli, Y. *Electrochim. Acta* **1999**, *45*, 67.

(119) Pyun, S.-I.; Bae, J.-S. *Electrochim. Acta* **1996**, *41* (6), 919.

(120) Lu, P.; Li, C.; Schneider, E. W.; Harris, S. J. *J. Phys. Chem. C* **2014**, *118* (2), 896.

(121) Wang, Q.; Sun, J.; Yao, X.; Chen, C. *Thermochim. Acta* **2005**, *437* (1–2), 12.

(122) Zinigrad, E.; Larush-Asraf, L.; Gnanaraj, J. S.; Sprecher, M.; Aurbach, D. *Thermochim. Acta* **2005**, *438* (1–2), 184.

(123) Yang, H.; Zhuang, G. V.; Ross, P. N. *J. Power Sources* **2006**, *161* (1), 573.

(124) Jones, J.; Anouti, M.; Caillon-Caravanier, M.; Willmann, P.; Lemordant, D. *J. Mol. Liq.* **2010**, *153* (2–3), 146.

(125) Tasaki, K. S. on the S. of L. S. F. on L. I. B. N. E. in O. S.; Harris, S. J. *J. Phys. Chem. C* **2010**, *114* (17), 8076.

(126) Tasaki, K.; Goldberg, A.; Lian, J.-J.; Walker, M.; Timmons, A. T.; Harris, S. J. *J. Electrochem. Soc.* **2009**, *156* (12), A1019.

(127) Bogart, T. D.; Chockla, A. M.; Korgel, B. a. *Curr. Opin. Chem. Eng.* **2013**, *2* (3), 286.

(128) Jorn, R.; Kumar, R.; Abraham, D. P.; Voth, G. a. *J. Phys. Chem. C* **2013**, *117* (8), 3747.

(129) Gu, M.; Li, Y.; Li, X.; Hu, S.; Zhang, X.; Xu, W.; Thevuthasan, S.; Baer, D. R.; Zhang, J.-G.; Liu, J.; Wang, C. *ACS Nano* **2012**, *6* (9), 8439.

(130) Xu, C.; Lindgren, F.; Philippe, B.; Gorgoi, M.; Björefors, F.; Edstrom, K.; Gustafsson, T. *Chem. Mater.* **2015**, 150312112229002.

(131) Nie, M.; Lucht, B. L. *J. Electrochem. Soc.* **2014**, *161* (6), A1001.

(132) Magasinski, A.; Zdyrko, B.; Kovalenko, I.; Hertzberg, B.; Burtovyy, R.; Huebner, C. F.; Fuller, T. F.; Luzinov, I.; Yushin, G. *ACS Appl. Mater. Interfaces* **2010**, *2* (11), 3004.

(133) Sina, M.; Thorpe, R.; Rangan, S.; Pereira, N.; Bartynski, R. A.; Amatucci, G. G.; Cosandey, F. *J. Phys. Chem. C* **2015**, *119* (18), 9762.

(134) Owejan, J. E.; Owejan, J. P.; DeCaluwe, S. C.; Dura, J. A. *Chem. Mater.* **2012**, *24* (11), 2133.

(135) Dupré, N.; Moreau, P.; Vito, E. De; Quazuguel, L.; Boniface, M.; Bordes, A.; Rudisch, C.; Bayle-Guillemaud, P.; Guyomard, D. *Chem. Mater. 0* (0), null.

(136) Park, C.-M.; Kim, J.-H.; Kim, H.; Sohn, H.-J. *Chem. Soc. Rev.* **2010**, *39* (8), 3115.

(137) Dalavi, S.; Guduru, P.; Lucht, B. L. *J. Electrochem. Soc.* **2012**, *159* (5), A642.

(138) Egerton, R. *Micron* **2004**, *35*, 399.

(139) Lin, F.; Markus, I. M.; Doeff, M. M.; Xin, H. L. *Sci. Rep.* **2014**, *4*, 5694.

(140) Cosandey, F.; Su, D.; Sina, M.; Pereira, N.; Amatucci, G. G. *Micron* **2012**, *43* (1), 22.

(141) Colder, A.; Huisken, F.; Trave, E.; Ledoux, G.; Guillois, O.; Reynaud, C.; Hofmeister, H.; Pippel, E. *Nanotechnology* **2004**, *15* (3), L1.

(142) Gu, M.; Xiao, X.-C.; Liu, G.; Thevuthasan, S.; Baer, D. R.; Zhang, J.-G.; Liu, J.; Browning, N. D.; Wang, C.-M. *Sci. Rep.* **2014**, *4*, 3684.

(143) Sina, M.; Pereira, N.; Amatucci, G. G.; Cosandey, F. *J. Phys. Chem. C* **2016**.

(144) Kimoto, Koji; Sekiguchi, Tomoko; Aoyama, T. *Japanese Soc. Electron Microsc.* **1997**, *46* (5), 369.

(145) He, Y.; Piper, D. M.; Gu, M.; Travis, J. J.; George, S. M.; Lee, S.-H.; Genc, A.; Pullan, L.;

Liu, J.; Mao, S. X.; Zhang, J.-G.; Ban, C.; Wang, C. *ACS Nano* **2014**, *8* (11), 11816.

(146) Sina, M.; Nam, K.-W.; Su, D.; Pereira, N.; Yang, X.-Q.; Amatucci, G. G.; Cosandey, F. *J. Mater. Chem. A* **2013**, *1* (38), 11629.

(147) Philippe, B.; Dedryvère, R.; Gorgoi, M.; Rensmo, H.; Gonbeau, D.; Edström, K. *Chem. Mater.* **2013**, *25*, 394.

(148) Philippe, B.; Dedryvère, R.; Gorgoi, M.; Rensmo, H.; Gonbeau, D.; Edström, K.; Dedryvere, R.; Edstrom, K. *J. Am. Chem. Soc.* **2013**, *135* (26), 9829.

(149) Leung, K.; Rempe, S. B.; Foster, M. E.; Ma, Y.; Martinez del la Hoz, J. M.; Sai, N.; Balbuena, P. B.; del la Hoz, J. M. M.; Sai, N.; Balbuena, P. B.; Martinez del la Hoz, J. M.; Sai, N.; Balbuena, P. B. *J. Electrochem. Soc.* **2014**, *161* (3), A213.

(150) Raji, A. O.; Villegas Salvatierra, R.; Kim, N. D.; Fan, X.; Li, Y.; Silva, G. A. L.; Sha, J.; Tour, J. M. *ACS Nano* **2017**, *11* (6), 6362.

(151) Zheng, G.; Lee, S. W.; Liang, Z.; Lee, H. W.; Yan, K.; Yao, H.; Wang, H.; Li, W.; Chu, S.; Cui, Y. *Nat Nanotechnol* **2014**, *9* (8), 618.

(152) Lin, D.; Liu, Y.; Liang, Z.; Lee, H. W.; Sun, J.; Wang, H.; Yan, K.; Xie, J.; Cui, Y. *Nat Nanotechnol* **2016**, *11* (7), 626.

(153) Zhang, H.; Li, C.; Piszcz, M.; Coya, E.; Rojo, T.; Rodriguez-Martinez, L. M.; Armand, M.; Zhou, Z. *Chem Soc Rev* **2017**, *46* (3), 797.

(154) Thompson, T.; Sharafi, A.; Johannes, M. D.; Huq, A.; Allen, J. L.; Wolfenstine, J.; Sakamoto, J. *Adv. Energy Mater.* **2015**, *5* (11), 1500096.

(155) Lee, J. Z.; Wang, Z.; Xin, H. L.; Wynn, T. A.; Meng, Y. S. *J. Electrochem. Soc.* **2016**, *164* (1), A6268.

(156) Dudney, N. J. *J. Power Sources* **2000**, *89*, 176.

(157) Sharafi, A.; Kazyak, E.; Davis, A. L.; Yu, S.; Thompson, T.; Siegel, D. J.; Dasgupta, N. P.; Sakamoto, J. *Chem. Mater.* **2017**, *29* (18), 7961.

(158) Liu, Y.; Lin, D.; Liang, Z.; Zhao, J.; Yan, K.; Cui, Y. *Nat Commun* **2016**, *7*, 10992.

(159) Younesi, R.; Veith, G. M.; Johansson, P.; Edström, K.; Vegge, T. *Energy Environ. Sci.* **2015**, *8* (7), 1905.

(160) Jeong, S.-K.; Seo, H.-Y.; Kim, D.-H.; Han, H.-K.; Kim, J.-G.; Lee, Y. B.; Iriyama, Y.; Abe, T.; Ogumi, Z. *Electrochem. commun.* **2008**, *10* (4), 635.

(161) Park, M. S.; Ma, S. B.; Lee, D. J.; Im, D.; Doo, S. G.; Yamamoto, O. *Sci Rep* **2014**, *4*, 3815.

(162) Jow, T. R.; Xu, K.; Borodin, O.; Makoto, U. *Electrolytes for lithium and lithium-ion batteries*; Springer, 2014; Vol. 58.

(163) Ding, F.; Xu, W.; Chen, X.; Zhang, J.; Engelhard, M. H.; Zhang, Y.; Johnson, B. R.; Crum, J. V; Blake, T. A.; Liu, X.; Zhang, J. G. *J. Electrochem. Soc.* **2013**, *160* (10), A1894.

(164) Zheng, J.; Lochala, J. A.; Kwok, A.; Deng, Z. D.; Xiao, J. *Adv. Sci.* **2017**, 1700032.

(165) Suo, L.; Hu, Y. S.; Li, H.; Armand, M.; Chen, L. *Nat Commun* **2013**, *4*, 1481.

(166) Kim, H.; Wu, F.; Lee, J. T.; Nitta, N.; Lin, H. T.; Oschatz, M.; Cho, W. Il; Kaskel, S.; Borodin, O.; Yushin, G. *Adv. Energy Mater.* **2015**, *5* (6), 1.

(167) Wang, J.; Yamada, Y.; Sodeyama, K.; Chiang, C. H.; Tateyama, Y.; Yamada, A. *Nat. Commun.* **2016**, *7*.

(168) Qian, J.; Henderson, W. A.; Xu, W.; Bhattacharya, P.; Engelhard, M.; Borodin, O.; Zhang, J.-G. *Nat. Commun.* **2015**, *6*, 6362.

(169) Miao, R.; Yang, J.; Feng, X.; Jia, H.; Wang, J.; Nuli, Y. *J. Power Sources* **2014**, *271*, 291.

(170) Wood, K. N.; Kazyak, E.; Chadwick, A. F.; Chen, K. H.; Zhang, J. G.; Thornton, K.; Dasgupta, N. P. *ACS Cent Sci* **2016**, *2* (11), 790.

(171) Bai, P.; Li, J.; Brushett, F. R.; Bazant, M. Z. *Energy Environ. Sci.* **2016**, *9* (10), 3221.

(172) Devika Sirohi Lei Sun, Thomas Klose, Theodore C. Pierson, Michael G. Rossmann, Richard J. Kuhn, Z. C. *Science (80-.).* **2016**, *352* (6284), 467.

(173) Bartesaghi, A.; Merk, A.; Banerjee, S.; Matthies, D.; Wu, X.; Milne, J. L. S.; Subramaniam, S. *Science (80-.).* **2015**, *348* (6239), 1147.

(174) Bai, X.-C.; McMullan, G.; Scheres, S. H. W. *Trends Biochem. Sci.* **2015**, *40* (1), 49.

(175) Qian, J.; Adams, B. D.; Zheng, J.; Xu, W.; Henderson, W. A.; Wang, J.; Bowden, M. E.; Xu, S.; Hu, J.; Zhang, J. G. *Adv. Funct. Mater.* **2016**, *26* (39), 7094.

(176) Aurbach, D.; Talyosef, Y.; Markovsky, B.; Markevich, E.; Zinigrad, E.; Asraf, L.; Gnanaraj, J. S.; Kim, H.-J. *Electrochim. Acta* **2004**, *50* (2), 247.

(177) Aurbach, D.; Daroux, M. L.; Faguy, P. W.; Yeager, E. *J. Electrochem. Soc.* **1987**, *134* (7), 1611.

(178) Barchasz, C.; Leprêtre, J. C.; Patoux, S.; Alloin, F. *Electrochim. Acta* **2013**, *89*, 737.

(179) Miao, R.; Yang, J.; Xu, Z.; Wang, J.; Nuli, Y.; Sun, L. *Sci. Rep.* **2016**, *6* (February), 21771.

(180) Zhang, Y.; Qian, J.; Xu, W.; Russell, S. M.; Chen, X.; Nasybulin, E.; Bhattacharya, P.; Engelhard, M. H.; Mei, D.; Cao, R.; Ding, F.; Cresce, A. V; Xu, K.; Zhang, J. G. *Nano Lett* **2014**, *14* (12), 6889.

(181) Sacci, R. L.; Dudney, N. J.; More, K. L.; Parent, L. R.; Arslan, I.; Browning, N. D.; Unocic, R. R. *Chem Commun* **2014**, *50* (17), 2104.

(182) Dingchang Lin Yi Cui, Y. L. *Reviving the lithium metal anode for high-energy batteries*; Nature, 2017; Vol. 12.

(183) Lee, J.-S.; Tai Kim, S.; Cao, R.; Choi, N.-S.; Liu, M.; Lee, K. T.; Cho, J. *Adv. Energy Mater.* **2011**, *1* (1), 34.

(184) Doron Aurbach and Alexander Schechter, Hagai Cohen, * Idit Weissman. *Langmuir* **1996**.

(185) Aurbach, D.; Gofer, Y. *J. Electrochem. Soc.* **1991**, *138* (12), 3529.

(186) Xu, K. *Chem. Rev.* **2004**, *104*.

(187) Gallagher, K. G.; Goebel, S.; Greszler, T.; Mathias, M.; Oelerich, W.; Eroglu, D.; Srinivasan, V. *Energy Environ. Sci.* **2014**, *7*, 1555.

(188) Barchasz, C.; Leprêtre, J.-C.; Patoux, S.; Alloin, F. *Electrochim. Acta* **2013**, *89*, 737.

(189) Suo, L.; Borodin, O.; Gao, T.; Olguin, M.; Ho, J.; Fan, X.; Luo, C.; Wang, C.; Xu, K. *Science (80-.).* **2015**, *350* (6263), 938.

(190) Suo, L.; Borodin, O.; Sun, W.; Fan, X.; Yang, C.; Wang, F.; Gao, T.; Ma, Z.; Schroeder, M.; von Cresce, A.; Russell, S. M.; Armand, M.; Angell, A.; Xu, K.; Wang, C. *Angew Chem Int Ed Engl* **2016**, *55* (25), 7136.

(191) Zhang, S. S. *J. Power Sources* **2006**, *162* (2), 1379.

(192) Brown, Z. L.; Jurng, S.; Lucht, B. L. *J. Electrochem. Soc.* **2017**, *164* (9), A2186.

(193) Zheng, J.; Yan, P.; Mei, D.; Engelhard, M. H.; Cartmell, S. S.; Polzin, B. J.; Wang, C.; Zhang, J.-G.; Xu, W. *Adv. Energy Mater.* **2016**, *6* (8), 1502151.

(194) Peled, E. *J. Electrochem. Soc.* **1979**, *126* (12), 2047.

(195) Xia, J.; Petibon, R.; Xiong, D.; Ma, L.; Dahn, J. R. *J. Power Sources* **2016**, *328*, 124.

(196) Xia, J.; Petibon, R.; Xiao, A.; Lamanna, W. M.; Dahn, J. R. *J. Electrochem. Soc.* **2016**, *163* (8), A1637.

(197) Chalasani, D.; Li, J.; Jackson, N. M.; Payne, M.; Lucht, B. L. *J. Power Sources* **2012**, *208*,

67.

(198) Li, B.; Xu, M. Q.; Li, T. T.; Li, W. S.; Hu, S. J. *Electrochem. commun.* **2012**, *17*, 92.

(199) Han, G. B.; Ryou, M. H.; Cho, K. Y.; Lee, Y. M.; Park, J. K. *J. Power Sources* **2010**, *195* (11), 3709.

(200) Manthiram, A.; Chemelewski, K.; Lee, E. S. *Energy Environ. Sci.* **2014**, *7* (4), 1339.

(201) Demeaux, J.; Lemordant, D.; Caillon-Caravanier, M.; Galiano, H.; Claude-Montigny, B. *Electrochim. Acta* **2013**, *89*, 163.

(202) Pieczonka, N. P. W.; Liu, Z. Y.; Lu, P.; Olson, K. L.; Moote, J.; Powell, B. R.; Kim, J. H. *J. Phys. Chem. C* **2013**, *117* (31), 15947.

(203) Xu, M. Q.; Tsiouvaras, N.; Garsuch, A.; Gasteiger, H. A.; Lucht, B. L. *J. Phys. Chem. C* **2014**, *118* (14), 7363.

(204) Chen, J.; Zhang, H.; Wang, M.; Liu, J.; Li, C.; Zhang, P. *J. Power Sources* **2016**, *303*, 41.

(205) Jarry, A.; Gottis, S.; Yu, Y.-S.; Roque-Rosell, J.; Kim, C.; Cabana, J.; Kerr, J.; Kostecki, R. *J. Am. Chem. Soc.* **2015**, *137* (10), 3533.

(206) Han, H. B.; Zhou, S. S.; Zhang, D. J.; Feng, S. W.; Li, L. F.; Liu, K.; Feng, W. F.; Nie, J.; Li, H.; Huang, X. J.; Armand, M.; Zhou, Z. B. *J. Power Sources* **2011**, *196* (7), 3623.

(207) Xu, K.; Angell, C. A. *J. Electrochem. Soc.* **2002**, *149* (7), A920.

(208) Ding, M. S.; von Cresce, A.; Xu, K. *J. Phys. Chem. C* **2017**, *121* (4), 2149.

(209) Ding, M. S.; Xu, K.; Zhang, S. S.; Amine, K.; Henriksen, G. L.; Jow, T. R. *J. Electrochem. Soc.* **2001**, *148* (10), A1196.

(210) Zugmann, S.; Fleischmann, M.; Amereller, M.; Gschwind, R. M.; Wiemhofer, H. D.; Gores, H. J. *Electrochim. Acta* **2011**, *56* (11), 3926.

(211) Cresce, A. V; Russell, S. M.; Borodin, O.; Allen, J. A.; Schroeder, M. A.; Dai, M.; Peng, J.; Gobet, M. P.; Greenbaum, S. G.; Rogers, R. E.; Xu, K. *Phys. Chem. Chem. Phys.* **2017**, *19* (1), 574.

(212) Chen, F. F.; Forsyth, M. *Phys. Chem. Chem. Phys.* **2016**, *18* (28), 19336.

(213) Giffin, G. A.; Moretti, A.; Jeong, S.; Passerini, S. *J. Power Sources* **2017**, *342*, 335.

(214) Seo, D. M.; Borodin, O.; Balogh, D.; O'Connell, M.; Ly, Q.; Han, S.-D.; Passerini, S.; Henderson, W. A. *J. Electrochem. Soc* **2013**, *160* (8), A1061.

(215) Katon, J. E.; Feairheller, W. R. *Spectrochim. Acta* **1965**, *21* (1), 199.

(216) Xuan, X.; Wang, J.; Lu, J.; Pei, N.; Mo, Y. *Spectrochim. Acta Part A Mol. Biomol. Spectrosc.* **2001**, *57* (8), 1555.

(217) Seo, D. M.; Borodin, O.; Han, S.-D.; Ly, Q.; Boyle, P. D.; Henderson, W. A. *J. Electrochem. Soc* **2012**, *159* (5), A553.

(218) Wu, F.; Borodin, O.; Yushin, G. *MRS Energy Sustain.* **2017**, *4*, 1.

(219) Xu, K.; von Cresce, A. *J. Mater. Chem.* **2011**, *21* (27), 9849.

(220) Sun, X. G.; Angell, C. A. *Electrochem. commun.* **2009**, *11* (7), 1418.

(221) Nie, M.; Abraham, D. P.; Seo, D. M.; Chen, Y.; Bose, A.; Lucht, B. L. *J. Phys. Chem. C* **2013**, *117* (48), 25381.

(222) Pan, Y.; Wang, G. L.; Lucht, B. L. *Electrochim. Acta* **2016**, *217*, 269.

(223) Xu, K. *J. Electrochem. Soc.* **2009**, *156* (9), A751.

(224) Tasaki, K.; Goldberg, A.; Winter, M. *Electrochim. Acta* **2011**, *56* (28), 10424.

(225) Besenhard, J. O.; Winter, M.; Yang, J.; Biberacher, W. *J. Power Sources* **1995**, *54* (2), 228.

(226) Wagner, M. R.; Albering, J. H.; Moeller, K. C.; Besenhard, J. O.; Winter, M. *Electrochem. commun.* **2005**, *7* (9), 947.

(227) Leung, K. *Phys. Chem. Chem. Phys.* **2015**, *17* (3), 1637.

(228) Kawaguchi, T.; Shimada, K.; Ichitsubo, T.; Yagi, S.; Matsubara, E. *J. Power Sources* **2014**, *271* (0), 431.

(229) Delp, S. A.; Borodin, O.; Olguin, M.; Eisner, C. G.; Allen, J. L.; Jow, T. R. *Electrochim. Acta* **2016**, *209*, 498.

(230) Suo, L.; Borodin, O.; Wang, Y.; Rong, X.; Sun, W.; Fan, X.; Xu, S.; Schroeder, M. A.; Cresce, A. V; Wang, F.; Yang, C.; Hu, Y.-S.; Xu, K.; Wang, C. *Adv. Energy Mater.* **2017**, 1701189.

(231) Yamada, Y.; Usui, K.; Chiang, C. H.; Kikuchi, K.; Furukawa, K.; Yamada, A. *ACS Appl Mater Interfaces* **2014**, *6* (14), 10892.

(232) Yamada, Y.; Furukawa, K.; Sodeyama, K.; Kikuchi, K.; Yaegashi, M.; Tateyama, Y.; Yamada, A. *J Am Chem Soc* **2014**, *136* (13), 5039.

(233) Edström, K.; Herstedt, M.; Abraham, D. P. *J. Power Sources* **2006**, *153* (2), 380.

(234) Kiyoshi Kanamura, H. T. and Z. T. .*l. Electroanal. Chem* **1992**, *333*.

(235) Bryngelsson, H.; Stjerndahl, M.; Gustafsson, T.; Edström, K. *J. Power Sources* **2007**, *174* (2), 970.

(236) Gu, W.; Borodin, O.; Zdyrko, B.; Lin, H.-T.; Kim, H.; Nitta, N.; Huang, J.; Magasinski, A.; Milicev, Z.; Berdichevsky, G.; Yushin, G. *Adv. Func. Mater.* **2016**, *26* (10), 1490.

(237) Shkrob, I. A.; Marin, T. W.; Zhu, Y.; Abraham, D. P. *J. Phys. Chem. C* **2014**, *118* (34), 19661.

(238) Budi, A.; Basile, A.; Opletal, G.; Hollenkamp, A. F.; Best, A. S.; Rees, R. J.; Bhatt, A. I.; O'Mullane, A. P.; Russo, S. P. *J. Phys. Chem. C* **2012**, *116* (37), 19789.

(239) Borodin, O.; Olguin, M.; Spear, C.; Leiter, K.; Knap, J.; Yushin, G.; Childs, A.; Xu, K. *ECS Trans.* **2015**, *69* (1), 113.

(240) Camacho-Forero, L. E.; Smith, T. W.; Balbuena, P. B. *J. Phys. Chem. C* **2016**.

(241) Wang, Y.; Xing, L.; Li, W.; Bedrov, D. *J. Phys. Chem. Lett.* **2013**, *4* (22), 3992.

(242) Xing, L. D.; Tu, W. Q.; Vatamanu, J.; Liu, Q. F.; Huang, W. N.; Wang, Y. T.; Zhou, H. B.; Zeng, R. H.; Li, W. S. *Electrochim. Acta* **2014**, *133*, 117.

(243) Borodin, O.; Behl, W.; Jow, T. R. *J. Phys. Chem. C* **2013**, *117* (17), 8661.

(244) Borodin, O.; Olguin, M.; Spear, C. E.; Leiter, K.; Knap, J. *Nanotechnology* **2015**, *26* (35), 354003.

(245) Tarascon, J.-M.; Armand, M. *Nature* **2001**, *414* (6861), 359.

(246) Dunn, B.; Kamath, H.; Tarascon, J.-M. *Science (80-.).* **2011**, *334* (Li), 928.

(247) Kim, S.-W.; Seo, D.-H.; Ma, X.; Ceder, G.; Kang, K. *Adv. Energy Mater.* **2012**, *2* (7), 710.

(248) Fouassier, C.; Delmas, C.; Hagenmuller, P. *Mater. Res. Bull.* **1975**, *10* (6), 443.

(249) Parant, J. P.; Olazcuaga, R.; Devalette, M.; Fouassier, C.; Hagenmuller, P. *J. Solid State Chem.* **1971**, *3* (1), 1.

(250) Xu, J.; Liu, H.; Meng, Y. S. *Electrochem. commun.* **2015**, *60*, 13.

(251) Bucher, N.; Hartung, S.; Franklin, J. B.; Wise, A. M.; Lim, L. Y.; Chen, H.-Y.; Weker, J. N.; Toney, M. F.; Srinivasan, M. *Chem. Mater.* **2016**, *28* (7), 2041.

(252) Kundu, D.; Talaie, E.; Duffort, V.; Nazar, L. F. *Angew Chem Int Ed Engl* **2015**, *54* (11), 3431.

(253) Han, M. H.; Gonzalo, E.; Singh, G.; Rojo, T. *Energy Environ. Sci.* **2015**, *8* (1), 81.

(254) Komaba, S.; Murata, W.; Ishikawa, T.; Yabuuchi, N.; Ozeki, T.; Nakayama, T.; Ogata, A.; Gotoh, K.; Fujiwara, K. *Adv. Funct. Mater.* **2011**, *21* (20), 3859.

(255) Xu, J.; Ma, C.; Balasubramanian, M.; Meng, Y. S. *Chem. Commun.* **2014**, *50*, 12564.

(256) Lu, Y. C.; Ma, C.; Alvarado, J.; Kidera, T.; Dimov, N.; Meng, Y. S.; Okada, S. *J. Power Sources* **2015**, *284*, 287.

(257) Lu, Y. C. Y. C.; Ma, C.; Alvarado, J.; Dimov, N.; Meng, Y. S. Y. S.; Okada, S. *J. Mater. Chem. A* **2015**, *0* (33), 1.

(258) Xiang, X.; Zhang, K.; Chen, J. *Adv. Mater.* **2015**, *27* (36), 5343.

(259) Xu, J.; Lee, D. a E. H. O. E.; Meng, Y. S. *Funct. Mater. Lett.* **2013**, *6* (1), 1330001.

(260) J. M. Paulsen; R. A. Donaberger, † and; Dahn*, J. R. **2000**.

(261) Lu, Z.; Dahn, J. R. *J. Electrochem. Soc.* **2001**, *148* (11), A1225.

(262) Lee, D. H.; Xu, J.; Meng, Y. S. *Phys. Chem. Chem. Phys.* **2013**, *15*, 3304.

(263) Clément, R. J.; Xu, J.; Middlemiss, D. S.; Alvarado, J.; Ma, C.; Meng, Y. S.; Grey, C. P. **2017**.

(264) Clément, R. J.; Bruce, P. G.; Grey, C. P. *J. Electrochem. Soc.* **2015**, *162* (14), A2589.

(265) Wu, X.; Guo, J.; Wang, D.; Zhong, G.; McDonald, M. J.; Yang, Y. *J. Power Sources* **2015**, *281*, 18.

(266) Wu, X.; Xu, G.-L.; Zhong, G.; Gong, Z.; McDonald, M. J.; Zheng, S.; Fu, R.; Chen, Z.; Amine, K.; Yang, Y. *ACS Appl. Mater. Interfaces* **2016**, *8* (34), 22227.

(267) Xu, J.; Lee, D. H.; Clément, R. J.; Yu, X.; Leskes, M.; Pell, A. J.; Pintacuda, G.; Yang, X.-Q.; Grey, C. P.; Meng, Y. S. *Chem. Mater.* **2014**, *26* (2), 1260.

(268) George, S. M. *Chem. Rev.* **2010**, 111.

(269) Memarzadeh Lotfabad, E.; Kalisvaart, P.; Cui, K.; Kohandehghan, A.; Kupsta, M.; Olsen, B.; Mitlin, D. *Phys. Chem. Chem. Phys.* **2013**, *15* (32), 13646.

(270) Jung, Y. S.; Cavanagh, A. S.; Dillon, A. C.; Groner, M. D.; George, S. M.; Lee, S.-H. *J. Electrochem. Soc.* **2010**, *157* (1), A75.

(271) Cheng, H.-M.; Wang, F.-M.; Chu, J. P.; Santhanam, R.; Rick, J.; Lo, S.-C. *J. Phys. Chem. C* **2012**, *116*, 7629.

(272) Lee, J. H.; Hon, M. H.; Chung, Y. W.; Leu, I. C. *Appl. Phys. A Mater. Sci. Process.* **2011**, *102* (3), 545.

(273) Zhao, J.; Qu, G.; Flake, J. C.; Wang, Y. *Chem. Commun.* **2012**, *48* (65), 8108.

(274) Liu, J.; Li, X.; Cai, M.; Li, R.; Sun, X. *Electrochim. Acta* **2013**, *93*, 195.

(275) Li, C.; Zhang, H. P.; Fu, L. J.; Liu, H.; Wu, Y. P.; Rahm, E.; Holze, R.; Wu, H. Q. *Electrochim. Acta* **2006**, *51* (19), 3872.

(276) Zhao, L.; Zhao, J.; Hu, Y.-S.; Li, H.; Zhou, Z.; Armand, M.; Chen, L. *Adv. Energy Mater.* **2012**, *2* (8), 962.

(277) Han, X.; Liu, Y.; Jia, Z.; Chen, Y.-C.; Wan, J.; Weadock, N.; Gaskell, K. J.; Li, T.; Hu, L. *Nano Lett.* **2014**, *14* (1), 139.

(278) Kaliyappan, K.; Liu, J.; Lushington, A.; Li, R.; Sun, X. *ChemSusChem* **2015**, *8* (15), 2537.

(279) Liu, Y.; Fang, X.; Zhang, A.; Shen, C.; Liu, Q.; Enaya, H. A.; Zhou, C. *Nano Energy* **2016**, *27*, 27.

(280) Wang, S.; Sina, M.; Parikh, P.; Uekert, T.; Shahbazian, B.; Devaraj, A.; Meng, Y. S. *Nano Lett.* **2016**, *16* (9), 5594.

(281) Kim, S.; Park, M. J.; Balsara, N. P.; Liu, G.; Minor, A. M. *Ultramicroscopy* **2010**, *111*, 191.

(282) Malmgren, S.; Ciosek, K.; Hahlin, M.; Gustafsson, T.; Gorgoi, M.; Rensmo, H.; Edström, K. *Electrochim. Acta* **2013**, *97*, 23.

(283) Lu, Z.; Dahn, J. R. *J. Electrochem. Soc.* **2001**, *148* (11), A1225.

(284) Mueller, S.; Tuth, R.; Fischer, D.; Wille-haussmann, B.; Wittwer, C. *201*.

(285) Kim, J. W.; Kim, D. H.; Oh, D. Y.; Lee, H.; Kim, J. H.; Lee, J. H.; Jung, Y. S. *J. Power Sources* **2015**, *274*, 1254.

(286) Su, Y.; Cui, S.; Zhuo, Z.; Yang, W.; Wang, X.; Pan, F. .

(287) Sun Park, J.; Meng, X.; Elam, J. W.; Hao, S.; Wolverton, C.; Kim, C.; Cabana, J. .

(288) Wise, A. M.; Ban, C.; Weker, J. N.; Misra, S.; Cavanagh, A. S.; Wu, Z.; Li, Z.; Whittingham, M. S.; Xu, K.; George, S. M.; Toney, M. F. *Chem. Mater.* **2015**, *27* (17), 6146.

(289) Liu, J.; Manthiram, A. *Chem. Mater.* **2009**, *21* (7), 1695.

(290) Li, X.; Liu, J.; Meng, X.; Tang, Y.; Banis, M. N.; Yang, J.; Hu, Y.; Li, R.; Cai, M.; Sun, X. *J. Power Sources* **2014**, *247*, 57.

(291) Riley, L. A.; Van Atta, S.; Cavanagh, A. S.; Yan, Y.; George, S. M.; Liu, P.; Dillon, A. C.; Lee, S.-H. *J. Power Sources* **2011**, *196* (6), 3317.

(292) Jung, S. C.; Kim, H. J.; Choi, J. W.; Han, Y. K. *Nano Lett.* **2014**, *14* (11), 6559.

(293) Ender, M.; Weber, A.; Ivers-Tiffée, E. *J. Electrochem. Soc.* **2012**, *159* (2), A128.

(294) Lu, Z.; Dahn, J. R. *J. Electrochem. Soc.* **2001**, *148* (7), A710.

(295) Guan, C.; Wang, X.; Zhang, Q.; Fan, Z.; Zhang, H.; Fan, H. J. *Nano Lett.* **2014**, *14* (8), 4852.

(296) He, Y.; Yu, X.; Wang, Y.; Li, H.; Huang, X. *Adv. Mater.* **2011**, *23* (42), 4938.

(297) Verdier, S.; El Ouatani, L.; Dedryvère, R.; Bonhomme, F.; Biensan, P.; Gonbeau, D. *J. Electrochem. Soc.* **2007**, *154* (12), A1088.

(298) Fleutot, S.; Dupin, J.-C.; Renaudin, G.; Martinez, H. *Phys. Chem. Chem. Phys.* **2011**, *13* (39), 17564.

(299) Quinlan, R. A.; Lu, Y.-C.; Kwabi, D.; Shao-Horn, Y.; Mansour, A. N. *J. Electrochem. Soc.* **2016**, *163* (2), A300.

(300) Verde, M. G.; Liu, H.; Carroll, K. J.; Baggetto, L.; Veith, G. M.; Meng, Y. S. *ACS Appl. Mater. Interfaces* **2014**, *6* (21), 18868.

(301) Edström, K.; Gustafsson, T.; Thomas, J. O. *Electrochim. Acta* **2004**, *50* (2–3), 397.

(302) Andersson, A. M.; Edström, K. *J. Electrochem. Soc.* **2001**, *148* (10), A1100.

(303) Gauthier, M.; Carney, T. J.; Grimaud, A.; Giordano, L.; Pour, ⊥ Nir; Chang, H.-H.; Fenning, D. P.; Lux, S. F.; Paschos, O.; Bauer, C.; Maglia, F.; Lupart, S.; Lamp, P.; Shao-Horn, Y. .